Dissertation zur Erlangung des Doktorgrades an der Fakultät für
Mathematik, Informatik und Naturwissenschaften
Fachbereich Geowissenschaften
Universität Hamburg

Oceanic internal gravity waves and turbulent mixing: observations and parameterizations

vorgelegt von Friederike Pollmann
Hamburg, 2017

- Korrigierte Fassung -
Tag der Disputation: 13.12.2017
Folgende Gutachter empfehlen die Annahme der Dissertation:
Prof. Dr. Carsten Eden
Prof. Dr. Dirk Olbers

Versicherung an Eides statt

Hiermit versichere ich an Eides statt, dass ich die vorliegende Dissertationsschrift selbständig verfasst und keine anderen als die angegebenen Quellen und Hilfsmittel benutzt habe. Diese Arbeit hat weder ganz noch in Teilen zu einem früheren Zeitpunkt an der Universität Hamburg oder an anderer Stelle einer Promotionskommission zur Erlangung des Doktorgrades vorgelegen.

Hamburg, den

Zusammenfassung

Durch die Vermischung der vertikalen Dicheteschichtung und den Transport von Gehalts- und Nährstoffen spielt kleinskalige Turbulenz in vielen marinen Ökosystemen sowie für die Energiebilanz des Ozeans eine zentrale Rolle. Als solche trägt sie unter anderem zur Aufrechterhaltung der großskaligen Ozeanzirkulation bei und ist daher auch für das globale Klimasystem von großer Bedeutung. Obwohl sie weitreichende Auswirkungen haben, sind die turbulenten Vermischungsprozesse selbst zu klein, um in Computermodellen aufgelöst zu werden, und müssen daher parametrisiert werden. Da Turbulenz im offenen Ozean hauptsächlich durch das Brechen interner Schwerewellen hervorgerufen wird, bildet deren Dynamik die Grundlage von konsistenten Turbulenz-Parametrisierungen. Das Modell IDEMIX ("Internal Wave Dissipation, Energy and Mixing") beschreibt die Entstehung, Ausbreitung und das Brechen interner Schwerewellen basierend auf einer vereinfachten Form der spektralen Energiebilanz. Die dissipierte Energie der Wellen wird der turbulenten kinetischen Energie zugeführt, sodass die Energetik der internen Schwerewellen letztlich die diapyknische Diffusivität und die Dissipationsraten der turbulenten kinetischen Energie bestimmt. IDEMIX ist daher ein wichtiger Bestandteil von energetisch konsistenten Ozeanmodellen, in denen der Energieaustausch zwischen den aufgelösten und parametrisierten dynamischen Komponenten ohne künstliche Energiequellen und -senken modelliert wird.

Ziel dieser Doktorarbeit ist es, IDEMIX im Vergleich mit Beobachtungen zu evaluieren. Feinstruktur-Messungen von Argo-Floats sind in großen Mengen nahezu überall in den Weltmeeren vorhanden und bilden daher eine ideale Referenz für diese Modell-Evaluation. Sie ermöglichen nicht nur die Berechnung von vertikalen Diffusivitäten und Dissipationsraten der turbulenten kinetischen Energie, sondern auch, wie in dieser Arbeit gezeigt wird, die Bestimmung des Energiegehalts der internen Schwerewellen. Die Unsicherheit dieser Größen wird beruhend auf einer Sensitivitätsanalyse bezüglich der Parametereinstellungen der Feinstruktur-Methode unter Berücksichtigung von Mess- und Statistikfehlern als ein Faktor 5 beziffert.

IDEMIX kann sowohl die Größe als auch die großskaligen geographischen Variationen der Argo-basierten Werte reproduzieren. Regionen mit hohen Energien und Dissipationsraten sind allerdings oftmals zu klein verglichen mit den Beobachtungen und die komplette vertikale Struktur wird selten richtig wiedergegeben. Dies impliziert, dass IDEMIX zu wenige physikalische Details beschreibt und verbessert werden könnte, indem sowohl die bereits implementierten Antriebsfunktionen genauer modelliert werden als auch Prozesse, die bisher vernachlässigt wurden, berücksichtigt werden. Dazu zählt die Definition regional veränderlicher Parameter, wie zum Beispiel die modale Bandbreite des Garrett-Munk-Modells oder die Höhe des Windenergieeintrags in die niederfrequenten Schwerewellen, die derzeit als globale Konstanten betrachtet werden. Gleichermaßen ist eine realistischere Beschreibung des Energieübertrags von mesoskaligen Wirbeln zu internen Schwerewellen, der im Moment nur stark vereinfacht in IDEMIX re-

präsentiert wird, wünschenswert. Motiviert wird dieser Ansatz durch die Beobachtung, dass diese Energiequelle selbst in ihrer vereinfachten Darstellung in Regionen hoher mesoskaliger Aktivität essentiell wichtig ist, um die Argo-basierten Dissipationsraten und Energiegehalte in IDEMIX zu reproduzieren. Alle diese Schritte erfordern die Synthese von analytischen, numerischen und Beobachtungsstudien, um die verschiedenen physikalischen Prozesse besser zu verstehen und sie korrekt zu modellieren.

Eine weitere Vereinfachung, auf die IDEMIX und andere Modelle interner Schwerewellen zurückgreifen, ist die richtungsunabhängige Betrachtung des Energieübertrags von den barotropen zu den baroklinen Gezeiten. Genau genommen sind die Geschwindigkeiten der Gezeitenströme sowie das Relief des Meeresbodens räumlich inhomogen, sodass die Energie der internen Wellen, die vom rauen Ozeanboden ausstrahlt, je nach Richtung variiert, was wiederum die geographische Verteilung der Stärke turbulenter Vermischungsprozesse im Nah- und Fernfeld beeinflusst. Im zweiten Teil dieser Doktorarbeit wird eine neue Methode präsentiert, die diese Diskrepanz aufhebt: Indem der Energieübertrag als integrierter Energiefluss anstatt, wie bisher üblich, als Integral über die Energiequellen berechnet wird, kann seine Winkelabhängigkeit basierend auf linearer Theorie berechnet werden. Da die Herleitung dieser Methode auf der Annahme beruht, die Tidengeschwindigkeiten seien konstant, wird der Meeresboden in sich teilweise überdeckende Kreise unterteilt und der Energieübertrag wird individuell in jedem einzelnen berechnet. Dabei wird der Einfluss der weiter entfernten Topographie vernachlässigt indem sie allmählich zum Kreisrand hin auf Null reduziert wird. Mit Hilfe idealisierter Topographie-Profile wird die Methode evaluiert und geeignete Einstellungen für die numerischen Parameter, zum Beispiel wie stark benachbarte Kreise sich überlagern, werden festgelegt. Für relevante Übertragungsraten ist die Übereinstimmung mit der analytischen Lösung sehr gut, solange der Kreisradius etwa neun Mal so groß wie die horizontale Wellenlänge der entsprechenden Vertikalmode der internen Welle ist und mindestens doppelt so groß wie der Abstand zwischen den Mittelpunkten benachbarter Kreise. Wenn die Methode auf eine Region mit realistischer Topographie im zentralen Nordatlantik angewandt wird, müssen diese Werte angepasst werden: der Kreisradius muss mindestens dreimal so groß sein wie der Abstand zwischen Kreismittelpunkten und, zumindest für den Fall mittlerer und hoher Moden mit größeren horizontalen Wellenzahlen, mindestens 12 Mal so groß wie die horizontale Wellenlänge. Diese Ergebnisse dienen als Orientierung für globale Berechnungen, die durch die guten Ergebnisse in idealisierten Szenarien sowie die Unterschiede zwischen der von IDEMIX berechneten Schwerewellenenergie in Simulationen mit richtungsabhängigem und -unabhängigem Gezeitenenergieeintrag motiviert werden.

Abstract

By mixing density in the vertical and by transporting tracers and nutrients, small-scale turbulence plays a key role in many oceanic ecosystems as well as for the ocean's energy budget. As such, it contributes to maintaining the large-scale ocean circulation and is therefore of great importance for the global climate system. Contrary to its large-scale implications, turbulent mixing itself is too small to be resolved in numerical models and consequently has to be parameterized. Because breaking internal gravity waves are a major source of open ocean turbulence, their dynamics form the basis of consistent mixing parameterizations. The model IDEMIX ("Internal Wave Dissipation, Energy and Mixing") describes the generation, propagation, and breaking of internal gravity waves based on a simplification of the spectral energy balance. The dissipated internal wave energy is transferred to turbulent kinetic energy, so that the diapycnal diffusivity and the turbulent kinetic energy dissipation rate are ultimately determined by internal gravity wave energetics. IDEMIX is therefore a pivotal component of energetically consistent ocean models, in which the energy exchange between the resolved and parameterized dynamical regimes is modeled without any spurious sources and sinks.

The aim of this PhD project is to evaluate IDEMIX against observations. Finestructure measurements from Argo floats are available in large numbers almost everywhere in the global ocean and are therefore chosen as the observational reference for this model-data comparison. They do not only allow the calculation of vertical diffusivities and turbulent kinetic energy dissipation rates, but also, as derived in this thesis, the computation of internal wave energy levels. These finestructure estimates' average uncertainty is determined as a factor of 5 based on a sensitivity analysis to the parameter settings of the finestructure method and the consideration of statistical and measurement uncertainties.

IDEMIX well reproduces the magnitudes as well as the large-scale geographic variations of the Argo-based estimates. Regions of high energy levels and dissipation rates, however, are often modeled too small compared the observations and the full vertical structure is rarely captured. This suggests that IDEMIX misses physical detail and could be improved both by better describing the forcing functions already implemented and by including processes which have been neglected so far. Possible steps include the definition of regionally variable parameters, such as the modal bandwidth of the Garrett-Munk model or the amount of wind energy input into near-inertial gravity waves, which are currently treated as global constants. Similarly, a more realistic description of the energy transfer from mesoscale eddies to internal gravity waves is desirable, which is at present only crudely represented in IDEMIX. This step is motivated by the observation that even in such a simplified form, this forcing is essential for IDEMIX to reproduce the Argo-based dissipation rate and energy level estimates in regions of enhanced mesoscale activity. All proposed measures require joint efforts from analytical, numerical, and observational studies to better understand the different physical processes and to model them correctly.

Another simplification currently used in IDEMIX and other internal wave models is to consider the barotropic to baroclinic tidal energy conversion as directionally invariant. In reality, however, the tidal velocity field as well as the seafloor topography are spatially inhomogeneous so that the amount of internal wave energy radiated away from the rough ocean bottom varies with direction, which in turn affects the geographic distribution of near- and far-field wave-induced mixing strength. The second part of this PhD thesis presents a new method to overcome this gap: By calculating the conversion as the integrated energy flux instead of, as previously done, the integrated energy sources, its angle dependence can be described following linear theory. As the flux is derived based on the assumption that tidal velocities are constant, the ocean floor is subdivided into overlapping circular patches and the conversion rate is calculated individually in each of them, neglecting the influence of remote topography by smoothly tapering it to zero toward the circle's boundary. Idealized topographic profiles are used to evaluate the method and to determine suitable numerical parameters such as the patch overlap. For relevant conversion rates, the agreement with the analytical solution is very good if the patch radius is about nine times the horizontal wavelength of the specific internal tide mode and at least twice the distance between neighboring patch centers. Considering a region of realistic topography in the central North Atlantic, these values need to be adjusted to three times the patch center distance and, for intermediate and higher modes with higher horizontal wavenumbers, to 12 times the horizontal wavelength. These results serve as a guideline for global calculations, which are motivated by the good performance of the method in idealized setups as well as the differences in internal wave energy modeled by IDEMIX in experiments with directionally variable compared to directionally constant tidal forcing.

Contents

1 Introduction

Turbulence is an irregular state of flow, whose energetic motion already fascinated Leonardo da Vinci (see Fig. 1.1). His remarkably modern description "The small eddies are almost numberless, and large things are rotated only by large eddies and not by small ones, and small things are turned by both small eddies and large." [quoted in Gad-el Hak, 2006] characterizes turbulence as a type of flow, in which swirling motions (so-called "eddies") of different spatial scales feature and interact. The effect of this edying motion is to stir the fluid, that is, to increase the area of contact between adjacent fluid volumes and to sharpen the gradients across them. Higher gradients lead to stronger molecular diffusion, so that turbulent mixing (the combination of stirring and diffusion) transfers momentum, heat, and tracers at much higher rates than molecular transports alone [Thorpe, 2007]. The transport of energy in turbulent flows is typically compared to a cascade, in which large eddies become unstable to smaller eddies, which in turn transfer their energy to ever smaller eddies [Richardson, 1920]. At millimeter to centimeter scales, the kinetic energy of the turbulent flow is finally transformed into heat, again supported by the creation of large gradients (of velocity) through turbulent stirring [Thorpe, 2007].

This turbulent transport of tracers has important consequences for ocean biota and ocean dynamics: Phytoplankton are affected by vertical mixing processes because they determine nutrient supply, light penetration, and, in case of non-motile diatoms, their mobility [Estrada and Berdalet, 1997]. Phytoplankton life cycles in turn affect those of marine herbivores and their predators, and phytoplankton blooms can affect sedimentation rates as well as overall ecosystem health in case of harmful algae blooms [Peeters et al. [2013]; Thomas and Gibson [1990] showed in laboratory experiments that active turbulence inhibits the growth of dinoflagellate red tides]. Turbulence in the surface layer drives air-sea gas exchange, influencing the oceanic uptake of oxygen, greenhouse gases, or volatile pollutants [Zappa et al., 2007], and contributes to transferring momentum from atmospheric winds to ocean currents [Dhanak and Xiros, 2016]. Due to its effective dispersion of tracers, turbulence also plays a crucial role in the assessment of climate change mitigation strategies such as deep ocean injection of carbon dioxide [Dewey and Stegen, 1999].

Possibly the most far-reaching impact of turbulent mixing is related to its vertical transport of heat and salt and the resultant changes in seawater density. These affect ocean currents of different sizes all the way to the global-scale overturning circulation. This giant conveyor-like circulation involves localized deep water formation in the North Atlantic

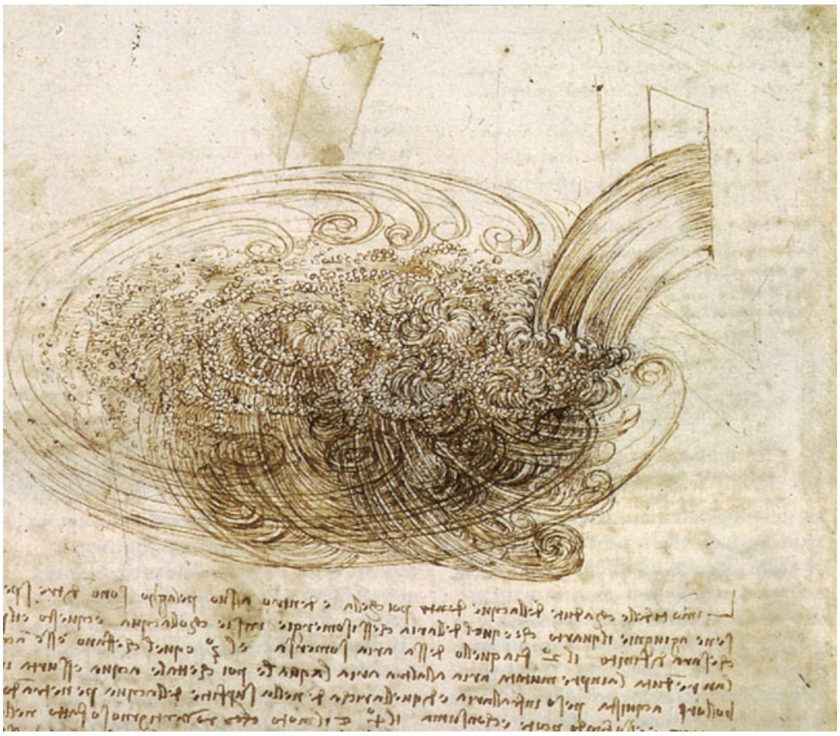

Figure 1.1: Sketch of turbulent motion in water by Leonardo da Vinci ("Studies of Water Passing Obstacles and Falling into a Pool", pen and brown ink over traces of black chalk on laid paper, Her Majesty Queen Elizabeth II, Royal Library, Windsor, RL 12660v. Source: https://simple.wikipedia.org/wiki/Fluid_mechanics, accessed 06/12/2017).

and in the Southern Ocean, the spreading of these water masses at depth, their upwelling to intermediate depths, and thermocline currents which close the loop. In the Atlantic Ocean, it induces an interhemispheric northward heat transport of up to 1.2 PW [Hall and Bryden, 1982]—heat that is at high latitudes lost to the atmosphere at rates comparable to the solar insolation during winter months and crucially shapes European climate [Toggweiler and Key, 2003]. Two mechanisms have been proposed to drive the global overturning circulation: the Ekman divergence induced by the strong westerly winds in the Southern Ocean, where water upwells to the surface from great depths due to the lack of zonal topographic barriers above 2500 m in Drake Passage [Toggweiler and Samuels, 1995], and diapycnal mixing in the ocean interior [Munk and Wunsch, 1998]. The relative importance of these mechanisms is still a topic of ongoing debate, especially since meso-scale eddies have been observed to counteract the wind-driven upwelling by flattening out isopycnals previously tilted by the wind [Johnson and Bryden, 1989; Olbers and Visbeck, 2005], but the general consensus based on analytical, observational, and numerical studies is that both processes play a vital role [e.g. Kuhlbrodt et al., 2007; Klocker and McDougall, 2010; Talley, 2013]. The schematic in Fig. 1.2 depicts the main features

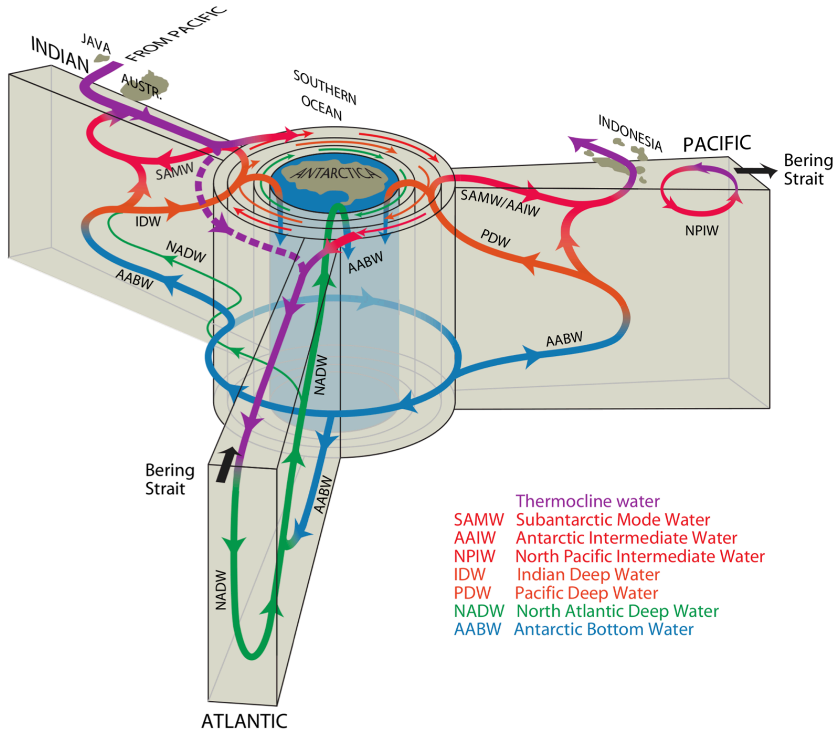

Figure 1.2: Schematic illustration of the global overturning circulation. The different colors refer to different water masses and the dashed purple line represents eddies shed from the Agulhas current. Returning North Atlantic Deep Water (NADW) to the surface involves both wind-driven upwelling in the Southern Ocean and upwelling generated by turbulent mixing in the Indian and Pacific Oceans [Talley, 2013].

of the global overturning circulation, illustrating that the pathways of the different water masses are intertwined throughout the different ocean basins and that these are subject to different forcing mechanisms. In a heat budget analysis, Talley [2013] concludes that about half of the heating required to return North Atlantic Deep Water to the surface results from diapycnal diffusion in the interior Indian and Pacific Oceans, underlining the importance of turbulent mixing processes for large-scale climate dynamics.

Oceanic mixing can be generated by a multitude of processes [Thorpe, 2007]: The breaking of wind-generated waves in the upper ocean produces turbulence which helps to sustain the ocean mixed layer. In the benthic boundary layer, turbulent motions arise because of the vertical shears associated with bottom friction. More localized sources include the geothermal heat flux from the seabed, where hydrothermal plumes can form that turbulently rise and entrain surrounding water [Thurnherr and St. Laurent, 2012], or Langmuir circulation near the ocean surface, characterized by counter-rotating vortices that can contribute to deepening the mixed layer [Li et al., 1995]. Double-diffusive convection, an instability caused by the different molecular diffusivities of heat and salt, manifests itself in elongated filaments termed “salt-fingers” or as a an overstable oscillation, depending on the sign of the vertical temperature and salinity gradients [Schmitt, 1998]. In both cases, the initial instability breaks down to form convective layers separated by thin interfaces, vertically mixing temperature and salinity in a way that transforms their initially smooth gradients into staircase-like profiles [Kelley et al., 2003; Schmitt et al., 2005]. Even biological sources have been suggested, such as small abundant animals that pull water along as they move in large schools or flocks [Kunze et al., 2006a; Katija and Dabiri, 2009]. Their relevance for the global ocean energy budget, however, is considered minor, since they create turbulent motions at such small scales that most of the associated energy is directly dissipated into heat [Visser, 2007; Subramanian, 2010].

The mechanisms described above are either confined to select conditions and environments, which renders their contribution to global budgets modest, or to the ocean surface [Thorpe, 2007]. The energy for mixing the abyssal ocean and thereby sustaining the global overturning circulation must hence be supplied by a different source. Internal gravity wave breaking, both in the ocean interior and near rough bottom topography, is considered the major contribution to deep ocean mixing [e.g Garrett and Munk, 1972a; Wunsch and Ferrari, 2004]. This process is the main subject of this thesis, in particular, its representation in numerical ocean models and its observation or estimation from standard measurement techniques in the real ocean. The following sections serve as an overview of these topics, the specific research questions governing this thesis and an overall outline are presented in Section 1.4.

1.1 Internal gravity waves and turbulent mixing

Internal gravity waves are oscillations sustained by the restoring force of gravity that arise in stratified fluids at the interface between layers of different density. They are observed for example in the atmosphere, where the drag associated with their breaking crucially reduces the amplitude of mesospheric zonal jets [Lindzen, 1981; Holton, 1983] or in the interior of stars, where their momentum transfer and deposition contributes to the nearly rigid rotation of Sun-like stars [Denissenkov et al., 2008; Fuller et al., 2014]. In the ocean, the currents and isopycnal displacements associated with internal gravity waves affect shipping, underwater navigation, and offshore engineering [Wilson, 2003; Sarkar and Scotti, 2017], while the turbulent motions induced by their breaking shape climate dynamics and life cycles of ocean biota as described in the previous section.

Oceanic internal gravity waves cover a vast range of spatial and temporal scales, with vertical (horizontal) wavelengths ranging from a few meters to a few kilometers (a few hundreds of kilometers) and periods between the inertial period, $2\pi/f$, and the buoyancy period, $2\pi/N$, where f is the Coriolis and N the buoyancy frequency [e.g. Olbers, 1983;

Olbers et al., 2012]. Occupying such a broad spectrum, the internal wave field's dynamical balance is necessarily intricate. Generation, propagation, and dissipation mechanisms are diverse and not understood in detail nor well constrained by observations.

1.1.1 Internal gravity wave generation

The processes considered to supply the bulk of internal wave energy, illustrated schematically in Fig. 1.3, are fluctuating winds at the ocean surface and the interaction of tidal and geostrophic motions with rough topography at the sea floor. Tidal motions are caused by the imbalance between the gravitational pull exerted by the Moon or the Sun and the centrifugal forces induced by the rotation of the Earth-Moon- or Earth-Sun-system around their common center of mass [refer e.g. to Pugh, 1996, for a thorough introduction to ocean tides]. The two resultant tidal bulges on opposite sides of the Earth (the semidiurnal lunar and solar tides, called "M_2" and "S_2") are affected by the shape and tilt of the Moon's and the Earth's orbit as well as the form of the ocean basins, which in turn generates tidal constituents of different frequencies. The relative position of Moon and Sun moreover leads to approximately fortnightly variations in tidal amplitudes, producing relatively large tide ranges when they are aligned and relatively small ones when they are at right angle (spring-neap-cycle). When these barotropic tidal currents flow back and forth over hills and seamounts at the ocean floor, they cause undulations in isopycnals that can radiate away as internal gravity waves of tidal frequency, the so-called "internal" or "baroclinic tides" [Zeilon, 1912; Baines, 1973]. The analysis of satellite altimetry data showed that a total of about 3.5 TW of barotropic tidal energy is dissipated in the ocean—involving approximately 2.5 TW for the M_2 tide alone—and that about 25-30 % of this dissipation occurs in the deep ocean [the remainder of the tidal energy dissipates through bottom friction in shallow seas and is thus not available for deep ocean mixing; Egbert and Ray, 2000]. Far away from the continental margins, bottom friction is estimated to account for 30 GW of tidal energy loss, underlining that the majority of tidal dissipation in the deep ocean is realized through internal tide generation [Garrett and St. Laurent, 2002]. Amounting to about 1 TW globally, the conversion from the barotropic tide is hence a significant source of energy for the internal wave field.

Satellite observations also demonstrated that internal gravity waves can radiate from different types of topography, both from isolated features such as islands, ridges, and trenches and from the gentler as well as more widespread regions of bottom roughness associated with sea floor spreading away from mid-ocean ridges [Egbert and Ray, 2001; Garrett and Kunze, 2007]. Analytical investigations of the linearized, two-dimensional problem indicate that the magnitude of the barotropic to baroclinic energy flux is set by the height and the slope of the topographic obstacle, the barotropic current speed, and the stratification [Bell, 1975a,b; Llewellyn Smith and Young, 2002; Sarkar and Scotti, 2017, see also Appendix 5.1]. Linear theory is generally believed to be applicable in large parts of the global ocean [Nycander, 2005; Garrett and Kunze, 2007], but since the underlying

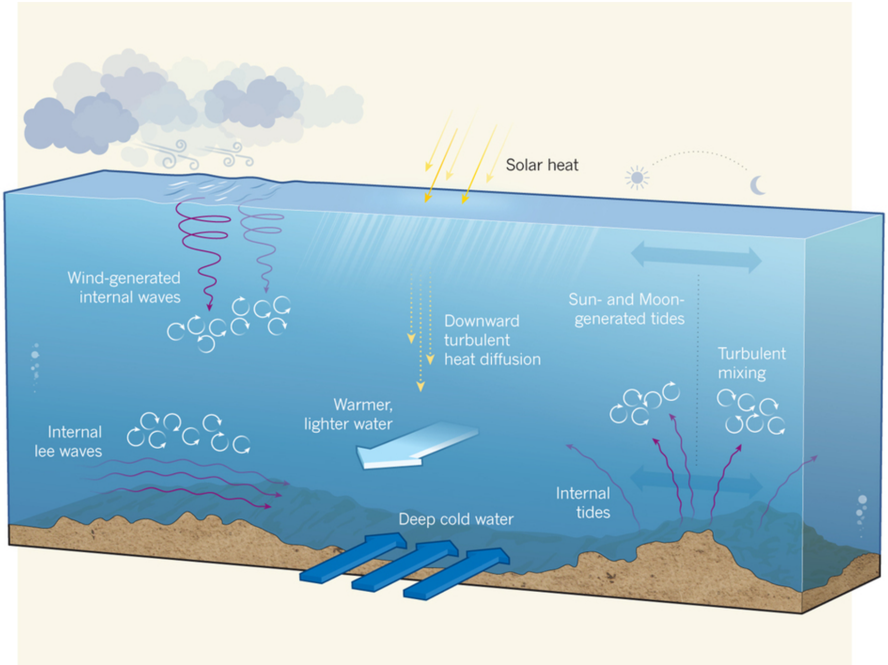

Figure 1.3: Schematic illustration of the main internal gravity wave generation mechanisms [MacKinnon, 2013], with about 1 TW of energy supplied from the barotropic tides [Egbert and Ray, 2000] and 0.2-0.75 TW through lee wave generation [Nikurashin and Ferrari, 2011; Wright et al., 2014] as tidal or geostrophic motions impinge upon rough bottom topography. Depending on the details of the calculation, the total rate of wind work through the ocean surface is estimated as 0.3-1.5 TW [Alford, 2001; Watanabe and Hibiya, 2002; Rimac et al., 2013], of which 10-25 % are found to leave the mixed layer and radiate into the ocean interior as near-inertial internal gravity waves [Crawford and Large, 1996; Furuichi et al., 2008; Rimac et al., 2016].

assumptions are not met everywhere, its application to realistic bottom topography is inevitably biased [Cummins and Oey, 1997; Melet et al., 2013a].

Not only the tides, but also the mean flow and mesoscale eddies can interact with bottom topography in a way that creates internal gravity waves. Similar to the generation of internal tides, the restoring force of buoyancy generates waves as a steady flow passes over a topographic obstacle in a stratified fluid [Bell, 1975a,b; Khatiwala, 2003]. Depending on the magnitude of the flow, the stratification, and the geometry of the topography, lee waves radiate away from the sea floor, transporting energy and momentum upward and thus balancing the net force on the bottom (the wave drag) induced by the pressure differences on both sides of the obstacle [Bell, 1975a, see also Appendix 5.1]. Nikurashin and Ferrari [2010] describe how these radiating lee waves induce a secondary wave generation mechanism: through their spatially nonuniform deposition of horizontal momentum in the overlying fluid, they cause near-inertial oscillations, which can in turn force internal gravity waves at frequencies close to the local inertial frequency (or harmonics thereof). Based on linear theory, Nikurashin and Ferrari [2011] estimate the global energy conversion from geostrophic motions (mean flow and eddies) into lee waves as 0.2 TW, half of which occurs in the Southern Ocean. Applying linear theory to different data sets (for example, with assimilation of bottom velocity observations), Scott et al. [2011] derive a lee wave generation rate of 0.34-0.49 TW, again with the dominant contribution from the Southern Ocean. Wright et al. [2014] on the other hand base their estimate of the energy flux into lee waves on bottom velocities obtained from current meter measurements, relying on a numerical model only to extrapolate these measurements to the entire ocean and for bias correction. This approach yields a global energy conversion of 0.75$\pm$0.19 TW. They speculate that their higher estimate is more realistic since ocean models are typically tuned at near-surface level where most of the reference observations are made and hence often exhibit negative biases in deep ocean velocities. When these authors used a different data set for the buoyancy frequency N, the global conversion rate decreased to 0.57$\pm$0.16 TW, which highlights that the differences between the available data products are a significant source of uncertainty for estimates of this internal gravity wave energy source.

At the ocean surface, wind stress fluctuations can generate resonant inertial motions in the upper ocean [e.g. D'Asaro, 1985]. Their horizontal scales are initially comparable to those of the synoptic storm systems that force them ($\mathcal{O}(100)$ km), but the variation of the Coriolis frequency with latitude as well as the interaction with the mesoscale eddy field can significantly reduce their horizontal extent [Kunze, 1985; D'Asaro et al., 1995; D'asaro, 1995a,b]. The convergences and divergences of these near-inertial motions lead to pressure gradients at the mixed layer base, which generate internal waves at near-inertial frequency (near-inertial gravity waves) in the stratified ocean below [e.g. Gill, 1984; Alford and Whitmont, 2007]. This source of internal wave energy is less well constrained than the tidal energy input: Based on slab model calculations, the work done by the wind on the global ocean surface is estimated as 0.3-0.7 TW [Alford, 2001; Watanabe and Hibiya, 2002]. These results were shown to be rather sensitive to the spatial and temporal resolution of the wind forcing by Jiang et al. [2005] and Rimac et al. [2013], who found global energy fluxes between 0.3 and 1.5 TW in their different scenarios. Numerical simulations produced slightly lower estimates, ranging from 0.3 to 0.5 TW [Furuichi et al., 2008; Simmons and Alford, 2012]. Although numerical models allow the description of the ocean mixed layer in more detail than an analytical slab ocean model does, the uncertainty caused by different wind products prevails and additional biases induced by parameterization schemes arise [Alford et al., 2016]. It is estimated that 75-90 % of this wind energy input into near-inertial motions dissipate in the upper ocean, while the rest can radiate into the ocean interior in the form of internal gravity waves [Crawford and Large, 1996; Furuichi et al., 2008; Rimac et al., 2016]. Recent studies demonstrate an influence of parameters such as the mixed layer depth or the dominant wavenumber of the wind stress spectrum on the amount of near-inertial energy dissipating within the mixed layer, which could hence locally reach 100 % [Rimac et al., 2016; Jurgenowski et al., 2017]. Considering its global average, however, this internal gravity wave energy source could amount to 0.2 TW and more, which is less than the estimated tidal forcing but in any event relevant for the waves' global energy budget.

Other sources of internal gravity waves include the resonant interaction of surface waves [Olbers and Eden, 2016; Haney and Young, 2017] and the spontaneous emission from slow, balanced motion [Vanneste, 2013, and references therein]. In the former case, internal wave motions are triggered by a vertical pumping at the mixed layer base. This mechanism is analogous to the effect of diverging near-inertial motions or Ekman currents, but is induced by the triad interaction of two surface waves with an internal wave [Olbers and Eden, 2016]. The global integral of the associated energy flux is estimated as (0.5-1)$\cdot 10^{-3}$ TW by these authors, which is about two orders of magnitude lower than the wind-induced near-inertial wave forcing; in more localized comparisons, however, the two energy sources were found to be comparable. The latter case refers to the generation of (near-inertial) gravity waves during frontogenesis [Hoskins and Bretherton, 1972; Alford et al., 2013], as a consequence of barotropic instability [Ford, 1994] analogous to the emission of sound waves by vortical motions described by Lighthill [1952], or during ageostrophic baroclinic instability [Brüggemann and Eden, 2015; Chouksey et al., 2017]. Too little is known about the details of these generation mechanisms to estimate the magnitude of the associated energy fluxes.

In sum, these internal gravity wave generating mechanisms could supply as much as the 2.1 TW of energy estimated necessary by Munk and Wunsch [1998] to sustain an upwelling of 30 Sv (1 Sv = $10^3 m^3 s^{-1}$) of bottom and intermediate water through vertical diffusion. In other words, vertical mixing induced by breaking internal gravity waves alone could provide the energy required to sustain the meridional overturning circulation, if it can be represented in such a simplified manner as the one-dimensional advection-diffusion balance analyzed by Munk [1966] and Munk and Wunsch [1998].

1.1.2 Internal gravity wave propagation and interaction

Once they are generated by any of the processes described in the previous section, internal gravity waves can freely propagate if their intrinsic frequencies ω_0 are larger than the local Coriolis frequency f and smaller than the local buoyancy frequency N [or vice versa; see e.g. Munk, 1981; Olbers, 1983; Olbers et al., 2012, for an introduction into internal gravity wave kinematcs as well as Appendix 5.1 for details]. In an environment of constant buoyancy and Coriolis frequencies, the dispersion relation of internal gravity waves is

$$\omega^2 = \omega_0^2 = N^2\frac{k^2}{K^2} + f^2\frac{m^2}{K^2} = N^2\cos^2\vartheta + f^2\sin^2\vartheta \tag{1.1}$$

where k is the amplitude of the horizontal wavenumber vector $\mathbf{k} = (k_1, k_2)$, K that of the three-dimensional wavenumber vector $\mathbf{K} = (\mathbf{k}, m)$ and ϑ denotes the angle of the wavenumber vector with the horizontal plane. Since the frequency only depends on the direction but not on the magnitude of the wavenumber vector, the group velocity $\mathbf{c}_g = \partial\omega/\partial\mathbf{K}$ is orthogonal to the wavenumber vector $\mathbf{K}$. For linear waves originating from a point source, all possible group velocity vectors hence lie on a cone whose apex is situated at the position of the source, with wavenumber vectors pointing away from the cone's surface at right angles [see e.g. Fig. 1 in Sarkar and Scotti, 2017]. The associated particle motion is normal to the direction of the wave vector for reasons of continuity. The vertical propagation of wave groups and hence energy occurs at velocities

$$c_{g,3} = \frac{\partial\omega}{\partial m} = -\frac{N^2 - f^2}{\omega}\frac{k^2 m}{(k^2 + m^2)^2}, \tag{1.2}$$

which can be approximated as $c_{g,3} \approx -N^2k^2/(m^3 f)$ for waves of near-inertial frequency. This implies that processes which reduce the horizontal extent of upper ocean near-inertial motions, described in the previous section, increase the vertical energy propagation of near-inertial gravity waves, so that tropical storms with their strong wind stresses and compact sizes are very efficient generators of these waves [Alford et al., 2016]. In the presence of a mean current $\mathbf{U}$, the intrinsic internal wave frequency given in Eq. 1.1 is Doppler shifted, i.e. $\omega = \omega_0 + \mathbf{kU}$.

In case of a realistic variable stratification, the wave equation can only be solved approximately. If the scales of variation of the background fields are larger than the wavelengths and periods of the internal waves, these can be described as slowly varying wave trains with a space- and time-dependent frequency $\omega = \Omega(\mathbf{k}, \mathbf{x}, t)$, which locally assumes the form given above (WKB-approximation, see also Appendix 5.2). For such waves, it is wave action $\mathcal{A} = \mathcal{E}/\omega$, where $\mathcal{E}$ is the spectral energy density, rather than energy itself which is conserved. A surprisingly universal description of the energy spectrum was provided in the early 1970s by Garrett and Munk [1972b], who combined the available observations into a spectral model (GM model) for a horizontally isotropic and vertically symmetric wave field (see Chapter 2 and Appendix 5.2 for details on this model, including the modifications introduced by Garrett and Munk [1975] and Cairns and Williams [1976]). Apart from regions under the direct influence of external forcing, the GM model is judged an adequate albeit smoothed representation of the internal gravity wave field in the deep ocean, suggesting a universality of at least some of the dominant forcing mechanisms [Briscoe, 1977; Müller et al., 1978; Olbers, 1983]. This is illustrated in Fig. 1.4, depicting an internal wave frequency spectrum observed in the North Pacific: apart from the near-inertial waves of frequency f and the M_2 internal tide, the remainder of the internal wave field is well represented by the GM model.

Propagating internal gravity waves can be reflected at the ocean surface or the (sloping) bottom; reflection also occurs at the interior turning depth where $\omega_0 = N$, and at the turning latitude where $\omega_0 = f$. For example, the turning latitude of the M_2 tidal constituent is 74.46°. A mean flow characterized by vertical shear can also decrease the

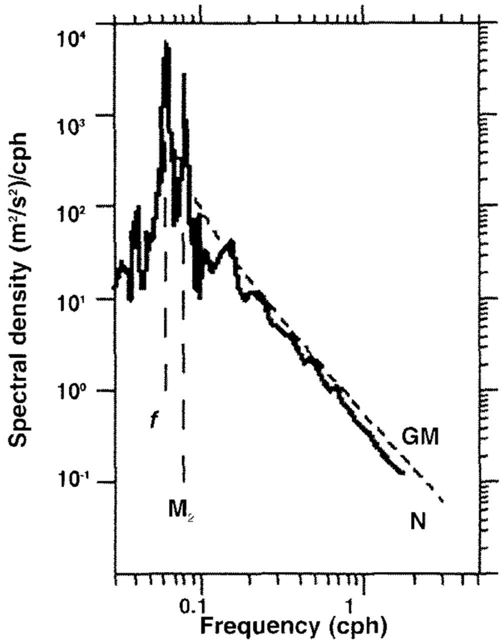

Figure 1.4: The spectral density of internal gravity wave horizontal kinetic energy as a function of frequency observed in the northeast Pacific at 140 m depth. Note the sharp peaks at the Coriolis frequency f and the M_2 tidal frequency. At higher frequencies, the GM model well reproduces the observed energy content [Müller and Briscoe, 1999, after M. Levine].

intrinsic frequency such that it approaches the local Coriolis frequency. In this case, the group velocity tends towards the horizontal and the waves are absorbed into the background flow and can break (critical layer absorption). Olbers [1981] discusses the situation of horizontally and vertically variable stratification and mean flow, demonstrating that the critical layers then act like a valve which allows waves approaching from one direction to penetrate into the critical layer while waves approaching from the opposite direction are absorbed.

Another important process affecting propagating internal gravity waves is the resonant coupling to other waves. This mechanism is pivotal to the oceanic energy budget, as it transfers energy through the internal wave spectrum from the large generation to the small dissipation scales, where it is transformed into turbulent motions that mix the fluid vertically and contribute to driving the large-scale overturning circulation. Nonlinear interactions involving a transfer of energy can occur if the resonance conditions

$$\begin{aligned} \omega_1 \pm \omega_2 &= \omega_3 \\ \mathbf{k}_1 \pm \mathbf{k}_2 &= \mathbf{k}_3 \end{aligned} \tag{1.3}$$

are met for the triad of waves denoted by subscripts 1-3. McComas and Bretherton [1977] identified three different classes of triad interactions, which dominate different portions of the internal wave energy spectrum: Induced diffusion describes a diffusion of wave action primarily in vertical wavenumber space associated with the shear content of a low-frequency wave that interacts with two waves of larger wavenumber and frequency. Elastic scattering involves the interaction of two waves which are almost vertical reflections of each other, i.e. with almost the same wavenumbers and frequencies but with opposite vertical wavenumber signs, with a nearly vertical low-frequency wave. This mechanism mainly transfers energy between the upward and downward propagating higher-frequency waves. Parametric subharmonic instability finally connects two waves of almost equal frequencies and almost opposite wavenumbers with a third wave of almost twice the frequency and much smaller wavenumber. It results in an energy transfer from larger to smaller spatial scales and frequencies, which is proportional to the energy of the larger wave and hence suggested to be most effective for waves of near-inertial frequencies, for which the energy content of the internal wave spectrum is largest (see Fig. 1.4). The time scales on which these processes are active are estimated to range from a few hours for short waves to more than 10 days for waves with vertical wavelengths of more than a kilometer. Cascading energy without changing its total amount to ever smaller scales, these nonlinear interactions are considered the main reason for the observed continuousness of the internal gravity wave energy spectrum [Olbers, 1976; McComas and Bretherton, 1977].

1.1.3 Internal gravity wave dissipation

Internal gravity waves can dissipate at critical layers or through wave breaking caused by gravitational or shear instability [e.g. Thorpe, 2007; Olbers et al., 2012]. For shear instability to occur, the stratification and vertical shear must be such that the Richardson number $\mathrm{Ri} = N^2/(dU/dz)^2$ is less than 1/4 somewhere in the flow, which underlines that breaking is not only related to the internal waves' characteristics but also to those of the ambient flow (which could in turn have been shaped by the presence of the internal wave field) [Olbers, 1983]. Figure 1.5 depicts the direct numerical simulation of shear-driven overturns, showing how waves at the interface between the two layers of different horizontal velocity roll up into Kelvin-Helmholtz billows, which merge and develop small-scale motions inside [Smyth et al., 2001]. These are associated with sharp gradients, a prerequisite for efficient molecular diffusion as described in the introductory paragraph. The turbulent motions become more energetic and spread almost through the entire domain until they decay, leaving behind stratified layers subject to secondary instabilities. These numerical simulations are contrasted in the figure with one of the rare occasions on which such billows in conjunction with an internal gravity wave were observed in the ocean [Moum et al., 2003]. The formation and breakdown of these billows

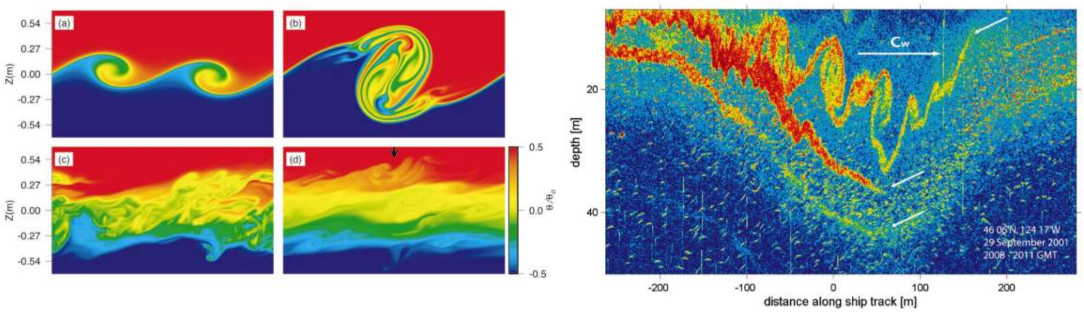

Figure 1.5: Left: Direct numerical simulation of shear instability and subsequent turbulent mixing [Smyth et al., 2001]. Shown is the scaled temperature field at different stages of the simulation with a) a pair of Kelvin-Helmholtz billows, b) a large, merged billow with turbulent motion inside and very sharp gradients outside of it, c) complex turbulent motion almost everywhere in the flow, d) stratified layers and decayed turbulence, with secondary instabilities inducing small-scale overturns and internal gravity waves propagating along the interfaces. Right: Turbulent overturns, reminiscent of the modeled Kelvin-Helmholtz billows shown on the left, on a propagating internal gravity wave observed off of Oregon's coast [Moum et al., 2003]. The high acoustic backscatter (red denotes high intensity) clearly shows billows and at the trailing end of the wave might indicate turbulent breakdown (since these billows propagate at the velocity of the background flow, which is less than the wave's speed c_w denoted by a white arrow, the age of the Kelvin-Helmholtz billows increases from right to left in the figure).

illustrates the release of turbulent kinetic energy (TKE) during wave breaking associated with shear instability.

The amount of TKE used to increase the potential energy of the fluid is rather small compared to the remainder, which is dissipated into heat. Their ratio, referred to as "mixing efficiency", is typically assumed to be 0.2 [Osborn, 1980], but numerical simulations and laboratory experiments show that depending on the dynamical circumstances, significantly higher and lower values might be representative of the real ocean [e.g. Thorpe, 1973; Peltier and Caulfield, 2003; Mashayek et al., 2013]. Under the condition of steady, isotropic turbulence, these two pathways of TKE—the dissipation into heat and the turbulent buoyancy flux— balance the TKE production. Assuming furthermore that this balance appears in fixed proportions and writing the buoyancy flux in terms of a down-gradient diffusion, the mixing efficiency δ relates the vertical diffusivity κ to the dissipation rate ϵ_{TKE} and the stratification N [Osborn, 1980, see also Section 1.2 for details]:

$$\kappa = \delta \frac{\epsilon_{TKE}}{N^2}. \tag{1.4}$$

If vertical diffusion is supposed to balance 30 Sv of deep water formation, the vertical diffusivity required to close such a simple overturning circulation was calculated as $\kappa \approx 10^{-4}\,\mathrm{m^2\,s^{-1}}$ by Munk [1966]. Observations in the open ocean, notably the North

Atlantic Tracer Release Experiment, however, gave vertical diffusivities that were an order of magnitude smaller than that theoretical estimate [Ledwell et al., 1993, 1998]. That internal gravity wave breaking is nevertheless crucial for closing the meridional overturning circulation was demonstrated during subsequent measurement campaigns in the abyssal ocean: diapycnal mixing was found to increase near the sea floor, with diffusivities occasionally exceeding $\kappa = 10^{-3}\ \mathrm{m^2\,s^{-1}}$ in the bottom 100 m of the water column [Polzin et al., 1995; Toole et al., 1997; Ledwell et al., 2000]. These elevated mixing rates were related to internal gravity waves breaking shortly after their generation at rough bottom topography. For example, the inertial oscillations induced by radiating lee waves cause high shear and hence promote wave breaking near the sea floor [Nikurashin and Ferrari, 2010], while the decay of the quasi-steady flow with height above the bottom can create critical layers and thus lead to the breaking of the radiating lee waves whose intrinsic frequency is near-inertial [Bell, 1975b]. Internal tides, typically described as vertically standing waves (modes), mainly radiate away from their generation sites, carrying their energy over thousands of kilometers until they break and contribute to interior mixing [Olbers, 1983]. Only the high modes, characterized by small vertical wavelengths and high shear, break close to the topography and add to the enhanced bottom mixing. In consequence, the canonical Munk-value of $\kappa = 10^{-4}\ \mathrm{m^2\,s^{-1}}$ should not be understood as a global constant, but rather as a representation of a combination of effects: on the one hand, low pelagic diffusivities, sustained by internal gravity waves carrying their energy over large distances before breaking, and on the other hand, very high diffusivities concentrated near the ocean boundaries, where shear-induced wave breaking and boundary layer dynamics lead to increased turbulence [Munk and Wunsch, 1998]. Since the strength of the meridional overturning circulation was shown to depend not only on the magnitude of the interior mixing but also on its vertical distribution [Samelson, 1998; Zhang et al., 1999; Melet et al., 2013b], this re-interpretation is crucial.

1.2 Modeling oceanic turbulence

As detailed above, diapycnal turbulent mixing plays a pivotal role for the energy budget of the large-scale ocean circulation. In order to correctly model its state and evolution in numerical simulations, it is hence crucial to take these turbulent motions into account. Fig. 1.6 depicts the time and space scales of the main dynamical regimes in the ocean, ranging from centimeters and seconds representative of small-scale turbulence to thousands of kilometers and years for the global overturning circulation. Mesoscale eddies are characterized by length scales of a few tens of kilometers and typically persist for several weeks, while the internal gravity wave field bridges the gap between large-scale flow and small-scale turbulence, spanning length scales of four orders of magnitude. The grey boxes denote the regimes which are currently resolved in global general circulation models of the ocean, with dashed lines indicating the scales presumably resolved in the

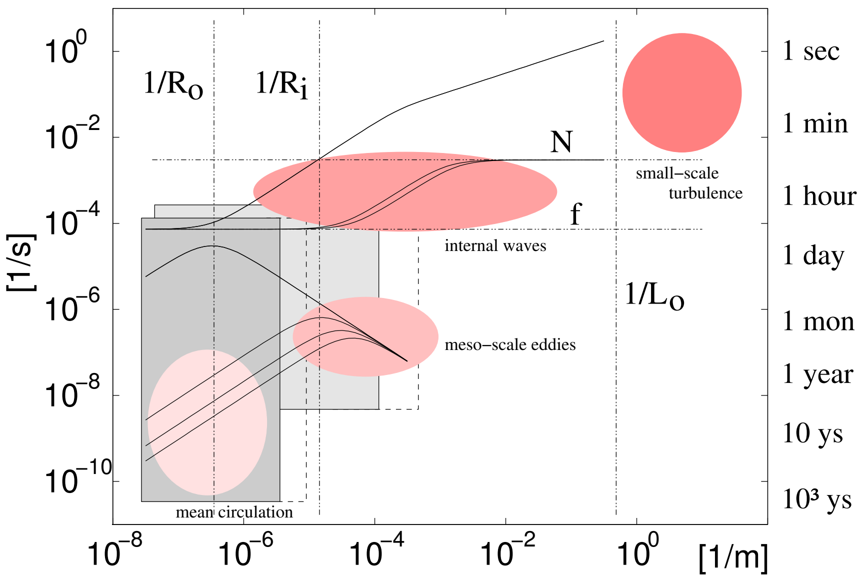

Figure 1.6: Space and time scales of dynamical regimes in the ocean, with solid lines showing the most important linear wave solutions [Eden et al., 2014, adopted from Olbers et al., 2012]. Grey boxes delimit the scales resolved in ocean models (non-eddy-resolving models in darker and eddy-permitting models in lighter shades), with the dashed lines illustrating how these boxes increase in size in the foreseeable future thanks to the expected gain in computational power. Relevant length scales are the barotropic and the baroclinic Rossby radii of deformation R_o and R_i, respectively, which characterize the scales at which rotation has a relevant impact on the evolution of the flow. The inverse of the Ozmidov scale L_o^{-1} is the upper wavenumber boundary of the inertial subrange, in which the energy of isotropic turbulence is determined solely by the input from larger-scale eddies and the dissipation to smaller-scale eddies, with a spectral slope of $k^{-5/3}$ [Kolmogorov, 1941b,a, see also textbooks such as Olbers et al., 2012].

next years with increased available computer power. Neither are even remotely close to the scales occupied by turbulence. In consequence, these small-scale motions have to be parameterized.

Decomposing the field variables into a statistical mean and a deviation thereof (Reynold's decomposition) and taking the average, shows that the equations governing the evolution of the mean components involve turbulent flux terms. For example, the zonal velocity is written as $u = \overline{u} + u'$, which introduces the flux terms $\overline{u'u'}$, $\overline{u'v'}$ and $\overline{u'w'}$ in the averaged momentum equation for the mean field $\overline{u}$ (the three-dimensional velocity vector is given by $\mathbf{u} = (u, v, w)$). Prognostic equations for these turbulent fluxes in turn involve third order moments such as $\overline{u'v'w'}$ and these third order correlations can only be expressed in terms of fourth order correlations and so forth. This emphasizes that modeling turbulence is not only complicated through the small spatial and temporal scales involved, but also through the lack of a closed analytical theory.

There are several possibilities for closure approximations, which are generally named after the highest order of prognostic equations solved. A first-order closure typically employed in ocean models is to describe the vertical turbulent fluxes as a downgradient Fickian diffusion [Olbers et al., 2012; MacKinnon et al., 2017]. For example, the vertical turbulent flux of buoyancy $b = -g\tilde{\rho}/\rho_0$, with the constant background potential density ρ_0 and a variation $\tilde{\rho}$, then becomes:

$$\overline{b'w'} = -\kappa \frac{\partial \overline{b}}{\partial z} = -\kappa N^2. \tag{1.5}$$

The horizontal turbulent fluxes can be represented analogously. Since it is the across-isopycnal rather than the along-isopycnal turbulent transport that can raise the center of mass and hence increase the ocean's potential energy, we focus on the vertical fluxes in this chapter (in the ocean's interior, the vertical and the diapycnal direction are almost aligned). The problem of parameterizing turbulent mixing is thus transformed into the problem of defining the diffusivity κ.

Early approaches simply took the canonical Munk value $\kappa = 10^{-4}$ m^2 s^{-1} as a spatial and temporal constant [Jochum, 2009]. Motivated by observational evidence of bottom-enhanced mixing, Bryan and Lewis [1979] proposed a vertically variable (but still horizontally and temporarily constant) profile with $\kappa = 0.3 \cdot 10^{-4}$ m^2 s^{-1} in the thermocline and $\kappa = 1.3 \cdot 10^{-4}$ m^2 s^{-1} in the abyss. Subsequent measurement campaigns, notably the North Atlantic Tracer Release Experiment, led to the adjustment of these values [e.g. Large et al., 1994]. Alternative formulations were for example proposed by Cummins et al. [1990] who, building on the work of Gargett [1984, 1986], scaled the vertical diffusivity with the inverse buoyancy frequency, or by Munk and Anderson [1948] and Pacanowski and Philander [1981], who wrote the vertical diffusivity as a function of the local Richardson number Ri. These approaches, however, did not account for the inherently different dynamical processes leading to turbulent mixing in the different parts of the water column nor for the spatial and temporal variability of these sources. As a first step, specific parameterizations for the ocean's boundary layers and its interior were developed.

In the surface layer, a commonly employed scheme is the K-profile parameterization (KPP) of Large et al. [1994], which expresses vertical mixing as the sum of a downgradient diffusion as in Eq. 1.5 and a non-local term $\overline{u'w'}_{nl} = \kappa\gamma$. This accounts for the observation that turbulent fluxes are not only driven by local property gradients, but are also influenced by the overall state of the boundary layer, for example in the case of convective mixing. The vertical diffusivity is then calculated as a function of boundary layer depth, a vertical velocity scale, and a non-dimensional vertical shape function, which are specified based on Monin-Obukhov similarity theory, and the non-local transports are parameterized in association with the surface kinematic forcing [see also Griffies et al., 2015, for a review]. Alternative formulations characterize the vertical diffusivity in the surface boundary layer as a function of TKE and a characteristic length scale, which is either determined from algebraic relations [Gaspar et al., 1990; Blanke and Delecluse, 1993] or from a second differential equation [e.g. Mellor and Yamada, 1982]. Other two-equation closures link TKE and the rate of TKE dissipation [Rodi, 1987; Wilcox, 1988], which are, along with the so-called “k-l”-closure by Mellor and Yamada [1982], captured by the generic length scale formulation of Umlauf and Burchard [2003]. Reffray et al. [2015] compared these one- and two-equation closures in a one-dimensional version of the ocean model NEMO (Nucleus for European Modelling of the Ocean), showing that both largely reproduce mixed layer deepening observed in a laboratory test scenario as well as the stratification and homogenization cycle observed at the ocean station PAPA, but also identifying the strong sensitivity of the one-equation closure of Blanke and Delecluse [1993] to its boundary conditions (the TKE penetration depth) as a potential source of complications when using this closure in global, three-dimensional simulations. If this is sufficient justification of the much higher computational expenses required for two-equation closures compared to their one-equation counterparts remains to be demonstrated [Olbers et al., 2012].

At the ocean bottom, frictional forces exert a drag on the flow which is typically modeled as a quadratic function of bottom velocity and is responsible for much of the dissipation of mean and tidal flow energy on the continental shelves [e.g. St. Laurent and Garrett, 2002; Griffies et al., 2015]. In order to account for the main barotropic tidal energy sink in the deep ocean, i.e. the generation of internal tides at rough topography, Jayne and St. Laurent [2001] added a second drag term to the momentum balance of their barotropic, shallow-water model. Based on linear theory [Bell, 1975a,b], this wave drag is proportional to the stratification and the height and wavenumber of the bathymetry; although the topographic wavenumber was taken as a globally constant tuning parameter, the modeled barotropic tides agreed better with satellite observations than before, when only frictional drag was implemented. Motivated by this improvement, St. Laurent et al. [2002] developed a mixing parameterization for the abyssal ocean that takes the enhanced mixing due to breaking internal tides into account:

$$\kappa = \kappa_0 + \frac{\delta q E_F(x, y) F(z)}{\rho N^2}. \tag{1.6}$$

Here, q describes the fraction of internal tide energy that dissipates locally, taken as a global constant of $1/3$, κ_0 a constant background diffusivity set to $0.1 \cdot 10^{-4}\,\mathrm{m^2\,s^{-1}}$, E_F the energy flux into the baroclinic tides, and F an exponential, vertical decay function with an ad hoc decay scale of 500 m. Implementing this parameterization in a coarse-resolution ocean model, Simmons et al. [2004] found that temperature and salinity biases were reduced compared to reference scenarios using either constant vertical diffusivities or the profile of Bryan and Lewis [1979]. This was one of the first demonstrations of the importance of physically-based parameterization of internal wave-driven mixing in ocean models and motivated the improvement of this scheme and its application to mixing sources other than near-field tidal energy dissipation: For example, Polzin [2009] proposed to describe the vertical decay function $F(z)$ in terms of an idealized internal wave energy spectrum for constant stratification. This formalism was implemented by Melet et al. [2013b], who showed that it i.a. led to an increased abyssal stratification and a weaker Indo-Pacific overturning circulation compared to the parameterization by St. Laurent et al. [2002] and thus concluded that not only the amount of available mixing energy but also its vertical distribution had important consequences for ocean dynamics. In addition, Melet et al. [2014] and Melet et al. [2016] both used variations of expression Eq. 1.6 [St. Laurent et al., 2002] to account for the mixing induced by internal tides and lee waves propagating far away from their generation sites before they break (far-field mixing). They, too, observed a robust sensitivity of the ocean's state and dynamics to these additional mixing sources in line with previous studies by Oka and Niwa [2013] or de Lavergne et al. [2016].

With the consensus from observations, laboratory experiments, and numerical studies that breaking internal gravity waves constitute the major source of diapycnal mixing in the ocean interior and at the seafloor near rough topography [e.g. Olbers et al., 2012; MacKinnon et al., 2017, and references therein; see also the previous sections of this introduction], approaches to express mixing parameterizations in terms of internal wave dynamics like the ones named above are undoubtedly necessary. Their disadvantage, however, is that they describe distinct aspects of the internal wave field in terms of empirically set global constants—for example, the fraction of locally dissipated internal tidal energy was estimated as $q = 0.08 - 0.25$ for the Hawaiian Ridge [Klymak et al., 2006], as $q = 0.44$ in the fjord Knight Inlet [Klymak and Gregg, 2004], or as $q = 0.01$ at Mendocino Escarpment [Althaus et al., 2003], supporting the notion that the amount of energy radiated away by internal tides varies depending on topography and flow characteristics [see also Kelly et al., 2013, for a global map of mode-1 M_2 tide energy dissipation sites]. Moreover, the different types of internal gravity waves and dynamical processes leading to their breaking and subsequent turbulent mixing are considered in isolation. Yet, in order to realistically model the observed variability and intermittency of oceanic turbulent mixing, a parameterization based on internal gravity wave energetics, describing the waves' generation, propagation, interaction, and breaking in a closed framework, is indispensable. Such a physically based, energetically consistent parameterization is prerequisite if past, present, and future climate states are to be modeled with sufficient reliability to verify or discard scientific theories or to stimulate political action. It is for this reason that the internal wave mixing module IDEMIX ("Internal Wave Dissipation, Energy and Mixing") was developed [Olbers and Eden, 2013; Eden and Olbers, 2014]. The main goal of this PhD project is to evaluate IDEMIX in a comparison with observations. The remainder of this section deals with the presentation of IDEMIX and the ocean model it is coupled to; methods to infer the rate of turbulent mixing from observations as well as the data base used for the evaluation of IDEMIX will be described in the following section.

1.2.1 The internal gravity wave model IDEMIX

A first approach to model internal wave-induced mixing in ocean models based on the waves' energy balance was developed by Müller and Briscoe [1999] and Müller and Natarov [2003]. Their internal wave action model (IWAM) incorporates several secondary parameterizations and consists of six spatial dimensions, which is impractically large considering that a mixing module is only one among many in a three-dimensional ocean general circulation model. This deficiency is overcome in IDEMIX, which involves a few reasonable assumptions about the characteristics of the internal wave field, allowing the description of its energy content by a simple partial differential equation in physical space [see, also for details on the following discussion, Olbers and Eden, 2013].

The derivation of the internal gravity wave model IDEMIX begins with the radiative transfer equation. It describes the variation of wave action $\mathcal{A} = \mathcal{E}/\omega$, which is conserved for WKB-waves propagating through a slowly changing medium (see also Section 1.1.2):

$$\frac{\partial \mathcal{A}}{\partial t} + \nabla \cdot (\dot{\mathbf{x}}\mathcal{A}) + \frac{\partial}{\partial z}(\dot{z}\mathcal{A}) + \nabla_k \cdot (\dot{\mathbf{k}}\mathcal{A}) + \frac{\partial}{\partial m}(\dot{m}\mathcal{A}) = S_{gen} + S_{ww} + S_{diss}. \quad (1.7)$$

Changes in wave action are caused by wave propagation ($\dot{\mathbf{x}}$ and $\dot{z}$ denote the horizontal and vertical group velocity), refraction in horizontal and vertical direction through $\dot{\mathbf{k}} = -\nabla\Omega$ and $\dot{m} = -\partial\Omega/\partial z$, respectively, and, as denoted by the terms on the right-hand side of Eq. 1.7, generation (S_{gen}), wave-wave interactions (S_{ww}), and dissipation (S_{diss}). The basic version of IDEMIX (IDEMIX1) treats all types of internal gravity waves as part of a horizontally homogeneous continuum with GM model type features. The follow-up version (IDEMIX2) also considered in this thesis explicitly models the horizontally propagating internal tides and near-inertial waves in addition to the continuum at higher frequencies (see for example Fig. 1.4) as well as the interaction of these compartments. Recent extensions of IDEMIX, too new to be taken into account in this PhD project, additionally take the internal wave field's interaction with the mean flow into account [Olbers and Eden, 2017; Eden and Olbers, 2017].

The pivotal step to reduce the complexity of the model is to integrate the energy balance (derived from Eq. 1.7) in wavenumber space, assuming horizontal homogeneity and differentiating between upward ($m < 0$) and downward ($m > 0$) propagating waves. The derivation as well as the main features of the model IDEMIX are presented in Section 2.3; Fig. 1.7 provides a simplified overview of the processes represented in IDEMIX as well as the underlying assumptions together with the vertical wavelength scales these relate to and the tuning parameters that emerge from these assumptions. Ranging from the generation to the dissipation scales, IDEMIX represents the entire internal gravity wave energy spectrum: At large scales, IDEMIX requires the formulation of energy sources, which are confined to the boundaries in the versions used here. At the surface, the energy flux F_{surf} is computed as 20 % of the wind energy input into near-inertial motions in the mixed layer following Jochum et al. [2013], at the bottom, the tidal forcing F_{bot} is parameterized as proposed by Jayne and St. Laurent [2001] and calculated globally as in Jayne [2009]. As a crude representation of lee wave generation through the interaction of mesoscale eddies with rough bottom topography, 20 % of the dissipated mesoscale eddy energy (F_{eddy}) is added to the internal wave energy at the bottom following Eden et al. [2014]. At intermediate scales, the interaction of different internal wave trains is assumed to symmetrize the wave field in vertical wavenumber space on times scales τ_v. Based on analytical and observational evidence, this number should be on the order of days [McComas and Bretherton, 1977; Eriksen, 1982]. Moreover, the upward and downward propagating waves are assumed to have the same group velocity c_0, which is calculated describing the energy spectrum in terms of the GM model. In consequence, the modal bandwidth j_* of the GM model enters as another tuning parameter, which is observed to range between 1 and 20 in the real ocean [Polzin and Lvov, 2011]. At the small wavelength end of the spectrum, the dissipation of internal wave energy, which was assumed to be symmetric with respect to m, is modeled as a function of the squared internal wave energy following existing scaling laws and parameterizations [Olbers, 1976; McComas and Müller, 1981; Henyey et al., 1986]. This introduces the third tuning parameter, μ_0, which combines a constant $\mu \approx 4$ of the parameterization of Henyey et al. [1986] and the function $acosh(N_0/|f_0|)$, representing the observed decrease of internal wave dissipation toward the equator [Gregg et al., 2003]. For reference values of $N_0/|f_0| \approx 10$, the tuning parameter amounts to $\mu_0 = 2/3$.

Considering time scales much longer than the symmetrization time scale τ_v, the evolution of the total internal wave energy E can then be described by a simple diffusion equation:

$$\frac{\partial E}{\partial z} - \frac{\partial}{\partial z}\left(c_0\tau_v\frac{\partial c_0 E}{\partial z}\right) - \nabla_h \cdot v_0\tau_h\nabla_h v_0 E = -\mu_0|f|acosh(N/|f|)\frac{m_*^2}{N^2}E^2, \quad (1.8)$$

where m_* is the GM model bandwidth in vertical wavenumber space. The last term on the left-hand side is a low-order truncation of the horizontal advection term in Eq. 1.7, accounting for lateral variations in an approximate manner when IDEMIX1 is used in global calculations, where the assumption of horizontal homogeneity does not hold. Here, v_0 is the horizontal group velocity and τ_h describes the symmetrization time scale for horizontal anisotropies, which is on the order of ten times larger than the vertical time scale τ_v based on simple scaling arguments for internal wave group velocities, wavelengths and typical distances traveled before breaking [Olbers and Eden, 2013]. In IDEMIX2 this term is redundant, because horizontal variations of the low-mode waves are explicitly modeled [Eden and Olbers, 2014]. In this model version, the energy balance (Eq. 1.8) describes the horizontally homogeneous continuum and is extended by a term W representing the interaction with the compartments for near-inertial waves and internal tides. To conserve energy, the interaction term W is the sum of wave-wave and wave-topography interactions of the near-inertial waves and the internal tides, where the corresponding coefficients are computed from analytical theory following Müller and Xu

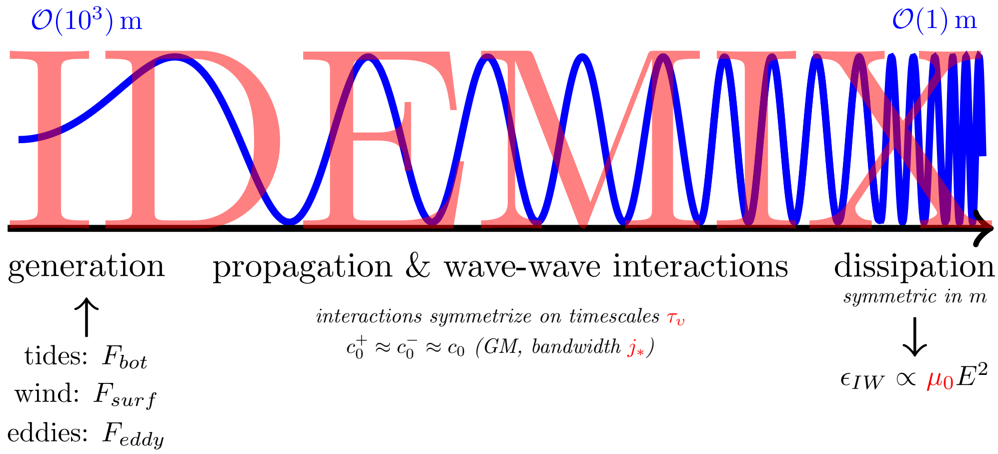

Figure 1.7: Schematic illustration of internal gravity wave model IDEMIX, covering the generation of internal gravity wave at large scales (the vertical wavelength is shown in blue) and the transfer of energy E through nonlinear wave-wave interactions toward smaller scales (high vertical wavenumbers), where finally the waves break and dissipate their energy. The main assumptions made in the derivation of the model, associated with the tuning parameters τ_v, j_*, and μ_0, are given in italics for the wavelength scales to which they apply (note that the final expression of IDEMIX is no longer a function of wavelength, as its derivation involves the integration over all wavenumbers). The quantity c_0 is the representative group velocity of the upward- and downward propagating waves, which is calculated assuming a GM type spectrum for the internal wave energy. The amount of energy that leaves the internal wave spectrum, ϵ_{IW}, can be used as an input for a turbulence model to calculate the vertical diffusivity for the downgradient turbulence closure. See the main text for further details.

[1992] or from the scattering integral for triad interactions [Olbers, 1976], respectively. The main aspects of IDEMIX2 are, too, summarized in Section 2.3.

As illustrated in Fig. 1.7, IDEMIX produces the dissipation rate of internal wave energy ϵ_{IW} as output. This can in turn be used as a source of TKE in a turbulence model to calculate the TKE dissipation rate ϵ_{TKE} and the vertical diffusivity κ. For example, equating the dissipated internal wave energy with the shear-production term in a TKE balance of steady, isotropic turbulence, leads to an expression of κ in terms of internal wave parameters if the Osborn-model and a downgradient closure for the vertical buoyancy flux as in Eq. 1.5 are applied:

$$\kappa = \frac{\epsilon_{IW} - \epsilon_{TKE}}{N^2} = \frac{\delta}{1+\delta}\mu_0 |f| \mathrm{acosh}(N/|f|) \frac{m_*^2}{N^4} E^2. \tag{1.9}$$

The concept of IDEMIX allows the computation of the propagation, interaction, and dissipation of internal gravity waves in a closed framework based on analytical theory or simplifications thereof, justified by observational, numerical, or analytical evidence. While on the one hand the variability of the internal wave field, the main contributor to mixing density in the deep ocean, is captured, these simplifications on the other hand render the implementation in ocean general circulation models feasible. As such, IDEMIX is a crucial component of energetically consistent ocean models, in which energy is transferred between the resolved and parameterized regimes without spurious sources or sinks [Eden et al., 2014; Eden, 2016]. The development of such models warrants more reliable results especially for long-term climate simulations, but is complicated both by conceptual and numerical issues and is hence far from complete.

1.2.2 Energetically consistent ocean models

On the one hand, the problem with most state-of-the-art ocean models is that the parameterized dynamical regimes are considered in isolation, so that energy is simply lost at some places and has to be produced again at others [Legg et al., 2006; Eden et al., 2014]. A consistent framework, however, would account for the total energy budget of the ocean, describing the energy transfer from where it is added to the system [e.g. through atmospheric or tidal forcing, see Thorpe, 2007] to the different dynamical regimes and between them until it is lost to heat. For example, the energy available for abyssal mixing would then only be controled by the forcing of the resolved, large-scale flow and the modeled link to the unresolved, parameterized regimes of mesoscale eddies, internal gravity waves, and turbulence [Eden et al., 2014]. The choice of an energy concept and of corresponding state variables in such a model requires care, especially under the Boussinesq approximation, which is typically applied in ocean general circulation models and contains the noteworthy feature that work done by compression is no longer fully reversible but can constitute an irreversible exchange with internal energy [Tailleux, 2012; Eden, 2015].

On the other hand, the discretization of the continuous governing equations on a numerical grid can cause significant errors. It has been known for decades that the choice of the numerical schemes used to describe spatial or temporal derivatives determines not only the run time of the simulation but also the stability and accuracy of its solution [e.g. Trefethen, 1996]. Because neutral surfaces—surfaces along which water parcels can be advected adiabatically and isentropically for short distances without experiencing any restoring force, that is, surfaces orthogonal to the direction in which mixing increases the ocean's potential energy [McDougall, 1987; Jackett and McDougall, 1997]—are not exactly aligned with horizontal or potential density surfaces, the standard ocean models using geopotential height or potential density as a vertical coordinate struggle to maintain the adiabacity of advection [Griffies et al., 2000; Rennau, 2011]. In such models, certain tracer advection schemes can introduce spurious numerical diffusion: Molenkamp

[1968] showed that the amount of numerical diffusion caused by a first-order upwind scheme is comparable to that of turbulent diffusion, while Griffies et al. [2000] described how dispersion and dissipation errors of tracer variance conserving schemes (e.g. centered differences) can induce unphysical convective mixing by creating large tracer and hence density extrema leading to static instability. Another discretization issue is that numerical stability requires large viscous damping [Eden, 2016] and, in the case of coarse resolution models, often unphysically large tracer diffusivities [Jochum, 2009]. These points stress that the construction of energetically consistent models not only requires parameterizations of subgrid-scale processes in a coherent and closed energy framework but also crucially depends on the development of suitable numerical discretization schemes. This effort might be beneficial in more than one regard, as Burchard [2002] showed that for a simple first-order time discretization method, energy consistency and improved numerical stability go hand in hand.

Although neither the physical nor the numerical details are fully understood, the existing knowledge and computational power are sufficient for the setup of (approximately) energetically consistent ocean models. One such first step was made with the development of pyOM [Eden, 2016, see also https://wiki.zmaw.de/ifm/TO/pyOM2], a hydrostatic ocean model in Boussinesq approximation which guarantees energy conservation up to machine accuracy through an energy concept based on dynamic enthalpy, through numerical schemes without implicit numerical mixing, and through the full account of the ocean's energy budget in terms of external forcing, dissipation to heat, and the interaction between the resolved and parameterized dynamical regimes. The enthalpy h is the sum of gravitational potential and internal energy, but can also be divided into potential and dynamic enthalpy to (approximately) differentiate between reversible and irreversible energy exchanges [McDougall, 2003; Young, 2010; Nycander, 2011]. The total energy is hence given by kinetic energy and enthalpy. The mean field, described by mean dynamic enthalpy h_m^d and mean kinetic energy $\overline{e}$, which can reversibly exchange energy, is externally forced by solar radiation and winds, respectively. Its energy sinks provide the energy input for the parameterized fields of mesoscale eddies—through eddy mixing in case of h_m^d and lateral friction in case of $\overline{e}$, both specified by a downgradient closure [Gent and McWilliams, 1990; Eden and Greatbatch, 2008]—and TKE—through dianeutral mixing from h_m^d and vertical friction from $\overline{e}$, with the corresponding diffusivity and viscosity calculated as in the mixed layer closure of Gaspar et al. [1990, refer also to the previous sections]. The dissipated eddy kinetic energy (EKE) on the other hand constitutes a source of internal gravity wave energy, which is modeled through IDEMIX with its external forcing by winds and tides and is in turn dissipated to TKE. TKE also gains energy from breaking surface waves (external) and irreversibly loses heat to potential enthalpy through frictional heating. The nonlinearities in the equation of state cause an irreversible energy transfer between potential and dynamic enthalpy [typically a sink for h_m^d, Eden, 2016].

Despite some remaining uncertainties inherent in the applied closures (the mesoscale eddy closure, following common practice in most ocean models, does not account for the forward energy cascade observed at large Rossby numbers [Capet et al., 2008; Molemaker et al., 2010] and only crudely models the generation of internal gravity waves by eddy-topography interaction [Nikurashin and Ferrari, 2011]) or simplifications in the setup (there is no sea ice model), the ocean model pyOM promises the smallest biases caused by conceptual or numerical inconsistencies and is hence the best choice for the evaluation of the mixing module IDEMIX.

1.3 Observing oceanic turbulence

A conceptually simple approach to quantify the average turbulent vertical mixing in the ocean is to infer it from the large-scale tracer concentration balance,

$$\frac{\partial C}{\partial t} + w\frac{\partial C}{\partial z} = \kappa_C \frac{\partial^2 C}{\partial z^2}, \tag{1.10}$$

which is based on the assumptions that the vertical diffusivity κ_C is constant, that the fluid is incompressible, and that horizontal gradients of the tracer concentration C can be neglected compared to the much larger vertical ones [e.g. Polzin et al., 1997; Klymak and Nash, 2009]. Considering a confined volume of water in steady state, Eq. 1.10 reduces to a volume-integrated advection-diffusion balance. Hogg et al. [1982] and Whitehead and Worthington [1982], for example, applied this inverse budget method to the real ocean, estimating the vertical diffusivity in the Brazil Basin and the North Atlantic Basin, respectively, from the heat and volume transports into these basins. Apart from the questionable steady-state assumption, the main deficiency of this method is that the volume as well as the velocities and temperatures measured at its boundaries must be well constrained, which requires an overwhelming amount of observational efforts in the open ocean and is the main reason why the technique is most reliably applied to basins with clear topographic boundaries such as the Brazil Basin [Klymak and Nash, 2009]. An alternative inverse method to estimate horizontal and vertical diffusion coefficients was derived by Schott and Zantopp [1980] and Olbers et al. [1985] following the beta-spiral method of Stommel and Schott [1977]: based on the linearized potential vorticity equation and the assumption of small relative vorticity, the three-dimensional velocity field as well as the tracer and vorticity diffusivities can be calculated by solving the least squares problem that relates these quantities to the observed density and potential vorticity fields as well as their spatial derivatives. This requires substantial hydrographic information and therefore motivates the application of the technique to climatological data as done by Olbers et al. [1985], who point out that because of the spatial and temporal averaging inherent in such a data base, the resultant diffusion coefficients are to be understood as upper bounds of the actual oceanic levels.

Tracer release experiments involve the injection of an inert chemical tracer such as fluorescent dye or sulphur hexafluoride into the ocean and the tracking of its vertical spread over time [e.g. Ledwell and Watson, 1991]. Following a parcel of water, Eq. 1.10 reduces to a diffusion balance, whose solution takes the form of a Gaussian with a standard deviation σ related to the vertical diffusivity κ_C as $\sigma = \sqrt{2\kappa_C t}$, where t is time [Fischer et al., 1979]. Observing the vertical tracer distributions at different points in time hence allows for the the calculation of κ_C based on the observed concentration variance [e.g. Ledwell et al., 1993; Rye et al., 2012]. Tracer release experiments provide a direct way to determine total vertical diffusivities in the ocean, but the introduction of the tracer at a specified location as well as the repeated ship-based measurements of its spreading are complicated and expensive [Watson et al., 1999; Klymak and Nash, 2009]. Moreover, the obtained diffusivities are representative of rather large areas and long periods and, relating to the tracer field's curvature rather than its gradient (Eq. 1.10 for $w = 0$), constitute a different mixing diagnostic than the one typically considered in ocean models such as pyOM, that is, the proportionality constant between turbulent tracer flux and concentration gradient [Eq. 1.5; Getzlaff et al., 2010; Hill et al., 2012; Abernathey et al., 2013; Eden et al., 2014]. In the following sections, measurement techniques and methods to infer vertical diffusivities and TKE dissipation rates on smaller spatial and temporal scales are presented and discussed.

1.3.1 Microscale measurements and mixing estimates

The average TKE dissipation rate, that is, the average loss of TKE through viscosity to heat, is in the Reynolds averaged TKE equation (see Section 1.2) expressed as

$$\epsilon_{\mathsf{TKE}} = 2\nu\langle D_{ij}^2\rangle, \tag{1.11}$$

where ν is the kinematic viscosity, the angle brackets denote an ensemble average, and the deformation tensor is given by $D_{ij} = 1/2(\partial u_i'/\partial x_j + \partial u_j'/\partial x_i)$ with $i, j = 1, 2, 3$ and the standard tensor notation (summation is over the three values of the two indices in Eq. 1.11) [e.g. Thorpe, 2007; Olbers et al., 2012]. It is the complexity of this tensor that renders the direct application of Eq. 1.11 in observations cumbersome and motivates the assumption of isotropic turbulence, which leads to the simplified formulation

$$\epsilon_{\mathsf{TKE}} = \frac{15}{2}\nu\left\langle\left(\frac{\partial u}{\partial z}\right)^2\right\rangle = \frac{15}{2}\nu\int_{m_1}^{m_2} S_{u_z} dm, \tag{1.12}$$

where S_{u_z} is the vertical shear spectrum [e.g. Greene et al., 2015]. This version is commonly applied as the majority of field campaigns employs vertically towed or falling instruments; in theory, the vertical shear of the zonal velocity $\partial u/\partial z$ can in Eq. 1.12 be replaced by any spatial derivative in the direction orthogonal to that of the flow. It is important to note that, although widely used, the assumption of isotropic turbulence is not met everywhere in the ocean: if the isotropy parameter $I = \epsilon_{TKE}/(\nu N^2)$ is smaller than about 200, turbulent motions become anisotropic at dissipation scales, a case often observed in more than 50 % of the pycnocline waters and in even higher fractions at depth [Gargett, 1989; Thorpe, 2007].

Some of the earliest measurements of oceanic turbulence were carried out by Grant et al. [1959] in the seawater channel east of Vancouver Island. They measured the turbulent velocity fluctuations using hot-film anemometers, which relate the velocity of the flow to the cooling it induces in electronically heated wires and the resultant variations of the electric current [e.g. Comte-Bellot, 1976], and were able to confirm a -5/3-power law of their one-dimensional energy spectrum for a large range of wavenumbers, representative of the inertial subrange of homogeneous turbulence as postulated by Kolmogorov [1941b,a].

Their approach is however only applicable to very energetic flows in unstratified waters and hence not suited for observing turbulence in the ocean interior [Thorpe, 2007]. The air-foil probe designed by Osborn [1974] overcomes this disadvantage, containing piezoelectric chrystals that sense variations in the lift force acting on the probe induced by turbulent velocity fluctuations. These sensors are calibrated so that the output voltage can be converted to the rate of change of velocity in the direction of the measured force component, which in turn is transformed into a spatial velocity gradient applying Taylor's frozen turbulence hypothesis—the assumption that spatial and temporal derivatives can be exchanged as the fluctuations are sampled much faster than they evolve—and used in Eq. 1.12 to calculate the TKE dissipation rate [Thorpe, 2007]. Such probes, together with temperature and other sensors, are commonly carried by microstructure profilers, e.g. the Advanced Microstructure Profiler (AMP) or High Resolution Profiler (HRP), which are streamlined, free-falling instruments recording fluctuations on scales of centimeters and below [Gregg et al., 1982; Polzin and Montgomery, 1996; Thorpe, 2007]. Since the probes are typically too large to resolve velocity shear up to the dissipation scales, the observed shear spectrum is often fitted to an empirical universal spectrum and extrapolated [Klymak and Nash, 2009]. Integration over a suitable wavenumber range determines the TKE dissipation rate, which can be linked to the vertical diffusivity based on the Osborn-method (Eq. 1.4). Their uncertainty is specified as less than a factor of 2 by Toole et al. [1994] and Moum et al. [1995], although it may reach a factor of 3-5 under strongly anisotropic conditions [Mashayek et al., 2013].

Measurement techniques that are not based on energy considerations like the one described above include for example the direct eddy correlation method or the Osborn-Cox-method [Osborn and Cox, 1972]. In the former case, the turbulent fluxes are directly calculated from the correlation of the velocity fluctuation and that of the tracer in question, for example temperature. Although arguably the most direct way to measure turbulent fluxes, this method is rarely applied to the open ocean [for one of these few cases, see Fleury and Lueck, 1994] because of the high resolution required to adequately resolve the vertical velocity variations, the long time series necessary for statistical significance

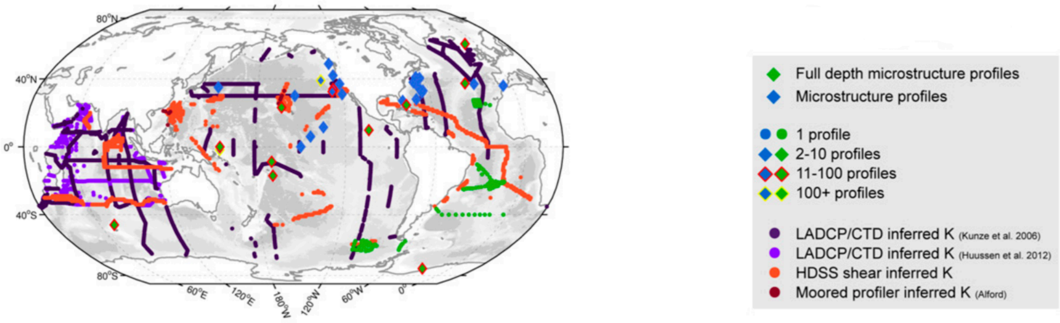

Figure 1.8: Geographic distribution of micro- and finestructure observations available for turbulent mixing estimates. The number and depth of microstructure profiles as well as the different finestructure campaigns are denoted in the legend on the right [Waterhouse et al., 2014].

of the correlation, and because of the difficulty of distinguishing the fluctuation from the mean using a single-direction profiler [Klymak and Nash, 2009]. Following the Osborn-Cox method, the turbulent diffusivity κ is determined by assuming a local balance of the destruction of temperature variance by molecular diffusion and its production through velocity fluctuations in the presence of a mean thermal gradient, writing the turbulent fluxes in terms of a downgradient closure as in Eq. 1.5 [Osborn and Cox, 1972; Fleury and Lueck, 1994]. The advantage of this method is that it directly quantifies the irreversible molecular mixing, but it suffers from the same weakness as any other method involving high-resolution temperature measurements: the insulation around thermistors, which infer temperature from the electric resistance of a metal, causes a small time lag before each measurement as the heat diffuses through to the sensor, which ultimately affects how well a turbulent event can be sampled and how many repeated profiles are taken at a given location, while microconductivity probes, which rapidly register temperature fluctuations as conductivity variations, are also sensitive to salinity changes [Klymak and Nash, 2009].

It is because of the complications and biases of the direct eddy correlation, budget and Osborn-Cox methods as well as for the general interest in the energetics of turbulence, that Eq. 1.12 is commonly invoked in combination with microstructure measurements of velocity shear to quantify the TKE dissipation rate. The trade-off of these high-resolution observations is that because of their elaborate, time-consuming and hence costly execution, there is a considerable paucity of such data, which can therefore only provide snapshots of ocean mixing, with very few parts of the global ocean covered and that only once. Lower-resolution finestructure measurements, recording variations on scales of meters, can be completed faster and therefore survey larger areas. This is illustrated in Fig. 1.8, presenting the geographic distribution of available micro- and finestructure observations that allow quantification of turbulent mixing. In total, there are only eleven locations in the global ocean where such microstructure campaigns involving more than ten vertical profiles were carried out—a coverage greatly improved by the available finestructure observations. The drawback of their lower resolution is that small-scale turbulence is not measured directly but must be inferred from the larger-scale features that can be resolved, which introduces higher uncertainties than those inherent in the methods described above. On the other hand, it might not even be necessary to resolve the small dissipation scales to adequately describe turbulent motions, because the larger, energy-containing scales, relating the external forcing to the small-scale dissipation, could be argued to be at least equally meaningful [Gargett and Garner, 2008]. Most importantly, understanding ocean dynamics around the globe and improving numerical models thereof requires an observational reference of preferably the same scope. Finestructure observations hence constitute a valuable contribution to that reference data base.

1.3.2 Finescale measurements and mixing estimates

A frequently used method to quantify finescale velocity variations exploits acoustic techniques: acoustic Doppler current profilers (ADCPs) allow determination of the flow speed from the Doppler shift an emitted sound pulse experiences as it is reflected from small particles moving through the sound beam [e.g. Pinkel, 1979; Lhermitte and Serafin, 1984]. Assuming steady and well-mixed conditions, the TKE dissipation rate can be equated with the TKE production by the mean shear flow and determined either based on dimensional analysis as a function of an eddy length scale and the small-scale velocity fluctuations [e.g. Taylor, 1935; Greene et al., 2015], or by deriving the turbulent stress $\tau = \rho_0 \langle u'w' \rangle$ and the mean flow velocity U from the averaged differences of the (squared) velocities observed in two ADCP-beams, which are oriented along and across the mean flow, yielding the TKE production $\tau dU/dz$ [Thorpe, 2007].

Finescale fluctuations of temperature and salinity are routinely observed using CTD (Conductivity, Temperature, Depth) sensors, typically attached to a large metal rosette wheel which is lowered vertically, towed horizontally, or fixed at a certain position to record these ocean tracers' variations in space or time [e.g. Thorpe, 2007]. Temperature is commonly measured with resistance thermometers, exploiting the sensitivity of a metal's electrical resistance to the surrounding temperature, salinity is inferred from conductivity, which is directly proportional to the dissolved salts in the water, and pressure, from which depth is inferred, with strain-gauge sensors [Thomson and Emery, 2014]. When cast from a ship, these metal wheels commonly also carry bottles for in situ water collection, which is i.a. used for sensor calibration [e.g. Wong et al., 2003]. Alternatively, these CTD sensors can even be carried by marine mammals [Roquet et al., 2014] or by autonomous robotic devices [for one of the earliest presentations of neutrally buoyant floats, see Swallow, 1955]. The latter option offers the possibility to survey the ocean over much larger areas and time periods than is feasible with ship-born instrumentation.

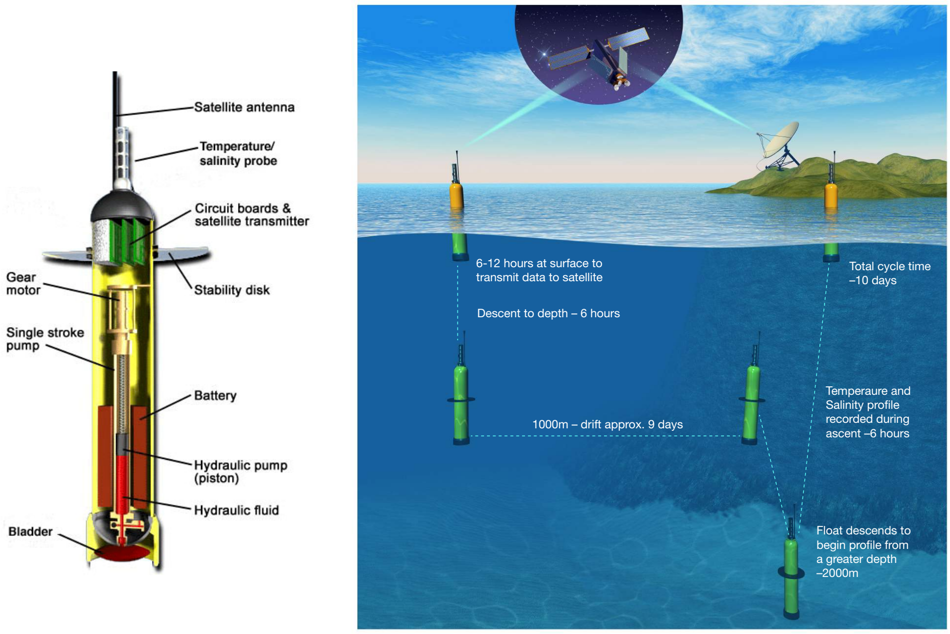

Figure 1.9: (Left) Argo float design and (right) mode of operation: Approximately every 10 days, the floats rise from a depth of 2000 m to the surface, taking about 200 temperature, salinity and pressure measurements. Together with other information such as float position or surface velocity, these data are communicated via satellite and stored at the Argo Data Centers, where it is made available freely within hours after collection. The floats hence consist of a data transmission system, a hydraulic system to regulate its buoyancy, the CTD probes, and processors controling these systems during the different cycle phases. See the main text for more information. (Source: http://www.argo.ucsd.edu/pictures.html, accessed 07/01/2017)

Probably the most extensive effort to monitor the ocean using autonomous equipment is the International Argo Program[1], which was launched in the year 2000. Part of the Global Ocean Observing System, it is a collaborative effort of 28 nations to deploy and sustain a global array of almost 4000 freely drifting floats that profile the ocean's upper 2000 m and record temperature, salinity, pressure, and, in recent years, also biogeochemical variables such as oxygen or nitrate [e.g. Riser et al., 2016]. Fig. 1.9 presents the design and the standard park-and-profile cycle of these floats [see e.g. Roemmich et al., 2001; Gould et al., 2004; Carval et al., 2014, or the program website for details]: Argo floats are built to be neutrally buoyant at a parking depth of 1000 m, where they are stabilized by having the appropriate mass and a lower compressibility than that of seawater[2]. The

[1] http://www.argo.ucsd.edu
[2] Neutral buoyancy is achieved when a submerged object has the same weight as the fluid it displaces, so that the forces of gravity and buoyancy are in balance. For such an equilibrium to be stable, the object's com-

external bladder at the lower end of the Argo floats can be filled and emptied (typically with oil) to regulate its volume and thereby control its buoyancy. Through this mechanism, the floats first descend to 2000 m after drifting at their parking depth for about 9 days, before rising to the surface while recording temperature, salinity, and pressure. At the surface, the floats transmit these data together with information on their position and the previous cycle timing via satellite, which requires several hours depending on weather conditions and the number of satellites within range. In recent years, the majority of floats was equipped with Iridium antennas, using the Global Position System for localization, because these can transmit more information within a shorter time compared to the older system (Système Argos) and thus permit a higher resolution of the CTD casts. The data is made available freely within hours after collection, but is also subject to comprehensive control and correction procedures at the Global Argo Data Assembly Centres, typically completed after several months [the so-called "delayed-mode data", Wong et al., 2015; Carval et al., 2014, see also Appendix 5.3].

The Argo Program has produced an unprecedented quantity of ocean data: Riser et al. [2016, see their Fig. 1] for example contrast the World Ocean Data Base 2009 [Boyer et al., 2009], comprising observational efforts from an entire century, and the data collected by the Argo Program until October 2015, illustrating that not only the sheer number of profiles is significantly increased (approximately 0.5 million vs 1.5 million profiles) but also that the geographic bias is reduced. The location of ship-board field campaigns is often determined by the accessibility of the region, which may vary seasonally, as well as the economic situation of the riparian states, leading to a prominent bias towards northern hemispheric waters and the summer months [Boyer et al., 2009]. Argo floats, on the contrary, are undeterred by rough weather and can also reach the more remote regions of the ice-free ocean. With almost all delayed-mode data meeting the accuracy requirements of 0.005 °C, 0.01 practical salinity units, and 2.5 dbar for temperature, salinity, and pressure, respectively, its quality, too, is sufficiently high to produce a valuable and indispensable archive of ocean observations [Riser et al., 2016].

The internal wave model IDEMIX was developed as an energetically consistent replacement of the heuristic, inconsistent mixing parameterizations currently implemented in ocean general circulation models. With the global ocean as the standard application, a general evaluation of IDEMIX should be based on an (approximately) global observational data base. The Argo profiles are practically the natural choice.

Estimates of TKE dissipation rates and, exploiting relation Eq. 1.5, vertical diffusivity can be obtained from finestructure information either by the analysis of density inversions in the water column [Thorpe, 1977] or by estimates of internal gravity wave energy [Gregg, 1989], which can be inferred from observations of strain ξ_z—the vertical change of isopycnal displacement ξ—and shear, based on the parameterizations of Mc-

pressibility must be smaller than that of the surrounding fluid, as otherwise the pressure decrease induced by the slightest upward perturbation would cause an increase in volume and hence buoyancy, reinforcing the original perturbation (and vice versa for downward perturbations) [e.g. Olbers et al., 2012].

Comas and Müller [1981] or Henyey et al. [1986] presented in Section 1.2. The former technique empirically relates the vertical scales of overturning motions induced by shear instability, the Thorpe scales L_T, to the outer scales of turbulence, the Ozmidov scale L_O (see Fig. 1.6), and hence the TKE dissipation rate $\epsilon_{TKE} = L_o^2 N^3$. The Thorpe scale is estimated as the root mean square displacement of water parcels that is required to sort a vertical profile of potential density such that it is gravitationally stable. Apart from contaminations from ship heave or propeller vibrations, the main shortcoming of this method is that the reliable detection of these density overturns necessitates a high vertical resolution and especially in low-mixing environments, instrument noise can represent a serious error source [Gargett and Garner, 2008]. While studies in regions of high stratification under favorable sampling conditions found a good agreement between the Thorpe-scale method and microstructure estimates of turbulent mixing [Ferron et al., 1998; Klymak et al., 2008], the method performs less well in more extreme environments: comparing vertical diffusivities in Drake Passage and over the smoother sea floor of the southeastern Pacific Ocean, Frants et al. [2013] noted that the Thorpe-scale method could not reproduce the factor 5 difference in diffusivities between these two locations observed with microstructure instruments.

The Gregg-Henyey-method, often simply denoted "finestructure method", links the TKE dissipation to breaking internal gravity waves, parameterizing the loss of TKE as a function of internal gravity wave energy, which is transported through the spectrum by nonlinear wave-wave interactions and at small scales to TKE (see Sections 1.1.2 and 1.1.3). This approach was introduced by Gregg [1989], who evaluated theoretical scaling laws of internal gravity wave energy dissipation ϵ_{IW} against observations. These scaling laws describe the internal wave energy loss for example as the energy flux out of the internal wave spectrum at high vertical wavenumbers based on ray tracing techniques [Henyey et al., 1986] or in terms of the probability of wave breaking as a function of the local Richardson number [Munk, 1981]. Relying on the GM model to represent the internal wave energy spectrum, the dissipation ϵ_{IW} becomes a function of the GM model energy density E_{GM} [e.g. $\epsilon_{IW} \propto E_{GM}^2$ in the parameterization of Henyey et al., 1986]. To test the accuracy of the various parameterizations, E_{GM} is in these formulations replaced by the actual energy density E_{IW}, which cannot be measured directly and is hence inferred from the observed shear variance:

$$E_{IW} = E_{GM} S_{10}^2 / S_{GM}^2, \tag{1.13}$$

where S_{10} is the vertical shear calculated over distances of 10 m and S_{GM} is the corresponding value of the GM model. The resultant expression of the internal wave energy dissipation based on the parameterization of Henyey et al. [1986] reproduced midlatitude microstructure observations of ϵ_{TKE}, varying by two orders of magnitude throughout the water column, within a factor of 2. Having been refined in further comparisons with observations and adjusted to also apply to wave fields that depart to some degree from the GM model description [e.g. Wijesekera et al., 1993; Polzin et al., 1995; Gregg et al., 2003; Kunze et al., 2006b], this expression is now widely used (see also Fig. 1.8) to infer TKE dissipation rates from relatively easily observed finestructure shear or strain variances:

$$\epsilon_{TKE} \propto \frac{\overline{N^2}\langle \xi_z^2 \rangle^2}{N_0^2 \langle \xi_{z,GM}^2 \rangle^2} h(R_\omega). \tag{1.14}$$

Here, $\overline{N}$ is the average buoyancy frequency, N_0 the GM model reference, and angle brackets denote an averaging procedure. The function $h(R_\omega)$, where R_ω is the shear-to-strain variance ratio, accounts for the frequency content of the wave field and represents the ratio of horizontal kinetic to available potential energy of a single wave [Kunze et al., 2006b]. Although Eq. 1.14 can alternately be expressed in terms of the finescale shear or strain variance relative to that of the GM model, both fields need to be know to adequately represent $h(R_\omega)$. Because the theoretical scaling laws described above form the backbone of Eq. 1.14, it is strictly speaking only valid for internal wave fields that are in steady state, that are only weakly nonlinear, and that approximately follow the GM model description [see e.g. Gregg, 1989; Wijesekera et al., 1993; Polzin et al., 1995, 2014]. Moreover, it is implicitly assumed that all observed finescale variance can be attributed to internal wave dynamics, which renders the method inaccurate in the mixed layer and mode water [Whalen et al., 2015].

The finestructure method has been adopted in various studies [e.g. Kunze et al., 2006b; Huussen et al., 2012] and has also successfully been applied to Argo data [Wu et al., 2011; Whalen et al., 2012]. In that case, velocity and hence shear information is missing and the shear-to-strain ratio R_ω is assumed to be constant. Both approaches, either with variable or constant R_ω, have been shown to reproduce TKE dissipation rates estimated from microstructure measurements within a factor of 2-3 in the upper 2000 m of the ocean [Sheen et al., 2013; Whalen et al., 2015], but the two methods can diverge quite drastically when the underlying assumptions are not met [e.g. on continental shelves, Frants et al., 2013; Polzin et al., 2014; MacKinnon et al., 2017, and references therein]. In the stratified ocean interior, however, finestructure estimates of turbulent mixing inferred from Argo profiles provide the most suitable reference data base for a general evaluation of IDEMIX, capturing the geographic and even seasonal variations of these small-scale ocean dynamics.

1.4 Thesis overview

The first aim of this thesis is a general evaluation of the internal gravity wave model and mixing module IDEMIX in comparison with Argo finestructure-derived mixing estimates. To that end, ten years of Argo data[3] were compiled into a global data base of TKE dissipation rate and vertical diffusivity estimates (for details and references see Sections 1.3.2, 2.3 and 5.3). Moreover, a new approach to directly calculate the internal gravity wave energy from finestructure strain information was developed and additionally used for the evaluation (see Section 2.4 and Appendix 5.2 for details). As the vertical diffusivity calculated by IDEMIX also depends on the buoyancy frequency modeled by pyOM (Eq. 1.4), the focus of the evaluation was on TKE dissipation rates in order to evaluate IDEMIX alone and not the ocean model it was coupled to. This evaluation is described in Chapter 2, where the following research questions are addressed:

1a How do the finestructure estimates of TKE dissipation rates and internal gravity wave energy levels vary geographically? What is the uncertainty of these estimates?

1b How well can IDEMIX reproduce these Argo-derived estimates in terms of their magnitude and their geographic variations? Which tuning parameter settings in IDEMIX lead to the best agreement?

1c How is the model-data agreement affected by using different model versions (IDEMIX1 vs IDEMIX2) and different forcing settings, particularly with respect to the role of mesoscale eddies?

Motivated by the conclusions drawn from the first part, the second part of this PhD thesis deals with a specific aspect of IDEMIX, that is, the bottom boundary forcing through the generation of internal tides at the rough sea floor. While current analytical methods to compute the energy flux from the barotropic tides into internal gravity waves consider this energy conversion to be the same in all horizontal directions, a new approach developed by Jonas Nycander[4] resolves the directional dependence of this flux. This new method is presented and evaluated in Chapter 3, where the following questions are discussed:

2a How can the direction of the energy flux from barotropic to internal tides be calculated? How can this method be applied to the global ocean?

2b How does this new method perform for idealized topographic settings? What are suitable numerical parameters for idealized and realistic topography?

2c How do internal gravity wave energy and TKE dissipation rates modeled by IDEMIX change when the tidal forcing varies with direction?

[3] Argo (2000). Argo float data and metadata from Global Data Assembly Centre (Argo GDAC). SEANOE. http://doi.org/10.17882/42182
[4] affiliated at the Department of Meteorology at Stockholm University

In light of the results presented in Chapters 2 and 3, these questions are revisited and answered in Chapter 4. Their discussion is followed by an outlook, identifying open questions as well as possible future lines of research. In particular, it serves as a synthesis of the different topics addressed in this PhD project and addresses its overarching research questions:

- Can IDEMIX provide a realistic description of oceanic turbulent mixing in global general circulation models?
- What further improvements or steps of evaluation might be necessary to (better) achieve that objective?

2 Evaluating the global internal wave model IDEMIX using finestructure methods

This chapter is a reprint of the abstract and Sections 1-6 of the paper "Evaluating the Global Internal Wave Model IDEMIX Using Finestructure Methods" to be published in the Journal of Physical Oceanography. The contents of the appendix of that publication are included and discussed in much more detail in Appendix 5.2 of this thesis; references to the appendices of this thesis were added where applicable.

Citation: Pollmann, F., Eden, C. and Olbers, D., 2017: Evaluating the Global Internal Wave Model IDEMIX Using Finestructure Methods, J. Phys. Oceanogr., DOI: 10.1175/JPO-D-16-0204.1, in press ©Copyright 2017 AMS[5]

2.1 Abstract

Small-scale turbulent mixing affects large-scale ocean processes such as the global overturning circulation but remains unresolved in ocean models. Since the breaking of internal gravity waves is a major source of this mixing, consistent parameterizations take internal wave energetics into account. The model IDEMIX ("Internal Wave Dissipation, Energy and Mixing") predicts the internal wave energy, dissipation rates, and diapycnal diffusivites based on a simplification of the spectral radiation balance of the wave field and can be used as a mixing module in global numerical simulations. In this study, it is evaluated against finestructure estimates of turbulent dissipation rates derived from Argo float observations. In addition, a novel method to compute internal gravity wave energy from finescale strain information alone is presented and applied. IDEMIX well reproduces the magnitude and the large-scale variations of the Argo-derived dissipation rate and energy level estimates. Deficiencies arise with respect to the detailed vertical structure or the spatial extent of mixing hotspots. This points toward the need to improve the forcing functions in IDEMIX, both by implementing additional physical detail and by better constraining the processes already included in the model. A prominent example is the energy transfer from the mesoscale eddies to the internal gravity waves, which is identified as an essential contributor to turbulent mixing in idealized simulations, but needs to be better understood by help of numerical, analytical, and observational studies in order to be represented realistically in ocean models.

2.2 Introduction

Despite being a small-scale phenomenon, turbulent mixing shapes regional- to global-scale processes, ranging from the distribution of passive tracers to the driving of the meridional overturning circulation [Munk and Wunsch, 1998; Wunsch and Ferrari, 2004; Kunze and Llewellyn Smith, 2004]. It is therefore crucial to find consistent parameterizations for this mixing in ocean models, where it remains unresolved and will presumably continue to be so even in the face of future computer power increases [Eden et al., 2014]. Typically, small-scale turbulence is represented by a vertical mixing of fluid properties, often in terms of a vertical diffusivity with a fixed value or varying as a function of depth or stability frequency [Munk, 1966; Bryan and Lewis, 1979; Cummins et al., 1990]. None of these approaches, however, accounts for the energy source for mixing. To overcome this issue, the model IDEMIX ("Internal Wave Dissipation, Energy and Mixing"), an energetically consistent parameterization for the diapycnal diffusivity induced by breaking internal gravity waves [Olbers and Eden, 2013], was developed. We here present a first assessment of its performance.

Internal gravity waves are a ubiquitous feature of the global ocean and can be excited i.a. by a fluctuating wind stress at the surface ("near-inertial waves"), the scattering of the barotropic tide at rough topography ("internal tides"), the dissipation of meso-scale eddies, or the geostrophic adjustment of large-scale disturbances [for a brief review, cf. e.g. Müller and Olbers, 1975; Garrett and Munk, 1979; St. Laurent et al., 2012]. A prominent characteristic of internal waves is their continuous energy spectrum both in terms of wavenumber and frequency—with the exception of the near-inertial and the tidal frequency bands, the energy spectrum can be described as a continuum of almost universal shape known as the Garrett-Munk (GM) spectrum [Garrett and Munk, 1972b]. The continuousness of the spectrum suggests an energy transfer in wavenumber space, generally thought to be induced by nonlinear wave-wave interactions [Olbers, 1976; McComas and Bretherton, 1977]. At the high-wavenumber end of the spectrum, the energy is converted to turbulent kinetic energy, which in turn cascades to ever smaller scales until it is dissipated into internal energy or creates potential energy by density mixing.

Not only because of the intricate properties of internal gravity waves, but also for reasons of physical consistency and the fact that observations of small-scale turbulence show strong temporal and spatial variations [Polzin and Lvov, 2011; Whalen et al., 2012], a mixing parameterization based on internal wave energetics is desirable. One such attempt was made by Müller and Natarov [2003] with the Internal Wave Action Model (IWAM); its application, however, is severly hindered by the fact that it involves six spatial dimensions. IDEMIX, while also based on the spectral radiation balance for internal waves, avoids this problem by way of integrating in wavenumber space. Assumptions about the effect of the integrated terms as well as a parameterization for internal wave energy dissipation then lead to a single partial differential equation for the internal wave energy. There are to date several IDEMIX-versions of increasing complexity; in this study, we will mainly focus on the first version as described in Olbers and Eden [2013], in which all internal waves are treated as part of a laterally isotropic continuum.

The aim of this study is to evaluate the model IDEMIX through a comparison with observations. Measurements that resolve turbulence, however, are sparse, especially on longer spatial and temporal scales. We therefore estimate the turbulent kinetic energy (TKE) dissipation rate and diapycnal diffusivity from finestructure data. The underlying concept is that turbulent mixing is the consequence of a nonlinear energy transfer through the internal wave spectrum, and that it can thus be described in terms of internal gravity wave energetics [Olbers, 1976; McComas and Müller, 1981; Henyey et al., 1986; Gregg, 1989; Polzin et al., 1995]. Assuming furthermore that the observed variance in shear or strain on the 10-100 m scale can be attributed solely to internal gravity waves, more commonly available datasets such as CTD or ADCP casts can be used to infer TKE dissipation rates and diapycnal diffusivities [Kunze et al., 2006b; Whalen et al., 2015]. A validation of the finestructure method was for example given by Whalen et al. [2015], who compared strain-based finescale estimates to microstructure observations and found that the mean dissipation rates agreed within a factor of 3 for 96 % of the comparisons. We here show that this method also allows the estimation of internal gravity wave energy from finescale strain or density information.

This paper is structured as follows: In Section 2.3, we briefly present the model IDEMIX, referring the reader to Olbers and Eden [2013]; Eden and Olbers [2014] for a detailed description. Section 2.4 deals with the finestructure method and details how to derive TKE dissipation rates and internal wave energy from finescale strain information. These fields are compared to those modeled by IDEMIX in Section 2.5, where we also analyze the sensitivity of this model-data comparison to tuning parameter and forcing settings in IDEMIX. A discussion of these results, involving a sensitivity analysis of the finestructure method, is given in Section 2.6; a summary and concluding remarks are presented in Section 2.7.

2.3 The model IDEMIX

The basic version of the model IDEMIX (IDEMIX1) consists in a single differential equation for the total energy E together with a parameterization for its dissipation ϵ_{IW} and the definition of bottom and surface forcing terms [Olbers and Eden, 2013; Eden and Olbers, 2014]. The internal wave energy varies according to

$$\frac{\partial E}{\partial t} - \frac{\partial}{\partial z}\left(c_0 \tau_v \frac{\partial c_0 E}{\partial z}\right) = -\epsilon_{IW}, \tag{2.1}$$

where c_0 is a weighted average group velocity, z the vertical coordinate, and τ_v a timescale on the order of days, describing a relaxation toward a symmetric state due to the parameterized effect of nonlinear wave-wave interactions. This equation is obtained from the radiative transfer balance for weakly interacting oceanic internal gravity waves [Hasselmann, 1967], making the following assumptions and approximations:

- The radiation balance is expressed in terms of the spectral energy and divided into upward and downward propagating parts, which are integrated over all horizontal wavenumbers $\mathbf{k} = (k_1, k_2)$ and the appropriate half-space of vertical wavenumbers m, assuming lateral homogeneity [i.e. $\omega = \Omega(\mathbf{k}, m, z)$] and that all generation processes are confined to the top and bottom boundaries.

- Equations for the sum E and the difference ΔE of the integrated upward and downward propagating energy are expressed and simplified assuming that the dissipation of internal wave energy is symmetric with respect to m. The integrated effect of nonlinear wave-wave interactions is assumed to eliminate these differences, ΔE, and is hence parameterized by a relaxation toward a symmetric state with a decay time scale τ_v.

- The emerging vertical energy flux terms are expressed in terms of E and ΔE. The associated average velocities are set to be equal for upward and downward propagating waves, $c^+ \approx c^- \approx c_0$, and calculated analytically assuming that the energy spectrum can be described by the GM model.

- Considering timescales much longer than τ_v, the equations for the total and the asymmetric energy can be combined to form Eq. 2.1.

In this study, we use the global version of IDEMIX1 described in Olbers and Eden [2013, cf. their Section 5], where the energy balance (Eq. 2.1), is extended to account for horizontal inhomogeneities:

$$\frac{\partial E}{\partial t} - \frac{\partial}{\partial z}\left(c_0 \tau_v \frac{\partial c_0 E}{\partial z}\right) - \nabla_h \cdot v_0 \tau_h \nabla_h v_0 E = -\epsilon_{IW}. \tag{2.2}$$

The parameters v_0 and τ_h denote the lateral group velocity and a time scale on which lateral anisotropies in the wave field are eliminated by nonlinear wave-wave interactions, set to 15 days.

The dissipation of total internal wave energy ϵ_{IW} is equated with the energy flux at the high-wavenumber end of the spectrum, where the vertical shear is large and shear instability and convective overturns are most likely to occur. Assuming furthermore that this flux is induced by nonlinear wave-wave interactions, an expression for ϵ_{IW} can be found based on a variety of already existing scaling laws [e.g. Olbers, 1976] and parameterizations [e.g. McComas and Müller, 1981; Henyey et al., 1986; Sun and Kunze, 1999; Polzin, 2004]. For the sake of simplicity, the parameterization implemented in IDEMIX is a combination of the formulations by McComas and Müller [1981], who calculated the energy flux across the high vertical wavenumber cutoff of the GM spectrum induced by parametric subharmonic instability and induced diffusion, and by Henyey et al. [1986], who used an Eikonal technique to estimate the energy flux toward high vertical wavenumbers:

$$\epsilon_{IW}(E) = \mu f \frac{\text{arccosh}(N/f) m_*^2}{\text{arccosh}(N_0/f_0) N^2} E^2 = \mu_0 f_e \frac{m_*^2}{N^2} E^2, \tag{2.3}$$

with the reference buoyancy and Coriolis frequencies N_0 and f_0 and the parameters $\mu_0 = \mu/\text{arccosh}(N_0/f_0)$ and $f_e = f\text{arccosh}(N/f)$. The quantity m_* is the GM model bandwidth in wavenumber space and $\mu \approx 2$ a constant from the parameterization by McComas and Müller [1981], so that $\mu_0 = 2/3$ for $N_0/f_0 \approx 10$ [note the factor of 2 error in the value for μ used in Olbers and Eden, 2013].

Equation 2.3 predicts the amount of energy that leaves the internal wave spectrum at high vertical wavenumbers and is dissipated to small-scale turbulence. It can be used as an input to a turbulence model, in this case, the Osborn-Cox model. Equating the dissipation of internal wave energy with the shear production term, i.e. $\epsilon_{IW} = -\overline{\mathbf{u}_h' w'} \partial \overline{\mathbf{u}}_h / \partial z$, and applying a downgradient closure for the vertical buoyancy flux, $\overline{b'w'} = -\kappa N^2$, yields the following steady-state TKE balance:

$$\epsilon_{IW} = -\overline{\mathbf{u}_h' w'} \partial \overline{\mathbf{u}_h} / \partial z = \epsilon_{TKE} + \kappa N^2. \tag{2.4}$$

Here, $\mathbf{u} = (\mathbf{u}_h, w)$ is the three-dimensional velocity vector, ϵ_{TKE} the dissipation of TKE, and κ the vertical diffusivity, with overbars denoting the mean quantities and primes the turbulent fluctuations. Assuming that the so-called "mixing efficiency" is constant [$\delta \approx 0.2$, Osborn, 1980] leads to the balance $\kappa N^2 = \delta \epsilon_{TKE}$, so that the vertical diffusivity κ can be expressed in terms of the dissipation of internal wave energy ϵ_{IW}:

$$\kappa = \frac{\delta}{1+\delta} \frac{\epsilon_{IW}}{N^2} = \frac{\delta}{1+\delta} \mu_0 f_e \frac{m_*^2 E^2}{N^4}. \tag{2.5}$$

We close the model IDEMIX by specifying the same boundary conditions as in Olbers and Eden [2013]: The energy flux at the surface F_{surf} represents internal waves radiating out of the mixed layer which is forced by a fluctuating wind stress; following Jochum et al. [2013], it is computed as 20 % of the wind input into the near inertial band in the mixed layer. The bottom energy flux F_{bot} is estimated as the conversion of barotropic tidal energy into internal wave energy using the parameterization by Jayne [2009], which is based on the barotropic tidal energy and the bottom roughness [cf. Fig. 2 in Olbers and Eden, 2013, for global maps of F_{surf} and F_{bot}]. Another important source of internal gravity waves is related to the wave field's interaction with mesoscale features, for example, through the generation of lee waves by mesoscale eddies [Nikurashin and Ferrari, 2011]. In the ocean model used in this study, their effect is parameterized by along-isopycnal mixing and an additional eddy-driven velocity for tracers, where the corresponding diffusivities are obtained from the closure by Eden and Greatbatch [2008]. These lateral diffusivities are the same as those obtained in the parameterization by Gent and McWilliams [1990] and are estimated via a mixing length assumption as well as an assumption for the form of the eddy dissipation based on the dissipation rates in small-scale turbulence; compare Eden et al. [2014]; Eden [2016] for details on the eddy closure and the link between the various parameterizations included in the ocean model. Little is known about the details of the energy sinks of mesoscale eddies; suggested pathways include lee wave generation by eddy-topography interaction [Nikurashin and Ferrari, 2011]; generation of ageostrophic instabilities, mainly in the surface mixed layer [Molemaker et al., 2005]; or a direct kinetic energy cascade to smaller scales [Capet et al., 2008; Brüggemann and Eden, 2015]. We here follow the approach by Eden et al. [2014], using the setup for which the best agreement with observations was observed, i.e. their scenario CONSIST-SURF. In this experiment, the dissipated eddy energy ϵ_{eddy} is partly injected into the internal wave field at the bottom (representing lee wave generation) and partly into small-scale turbulence at the surface (representing dissipation via ageostrophic instability). The internal wave energy equation thus reads:

$$\frac{\partial E}{\partial t} - \frac{\partial}{\partial z}\left(c_0 \tau_v \frac{\partial c_0 E}{\partial z}\right) - \nabla_h \cdot v_0 \tau_h \nabla_h v_0 E = -\epsilon_{IW} + 0.2\epsilon_{eddy}. \tag{2.6}$$

Newer versions of the model IDEMIX explicitly treat near-inertial waves and internal tides as well as their interaction with the wave continuum ["IDEMIX2", Eden and Olbers, 2014]. For these low mode compartments, the assumption of lateral isotropy no longer holds. IDEMIX2 thus resolves lateral propagation and refraction by integrating the energy over the wavenumbers $0 \leqslant m \leqslant m_l$, where m_l is the wavenumber separating the continuum from the low modes, as well as over the local near-inertial frequency band for the near-inertial waves. The interaction of near-inertial waves and the continuum is sufficiently small to be disregarded [cf. Appendix 1 in Eden and Olbers, 2014]; for the M_2 tidal constituent, wave-wave and topography interaction terms are for example derived from Müller and Xu [1992] and Olbers et al. [2012]. Since only the M_2 tide is considered in this model version, 50 % of the tidal forcing F_{bot} are injected at the bottom to account for the effect of the other tidal constituents.

Note that several other assumptions made in the derivation of IDEMIX1 (e.g. the absence of interior sources) can easily be relaxed and different or additional forcing functions can readily be implemented. In this study, however, we focus on the versions described above.

2.4 Method

2.4.1 Finestructure estimates of turbulent mixing

We closely follow the approach by Whalen et al. [2012] and estimate the TKE dissipation rate from Argo data. The Argo program maintains an array of almost 4000 freely drifting floats that are equipped with CTD sensors, which profile conductivity, temperature and pressure down to 2000 m every ten days (http://doi.org/10.17882/42182). We use all profiles from the years 2006-15 that have a quality flag "A" (all real-time quality tests passed) for all three CTD sensors and a vertical resolution of at most 10 m, taking the thoroughly tested and corrected delayed mode data whenever possible. Starting at the bottom of each profile, we divide these into half-overlapping segments of 200 m length and calculate the buoyancy frequency N^2 based on the adiabatic leveling method as in IOC et al. [2010]. Both for CTD profiles as well as these 200 m segments, we apply the same quality control measures as detailed in Whalen et al. [2012, see also Appendix 5.3].

Strain, a measure of how internal waves deform isopycnals, is computed for each 200 m segment as

$$\xi_z = \frac{N^2 - N^2_{fit}}{\overline{N^2}}, \tag{2.7}$$

where N^2_{fit} is a quadratic fit to the data and $\overline{N^2}$ the average of the respective segment [e.g. Desaubies and Smith, 1982]. The strain segments are detrended, windowed using a $\sin^2$ 10 % taper, and spatially Fourier transformed to obtain the power spectra $S_{\xi_z}(m)$, where m is again the vertical wavenumber. In order to correct for the loss of variance due to first-differencing (the gradient operator inherent in the computation of N^2), the Fourier amplitudes are divided by the transfer function $T_{corr} = \text{sinc}^2\,(\Delta z/\lambda_z)$, where Δz is the vertical resolution of the segment and $\lambda_z = 2\pi/m$ the vertical wavelength.

They are also divided by $W_{corr} = L^{-1} \sum_{t=1}^{L} h_t^2$, where h_t is the window function and L the length of the data window, to correct for the application of the taper [von Storch and Zwiers, 2001].

Strain variance $\langle \xi_z^2 \rangle$ is then computed by integrating over the corrected spectra between wavenumbers $m_1 = 2\pi/100\,\text{m}^{-1}$ and $m_2 = 2\pi/10\,\text{m}^{-1}$. As an additional constraint, m_2 is adjusted such that $\langle \xi_z^2 \rangle \leqslant 0.1$ to avoid underestimating the variance when the spectrum becomes saturated at large wavenumbers [cf. Gargett, 1990; Kunze et al., 2006b]. By integrating over the same wavenumber range, the corresponding value for the GM model is obtained:

$$\langle \xi_{z,GM}^2 \rangle = \int_f^N \int_{m_1}^{m_2} m^2 \frac{1}{\omega} \frac{\omega^2 - f^2}{N^2 - f^2} S_E^{GM}(m, \omega) dm d\omega, \tag{2.8}$$

where $S_E^{GM} = E_{GM} A_{GM} B_{GM}$ is the GM model energy spectrum factorized into the energy density E_{GM}, a wavenumber-dependent function A_{GM}, and a frequency-dependent function B_{GM} [Cairns and Williams, 1976]. Details on these functions and on how to solve Eq. 2.8 are given in the following section. The GM model parameters used are the idealized profile $N = N_0 e^{-z/b}$ with the scale depth $b = 1300\,\text{m}$ and the reference buoyancy $N_0 = 5.24 \times 10^{-3}\,\text{s}^{-1}$; the dimensionless energy level $E_0 = 6.3 \times 10^{-5}$, obtained by scaling the GM energy density $E_{GM} = 3 \times 10^{-3}\,\text{m}^2\,\text{s}^{-2}$ by $(bN_0)^2$; the modal bandwidth $j_* = 3$; and the bandwidth in wavenumber space $m_* = \pi j_* N/(bN_0)$ [Munk, 1981].

The finestructure method is based on the approach by Gregg [1989], who applied theoretical scaling laws for internal wave energy dissipation ϵ_{IW} [i.a. those by McComas and Müller, 1981; Henyey et al., 1986, combined in Eq. 2.3] to observations. To this end, he replaced the GM energy density E_{GM} in these laws by the observed energy E_{IW}, which cannot be measured directly and was hence inferred from the relation $E_{IW}/E_{GM} = S_{10}^2/S_{GM}^2$, where S_{10} is the observed shear measured over 10 m depth intervals and S_{GM} the corresponding value for the GM model. The resultant expression for ϵ_{IW} was found to agree within a factor of 2 with microstructure measurements of TKE dissipation rates ϵ_{TKE} in the midlatitude thermocline. This motivated the evaluation against and subsequent adjustment to other observations of ϵ_{TKE} [cf. i.a. Wijesekera et al., 1993; Polzin et al., 1995; Gregg et al., 2003; Kunze et al., 2006b] and the application of the refined expression as a parameterization of TKE dissipation rates. The formulation used in this study is given by:

$$\epsilon_{TKE} = \epsilon_0 \frac{\overline{N^2} \langle \xi_z^2 \rangle^2}{N_0^2 \langle \xi_{z,GM}^2 \rangle^2} h(R_\omega) L_f(f, N) \tag{2.9}$$

with $\epsilon_0 = 6.73 \times 10^{-10}\,\text{W}\,\text{kg}^{-1}$ [Whalen et al., 2012]. The function $L_f(f, N)$ is a latitudinal correction for the dependence of internal wave characteristics on the Coriolis frequency, f:

$$L_f(f, N) = \frac{f \operatorname{arccosh}\left(\frac{N}{f}\right)}{f_{30} \operatorname{arccosh}\left(\frac{N_0}{f_{30}}\right)}, \tag{2.10}$$

where f_{30} is the Coriolis frequency at 30° latitude. The function $h(R_\omega)$ accounts for the frequency content of the internal gravity waves:

$$h(R_\omega) = \frac{1}{6\sqrt{2}} \frac{R_\omega(R_\omega + 1)}{\sqrt{R_\omega - 1}}. \tag{2.11}$$

R_ω is the shear-to-strain ratio, which is the ratio of horizontal kinetic energy and available potential energy—due to the lack of shear information, it has to be set constant. Following Whalen et al. [2012], we use the GM model value of three, which is a reasonable estimate in the upper ocean [Kunze et al., 2006b] and reduces the function $h(R_\omega)$ to unity. If R_ω underestimates the actual shear-to-strain ratio, $h(R_\omega)$ is also too small and vice versa.

Assuming a constant mixing efficiency of $\delta = 0.2$, the diffusivity is finally estimated as

$$\kappa = \delta \frac{\epsilon_{TKE}}{N^2}. \tag{2.12}$$

2.4.2 Internal Wave Energy

The internal gravity wave energy $E(z)$ is computed from vertical spectra of strain and potential density assuming that the total energy spectrum S_E features the same wavenumber and frequency dependence as the GM energy spectrum:

$$S_E(m, \omega) = E(z) A_{GM}(m) B_{GM}(\omega), \tag{2.13}$$

with

$$A_{GM}(m) = \frac{n_A}{1 + \frac{m^2}{m_*^2}} \frac{1}{m_*} \qquad B_{GM}(\omega) = \frac{f}{\omega} \frac{n_B}{\sqrt{\omega^2 - f^2}} \tag{2.14}$$

where m_* is the vertical wavenumber bandwidth and m_h and m_l are high and a low wavenumber cutoffs, respectively[6]. The terms n_A and n_B are normalization factors defined such that A_{GM} and B_{GM} integrate to unity and $\iint S_E \, dm d\omega = E(z)$:

$$n_A = \left[\arctan\left(\frac{m_h}{m_*}\right) - \arctan\left(\frac{m_l}{m_*}\right)\right]^{-1}, n_B = \frac{2}{\pi}\left[1 - \frac{2}{\pi}\arcsin\left(\frac{f}{N}\right)\right]^{-1}. \tag{2.15}$$

[6]Note that we refer to this version of the GM model as GM76 (due to its first appearance in Cairns and Williams [1976]) in contrast to the modified GM75-model, here denoted as GM75m, which is characterized by a wavenumber dependence $A_{GM}(m)$ proportional to $(m + m_*)^{-2}$ [described in the appendix of Gregg and Kunze, 1991, as GM76]. We do not adjust the modal bandwidth j_* when changing between these two GM model versions as the effect on the equivalent bandwidth is negligible.

Beginning with the eigenvector (polarization vector) notation for internal gravity waves, the following relation between the energy spectrum and the spectra of strain ξ_z or potential density ρ' can be found [e.g. Willebrand et al., 1977; Munk, 1981; Olbers et al., 2012]:

$$S_{\xi_z}(m,\omega) = m^2 \frac{1}{\omega^2} \frac{\omega^2 - f^2}{N^2 - f^2} S_E(m,\omega), \quad \text{and} \tag{2.16}$$

$$S_{\rho'}(m,\omega) = \frac{\rho_0^2}{g^2} N^4 S_{\xi_z}(m,\omega) = \frac{\rho_0^2}{g^2} N^4 \frac{1}{\omega^2} \frac{\omega^2 - f^2}{N^2 - f^2} S_E(m,\omega), \tag{2.17}$$

where $\rho' = \rho - \rho_{fit}$ is the potential density perturbation, $\rho_0 = 1027\,\mathrm{kg\,m^{-3}}$ the constant background density, and ρ_{fit} a vertical fit to the data within each 200 m segment (equivalent to N_{fit}). In order to calculate the total internal wave energy $E(z)$ from Argo data, $S_E(m,\omega)$ is expressed using Eq. 2.13 and the above equations are integrated over all frequencies and a suitable wavenumber range (the same as considered for the dissipation rate estimates, i.e. between $m_1 = 2\pi/100\,\mathrm{m^{-1}}$ and $m_2 = 2\pi/10\,\mathrm{m^{-1}}$):

$$\begin{aligned} \langle \xi_z^2 \rangle &= E_{\xi_z}(z) \int_{m_1}^{m_2} \int_f^N m^2 \frac{1}{\omega^2} \frac{\omega^2 - f^2}{N^2 - f^2} A_{GM}(m) B_{GM}(\omega)\, dm\, d\omega \\ \Leftrightarrow E_{\xi_z}(z) &= \frac{\langle \xi_z^2 \rangle}{n_B n_A G C_1} \end{aligned} \tag{2.18}$$

Rewriting Eq. 2.18 in terms of the GM fields illustrates the analogy to the parameterization of TKE dissipation rates given in Eq. 2.9:

$$E_{\xi_z}(z) = E_{GM} \frac{\langle \xi_z^2 \rangle}{\langle \xi_{z,GM}^2 \rangle}. \tag{2.19}$$

The strain variance $\langle \xi_z^2 \rangle$ is calculated from CTD casts as outlined in the previous section, the variances of potential density are obtained in likewise manner. The functions G and C_1 describe the integrated frequency and wavenumber part of Eq. 2.16, respectively, and are given in the Appendix 5.2 together with an in-depth derivation of Eq. 2.18. When considering density variance, the procedure is the same but for the function C_1, which changes due to the different wavenumber dependence in Eq. 2.17 (cf. Appendix 5.2).

Note that the frequency-dependent part of the GM model (cf. Eq. 2.14) is zero at the equator, while it yields non-zero results upon integration over all frequencies (cf. Eq. 5.27). Due to this discrepancy between the integrated and frequency-dependent GM model formulations, the dissipation rate and energy estimates close to the equator need to be treated carefully. For the comparison with IDEMIX we therefore only consider latitudes higher than three degrees.

2.5 Results

In this section, we present global maps of dissipation rates and energy levels obtained from Argo data (see Appendix 5.4 for additional maps) and the evaluation of the parameterization IDEMIX based on these finestructure estimates. A discussion of these results is provided in Section 2.6.

2.5.1 Argo-based estimates of dissipation rates and internal wave energy

Global maps of average TKE dissipation rates estimated from finestructure-strain data [analogous to Fig. 1 in Whalen et al., 2012] are depicted in Fig. 2.1. We consider the depth ranges 250-500 m, 500-1000 m, and 1000-2000 m, where especially in the Atlantic and the Southern Ocean data coverage strongly decreases with depth. In each depth range, the spatial variations in dissipation rates span at least three orders of magnitude. Strong mixing is observed in the western boundary currents and regions of high mesoscale activity, particularly in the subtropical gyres and the western boundary of the Pacific Ocean and in the Antarctic Circumpolar Current (ACC). The former signal is most prominent close to the surface, while mixing hotspots like Drake Passage or the Kuroshio and the Gulf Stream as well as their extensions can be identified as such at all depths. In general, a decrease in dissipation rates of about an order of magnitude between the upper and lower depth range can be observed, although locally sometimes the inverse is the case.

Internal gravity wave energy is shown in Fig. 2.2 for the depth range 250-500 m (see Appendix 5.4 for information on the other depth ranges). Highly energetic regions with values of more than 10^{-2} m^2 s^{-2} (i.e. three times higher than the GM model value) are the subtropical northwest Pacific, the wind-driven gyres of the Pacific and the tropics. In general, energy levels decrease by about two orders of magnitude from the equator to the poles. Longitudinal gradients are smaller and exist only outside of the tropics, where energy levels decrease slightly from west to east in all ocean basins. These signals are the same at all depths. On average, energy levels E_{ξ_z} (E_ρ) are 2.0 (3.5) times higher in the upper depth range than in the lower one, but energy levels increasing with depth can also be observed at some locations. Depending on the depth range, energy levels computed from potential density spectra are up to a factor of 2 higher than those calculated from strain spectra.

2.5.2 Evaluation of IDEMIX

IDEMIX is coupled to the primitive equation model "pyOM", in which energy is exchanged consistently between the the mean flow, parameterized mesoscale eddies, TKE, and, in the form of IDEMIX, internal gravity waves [cf. Eden et al., 2014; Eden, 2016,

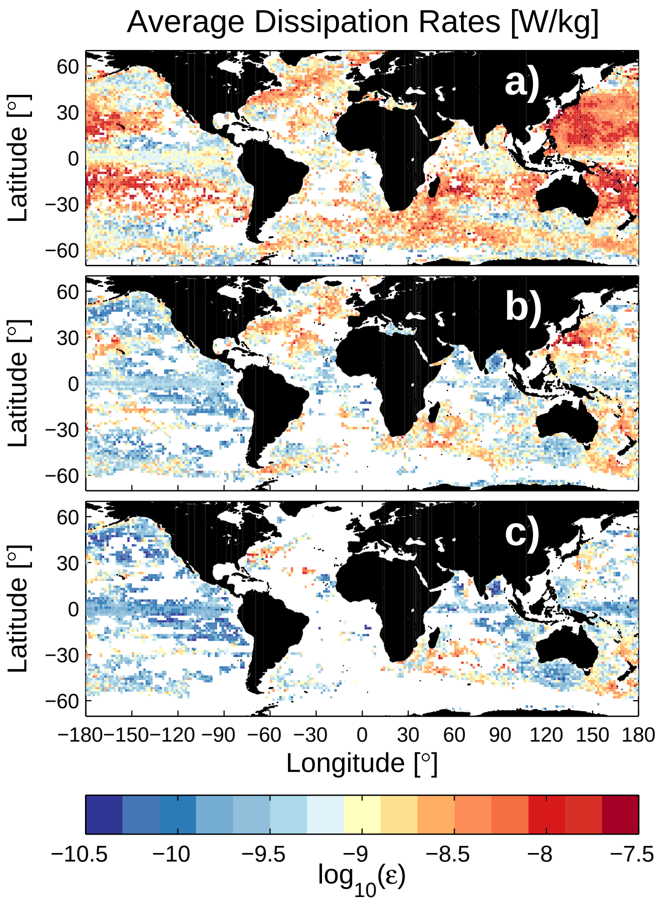

Figure 2.1: Global maps of average TKE dissipation rates ϵ_{TKE} estimated from Argo data. Results are averaged over the years 2006-15 and into 1.5×1.5 degree bins. Dissipation rates are plotted if at least four estimates exist per bin and depth range of (a) 250-500 m, (b) 500-1000 m, and (c) 1000-2000 m. The total number of individual estimates contributing to the shown averages are about (a) 502000, (b) 426000, and (c) 3071000, accumulating to more than 1.2 million dissipation rate estimates in the global ocean between 250 and 2000 m depth. Note that only the integrated form of the GM model, but not the frequency-dependent version, can be evaluated at the equator, which is why the estimates in this region need to be treated with some skepticism.

Section 3 for details on the model and https://wiki.zmaw.de/ifm/TO/pyOM2 for the documentation and code]. We use a horizontal resolution of 1° with 115 vertical levels and run the full model until it reaches a dynamic equilibrium (about 200 years). The standard tuning parameter settings are $\mu_0 = 1/3$, $\tau_\nu = 2$ days, and $j_* = 5$ for the model version described in Eq. 2.6. We compare TKE dissipation rates, calculated from Eqs. 2.3 and 2.4, and energy levels (Eq. 2.6) with Argo-based estimates.

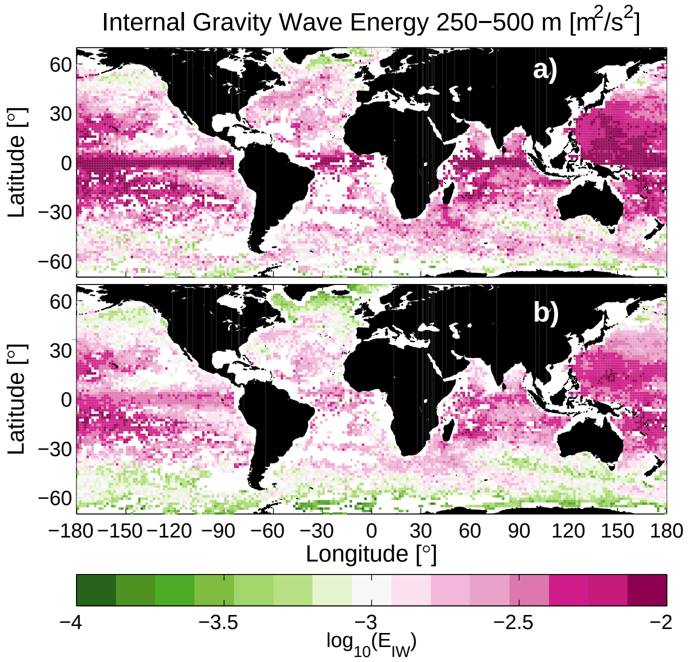

Figure 2.2: Global maps of internal gravity wave energy estimated from Argo data. Results are averaged over the years 2006-15 and into 1.5×1.5 degree bins in the 250-500 m range. Energy levels obtained from (a) potential density and (b) strain spectra are plotted if at least four estimates exist per bin. Note that the estimates close to the equator need to be viewed critically since the GM model energy is zero there in its frequency-dependent formulation.

2.5.2.1 Global Maps

The TKE dissipation rates modeled by IDEMIX are shown in Fig. 2.3 a-c. They vary horizontally by three orders of magnitude, with maximum values in the western boundary currents of all three ocean basins. Elevated dissipation rates can be observed near the equator and in parts of the ACC as well as in the central Atlantic and near the continental margins where the tidal forcing signal becomes apparent. The dissipation rates are modeled to be weakest over wide areas of the central and eastern ocean basins and in parts of the Southern Ocean. They decrease on average by a factor of 3 between the upper and lower depth range. A qualitative comparison to Fig. 2.1 demonstrates that IDEMIX reproduces the mixing patterns obtained from Argo data: overall, the spatial variations and their magnitude agree well. However, the different mixing hotspots are more spatially confined (e.g. the western boundary currents and their extensions) and the large areas of high dissipation rates observed in the subtropical gyres of the western Pacific are but partially mirrored in IDEMIX. Moreover, IDEMIX simulates higher dissipation rates at the continental margins and lower dissipation rates in regions of weak mixing, e.g. south

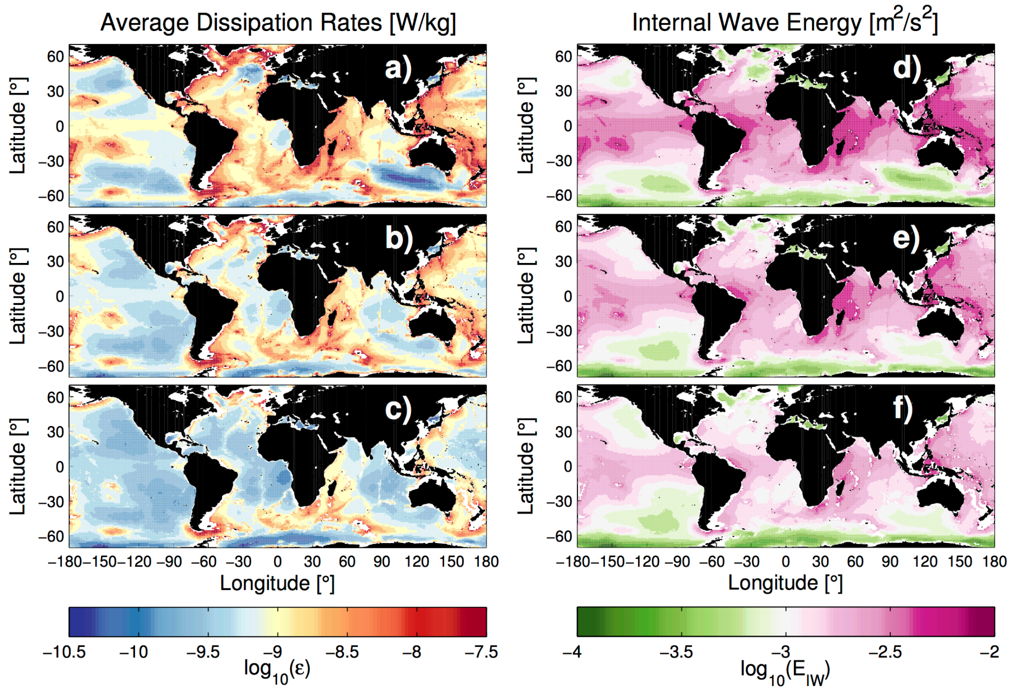

Figure 2.3: Global maps of average TKE dissipation rates (left) and energy levels (right) calculated by IDEMIX for the depth ranges (a),(d) 250-500 m, (b),(e) 500-1000 m, and (c),(f) 1000-2000 m.

of Australia or in the central to eastern North Atlantic, particularly in the upper ocean. In consequence, horizontal correlation coefficients are rather low, varying between 0.1 and 0.2 below and above 1000 m, respectively (cf. Table 2.1). In a regional comparison, values of up to 0.4 are found in the Southern Ocean and the northwest Pacific (120-180° E, 3-39° N), while correlation coefficients remain below 0.1 at all depths in the North Atlantic (3-78° N, 75° W-30° E). In a global comparison, 60-75 % of the data agree within a factor of 3 with the Argo-based estimates (cf. Table 2.2). Comparable (and higher) values are determined for the Southern Ocean and the northwest Pacific, while they remain below 60 % at any depth in the North Atlantic. Differentiating between regions of high and low dissipation rates (taking a threshold value of $\epsilon_{\mathrm{TKE,crit}} = 3 \cdot 10^{-9}$ W kg^{-1}), IDEMIX is seen to perform better in regions of weak dissipation: In a global comparison, about 70 % of the data agree within a factor of 3 above 1000 m (where there is a significant number of estimates available for both scenarios), compared to about 50 % of the data in regions of strong dissipation. On regional scales, the behavior is similar, with the noteworthy exception of the Southern Ocean, where above 500 m about 70 % of the data agree within a factor of 3, both in the weak and the strong dissipation scenarios.

The performance of IDEMIX is even better with respect to internal wave energy levels (cf. Fig. 2.3 d-f; note that we consider E_{ξ_z} rather than E_ρ in order to base this model-

Table 2.1: Coefficients of horizontal correlation between IDEMIX- and Argo-based estimates. The upper depth range is 250-500 m, the middle 500-1000 m and the lower 1000-2,2000000 m. The scenario $F_{eddy} = 0$ corresponds to setting $0.2\epsilon_{eddy} = 0$ in Eq. 2.6. The area between 3° S and 3° N is excluded from this otherwise global comparison because of a singularity of the GM model at the equator.

Scenario	Energy			Dissipation Rate		
	upper	middle	lower	upper	middle	lower
Idemix1 1 deg.	0.72	0.67	0.38	0.14	0.20	0.11
Idemix1 2.8 deg. (I1)	0.69	0.63	0.35	0.20	0.27	0.07
I1: no hor. diffusion	0.53	0.52	0.28	0.22	0.25	0.07
Idemix2 2.8 deg.	0.70	0.64	0.36	0.20	0.29	0.10
I1: 0.5 F_{surf}	0.69	0.63	0.35	0.20	0.27	0.07
I1: 1.5 F_{surf}	0.69	0.63	0.34	0.20	0.28	0.07
I1: 0.5 F_{bot}	0.67	0.63	0.36	0.21	0.30	0.11
I1: $F_{eddy} = 0$	0.70	0.60	0.31	0.19	0.25	0.05
I1: $F_{bot} = F_{surf} = 0$	0.55	0.54	0.34	0.14	0.25	0.21

Table 2.2: Same as Table 2.1 but for percentage of IDEMIX data agreeing with Argo-based estimates within a factor of 2 (in parentheses) and 3.

Scenario	Energy			Dissipation Rate		
	upper	middle	lower	upper	middle	lower
Idemix1 1 deg.	96 (82)	94 (77)	93 (75)	63 (43)	75 (55)	69 (52)
Idemix1 2.8 deg. (I1)	96 (82)	94 (78)	95 (85)	61 (40)	76 (54)	72 (55)
I1: no hor. diffusion	94 (74)	96 (83)	95 (83)	45 (29)	70 (49)	62 (45)
Idemix2 2.8 deg.	96 (82)	94 (76)	95 (85)	62 (42)	75 (53)	72 (53)
I1: 0.5 F_{surf}	96 (81)	94 (78)	95 (85)	60 (40)	76 (54)	72 (55)
I1: 1.5 F_{surf}	96 (82)	94 (77)	95 (85)	61 (40)	76 (54)	72 (54)
I1: 0.5 F_{bot}	97 (81)	97 (86)	95 (88)	52 (34)	78 (55)	72 (55)
I1: $F_{eddy} = 0$	84 (67)	94 (80)	93 (79)	38 (23)	58 (39)	57 (38)
I1: $F_{bot} = F_{surf} = 0$	89 (64)	99 (88)	95 (79)	32 (19)	63 (45)	52 (35)

data comparison on the same spectra as for dissipation rates): the magnitudes as well as the spatial variation characterized by a high equator-to-pole and, at higher latitudes, a weaker west-to-east gradient are well reproduced. In detail, however, there are some shortcomings: similar to the case of TKE dissipation rates, regions of high energy levels—

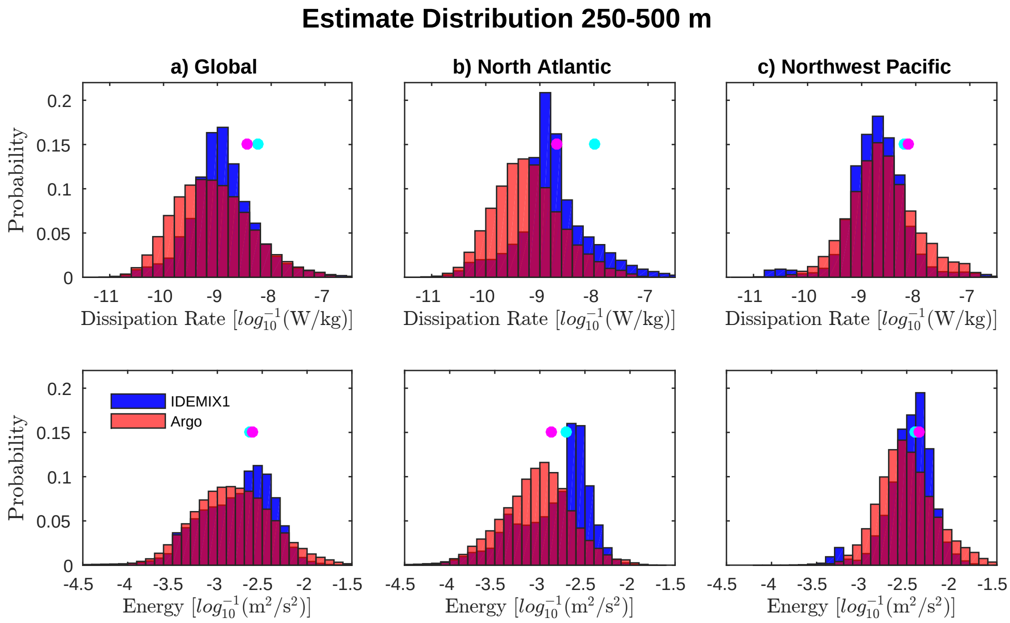

Figure 2.4: Normalized histogram (i.e. the sum of the bar heights amounts to unity) of Argo- and IDEMIX-based estimates of (top) TKE dissipation rates and (bottom) internal wave energy levels. Estimates from the upper depth range of 250-500 m are compared in (a) the global ocean, (b) the North Atlantic (3-78° N, 75° W-30° E), and (c) the northwest Pacific (3-39° N, 120-180° E). The bin width is $2{\cdot}10^{-10}$ W kg^{-1} for dissipation rates and $4{\cdot}10^{-4}$ m^2 s^{-2} for energy. Average values of IDEMIX- and Argo-based estimates are shown as cyan and pink dots, respectively.

particularly the strong signal in the central and eastern subtropical Pacific—are often smaller than in the Argo-based global maps and at the continental margins, energy levels are higher than estimated from the finestructure data. Both the qualitative and the quantitative agreement with Argo data is better than that of dissipation rates: Horizontal correlation coefficients amount to around 0.7 in the upper and middle and 0.3 in the lower depth range, and in all depth ranges, more than 90% of the energy estimates agree within a factor of 3 with the Argo-derived values (cf. Tables 2.1 and 2.2). This also holds true in a regional comparison, where the best quantitative agreement is again observed in the northwestern Pacific Ocean; the best qualitative agreement is achieved in the global comparison as well as in the upper North Atlantic. The performance of IDEMIX is equally good for regions of high and low energy (setting $E_{\xi_z,\mathtt{crit}} = 0.003$ m^2 s^{-2} as the threshold value), with more than 90 % of the Argo- and IDEMIX data agreeing within a factor of 3 in all depth ranges in a global and a regional comparison.

The quantitative differences between Argo- and IDEMIX-derived TKE dissipation rates and energy levels discussed above are supported and elucidated further by a comparison of the respective distributions of the estimates (cf. Fig. 2.4 for the upper depth

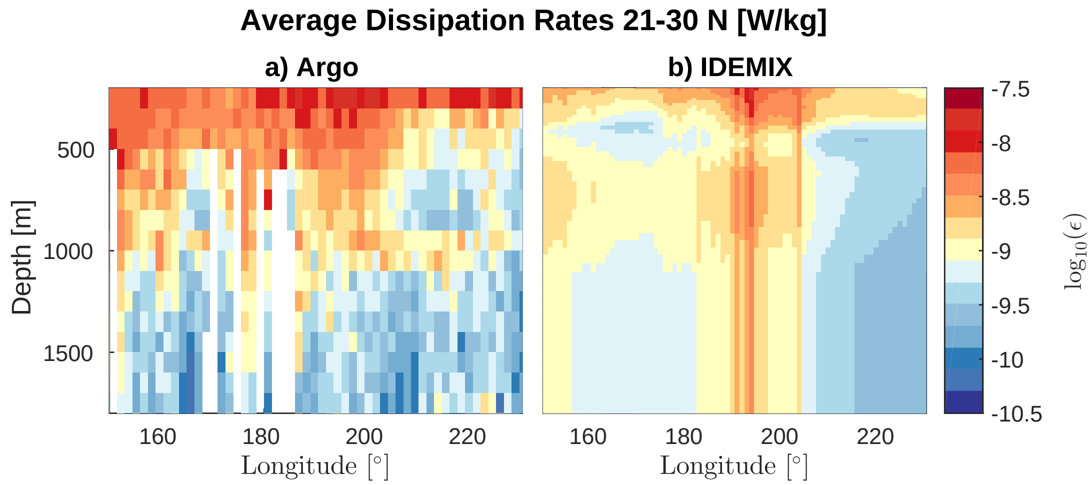

Figure 2.5: Variation of TKE dissipation rates with depth in the northwestern Pacific Ocean as (a) derived from Argo-finestructure data and (b) computed by IDEMIX. Results are averaged over a latitude band of 9 degrees (21-30° N), which lies over the WOCE-transect P03. All available estimates in this latitude range from the years 2006-15, averaged into 100 m vertical bins, are shown. Note that the vertical resolution in IDEMIX changes with depth, but in the depth range shown here, the grid cells are shorter than 100 m in the vertical. The strong signal in the Argo data around 210° longitude near 1000 m depth are caused by profiles taken in the vicinity of the Hawaiian Ridge, where the ocean sometimes is shallower than 1500 m.

range); the two curves overlap most strongly in the northwest Pacific and the overlap is generally larger for energy levels than for dissipation rates. Typically, the distribution of Argo-based estimates is shifted toward lower values compared to that of the IDEMIX-derived estimates and features a less sharp peak, which also holds true in the middle and lower depth range (not shown). The distribution of IDEMIX-values is in some cases characterized by a second, albeit much smaller, maximum, which is not observed in the more smoothly varying Argo-distribution.

Figure 2.5 illustrates how dissipation rates derived from Argo data (Fig. 2.5a) and computed by IDEMIX (Fig. 2.5b), respectively, vary with depth in the subtropical Pacific Ocean, where the number of available Argo-estimates is highest. The spatial variation computed by IDEMIX can be seen to reproduce the high dissipation rates estimated from Argo data at the surface with the maximum at around 180-200° longitude and with elevated mixing rates reaching farther down at around 150-160° and 180-200° longitude. The low dissipation rates east of 200° longitude in the Argo-based estimates, reaching closer to the surface farther eastward, are also simulated by IDEMIX. Additional biases arise in terms of magnitudes and spatial gradients, which are weaker in IDEMIX than in the finestructure data, and in terms of the detailed spatial pattern: for example, the two streaks of high dissipation rates reaching down from near the surface at 150-160° and

180-200° longitude are more pronounced and extend deeper down in IDEMIX than in the Argo-derived map. Moreover, the strong signal in the Argo-derived dissipation rates near 210° longitude around 1000 m depth, which can be linked to the vigorous tidal forcing at the Hawaiian Ridge, is not reproduced by IDEMIX. At other latitudes and in other ocean basins, for example, in the North Atlantic, IDEMIX performs much worse with respect to vertical variations of dissipation rates and energy levels (not shown).

2.5.2.2 Sensitivity Analysis

In this section, we describe the sensitivity of how well IDEMIX reproduces Argo-based estimates of E_{ξ_z} and ϵ_{TKE} to the model's tuning parameters and forcing settings. The analysis was carried out using the same model setup as described in the section above, but in order to save computational time, the resolution was set to 2.8×2.8 degrees in the horizontal with 45 vertical levels. Note that we do not explore the three-dimensional parameter space but keep two parameters at their reference value—as before, $\mu_0 = 1/3$, $j_* = 5$, and $\tau_\nu = 2$ days—while varying the third. Representative values for the global ocean range between $1 \leqslant j_* \leqslant 20$ [Polzin and Lvov, 2011] and $1 \leqslant \tau_\nu \leqslant 10$ days [Olbers, 1974]. The values of $\mu_0 = \mu/\text{arccosh}(N_0/f_0)$, with $\mu \approx 2$, tested here correspond to ratios N_0/f_0 ranging between 1.4 for $\mu_0 = 2$ and 10^3 for $\mu_0 = 1/6$. This is an adequate representation of the Argo-based buoyancy frequency estimates (see Appendix 5.4), which reach values of $N_0/f_0 \approx 10^2$ in the tropics and subtropics above 500 m, while they amount to $N_0/f_0 \approx 10$ in the middepth range (500-1000 m) and remain around unity below.

We investigate both the qualitative and quantitative agreement between Argo- and IDEMIX-based estimates in terms of horizontal correlation coefficients and the percentage of data agreeing within a factor of 3 (cf. Fig. 2.6 for internal wave energy). The quantitative agreement is best for intermediate values of μ_0 and j_*, while it is in all depth ranges insensitive to the investigated variations of τ_ν. For the standard settings $j_* = 5$ and $\mu_0 = 1/3$, the agreement is not only high or maximized, but also almost the same in all depth ranges. Increasing j_* or μ_0 above their standard values affects the agreement most strongly in the upper and least so in the lower depth range. Correlation coefficients, on the other hand, are barely affected by the investigated variations of j_*, μ_0, or τ_ν. A clear distinction with depth is observed, with values of around 0.3 in the lower and around 0.6-0.7 in the upper and middepth range. Intermediate values of j_* and μ_0 as well as low values of τ_ν yield the strongest horizontal correlation. In terms of TKE dissipation rates (not shown), the quantitative agreement is less sensitive, especially with respect to variations of μ_0. Correlation coefficients exhibit a stronger sensitivity than for energy, particularly in the upper depth range. The best agreement is not always achieved for the same parameter settings as for energy and not always for the same settings at all depths.

The sensitivity of the quantitative and qualitative agreement between Argo- and IDEMIX-based dissipation rate and energy level estimates to different (forcing) scenar-

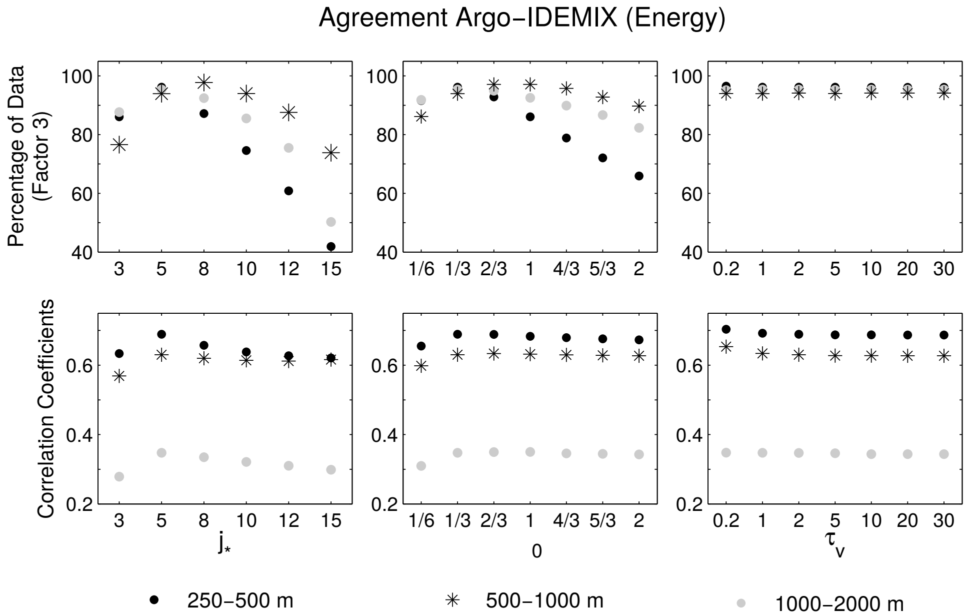

Figure 2.6: Sensitivity analysis of how well IDEMIX reproduces energy levels derived from Argo-based strain spectra with (top) the percentage of data agreeing within a factor of 3 and (bottom) the horizontal correlation coefficients. The tuning parameters are the time scale τ_v on which nonlinear wave-wave interactions symmetrize the internal wave field with respect to the vertical wavenumber m, the modal bandwidth of the GM model j_*, and the factor μ_0 related to the dissipation of internal wave energy as a result of nonlinear wave-wave interactions (cf. Eqs. 2.1 and 2.3). Reference settings are the same as for the global maps presented in the previous figures, i.e. $\tau_v = 2$ days, $\mu_0 = 1/3$, and $j_* = 5$ for the model version described in Eq. 2.6, but for a decreased resolution of the ocean model IDEMIX is coupled to with a grid spacing of $2.8° \times 2.8°$ in the horizontal and 45 vertical levels. Note that the area between 3° S and 3° N is excluded from this otherwise global comparison because of a singularity of the GM model at the equator.

ios is enlisted in Tables 2.1 and 2.2. Taking 10 % or 30 % instead of 20 % as the amount of the near-inertial energy that leaves the mixed layer and acts as F_{surf} on the internal wave field is still well within the range given by Furuichi et al. [2008] or Alford et al. [2012]; the other scenarios, however, are arbitrarily chosen to illustrate the general influence of the respective forcing term. Most of the variations, such as using IDEMIX2 instead of IDEMIX1 or halving the surface or bottom forcing, barely affect the agreement with the Argo-derived estimates (albeit slightly more on regional and seasonal scales, not shown). The strongest impact is observed when removing either the eddy or the boundary forcing completely or, in the case of dissipation rates, removing the lateral diffusion term in Eq. 2.6. In those cases, 10-50 % fewer data points than in the reference scenario

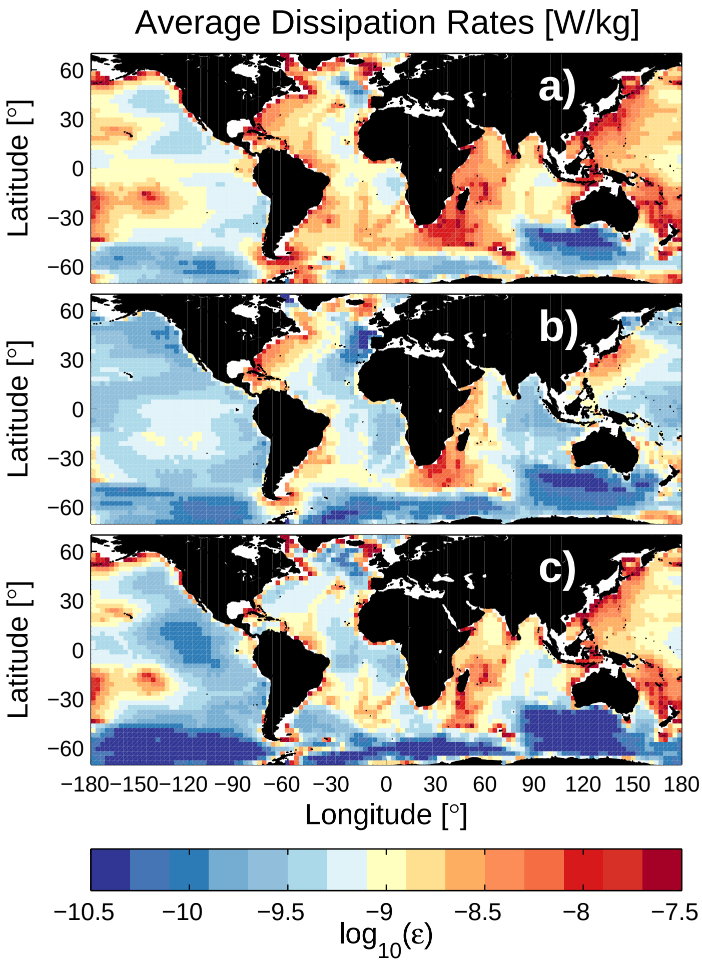

Figure 2.7: Global maps of average TKE dissipation rates computed by IDEMIX in the 250-500 m depth range for different forcing settings: (a) the default setting with bottom, surface and eddy forcing (cf. Eq. 2.6), (b) only eddy forcing, i.e. $F_{surf} = F_{bot} = 0$, and (c) only bottom and surface forcing, i.e. $F_{eddy} = 0.2\epsilon_{eddy} = 0$ in Eq. 2.6.

agree with the Argo-results within a factor of 3—except for energy levels in the upper (middle) depth range, where the qualitative (quantitative) agreement is actually slightly improved. Note that these results depend on the reference parameters used: taking the standard settings of Olbers and Eden [2013], i.e. $j_* = 10$, $\mu_0 = 4/3$, and $\tau_\nu = 1$ day, as the reference, the removal of the eddy forcing term in Eq. 2.6 leads to 4-5 times fewer energy data points agreeing with the finestructure estimates within a factor of 3 than in the reference case (not shown). The horizontal correlation coefficients (cf. Table 2.2) are less sensitive to variations in the forcing settings, especially with respect to energy levels. Again, the absence of the eddy or boundary forcing or of the lateral diffusion term most strongly affects the agreement with the Argo-based estimates.

The effect of the eddy and the boundary forcing is illustrated in Fig. 2.7 for the upper depth range of 250-500 m. Without the eddy forcing (Fig. 2.7 c), the high dissipation rates observed in the western boundary currents are not fully reproduced. This holds especially true for the Atlantic Ocean, where TKE dissipation in the Gulf Stream and its extension is modeled to be quite weak when using bottom and surface forcing only. Also for the mixing hotspots in Drake Passage and the Agulhas Current, the eddy forcing is of central importance (Fig. 2.7 b). A comparison to Fig. 2.7 c also underlines that dissipation rates are too low in the ACC and the eastern Pacific when the transfer of mesoscale eddy energy to the internal wave field is not accounted for. In the middle and lower depth range, the influence of the mesoscale eddy forcing is less pronounced (not shown). The high dissipation rates observed at the continental margins, for example, in the North Pacific or around Antarctica, and in the central and western Pacific are almost exclusively related to the bottom and surface forcing (cf. Fig. 2.7 c).

2.6 Discussion

2.6.1 Uncertainty of the Finestructure Estimates

In order to assess the uncertainties of the evaluation of IDEMIX, the uncertainties inherent in the finestructure method need to be examined. Whalen et al. [2015] compared dissipation rates and diffusivities from microstructure profiles from six different campaigns, representing diverse environments and open-ocean conditions, to Argo-based finestructure estimates. They found a factor 2 agreement for 81 % and a factor 3 agreement for 96 % of the data. In a locally more confined comparison, Sheen et al. [2013] report a systematic overprediction of dissipation rates estimated from CTD and LADCP finestructure data collected in the ACC during the Diapycnal and Isopycnal Mixing Experiment in the Southern Ocean (DIMES) compared to microstructure observations from the same campaign, ranging from a factor of 2 to 4 for transect mean values (cf. their Tables 1 and 2). Factor of 4 differences, however, are mainly found in the bottom kilometer, where Argo floats do not reach; farther up in the water column, the uncertainty estimated by Sheen et al. [2013] agrees with the factor 2-3 identified by Whalen et al. [2015]. The sensitivity of microstructure measurements to sensor calibration, response functions, and, most importantly, the assumption of isotropic turbulence is specified as no more than factor of 2 for values greater than the noise level by Toole et al. [1994] and Moum et al. [1995], but can under some conditions become as large as a factor of 3-5 [Mashayek et al., 2013].

The uncertainty found by Whalen et al. [2012] and Sheen et al. [2013] gives an idea of how well the local internal wave field adheres to the characteristics it is assumed to have in the finestructure method, and if the measures taken to correct for those cases when it does not are sufficient. Such a case was for example observed by MacKinnon and Gregg

[2003] on the New England Shelf, where internal wave characteristics were significantly different from the well-defined, slowly evolving shape typically assumed in spectral models. Polzin et al. [2014] in detail discuss the biases due to the assumptions inherent in the finestructure method—such as spatial homogeneity or a vertical scale separation between a time-mean and a finescale variability in the buoyancy gradients—and practical issues—such as instrument noise and lack of resolution—, concluding that the total bias of the finestructure method should be "substantially less than an order of magnitude over much of the ocean" [Polzin et al., 2014, p. 1414] if it was implemented with care. To elucidate this further, we here analyze the method's sensitivity to the parameter settings involved by investigating how dissipation rate and energy estimates vary in the Atlantic Ocean when our standard settings are modified. These are a combination of the settings by Whalen et al. [2012] and Kunze et al. [2006b]: we set $\xi_z = (N^2 - N^2_{fit})/N^2_{mean}$ where N^2_{fit} is a quadratic fit to N^2, the GM model version as described by Cairns and Williams [1976] with a wavenumber dependence proportional to $(m^2+m_*^2)^{-1}$ (GM76), a segment length of 200 m with a resolution of 10 m, $\langle\xi_z^2\rangle \leqslant 0.1$, $R_\omega = 3$, $\lambda_{min} = 10$ m, and $\lambda_{max} = 100$ m. We change one of these parameters at a time and perform a Welch's t test to determine if dissipation rates and energy levels significantly deviate from those obtained in the reference scenario for a significance level of $\alpha = 0.05$. Note that we do not seek to suggest different settings for the finestructure-strain method than the standards developed and tested during the last decades but to evaluate the significance of our model-data comparison.

Figure 2.8 shows the average dissipation rates and energy levels calculated from Argo data from the year 2011 in the depth ranges 250-500 m, 500-1000 m, and 1000-2000 m in the Atlantic Ocean, when one of the parameters enlisted above is changed while the rest are kept at their reference value. Independent of depth, significant deviations from the reference dissipation rate are obtained when taking an earlier GM model version with a wavenumber dependence proportional to $(m + m_*)^{-2}$ (GM75m, used e.g. by Whalen et al. [2012] and Kunze et al. [2006b]) and when changing the shear-to-strain ratio to $R_\omega = 2$ or $R_\omega = 5$ (in the upper 2000 m, Kunze et al. [2006b] observe values between 2 and 7 and even higher values in the Southern Ocean, cf. their Figs. 13-16). Most of the other parameter variations cause significant deviations from the reference dissipation rate only in the uppermost depth range. The strongest deviation is a factor of 2 difference observed in the 1000-2000 m depth range for the scenario with $\langle\xi_z^2\rangle \leqslant 0.2$ (used e.g. by Whalen et al. [2012]).

Energy estimates obtained from finescale strain spectra are less sensitive to the parameter variations investigated. The only exception is the factor 3-4 decrease in energy in the upper and lower depth range when taking GM75m instead of GM76. In all other cases, the observed differences are well below a factor of 2 and only few of them are significant according to the Welch's t test, excluding the GM75m-scenario in the upper depth range. The only scenario inducing significant changes independent of depth is the one with $\langle\xi_z^2\rangle \leqslant 0.2$. Considering that in the 1000-2000 m depth range only about 1000 in-

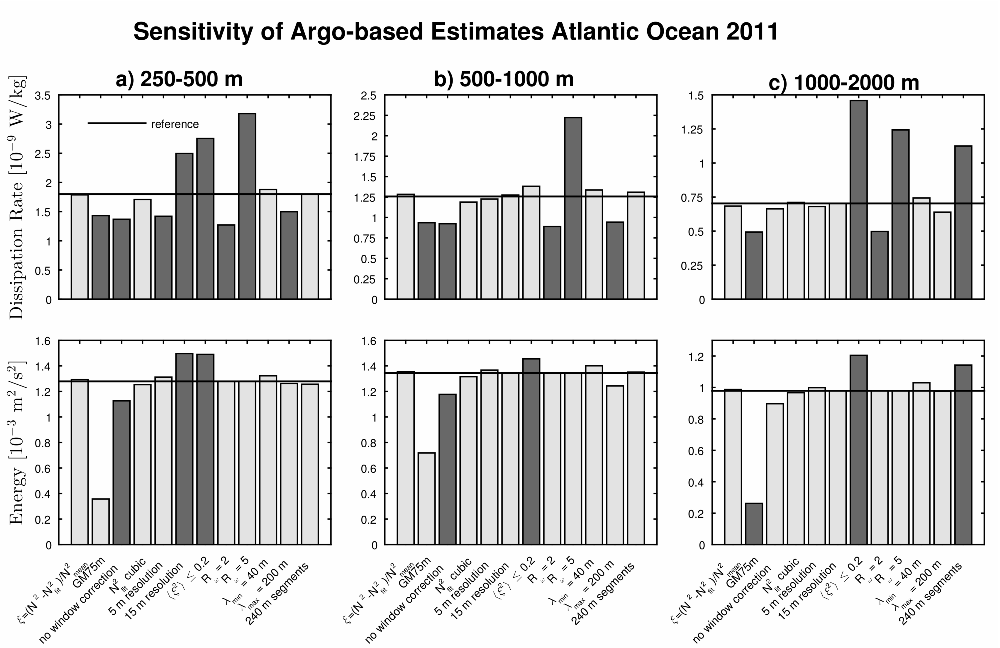

Figure 2.8: Sensitivity test of the finestructure method applied to Argo data from the entire Atlantic Ocean in the year 2011. For the three depth ranges (a) 250-500 m, (b) 500-1000 m, and (c) 1000-2000 m, the average (top) TKE dissipation rate and (bottom) energy level is shown when one parameter at a time is changed with respect to the reference settings (note the different axes). These are represented by the horizontal line and given by $\xi_z = (N^2 - N^2_{fit})/N^2_{mean}$ as in Whalen et al. [2012], where N^2_{fit} is a quadratic fit to N^2 and N_{mean} the segment average, the GM model version as described by Cairns and Williams [1976] with a wavenumber dependence proportional to $(m^2 + m_*^2)^{-1}$, a resolution of 10 m, $\langle \xi_z^2 \rangle \leqslant 0.1$, $R_\omega = 3$, $\lambda_{min} = 10$ m, $\lambda_{max} = 100$ m, a segment length of 200 m, and a window correction according to von Storch and Zwiers [2001]. Note that GM75m denotes a wavenumber dependence proportional to $(m + m_*)^{-2}$ (refer to main text for details on the terminology). Bars are shown in dark gray when the null hypothesis assuming equal mean dissipation rates in the reference case and the scenario in question of a Welch's t test can be discarded for a significance level of $\alpha = 0.05$; lighter bars denote the failure to do so. Depending on the parameter settings and the chosen depth range, about 700-15,000 individual estimates contribute to the shown statistics.

dividual estimates are available for the entire Atlantic Ocean, which renders this depth range least suitable for a comparison to IDEMIX, and that in sum all the uncertainties from the different scenarios nearly compensate, we conclude that for our reference settings the technical details of the finestructure method cause at most a factor 2 uncertainty in the dissipation rate and energy estimates.

This uncertainty due to parameter choices and different modeling approaches becomes apparent in a comparison of our dissipation rate estimates (Fig. 2.1) to the global maps published by Whalen et al. [2012, 2015]. We observe the same order of magnitude variations and the same spatial pattern, but our dissipation rates (and diffusivities, not shown) are higher almost everywhere. These differences are smaller than the combined uncertainties described in this section and generally lie within the 90 % bootstrapped confidence intervals given by Whalen et al. [2012, cf. their Fig. S4] for their averages of the years 2006-11. Inferring from their Fig. S3 that we keep significantly more data points even for the same parameter settings and input data (not shown), we link these differences not only to the disparate parameter choices (e.g. resolution or GM model version) but also to potential differences in data quality requirements and details of the data processing (e.g. despiking) or averaging routines used.

We assess the statistical uncertainty by computing 90% bootstrap confidence intervals derived for 1000 samples for all bins with at least 10 individual dissipation rate or energy estimates (see Appendix 5.4). For both variables, the variation decreases with depth, ranging between 60% and 80% of the mean for dissipation rates, 20% and 30% for energy levels obtained from strain and 20% and 40% for those obtained from potential density spectra. For the evaluation of IDEMIX, we focus on strain-derived energy levels in order to use the same spectra as for the comparison of dissipation rates. These energy levels are on average 1.5-2 times lower than those derived from potential density spectra (cf. Fig. 2.2 for the 250-500 m depth range). This difference gives a rough idea of the uncertainty of our approach to compute energy levels from finescale strain information, which involves much less testing and refinement than what the finestructure method for turbulent dissipation rates has undergone in the last decades. The decrease of the energy levels with depth mirrors the proportionality of wave energy $E(z)$ to a decreasing buoyancy frequency $N(z)$, as found for internal waves with the WKB-approximation[7]. Dissipation perturbs this linear wave behavior, but the Argo-derived energy levels still pick up this dependence [the same holds true for wave energy in IDEMIX, where the decrease with depth was shown to be independent of the location (top or bottom) of the forcing, see Olbers and Eden, 2013]. The resemblance of the horizontal variations of our finestructure energy estimates to global patterns of wind power input into near-inertial motions and corresponding horizontal energy fluxes [Alford, 2003; Furuichi et al., 2008; Alford et al., 2016] and of energy fluxes from geostrophic motions to internal lee waves [Nikurashin and Ferrari, 2011] as well as the general agreement in terms of magnitude with the observations based on CTD and LADCP data in the Southern Ocean by Waterman et al. [2013] render us confident that our finestructure energy estimates are sufficiently reliable for the purpose of this study. The combined uncertainty resulting from procedural

[7]For linear waves satisfying the WKB-conditions the vertical energy flux (group velocity times energy) remains constant, leading for $N^2 \gg \omega^2$ to $E(z) \sim N(z)$.

(strain- or density-based) and statistical issues thus amounts to a factor of 1.7 in the middle and up to a factor of 2.5 in the upper and lower depth range.

We estimate the overall uncertainty of our finestructure estimates as the sum of the different uncertainties described in this section, arguing that the factor 2-3 uncertainty identified by Whalen et al. [2015] in a comparison with microstructure estimates should to a large extent represent the uncertainty related to the method's sensitivity to parameter settings discussed above (these could have been adjusted to improve the agreement with the microstructure estimates). For dissipation rate estimates, we therefore consider 1) the uncertainty of microstructure measurements, 2) the difference between fine- and microstructure estimates, and 3) the statistical uncertainty. In the case of energy level estimates, we consider 1) the parameter sensitivity, 2) the difference between the two methods proposed (E_ρ vs E_{ξ_z}), and 3) the statistical uncertainty. Because we aim to evaluate IDEMIX on a global scale, we use average instead of maximum values whenever the uncertainty estimates were seen to vary in space—caused by changing characteristics of the internal wave field and hence the differing applicability of the assumptions made and parameters used. This leads to a total uncertainty of about a factor of 5 for both dissipation rates and energy levels (compared to eight for the worst-case scenario). As we observe spatial variations of up to three orders of magnitude in TKE dissipation rates and up to two orders of magnitude in energy levels, even in this worst case-scenario a general comparison of IDEMIX- and Argo-based estimates is still feasible.

2.6.2 Uncertainty of IDEMIX

The assumptions made during the derivation of IDEMIX do not necessarily hold everywhere in reality. Without detailed knowledge of the energy spectra in the ocean, these uncertainties cannot be quantified, but they should nevertheless be noted. One important aspect is that IDEMIX—just like the finestructure method—relies on oceanic conditions being close to those assumed in the GM model (for example, in the computation of the representative group velocity c_0). Another source of uncertainty is the parameterization for the dissipation of internal wave energy ϵ_{IW} based on the scalings by Olbers [1976], Henyey et al. [1986], and McComas and Müller [1981], which might neglect processes that are important for the internal wave energy cascade in the real ocean. Moreover, the assumption that the nonlinear wave-wave interactions render the wave field symmetric with respect to m, made in the derivation of IDEMIX, might not be justified under all conditions. The same holds true for the assumption of vertical symmetry, allowing for the approximation $c^+ \approx c^- \approx c_0$ (cf. Section 2.3), or, in IDEMIX2, that properties of the first baroclinic mode are representative of the entire wave field, but these are minor issues in comparison. In addition, the Osborn-Cox-relation used to link internal wave energy dissipation to TKE dissipation is a reasonable approximation in the stratified interior of the ocean, but less so near the boundaries.

The type and characteristics of the forcing functions included in IDEMIX could also lead to significant errors. The models and parameterizations used to compute the surface and bottom forcing [Jayne, 2009; Jochum et al., 2013] suffer themselves from biases and might be too simplified under certain conditions. For example, the surface energy input in IDEMIX is set to zero near the equator because the approach of Jochum et al. [2013] to estimate the inertial velocity components is only valid outside the deep tropics [cf. Fig. 2 in Olbers and Eden, 2013]. The global maps of F_{surf} and F_{bot} are obtained from model simulations with the associated numerical biases and uncertainties introduced by the various parameterizations involved, and additional biases arise when extrapolating these results to the numerical grids used in the ocean model IDEMIX is coupled to. The settings chosen in the simulations presented here are also biased: The energy content of the M_2 tidal constituent, set to 50% of the total tidal forcing in IDEMIX2, is probably an overestimate [Falahat et al., 2014b]. Moreover, the fraction of the wind power input into near-inertial motions that leaves the mixed layer is not a global constant (here, 20% are used) but varies in both space and time (Furuichi et al. [2008]; Alford et al. [2012];Voelker et al. 2016, unpublished manuscript). The missing implementation of physical processes other than near-inertial wind forcing (F_{surf}), internal tide generation (F_{bot}), and the formation of lee waves by mesoscale eddies (F_{eddy}) also contributes to the model's biases. We will address these issues in detail in the Conclusions.

2.6.3 Evaluation of IDEMIX

Comparing the global maps of TKE dissipation rates and internal wave energy levels shows that IDEMIX reproduces both the spatial pattern and the magnitude of the Argo-derived finestructure estimates. This comparison is most reliable in the upper depth range, where biases due to missing Argo data are smallest, as well as away from the continental margins or the equator. At these locations, the limited applicability of the finestructure method and of assumptions made in the derivation of IDEMIX, or the discrepancy between the frequency-dependent and the integrated GM model increase the uncertainty of the Argo- and IDEMIX-based estimates.

The model-data agreement is better for energy levels than for dissipation rates, both in a qualitative and in a quantitative sense. The sensitivity of the quantitative and qualitative agreement to the model's tuning parameters also differs. This is somewhat surprising, considering that in IDEMIX dissipation rates are computed from energy levels and both variables are related via the same formula that forms the basis of the finestructure method (cf. Eq. 2.3). We surmise that two aspects contribute to this issue: First, dissipation rates are described by the amount of energy leaving the internal wave spectrum and are thus—in an energetically consistent framework—dependent on the amount of energy entering the internal wave field, that is, the external forcing functions. Energy levels, on the other hand, are directly influenced by the local characteristics of the internal wave field and hence the model's tuning parameters. Second, the much higher amount of testing and refinement inherent in the finestructure method for TKE dissipation rates compared to our method for the calculation of internal wave energy could also explain to some degree why IDEMIX performs differently with respect to energy.

Particularly the quantitative agreement between Argo- and IDEMIX-based estimates of energy levels and TKE dissipation rates is most sensitive to changes in the tuning parameter j_*. None of the scenarios presented in Fig. 2.6, however, causes significant deviations from the reference settings if a factor of 5 uncertainty for the finestructure estimates is assumed—less than 10 % of the data would have to agree within a factor of 3 for a significant deviation from the reference with $j_* = 5$, which we speculate could occur for $j_* \geqslant 20$, but not for any realistic setting of τ_ν or μ_0 (nor for any any realistic setting with respect to TKE dissipation rates due to their reduced sensitivity to tuning parameter variations). The improvement of the current reference settings ($j_* = 5$, $\tau_\nu = 2$ days, and $\mu_0 = 1/3$) over the ones used in Olbers and Eden [2013] is at most a factor of 4 (for energy levels in the upper depth range) and hence not significant either. The same holds true for the changes induced by varying the forcing functions when their effect on the global averages is considered (cf. Tables 2.1 and 2.2); locally, however, these changes can be significant. Considering a box encompassing the Agulhas Current (30°-60° S, 10°-40° E), TKE dissipation rates are found to be decreased by a factor of 6-7 (depending on the depth range considered) compared to the reference scenario when the eddy forcing is removed. The absence of bottom and surface forcing barely affects the modeled TKE dissipation rates in this region, identifying the eddy forcing as the main contributor to the high observed dissipation rates. Energy levels are only decreased by a factor of 2 in the area around the Agulhas Current for $F_{eddy} = 0$, which supports our interpretation that TKE dissipation rates are mainly affected by the forcing functions, while energy levels are mainly influenced the local shape of the internal gravity wave field and thus the model's tuning parameters. In Drake Passage (50°-70° S, 50°-70° W), on the other hand, both the eddy and the surface and bottom forcing are significant above 1000 m depth, with a reduction of TKE dissipation rates by a factor of 10-13 for $F_{eddy} = 0$ and a factor of 7-8 for $F_{bot} = F_{surf} = 0$ compared to the reference scenario.

Note that the sensitivity analysis was carried out using a coarser resolution to save computation time. This does not affect the quantitative agreement with the Argo-based estimates, but the qualitative agreement is modified, especially with respect to dissipation rates (cf. Table 2.2). This could be related to the higher amount of small-scale structures resolved in the forcing functions of the 1°-simulation; nevertheless, we expect a sensitivity analysis to yield comparable results to that using a 2.8°-resolution since the impact of the tuning parameters or the forcing functions on the internal wave field is not resolved in any of the two and always parameterized in the same way.

For most modeling purposes, the parameter of interest is typically the diapycnal or vertical diffusivity rather than the turbulent dissipation rate. In general, IDEMIX can reproduce diffusivities equally well as dissipation rates with two major exceptions: in the Atlantic Ocean at high northern latitudes ($\geqslant 60°$) and in the Southern Ocean, diffusivities are much larger than suggested by finestructure estimates (not shown). This can be linked to a much too low buoyancy frequency in the model at these locations and is thus not a shortcoming of IDEMIX but of the ocean model it is coupled to. Note that when the diapycnal diffusivity is concerned, an additional bias arises due to the mixing efficiency δ, which is treated as constant both in IDEMIX and in the finestructure method, but has been found to be variable [cf. e.g. Gargett and Moum, 1995; Mashayek et al., 2013]. Another point worth noting is the well-known issue of resolving characteristic ocean features in numerical models. The weak agreement between IDEMIX- and Argo-based estimates in the North Atlantic could not only be related to the wave field's local divergence from the global reference assumed in IDEMIX, but potentially also to an inadequate representation of the Gulf Stream path in the ocean model IDEMIX is coupled to [cf. e.g. Chassignet and Marshall, 2008].

2.7 Summary and conclusions

We here present a first evaluation of the mixing parameterization IDEMIX, which describes the propagation and dissipation of internal gravity wave energy in the ocean and computes the induced diapycnal diffusivities in an energetically consistent framework. The evaluation is based on a comparison with TKE dissipation rate and energy level estimates obtained from Argo-CTD profiles; to our knowledge, ours is the first attempt to calculate energy levels from finescale strain information alone. The Argo-program maintains a nearly global array of a few thousand freely drifting floats profiling the ocean's upper 2000 m several times a month, producing a data base that is well suited for the evaluation of IDEMIX in its typical application, that is, coupled to a global ocean model. The drawback of this approach is the high uncertainty associated with these finestructure estimates, which we estimate as a factor of 5. In our evaluation, we therefore only consider the large-scale variations of the TKE dissipation rate and internal wave energy fields, which cover two to three orders of magnitude.

These large-scale signals can be seen to be well reproduced by IDEMIX: regions of particularly high or low dissipation rates or energy levels are identified as such and the corresponding magnitude is usually well simulated. Discrepancies with the Argo-based estimates are mainly related to the spatial extent of these hotspots. The agreement with Argo-derived estimates differs regionally, particularly with respect to the simulation of vertical variations or the detailed data distribution.

In light of the high uncertainty of the finestructure method, tuning IDEMIX to the Argo-derived estimates in order to overcome these discrepancies is not an option. Instead, we draw the following conclusions from the results presented in Section 2.5:

1. The internal wave field is spatially inhomogeneous and hence not represented equally well everywhere by a global set of parameters. This could be improved by

defining regionally variable parameters such as the modal bandwidth j_* [Polzin and Lvov, 2011], but that kind of detail is so far precluded by the lack of a unifying theory.

2. The difference between the model versions IDEMIX1 and IDEMIX2 in terms of reproducing the Argo-based dissipation rates or energy levels is very small. The additional computational power required by adding low-mode compartments to IDEMIX1 is therefore not necessary if only a general reproduction of the Argo-derived estimates is desired. Locally and also seasonally, the differences between IDEMIX1 and IDEMIX2 are more pronounced, especially in the upper ocean. None of these improvements is significant within the uncertainty of the method, but they illustrate that a realistic simulation of the detailed structure of internal wave energy and its dissipation requires the simulation of more processes than are currently considered in IDEMIX1 (and presumably IDEMIX2). In this context, the role of parametric subharmonic instability (PSI), which is modeled in IDEMIX2 [cf. Appendix A of Eden and Olbers, 2014] but not in IDEMIX1, can also be evaluated. This triad interaction transfers energy from a low wavenumber component to two high-wavenumber components of half the frequency and has been suggested to substantially shape the internal wave energy budget and potentially also turbulent mixing in several numerical studies [cf. Hibiya et al., 2002; Furuichi et al., 2005; MacKinnon and Winters, 2005]. Observational studies, however, reach diverging conclusions, with some supporting the importance of PSI [e.g. Nagasawa et al., 2002], while others stress the minor effect of PSI on internal wave energy levels [MacKinnon, 2013; Zhao and Alford, 2009]. Additional uncertainties arise because of potentially misleading results produced by bispectrum and bicoherence estimators, typically applied to infer the presence of PSI, [Chou et al., 2014] as well as resolution or dimensionality limitations of the above named numerical studies. The comparison of IDEMIX1 and IDEMIX2 indicates that with respect to the reproduction of Argo-derived dissipation rate or energy level estimates, the role of PSI could be important locally, but is negligible on the large scales analyzed here.

3. The different forcing functions included in IDEMIX are of varying importance in different parts of the global ocean: In most areas, mixing hot spots are induced by a combination of strong eddy and boundary (wind and tidal) forcing. In the central subtropical Pacific or the northern Indian Ocean, however, it is the boundary forcing alone that causes elevated dissipation rates and energy levels, while for example in the Gulf Stream or the Agulhas Current the high values are brought about mainly by the mesoscale eddy forcing. In the vicinity of these currents, the absence of the eddy forcing term in IDEMIX causes significant deviations of TKE dissipation rates from the reference scenario, underlining that in these areas, the finestructure estimates cannot be reproduced without taking the energy transfer

from mesoscale eddies to the internal gravity wave field into account. The different effect of removing this eddy forcing term in the three depth ranges considered suggests that the interaction between internal gravity waves and the mesoscale as well as its role for mixing differs depending on where in the water column it takes place. This is supported by the findings of Eden et al. [2014], who observed differences in Southern Ocean diffusivities depending on whether mesoscale eddy energy was transferred to internal gravity waves mainly in the mixed layer, at the bottom, or in the ocean's interior. It is hence crucial to better understand where and how mesoscale eddies dissipate and which processes shape their interaction with the internal gravity wave field in order to realistically implement this forcing term in IDEMIX and to help reduce the bias between the model and Argo-based estimates.

4. The relative probability distributions for Argo- and IDEMIX-based estimates of dissipation rates and energy levels overlap to different degrees in different parts of the ocean. Moreover, the distribution for Argo-derived estimates varies more smoothly and peaks at lower values than the one describing IDEMIX-based estimates. The forcing mechanisms incorporated in IDEMIX might hence be to different degrees representative of the real forcing processes in different parts of the ocean, both with respect to their magnitude as well as their regional structure. For example, IDEMIX seems to capture much of the forcing processes at work in the real ocean in the northwest Pacific, but to fall short in the North Atlantic. The results presented in Tables 2.1 and 2.2 underline that decreasing the magnitude of the forcing—an apparent possibility to reduce the shift between the maxima of the distributions for Argo- and IDEMIX-based estimates— barely affects the model-data agreement. Rather, as the generally smoother distribution of the finestructure estimates suggests an interplay of several forcing mechanisms, more detail in the simulated forcing appears to be required. This is also suggested by the incomplete simulation of vertical variations in the Argo-derived TKE dissipation rates, especially near locations characterized by strong tidal forcing (Fig. 2.5).

Together with the observation that regions of strong dissipation are often significantly too small in IDEMIX, these conclusions point toward the need to improve the forcing functions and modeled physical processes in IDEMIX. This holds especially true for the generation of lee waves by the flow of geostrophic eddies over rough topography, which has been shown to be an important energy source for internal gravity waves, particularly in the Southern Ocean [Nikurashin and Ferrari, 2011]. In the current model version, this process is only crudely represented by injecting 20% of the dissipated eddy energy into the internal wave field at the ocean bottom. One possibility to add physical detail to IDEMIX is to compute, following Nikurashin and Ferrari [2011], the energy conversion from geostrophic motions to lee waves based on linear theory [Bell, 1975a], which requires knowledge of the bottom velocity, bottom stratification and topographic spectra.

Additionally, mesoscale eddies have been shown to shape the internal wave field not only at the ocean bottom, but also near the surface, where their presence can affect the near-inertial wave field and hence potentially also turbulent mixing [Kunze, 1985; Young and Jelloul, 1997; Kawaguchi et al., 2016]. Especially for this type of eddy-wave interaction, however, more research is required to adequately represent it in global-scale models.

This should not imply that the wind and the tidal forcings are well constrained. On the contrary, crucial aspects such as the exact amount of near-inertial energy entering the ocean interior or the directional dependence of the barotropic energy flux are currently not well understood and hence lead to additional biases in IDEMIX. The combined effort of observational, numerical, and analytical investigations will be necessary to shed light on the details of these processes and to reduce the associated uncertainties in IDEMIX.

Other processes that are still missing in IDEMIX include the interaction between surface and internal gravity waves [Olbers and Herterich, 1979; Olbers and Eden, 2016], additional tidal constituents (currently, IDEMIX2 describes only the M_2 tide), or the interaction of gravity waves with the balanced flow [Polzin, 2010]. Lastly, note that IDEMIX (similarly to the finestructure method) only computes internal wave-induced turbulence. Processes such as double-diffusive convection are also known to lead to turbulent motions in the ocean and will also need to be considered in an all-embracing turbulence model.

Although it is reasonable to assume that a more realistic description of the forcing functions in IDEMIX will improve the spatial pattern of the modeled TKE dissipation rates and hence the agreement with the Argo-based estimates, it is by no means certain that these improvements will be significant within the high uncertainty of the finestructure method. Moreover, the fact that Argo floats currently do not reach farther down than 2000 m prevents a comprehensive assessment of how well IDEMIX describes the topographically induced energy conversion, independent of the amount of detail that goes into that description. The latter issue could be solved at least to some extent in the next years with the implementation of Deep Argo, consisting of floats that profile down to 6,000 m [Riser et al., 2016]. This would also add much information to our maps of the strain-derived internal wave energy content, which currently only reflect the total tidal forcing in the few locations where the ocean is shallower than 2000 m and hence mainly account for the wind energy input. Locally, the solution to both problems is to evaluate IDEMIX against measurements that actually resolve turbulence. Especially in regions where a strong discrepancy between Argo- and IDEMIX-based estimates is observed, such as the subtropical Pacific Ocean or in the vicinity of island chains, an important next step in the assessment of IDEMIX is the local comparison with microstructure measurements. These have lower uncertainties than finestructure estimates and thus allow identification of the detailed shortcomings of IDEMIX and to finetune the model. In addition, it would also be insightful to compare other IDEMIX variables to observations, such as diapycnal diffusivities to those obtained from tracer release experiments [e.g. Ledwell et al., 1993] or internal wave energy fluxes to those derived from high-resolution glider measurements [e.g. Johnston et al., 2013].

Considering that IDEMIX was shown i.a. to improve the modeled oceanic northward heat transport—which in turn affects many climate variables—compared to other, energetically inconsistent parameterizations [Eden et al., 2014], the improvements of IDEMIX discussed in this section are of more than just theoretical interest.

Acknowledgements

We thank Caitlin Whalen and Eric Kunze for insightful discussions and helpful comments on the finestructure method as well as the three reviewers, whose constructive criticism helped to improve the manuscript. F.P. was supported through the Cluster of Excellence cliSAP (EXC177), funded by the German Research Foundation (DFG). This work is a contribution to the Collaborative Research Centre TRR 181 on Energy Transfer in Atmosphere and Ocean funded by the DFG.

3 Resolving the horizontal direction of internal tide generation

This chapter is a reprint of the manuscript entitled "Resolving the horizontal direction of internal tide generation", which is in preparation for submission. Section 3.7 is not part of this manuscript and Sections 3.1 and 3.8 were adjusted accordingly. Additional information is presented in Appendix 5.1 of this thesis to which references were added in this chapter where applicable.

Citation: Pollmann, F., Nycander, J., Eden, C. and Olbers, D., 2017: Resolving the horizontal direction of internal tide generation. In preparation for submission.

3.1 Abstract

The mixing induced by breaking internal gravity waves is an important contributor to the ocean's energy budget, shaping i.a. nutrient supply, water mass transformation, and the large-scale overturning circulation. Much of the energy input into the internal wave field is supplied by the conversion of barotropic tides at rough bottom topography, which hence needs to be described realistically in internal gravity wave models and mixing parameterizations based thereon. A new semi-analytical method to describe this internal wave forcing, calculating not only the total conversion but for the first time also the direction of this energy flux, is presented. It is based on linear theory for variable stratification and finite depth, that is, it computes the energy flux into the different vertical modes for subcritical topography and small tidal excursion. In contrast to earlier semi-analytic approaches, the new one gives a positive definite conversion field. Sensitivity studies using both idealized and realistic topography allow the identification of suitable numerical parameter settings and, in the former case, corroborate the accuracy of the method. This motivates the application to the global ocean in order to better account for the geographic distribution of diapycnal mixing induced by low mode internal gravity waves, which can propagate over large distances before breaking. First results highlight the significant differences of energy flux magnitudes with direction and demonstrate a robust sensitivity of internal gravity wave energy levels and turbulent kinetic energy dissipation rates to resolving the direction of the tidal forcing in a simplified setup of the internal gravity wave model IDEMIX. This confirms the relevance of this more detailed approach for energetically consistent mixing parameterizations in ocean models and motivates its application in the global ocean.

3.2 Introduction

Besides wind-driven upwelling in the Southern Ocean, interior mixing has been identified as a major contributor to maintaining the global ocean circulation [e.g. Munk and Wunsch, 1998; Talley, 2013, and references therein]. Much of this mixing energy is contained in the internal wave field, and up to half of the internal wave energy is estimated to stem from tidal flow over abyssal topography [Egbert and Ray, 2001; Wunsch and Ferrari, 2004]. This tidal forcing is anisotropic, because the energy conversion from the tides to the internal waves depends on the shape of the topography and the orientation of the tidal ellipse. Existing (semi-)analytical models of internal tide generation [e.g. Bell, 1975b; Nycander, 2005, see following paragraphs], however, do not take that directional dependence into account. To close this gap and to help improve mixing parameterizations based on internal wave dynamics, we here present a new semi-analytical method to calculate both the horizontal direction and the magnitude of the barotropic to baroclinic tidal energy flux.

The spatial structure of the tidal energy conversion is best resolved in full three-dimensional simulations as performed e.g. by Niwa and Hibiya [2004] or Zilberman et al. [2009]. The high computational expense, however, renders this approach impractical for global calculations with high-resolution topography; additional complications arise because these models rely on assumptions as to how and where baroclinic tidal energy dissipates [Falahat et al., 2014b]. This motivates the semianalytical treatment of the internal tide generation problem. One of the first to follow this approach was Bell [1975a,b], who computed the energy conversion for an infinitely deep ocean with constant stratification. The underlying assumptions which render the problem analytically tractable are that the topographic heights are small compared to the vertical wavelength of the waves and that the topographic slopes are much less than the slope of the tidal beam (see Appendix 5.1 for details). Llewellyn Smith and Young [2002, hereafter LSY02] removed the restriction of infinite depth and constant stratification by decomposing the wave field into vertical normal modes. They found that the main effect of finite depth is that conversion rates are significant only for horizontal topographic scales smaller than the horizontal wavelength of the first mode internal tide. Using the WKB-approximation, they moreover showed that the properties of the stratification relevant for the energy conversion are the buoyancy frequency's vertical average and its value at the bottom, N_B.

Calculations of the energy conversion rate in the global ocean building on these results were performed for example by Egbert et al. [2004], Nycander [2005] and Falahat et al. [2014b]. The former authors implemented a computationally less expensive, approximate version of the convolution integral derived by LSY02 in a hydrostatic shallow-water model, showing that the modeled tidal elevations could reproduce those estimated from altimetry data with an RMS-error of 5 cm. The formalism of Nycander [2005] is not directly based on the expression of LSY02 either, but introduces a filter to that of Bell [1975a,b], thereby suppressing internal tide radiation from long topographic scales in line with the findings by LSY02. The total conversion rates were in good agreement with the numbers found by Egbert and Ray [2001] from satellite altimetry data; the more detailed evaluation performed by Green and Nycander [2013], testing different wave drag parameterizations in a barotropic tidal model, confirmed the positive assessment of the method. Further support of the semi-analytical approach was given by the reasonable correlation between microstructure measurements of turbulent kinetic energy dissipation rates and energy conversion rates calculated using a variation of Nycander's formalism [Falahat et al., 2014a]. Falahat et al. [2014b] on the other hand based their global calculations on the approach by LSY02 and solved the vertical eigenvalue problem for the first internal tide modes. They contrasted their results with that of Nycander [2005] and found that the two methods diverged most strongly in the upper ocean, with the global integrals of the energy conversion rate differing by 16%. In idealized test cases, taking the full vertical structure of the stratification into account led to more accurate results than the WKB-based method of Nycander [2005].

Our objective is to specify the horizontal characteristics of the internal tide field by describing the directional dependence of the tidal energy conversion. Following the vertical mode treatment of LSY02, this is possible when the energy conversion is calculated as the integral over the energy flux instead of, as done by Nycander [2005] and Falahat et al. [2014b], the integral over all energy sources. Apart from providing information on the direction, another important advantage of the new method is that the integrated energy flux is a positive definite function, whereas the integral of the energy sources can produce negative conversion rates [e.g. Falahat et al., 2014b]. The application of this new method to the global ocean requires care, because it is based on the assumptions of a bounded source region and a horizontally constant tidal velocity. We hence propose to subdivide the seafloor into overlapping circular patches. By multiplying the topography within each patch by a Gaussian, the effect of the remote topography on the conversion rates is neglected and the far-field expression, a function of the Fourier transformed topography within the patch, is locally valid. Considering each patch in turn, finally the energy conversion for the entire ocean floor can be calculated.

Section 3.3 describes the derivation of the relevant equations. In Section 3.4, we discuss the numerical implementation of the method for global calculations. Section 3.5 deals with the evaluation of the method based on idealized test cases, which allows the identification of suitable parameter settings such as the overlap of neighboring patches. The energy conversion for a region of realistic topography is shown in Section 3.6 and the effect of applying this forcing in the internal gravity wave model IDEMIX compared to the standard, directionally invariant scenario, in Section 3.7. A summary and conclusions are presented in Section 3.8. The focus of this paper is on the presentation of the new method and its evaluation; global calculations of the angular energy flux into vertical modes using realistic topography, tidal velocities and stratification will be presented in a follow-up publication.

3.3 Derivation of the energy flux

LSY02 derive the expression of the energy conversion into vertical normal modes for an ocean of nonuniform finite depth with the ocean bottom at depth $z_B = -H + h(x, y)$, where H is a constant. Following Bell [1975a,b], they make the following approximations: First, the topography is assumed to be weak, so that the bottom boundary condition can be applied at the flat bottom $z = -H$, which requires that topographic slopes ∇h are much less than the slope of the tidal beam ("subcritical topography") and that the height of the topography is smaller than the vertical wavelength of the internal waves. Second, the tidal excursion is assumed to be small compared to the horizontal scale of the topography L, i.e. $U_0/(\omega L) \ll 1$, so that advective effects of the barotropic tide can be neglected. Here, U_0 is the amplitude of the tidal velocity and ω the fundamental tidal frequency. Third, they use the hydrostatic approximation, which is justified as long as $\omega/N \ll 1$, where N is the buoyancy frequency.

In order to describe the generation of internal tides of vertical mode m, we must solve the inhomogeneous Helmholtz equation for the modal pressure amplitude P_m:

$$\nabla^2 P_m + \kappa_m^2 P_m = \sigma. \tag{3.1}$$

This equation is derived from the linearized hydrostatic Boussinesq equations, representing the internal wave disturbance induced by tidal flow over rough bottom topography, by projection onto vertical normal modes (see LSY02). The magnitude of the energy conversion depends on the source function σ and hence on the specific aspects of the vertical eigenvalue problem; following LSY02 (their Eq. 33), it is given by

$$\sigma = i\kappa_m \zeta_m f \sqrt{1 - \frac{f^2}{\omega^2}} \mathbf{U} \cdot \nabla h = i\sigma_0. \tag{3.2}$$

Note that σ_0 is real. The pressure and tidal velocity fields are assumed to have a sinusoidal time dependence and complex amplitude P_m and $\mathbf{U}$, respectively:

$$p_m(t, \mathbf{r}) = \Re\{P_m(\mathbf{r})e^{-i\omega t}\}, \tag{3.3}$$

$$\mathbf{u}(t) = \Re\{\mathbf{U}e^{-i\omega t}\}, \tag{3.4}$$

with coordinate vector $\mathbf{r} = (x, y)$, its modulus $r = |\mathbf{r}|$, and the corresponding unit vector in radial direction $\hat{\mathbf{r}} = \hat{\mathbf{x}}\cos\phi + \hat{\mathbf{y}}\sin\phi$, involving the eastward and northward unit vectors $\hat{\mathbf{x}}$ and $\hat{\mathbf{y}}$, respectively. $\Re$ denotes the real part. The remaining variables originate from the normal mode projection. These modes are defined by the eigenvalue problem

$$\frac{d^2 a_m}{dz^2} + \frac{N^2}{c_m^2} a_m = 0 \qquad a_m(0) = a_m(-H) = 0, \tag{3.5}$$

where c_m is the mode-m internal tide phase speed related to the horizontal wavenumber κ_m, the Coriolis frequency f, and the barotropic frequency ω as

$$c_m = \frac{\sqrt{\omega^2 - f^2}}{\kappa_m}. \tag{3.6}$$

The eigenfunctions satisfy the following orthogonality condition:

$$\int_{-H}^{0} a_m(z) a_m(z) N^2(z) dz = f c_m \delta_{mn}, \tag{3.7}$$

and link the modal fields to their corresponding three-dimensional counterparts, e.g. for the perturbation pressure p (see LSY02, Eqs. 22, 23):

$$p = \sum_{m=1}^{\infty} \frac{c_m}{f} p_m a_m'(z). \tag{3.8}$$

The dimensionless quantity ζ_m related to the vertical derivative of the eigenfunctions, $a'_m = da_m/dz$, is defined as

$$\zeta_m = a'_m(-H)\frac{c_m}{f}. \tag{3.9}$$

For the normal mode decomposition described above, the modal conversion rate was identified by LSY02 (see their Eq. 28) as

$$C_m = \rho_0 \zeta_m \int \langle p_m \mathbf{u} \rangle \cdot \nabla h d\mathbf{r}, \tag{3.10}$$

where we have set, without loss of generality, a dimensionless normalization constant to unity. Note that for constant stratification, Eq. 3.5 can be solved analytically and

$$\kappa_m = \sqrt{\omega^2 - f^2}\frac{m\pi}{NH}, \qquad \zeta_m^2 = \frac{2}{m\pi}\frac{N}{f}. \tag{3.11}$$

In the following, we derive the energy flux into a specific mode as a function of direction and drop the subscript "m" for simplicity. We first transform Eq. 3.1 into an energy equation by multiplication with P^*, the complex conjugate of P:

$$\nabla \cdot (P^* \nabla P) - |\nabla P|^2 + \kappa^2 |P|^2 = P^* \sigma. \tag{3.12}$$

Taking the imaginary part $\Im$, this reduces to

$$\nabla \cdot \Im\{P^* \nabla P\} = \Im\{P^* \sigma\}. \tag{3.13}$$

Up to a real multiplicative coefficient, the LHS of Eq. 3.13 can be identified as the divergence of the energy flux through a comparison to the time-dependent form of the two-dimensional forced wave equation and the resultant energy conservation equation (see Section 3.9.1). For the internal tide generation problem, this coefficient is determined by the expressions of the source function σ_0 and of the modal conversion rate derived by LSY02 (see their Eqs. 28 and 33), given in Eqs. 3.2 and 3.24. In consequence, the barotropic to baroclinic tidal energy flux $\mathbf{F}$ is related to the pressure according to

$$\langle \mathbf{F} \rangle = \frac{\omega}{2}\Im\{P^* \nabla P\}, \tag{3.14}$$

where angle brackets denote the average over a tidal period, and the energy source density is given by $\omega/2\Im\{P^*\sigma\}$. The energy conversion can then be computed either as the integral of the energy flux $\mathbf{F}$ across a closed curve C around the source region,

$$E = \oint_C \mathbf{F} \cdot \hat{\mathbf{n}} dl, \tag{3.15}$$

where $\hat{\mathbf{n}}$ denotes the unit vector pointing outwards at the boundary and C the closed curve, or as the integral over the source density,

$$E = \frac{\omega}{2} \int \Im\{P^* \sigma\} d\mathbf{r}. \tag{3.16}$$

In both cases, the pressure field needs to be known; here, we need to follow the first approach (Eq. 3.15) in order to describe the direction of the energy conversion.

The solution of Eq. 3.1 can be expressed in terms of a Green's function G:

$$P(\mathbf{r}) = \int G(\kappa|\mathbf{r} - \mathbf{r}'|)\sigma(\mathbf{r}')d\mathbf{r}'. \tag{3.17}$$

The Green's function describes the radiation from a point source on an infinite plane [e.g. Jensen et al., 2000]. In essence, the bottom topography is described as a distribution of point sources and the total pressure field as the superposition of the Green's functions that solve Eq. 3.1 for the individual sources [e.g. Robinson, 1969; Pétrélis et al., 2006; Echeverri, 2009]. Since the energy flux must be directed radially outward, G is given by

$$G(\xi) = -\frac{i}{4} H_0^1(\xi) = \frac{1}{4} \left[Y_0(\xi) - i J_0(\xi) \right], \tag{3.18}$$

where H_0^1 denotes the zero order Hankel function of the first kind and J_0 and Y_0 are zero order Bessel functions of the first and second kind, respectively.

When the pressure field is evaluated at a point far away from all sources, the asymptotic expansion of the Hankel transform

$$H_0^1(\xi) \sim \sqrt{\frac{2}{\pi\xi}} e^{i(\xi - \pi/4)} \qquad \text{for} \quad \xi \gg 1 \tag{3.19}$$

can be used in Eq. 3.17. As a result, the pressure field can be approximated as

$$P(\mathbf{r}) \approx \frac{1}{4} \sqrt{\frac{2}{\pi\kappa r}} e^{i(\kappa r - \pi/4)} \tilde{\sigma}_0(\kappa\hat{\mathbf{r}}), \tag{3.20}$$

where the tilde denotes the Fourier transform

$$\tilde{\sigma}_0(\mathbf{k}) = \int e^{-i\mathbf{k}\cdot\mathbf{r}} \sigma_0(\mathbf{r}) d\mathbf{r} \tag{3.21}$$

and $\mathbf{k}$ is the two-dimensional wavenumber vector (see Section 3.9.2 for details of the derivation). Inserting Eq. 3.20 into Eq. 3.14 leads to the following expression of the far-field energy flux

$$\mathbf{F} = \hat{\mathbf{r}} \frac{\omega}{16\pi r} |\tilde{\sigma}_0(\kappa\hat{\mathbf{r}})|^2, \tag{3.22}$$

whose magnitude is the same on opposite sides of the sources because of $\tilde{\sigma}_0^*(\mathbf{k}) = \tilde{\sigma}_0(-\mathbf{k})$. Expressing the radial unit vector in terms of the Cartesian counterparts, $\hat{\mathbf{r}} = \hat{\mathbf{x}}\cos\phi + \hat{\mathbf{y}}\sin\phi$, underlines that this expression is indeed the directional energy flux in terms of the horizontal angle ϕ. Following Eq. 3.15, the total energy conversion becomes

$$E = \frac{\omega}{16\pi}\int_0^{2\pi} |\tilde{\sigma}_0(\kappa\hat{\mathbf{r}})|^2 d\phi. \tag{3.23}$$

The same expression can also be obtained by using Eqs. 3.17 and 3.18 in Eq. 3.16 and exploiting symmetry:

$$E = \frac{\omega}{8}\iint J_0(\kappa|\mathbf{r}-\mathbf{r}'|)\sigma_0(\mathbf{r})\sigma_0(\mathbf{r}')d\mathbf{r}d\mathbf{r}'. \tag{3.24}$$

This equation was used by Falahat et al. [2014b] to compute the global energy conversion. It can be rewritten by means of the following known expression of the Fourier transform of the Bessel function J_0

$$\int J_0(ar)e^{-i\mathbf{k}\cdot\mathbf{r}}d\mathbf{r} = \frac{2\pi}{a}\delta(k-a), \tag{3.25}$$

which leads indeed to the same expression as Eq. 3.23. An advantage of the first approach based on the approximate Hankel function is that it requires a more explicit treatment of what the applicability of the radiation condition, underlying both approaches, implies (see Section 3.9.2).

3.4 Implementation

The numerical implementation is based on Eq. 3.22. Substituting σ_0 by its full expression (cf. Eq. 3.2), the flux magnitude $F = |\mathbf{F}|$ can be written as

$$F = \frac{1}{2}\mathbf{U}\cdot\mathbb{R}\cdot\mathbf{U}^* \tag{3.26}$$

with the symmetric tensor

$$\mathbb{R} = \frac{\omega B^2}{16\pi r}|\tilde{h}(\kappa,\phi)|^2\kappa^2\hat{\mathbf{r}}\hat{\mathbf{r}}. \tag{3.27}$$

The advantage of treating the tidal velocity separately is that for example the spring-neap tidal cycle can be taken into account when applying the method as a parameterization in ocean general circulation models. Using

$$\hat{\mathbf{r}}\hat{\mathbf{r}} = \hat{\mathbf{x}}\hat{\mathbf{x}}\cos^2\phi + (\hat{\mathbf{x}}\hat{\mathbf{y}} + \hat{\mathbf{y}}\hat{\mathbf{x}})\cos\phi\sin\phi + \hat{\mathbf{y}}\hat{\mathbf{y}}\sin^2\phi, \tag{3.28}$$

the tensor $\mathbb{R}$ can be transformed into Cartesian coordinates. For the vertical eigenvalue problem and the orthogonalization described by LSY02, the constant B in Eq. 3.27 is given by

$$B = \kappa\zeta f\sqrt{1 - f^2/\omega^2}. \tag{3.29}$$

Equation 3.27 shows that the directional energy flux depends on the Fourier transform of the topography in polar coordinates. The apparently straightforward approach would be to first calculate the Fourier transform of the topography in Cartesian coordinates and to interpolate it then onto a polar grid in spectral space. Simple tests comparing Eqs. 3.15 and 3.16 for idealized topography such as top hat or Gaussian seamounts, however, demonstrate that the interpolation of the Fourier transformed topography requires a very high spatial resolution. The more practical alternative, both in terms of accuracy and computational speed, is to calculate the Fourier transform in polar coordinates. Baddour [2009] showed that taking the 2D-Fourier transform of a function is, after appropriate scaling, equivalent to first determining its Fourier series expansion in the angular direction and then calculating the n^{th} order Hankel transform of the radial variable. This implies that the transform needs to be calculated for one specific wavenumber only instead of all of them, which additionally reduces the computational expenses. In consequence, the implementation involves the following steps:

1. Interpolation to a polar grid: The topography $h(x, y)$ is on the Cartesian grid represented by a bivariate spline, which is then evaluated at the polar grid points. This gives $h(r, \phi)$.

2. Calculation of angular modes: A Fourier expansion (FFT) of $h(r, \phi)$ in ϕ-direction is performed to compute the angular modes $h_n(r)$, where n is the angular mode number:

$$h(r, \phi) = \sum_{n=-\infty}^{n=\infty} h_n(r)e^{in\phi}. \tag{3.30}$$

3. Hankel transform: We are interested in the Fourier transformed angular modes $\tilde{h}_n(k)$. As shown by Baddour [2009], these are related to the angular modes calculated in step 2, $h_n(r)$, through the Hankel transform:

$$\tilde{h}_n(k) = \frac{2\pi}{i^n}\int_0^\infty h_n(r)J_n(kr)r dr. \tag{3.31}$$

This integral is solved using numerical quadrature (Simpson's rule) for the specific wavenumber $k = \kappa$.

4. Calculation of the Fourier transformed topography as a function of angle: An inverse Fourier transform relates the modes $\tilde{h}_n(\kappa)$ to the Fourier transform of the topography, $\tilde{h}(\kappa, \beta)$:
$$\tilde{h}(\kappa, \beta) = \sum_{n=-\infty}^{n=\infty} \tilde{h}_n(\kappa) e^{in\beta}. \tag{3.32}$$
This can be evaluated at $\beta = \phi$.

In the real ocean, the sources are not confined to small, bounded regions, nor are the tidal velocity or the horizontal wavenumber constant, as assumed in the derivation of Eq. 3.1. Therefore, the far-field expression derived in the previous section cannot be applied directly. The same problem arises when computing the energy conversion as the integral over the source density using Eq. 3.24, as was done by Falahat et al. [2014b]. They dealt with this issue by truncating the Bessel function in the integral after a certain number of zeros, which effectively neglects the influence of topography far away from the point at which the conversion is calculated. In the same spirit, we only consider the topography in a certain area around the point of interest to be relevant for the energy conversion. To that end, we subdivide the topography into overlapping circular patches of radius r_p. In each of these circles, identified by indices i, j and centered at $\mathbf{r}_{i,j}$, the topography is multiplied by a Gaussian and interpolated onto a polar grid, which is also centered at $\mathbf{r}_{i,j}$:
$$h_{i,j}(\mathbf{r}) = h(\mathbf{r}) e^{-|\mathbf{r}-\mathbf{r}_{i,j}|^2/2r_g^2}. \tag{3.33}$$
This "screened" topography $h_{i,j}(\mathbf{r})$ is hence confined to a region of length scale r_g and we can therefore, if r_g is small enough, apply the far-field expression for each patch individually. In other words, for each patch, we follow steps 1-4 and calculate the angular energy flux $rF_{i,j}$ based on Eqs. 3.26 and 3.27, thereby covering the entire ocean floor. The mean angular flux density per unit area at the patch center
$$D_{i,j} = \frac{rF_{i,j}}{a_{i,j}}. \tag{3.34}$$
is obtained by normalizing the energy flux by the effective patch area $a_{i,j}$
$$a_{i,j} = \int \left(e^{-|\mathbf{r}-\mathbf{r}_{i,j}|^2/2r_g^2} \right)^2 d\mathbf{r} = \pi r_g^2, \tag{3.35}$$
where the square in the integral accounts for the quadratic dependence of the energy conversion on the screened topography. The procedure is illustrated in Fig. 3.1.

For the numerical implementation, the following parameters have to be set:

1. $f_l = r_p/r_g$, the size of the patch relative to that of the Gaussian;
2. $f_\kappa = \kappa r_g$, the size of the Gaussian itself relative to the wavenumber for which the conversion is calculated;

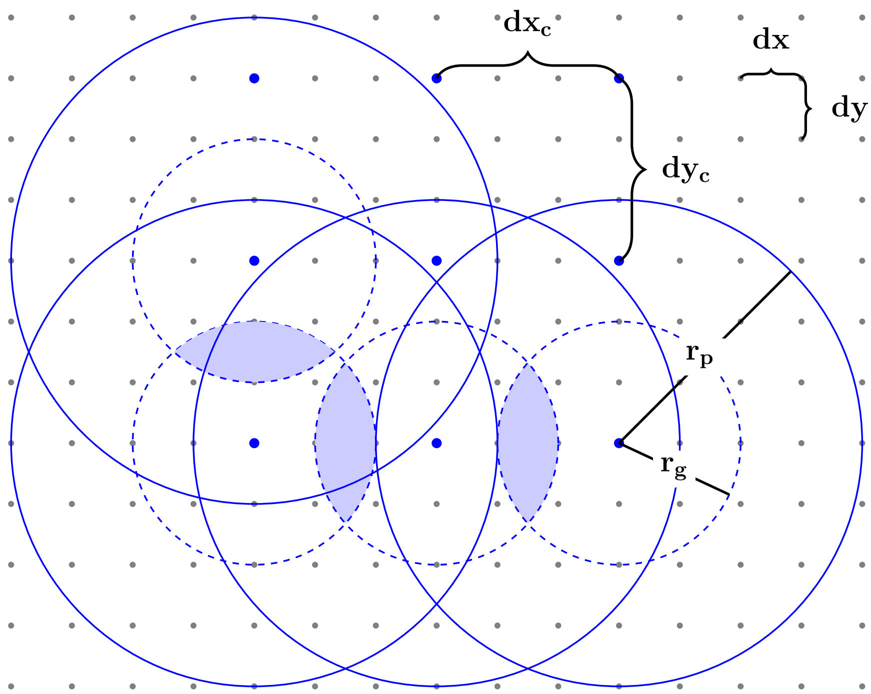

Figure 3.1: Illustration of the method: The topography is given on a Cartesian grid with spacing dx and dy (grey points). The total domain is subdivided into circular patches of radius r_p, whose centers are spaced at a distance of dx_c and dy_c (blue points). In each patch, the topography is interpolated onto a polar grid and multiplied by a Gaussian, whose width (standard deviation) is given by r_g. The numerical parameters which have to be set are 1) the patch size relative to that of the Gaussian, controled by the parameter $f_l = r_p/r_g$, 2) the size of the Gaussian relative to the wavenumber for which the conversion is calculated, controled by the parameter $f_\kappa = \kappa r_g$, 3) the grid spacing dy_c and dy_c relative to the Gaussian width, i.e. to what extent the effective patch area πr_g^2 overlaps (shaded blue areas), controled by the parameter $f_p = r_g/dx_c$, and 4) the resolution of the polar grid within each patch, $dr = r_p/n_r$ and $d\phi = 2\pi/n_\phi$, where n_r and n_ϕ denote the number of grid points in radial and angular direction.

3. $f_p = r_g/dx_c$, the extent to which neighboring patches overlap, relating the Gaussian width r_g to the patch center spacing dx_c;

4. the resolution of the polar grid in each patch, $dr = r_p/n_r$ and $d\phi = 2\pi/n_\phi$, where n_r is the number of points in radial and n_ϕ the number of points in angular direction. The parameter n_ϕ thus determines the resolution of the angular energy flux $\mathbf{F}$.

Suitable parameter settings are determined in convergence tests using idealized topography, which are presented in the following section.

3.5 Tests with idealized topography

The basic evaluation of the method achieved through the comparison of Eq. 3.15, describing the conversion as the integrated energy flux, and Eq. 3.16, defining the conversion in terms of the integrated source density, showed that for top-hat and stretched Gaussian topographies, the two solutions for the conversion rate agree well (see also Appendix 5.1 for more information on these idealized topographic profiles). For a more detailed evaluation and in order to determine the numerical parameters introduced in the previous section, we focus on the so-called "Witch of Agnesi"-profile, for which it is possible to calculate the conversion rate analytically. This idealized topography is described as

$$h(x) = \frac{h_0}{1 + \frac{x^2}{\Lambda^2}}, \tag{3.36}$$

where Λ denotes the topographic length scale (half-width of the ridge) and h_0 the maximum ridge height. Tidal currents flowing over this idealized topography will generate parallel wave trains propagating away from the ridge in x-direction—buoyancy oscillations and propagating internal gravity waves can only originate from flow over, not along, the topographic obstacle. This demonstrates that the orientation of the tidal ellipse essentially determines the magnitude of the energy conversion for approximately one-dimensional topography and implies that in this case, the conversion per unit length in y-direction (W m^{-1}) is a function of the zonal velocity component only [see e.g. Falahat et al., 2014b]:

$$C_m = \frac{1}{4}\rho_0 f \kappa_m^2 \zeta_m^2 \sqrt{1 - \frac{f^2}{\omega^2}} U_0^2 |\tilde{h}(\kappa_m)|^2 \tag{3.37}$$

with the Fourier transform of the topography

$$\tilde{h}(\kappa_m) = h_0 \Lambda \pi e^{-|\kappa_m|\Lambda}. \tag{3.38}$$

We follow Falahat et al. [2014b] and set $h_0 = 100$ m, $H = 4$ km, $f = 8 \cdot 10^{-5}$ s^{-1}, the mean seawater density to $\rho_0 = 1040$ kg m^{-3}, the tidal frequency corresponding to that of the M_2-tide, $\omega = 1.4 \cdot 10^{-4}$ s^{-1}, and the tidal amplitude to $U_0 = 4$ cm s^{-1}. The ridge is located at the center of a domain which extends 4000 km in each direction with a grid spacing of $dx = dy = 1$ km. For topographic scales Λ = (2.5, 5, 10, 20) km, the underlying assumptions of weak topography and small tidal excursion are met.

We compare the analytical and the numerical solution for these different topographic scales and different horizontal wavenumbers κ in order to determine suitable choices of the numerical parameters. We first consider the case of uniform stratification with $N = 9.02 \cdot 10^{-4}$ s^{-1}, so that $\kappa_m = m \cdot 0.1$ km^{-1} (see Eq. 3.11). The resolution of the polar grid is set such that at the outer patch boundary, the resolution is the same as that of the Cartesian grid, i.e. $n_r = r_p/dx$ and $n_\phi = 2\pi\, n_r$. For most test cases, this is a much higher resolution than necessary for reproducing the analytical solution within one percent, but

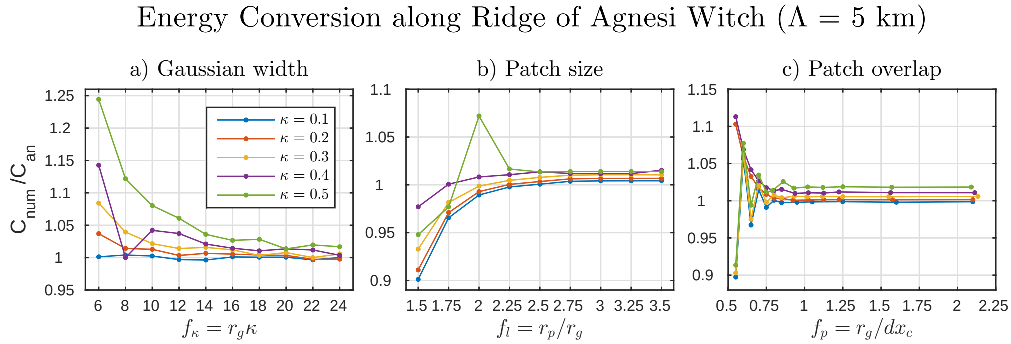

Figure 3.2: Ratio of numerical and analytical solution, C_{num} and C_{an}, for the Agnesi Witch-profile with a topographic length scale of $\Lambda = 5$ km. Other settings are given in the main text. Note the different y-axis scalings. One parameter at a time is varied while keeping the other two at their reference value: in (a) and (b), $f_p = 0.8$, in (a) and (c), $f_l = 2.5$, and in (b) and (c), $f_\kappa = 20$.

we keep it that high in order not to lose any information [Nycander, 2005, showed that insufficient resolution of topography is the most important error source in real applications].

Fig. 3.2 shows the convergence of the numerical solution toward the analytical one (see Eq. 3.37) for a topographic scale of $\Lambda = 5$ km, using increasing values of the Gaussian width, the patch size relative to that of the Gaussian, and the patch overlap. The latter is described as the ratio of Gaussian width r_g and patch center spacing dx_c, which is related to the area overlap relative to the effective patch area, O_p, according to:

$$O_p = 2\left(r_g^2 \operatorname{acos}\left(\frac{dx_c}{2r_g}\right) - \frac{1}{4}dx_c\sqrt{4r_p^2 - dx_c^2}\right)/(\pi r_g^2). \tag{3.39}$$

For values of κ between 0.1 km^{-1} and 0.5 km^{-1}, the numerical solution agrees very well with the analytical one for settings of $f_\kappa \geqslant 20$, $f_l \geqslant 2.5$, and a patch center distance comparable to the Gaussian width, that is, $f_p \geqslant 0.8$ or $O_p \geqslant 0.25$. This requires (17, 33, 49, 65, 80) patches in each direction, or in other words, a patch center spacing of $dx_c = dy_c = (235.3, 121.2, 81.6, 61.5, 50.0)$ km. The deviation from the analytical solution is about 1 % for modes 3-5 and less for modes 1 and 2. These threshold values are hence chosen as the reference settings for the following simulations. Note that we do not explore the three-dimensional parameter space, but keep two parameters fixed at their reference value while varying the third.

In the following step, these reference settings are evaluated for the different values of the ridge width Λ given above (see Fig. 3.3a). These test cases show that for wider ridges, the proportion of energy flux into the first vertical mode increases—for $\Lambda = 20$ km, the only mode carrying a significant amount of energy is the first one. Moreover, these tests demonstrate that the agreement with the analytical solution is very good except for

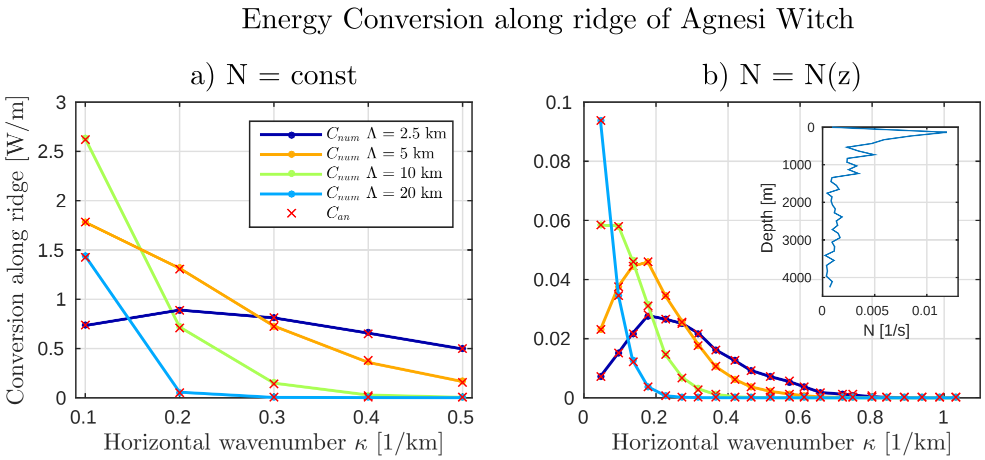

Figure 3.3: Energy conversion along Witch of Agnesi-ridge for four different topographic scales as a function of horizontal wavenumber for (a) constant and (b) variable stratification, with red crosses showing the analytical solution given by Eq. 3.37. In the former case, the Coriolis frequency is $f = 8 \cdot 10^{-5}$ s^{-1}, in the latter it is adjusted to the specific latitude of the N^2-profile, taken from the WOCE-database from 25° N, 43° W and shown in a vertically smoothed version in the inset in subplot (b), i.e. $f = 6 \cdot 10^{-5}$ s^{-1}. The other parameters are the same in both scenarios and given in the main text. The numerical parameter settings are $f_l = 2.5$, $f_\kappa = 20$, and $f_p = 0.8$. In the test cases with variable stratification (b), deviations from the analytical solution by more than 10 % are observed for $\kappa \geqslant (0.75, 0.80, 0.46, 0.23)$ km^{-1} for $\Lambda = (2.5, 5, 10, 20)$ km; conversion rates higher than 0.001 Wm^{-1} are very well reproduced. Assuming a constant stratification $N = 9.02 \cdot 10^{-4}$ s^{-1} (a), such deviations only occur for $\kappa \geqslant 0.5$ for $\Lambda = 10$ km and for $\kappa \geqslant 0.3$ for $\Lambda = 20$ km, when conversion rates decrease below 0.002 Wm^{-1}.

scenarios with very low conversion rates. Setting $\Lambda = 20$ km, the analytical solutions decrease below 0.002 Wm^{-1} as $\kappa \geqslant 0.3$ km^{-1} and the corresponding numerical solutions deviate by more than 10 % from the analytical values. In the most extreme case investigated here ($\kappa = 0.5$ km^{-1}), the numerical solution is $O(10^3)$ higher than the analytical conversion rate of $C_{an} = 8 \cdot 10^{-7}$ Wm^{-1}, a ratio which only decreases significantly for impractically fine resolutions. Very low energy conversion rates are hence typically overestimated by this method, but fortunately of minor importance for the energy budget of the internal tide field. Conversion rates above 0.002 Wm^{-1}, on the other hand, are reproduced within 10 % and rates above 0.2 Wm^{-1} within 1 %, mostly better. As depicted in Fig. 3.3a, the total energy conversion is considerably higher than 0.2 Wm^{-1} for the four different ridge length scales. For relevant energy conversion rates, the proposed method with standard settings $f_\kappa = 20$, $f_l = 2.5$, and $f_p = 0.8$ is thus confirmed for this idealized topography with constant stratification and a ridge width Λ varying between 2.5 km and 20 km.

This also holds true for vertically variable stratification (see Fig. 3.3b). In this case, the full eigenvalue problem given in Eq. 3.5 has to be solved, which is done numerically following the method described by Chelton et al. [1998]. We use a N^2-profile from the WOCE Global Climatology [Koltermann et al., 2011][8] from 25° N, 43° W, which is characterized by a bottom value of $N_B = 1.42 \cdot 10^{-7}$ s^{-1} and shown in the inset of Fig. 3.3b. We adjust the Coriolis parameter to a representative value of $f = 6 \cdot 10^{-4}$ s^{-1} and keep the other parameters at their former values listed above. As already observed for the test cases with constant stratification, the energy flux into higher modes decreases for wider ridges. It is interesting to note that in this idealized case with one-dimensional topography, there is a clear relation between ridge width and wavelength $\lambda = 2\pi/\kappa$ of maximum energy conversion: $\lambda(C_{max}) = 4\pi\Lambda$. This explains why the maximum conversion is observed for lower modes when increasing Λ and is a useful relation to determine the Gaussian width for the Agnesi Witch-profile. It is not suited, however, for calculations with realistic topography, which is characterized by many different topographic length scales.

As illustrated in Fig. 3.3b, the numerical solution well reproduces the analytical one as long as conversion rates are higher than 0.001 Wm^{-1}. Deviations from the analytical solution by more than 10 % are found for modes higher than (15, 17, 9, 4), i.e. the critical wavenumber is $\kappa_{crit} = (0.75, 0.80, 0.46, 0.23)$ km^{-1} for $\Lambda = (2.5, 5, 10, 20)$ km. The corresponding conversion rates amount to $C_{an} = (0.001, 1.34 \cdot 10^{-5}, 1.45 \cdot 10^{-4}, 6.32 \cdot 10^{-4})$ Wm^{-1} and are hence much lower than the total energy conversion into the lower modes with $\kappa < \kappa_{crit}$. In conclusion, the new method based on circular patches and using the standard settings defined above well accounts for the bulk of the energy flux into baroclinic tides.

3.6 Energy conversion for a region of realistic topography

In order to determine suitable numerical parameter settings for realistic topography, we choose a region over interesting topography that involves no land points and is large enough to incorporate a reasonable number of circular patches for a variety of parameters: spanning 30.85-55.83° W and 10.83-35.83° N, it covers an area of $2.78 \cdot 10^3$ km in latitudinal and $2.55 \cdot 10^3$ km in longitudinal direction (at the center at about 23° N) over the Mid-Atlantic Ridge (MAR). In addition, about 500 km of the surrounding topography, tapered by a $\sin^2$-function, as well as about 900 km of zeroes are added on all four sides of the domain to ensure a smooth decrease of the topography toward zero. The topographic elevation was taken from Becker et al. [2009] in a resolution of 30 arc-seconds, which corresponds to 0.93 km at the equator. We set $f = 6 \cdot 10^{-5}$ s^{-1}, but keep all the other parameters as before. Due to the lack of an analytical reference solution, suitable numerical parameters are determined by successively increasing their values until the

[8]This profile was downloaded from the eWOCE-website maintained by R. Schlitzer at the Alfred Wegener Institute for Polar and Marine Research, Bremerhaven, Germany.

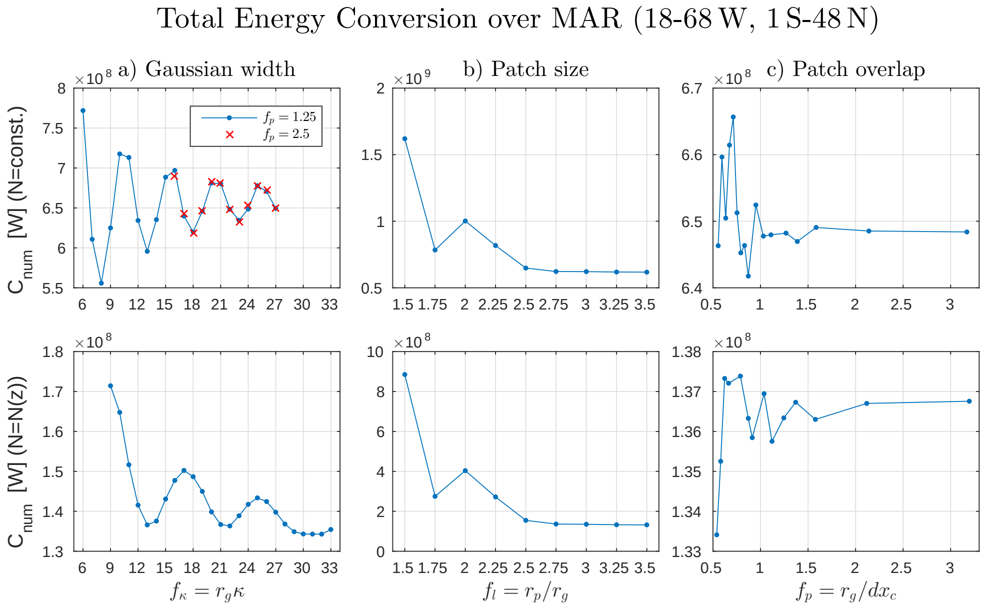

Figure 3.4: Sensitivity analysis of the total energy conversion over the MAR at 18°-68° W and 1° S-48° N (refer to Fig. 3.6 for an illustration of the topography, where the surrounding band of zeros was cropped) for (top) constant stratification with $N = 9.02 \cdot 10^{-4}$ s^{-1} and $\kappa_1 = 0.1$ km^{-1} and (bottom) variable stratification with the N^2-profile from 25° N, 43° W and $\kappa_2 \approx 0.1$ km^{-1}. Refer to the main text for details. One parameter is varied at a time, while the other two are kept constant. The reference settings are (top) $f_p = 1.25$, $f_l = 2.5$, and $f_\kappa = 22$ and (bottom) $f_p = 1.25$, $f_l = 2.75$, and $f_\kappa = 22$. Note the different y-axis scalings.

total energy conversion saturates. This form of convergence test is made possible by the tapering of the topography at the boundary of the region.

Fig. 3.4 depicts these sensitivity studies, showing the total energy conversion in the entire domain both for constant and for vertically variable stratification. In the first case, we set $N = 9.02 \cdot 10^{-4}$ s^{-1} with $\kappa = \kappa_1 = 0.1$ km^{-1}, $f_l = 2.5$, $f_\kappa = 22$, and $f_p = 1.25$ (that is, $n_{xc} = n_{yc} = 33$ and $O_p = 0.5$). In the second case, we use the N^2-profile from 25° N, 43° W (see Fig. 3.3b) and show the convergence of the numerical solution for $\kappa = \kappa_2 \approx 0.1$ km^{-1} with reference settings of $f_l = 2.75$, $f_\kappa = 22$, and $f_p = 1.25$ (that is, $n_{xc} = n_{yc} = 31$ or $O_p = 0.5$) The influence of variable stratification is evident, with somewhat lower total energy conversion rates observed in the scenario with $N = N(z)$.

The parameter f_l induces the largest oscillations when too small, but interestingly, convergence is observed for roughly the same threshold value as in the idealized case, i.e. $f_l \geqslant 2.5$. The smallest variations are observed when varying the patch overlap, which almost disappear for $f_p = r_g/dx_c$ higher than unity. For the Gaussian width, however, there is no smooth convergence; instead, smaller and smaller oscillations around the asymptotic value can be observed. These are no artifact of too low a resolution, as they prevail when the patch overlap is increased to $f_p = 2.5$ ($O_p = 0.75$) in the scenario with a constant stratification. We hypothesize that the reason for these oscillations is the fact that applying the Gaussian effectively smoothes the conversion field and that the degree of smoothing depends on its width r_g. This is illustrated in Fig. 3.5, where the zonally integrated energy flux density is shown as a function of latitude, demonstrating that the meridional structure of the flux is resolved best for smaller patch sizes, i.e. smaller values of f_κ. Consequently, there is a trade-off between angular and spatial resolution of the energy flux: considering the topography in a larger area around the point where the conversion rate is to be calculated leads to a higher number of angular modes n_ϕ and hence better resolves the direction of the energy flux at each individual patch center, but as the number of patches in the entire domain is decreased, this misses the smaller-scale geographic variations.

With sources of different length scales everywhere in the ocean, there is no single correct degree of smoothing, which makes it difficult to decide on a value for f_κ. Two opposite constraints should be satisfied: on the one hand, the total energy conversion should have reached an asymptotic solution with little if any variation around it, while on the other hand the circular patches must not be too large for an adequate geographic resolution of the conversion field and for the assumptions of constant tidal velocity and constant wavenumber within the patch to hold. For the scenario of variable stratification with $\kappa = \kappa_2$ depicted in Fig. 3.4, we therefore choose $f_\kappa = 22$, which yields the smallest patch size among those values of f_κ for which oscillations in total energy conversion have reduced to less than 5 % of the asymptotic value.

The directional energy flux for this realistic topography is presented in Fig. 3.6 for the mode-2 internal tide with $\kappa_2 \approx 0.1\ \mathrm{km}^{-1}$. Based on the sensitivity study shown in Fig. 3.4, the numerical parameters are set to $f_p = 1.25$, $f_\kappa = 22$, and $f_l = 2.75$. The Gaussian width hence amounts to 230 km and the total patch radius to 634 km. With a zonal tidal current $\mathbf{U} = (4, 0)\ \mathrm{cm\,s}^{-1}$, the energy flux is largest along the northeast-southwest axis, particularly west of the MAR. East of the MAR, the energy flux is much smaller and mainly unidirectional. At no location is the energy flux the same in all directions, underlining the necessity to explicitly model these horizontal variations in order to realistically implement the tidal forcing in internal gravity wave models.

How these results are influenced by the direction of the barotropic tidal currents is illustrated in Fig. 3.7. At a given location over the MAR (26° N, 45° W; the corresponding patch center is denoted by a red dot in Fig. 3.6), the direction of the energy flux into the first four baroclinic tide modes is shown for eastward, northward and northeastward barotropic flow. For modes 1,3, and 4, the sensitivity study to the parameter f_κ was repeated, showing that suitable settings are $f_\kappa = 14$, $f_\kappa = 30$, and $f_\kappa = 29$. These values were determined as those for which oscillations in total energy conversion reached 5 % of the asymptotic value; in order to avoid patch diameters comparable to the domain width (concerning particularly the lower modes), higher values of f_κ leading to stronger convergence were not used. For mode 5 (not shown) the corresponding threshold value

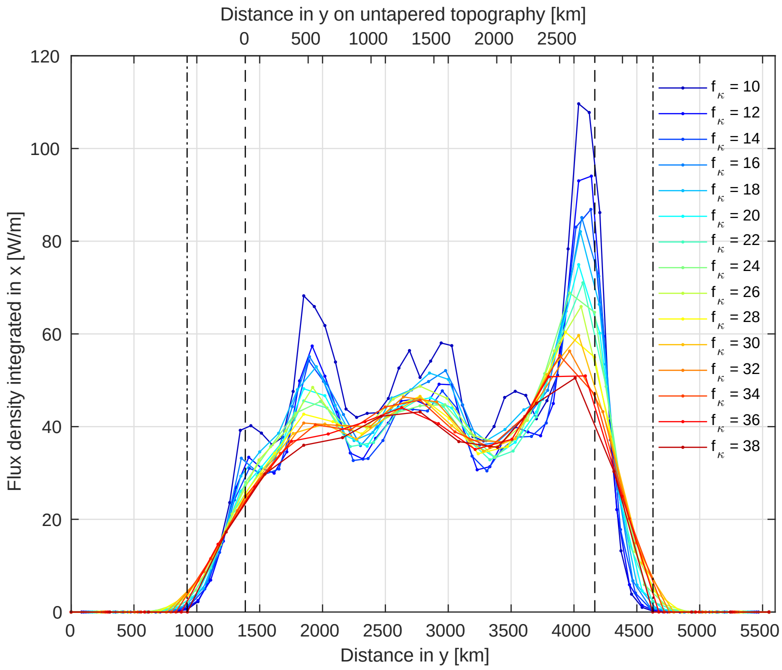

Figure 3.5: Zonally integrated flux density as a function of latitudinal distance across the domain of realistic topography shown (without the surrounding band of zeros) in Fig. 3.6 for different choices of f_κ. The dashed lines mark the region of untapered topography, the dashed-dotted lines mark the border between zero and tapered topography. The results are shown for $\kappa_2 \approx 0.1\,\mathrm{km}^{-1}$ with the same settings as described in the caption of Fig. 3.4 for variable stratification.

was also determined as $f_\kappa = 29$, which suggests that this numerical parameter indeed converges toward a common value for the higher modes with wavelengths shorter than 50 km ($n \geqslant 3$).

The direction of the barotropic tidal flow influences both the magnitude and the direction of the energy flux into the internal tides: The lowest conversion rates are observed for eastward and the highest for northward flows, respectively. This can be attributed to the orientation of the bottom topography in this patch: at locations where the topography is predominantly zonal (e.g. in the northwestern corner of the domain), the energy conversion is much higher for meridional than for zonal flow and only peaks in the direction of the barotropic flow (not shown). In the patch analyzed here, there are strong signals also in directions other than that of the barotropic flow, highlighting the complexity of the topography in that area. In any event, there are no energy flux in the direction orthogonal to that of the barotropic flow, illustrating that not only the bathymetry, but also the barotropic currents need to be modeled correctly for realistic simulations of the tidal energy conversion. The energy flux is highest into mode-3 and mode-4 internal tides, which points toward intermediate dominant topographic length scales at this location (a ridge

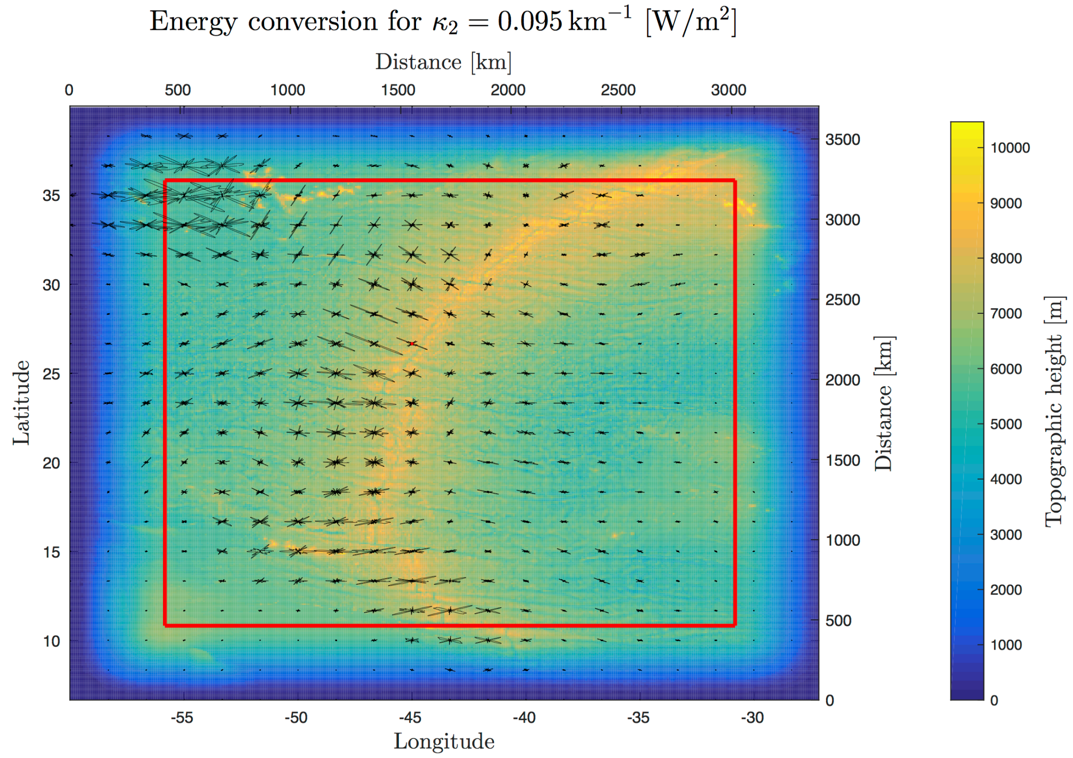

Figure 3.6: Energy conversion for variable stratification and realistic topography: At each patch center, the magnitude of the barotropic to baroclinic tidal energy flux, scaled by one half of the maximum conversion observed in the entire domain and represented by the distance to the patch center, is shown in each direction ($n_\phi = 4310$). The underlying topography is represented in color, with red lines delimiting the untapered topography at the center of the domain (the resolution of the topography input used in the calculations is ten times higher in each dimension than in this figure). Note that the 900 km of zeros, which were added on each side of the tapered topography to ensure a smooth decrease of the conversion rates at the boundaries, was cropped here for clarity. The stratification is assumed to be horizontally constant, taking the same vertical profile from 25° N, 43° W as used before, and setting $\mathbf{U} = (4, 0)\,\mathrm{cm\,s^{-1}}$ and $f = 6 \cdot 10^{-5}\,\mathrm{s^{-1}}$. The energy conversion is shown for the mode-2-internal wave with $\kappa_2 \approx 0.1\,\mathrm{km}^{-1}$, setting $f_\kappa = 22$, $f_l = 2.75$, and $f_p = 1.25$ ($n_{xc} = n_{yc} = 31$ or $O_p = 0.5$). The small red dot at 26° N, 45° W identifies the patch analyzed in more detail in Fig. 3.7.

of width Λ will force internal tides of comparable horizontal wavenumbers, $k \sim \Lambda^{-1}$, e.g. LSY02). The energy flux magnitude varies strongly with direction, supporting the conclusion already drawn from Fig. 3.6: modeling the direction of this internal gravity wave forcing is crucial for realistic simulations of these waves' energy content and ultimately the energy available for mixing.

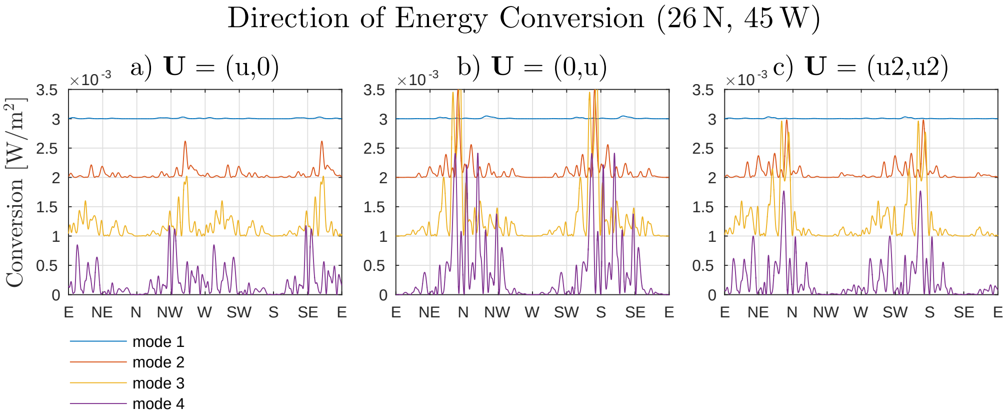

Figure 3.7: The energy conversion density D (see Eq. 3.34) at a patch centered on the MAR (26° N, 45° W, denoted by a red dot in Fig. 3.6) is shown as a function of direction for the first four modes, offset by 10^{-3} Wm^{-2}. The tidal velocity is (a) eastward, (b) northward, and (c) northeastward with an amplitude of $u = 4$ cm s^{-1} ($u2 = u/\sqrt{2}$). The other settings are as in the previous figure except for the Gaussian width, which was set to $f_\kappa = (14, 22, 30, 29)$ for modes 1 through 4, which are characterized by wavenumbers $\kappa = (0.046, 0.095, 0.135, 0.178)$ km^{-1}. The number of patches in the entire domain is $n_{xc} = n_{yc} = (24, 31, 32, 44)$ to ensure an overlap of 50 % of the effective patch area πr_g^2, that is, $f_p = 1.25$. Note that the different patch size for the different modes implies that the topography used in the individual calculations of the conversion rates is also different.

3.7 Effect on internal wave parameters in IDEMIX

In order to further motivate the application of the new method in mixing parameterizations of global general circulation models, the directionally variable forcing shown in Fig. 3.6 is implemented in the internal gravity wave model IDEMIX [see Olbers and Eden, 2013; Eden and Olbers, 2014, as well as Section 1.2.1 and Chapter 2]. Based on a simplified version of the radiative transfer equation, this model predicts the generation, propagation, and dissipation of internal gravity wave energy and provides a closed and energetically consistent parameterization of wave-induced turbulent mixing by relating the dissipated internal wave energy to the production of TKE. As detailed in Section 1.2.1 and Chapter 2, the model version IDEMIX2 explicitly describes near-inertial waves and internal tides as well as their interaction with the horizontally homogeneous internal wave continuum. In the case of internal tides, this interaction occurs in the form of nonlinear wave-wave interactions, which are enhanced equatorwards of the critical latitude of parametric subharmonic instability (see also Sections 1.1.2 and 2.7), and scattering at rough topography [refer to Appendix 1 of Eden and Olbers, 2014, for details]. The corresponding interaction terms are quadratic and linear functions of the internal wave energy, respectively, and calculated following Olbers [1976], Pomphrey et al. [1980], and

Müller and Xu [1992], except for the scattering time scale at the continental margins, for which no analytical theory exists and which is hence simply set to 7 days at points closer than 300 km to the shore [Eden and Olbers, 2014]. This is a typical width of the continental shelves, where Kelly et al. [2013] estimate that 40 % of the incident M_2 tidal energy are scattered into higher modes, while another 40 % are reflected and the remaining 20 % are dissipated.

To assess the effect of using a directionally variable instead of a constant tidal forcing, we use a stand-alone version of IDEMIX2, in which the internal gravity waves are modeled in an ocean at rest with a climatological stratification taken from Gouretski and Koltermann [2004]. The tidal forcing is the one presented in Section 3.6 and shown in Fig. 3.6, that is, the barotropic to baroclinic energy flux into the mode-2 M_2 internal tide, characterized by a horizontal wavenumber of $\kappa_2 = 0.095\,\mathrm{km}^{-1}$, for a horizontally constant stratification and an eastward tidal velocity of $\mathbf{U} = (4, 0)\,\mathrm{cm\,s}^{-1}$. This calculation covers an area of roughly 26 million square kilometers over the MAR (including the band of tapered topography and added zeroes to ensure a smooth decrease of the forcing toward the boundaries); everywhere else in the model domain of IDEMIX, which is here restricted to the North Atlantic, this tidal forcing is set to zero. Moreover, near-inertial gravity waves as well as any energy transfer to the continuum by mechanisms other than the interaction with the mode-2 M_2 tide (e.g. by interaction with higher modes or other tidal constituents) are neglected. In order to save computational time, the angular resolution of the conversion field is reduced from 4310 to 36 directions. In the reference simulation, each patch's average energy flux is used in all directions.

The vertically integrated energy of the internal wave continuum in these two scenarios is depicted in Figs. 3.8a,b. Because of the reduced forcing, the internal wave energy is lower than in the simulations presented in Chapter 2. As to be expected, its large-scale structure, which varies by more than two orders of magnitude, is not significantly altered when resolving the direction of the internal tide generation. In detail, however, the horizontal distribution of the continuum's energy changes: as illustrated in Fig. 3.8c, there is up to a 100 % increase or decrease of vertically integrated energy levels compared to the simulation with a directionally invariant tidal forcing. As explained in Section 3.5, the energy conversion is highest for flow across rather than along a topographic ridge. Since the tidal velocity is purely zonal in the experiment shown here, the general effect of resolving the direction of the internal tide generation is that higher energy levels are observed east and west of the MAR and lower levels are found in the northern and southern parts of the domain. The smaller-scale variations of the bottom topography and its orientation with respect to that of the tidal flow induce the additional detail in the geographic structure of the internal wave energy difference between the two scenarios. Fig. 3.8d shows the corresponding differences in TKE dissipation rates. Their spatial pattern closely mirrors that of the energy level differences, but the deviations from the reference scenario with a directionally constant energy flux are higher with up to a fourfold increase and up to a factor 10 decrease in dissipation rates at some locations.

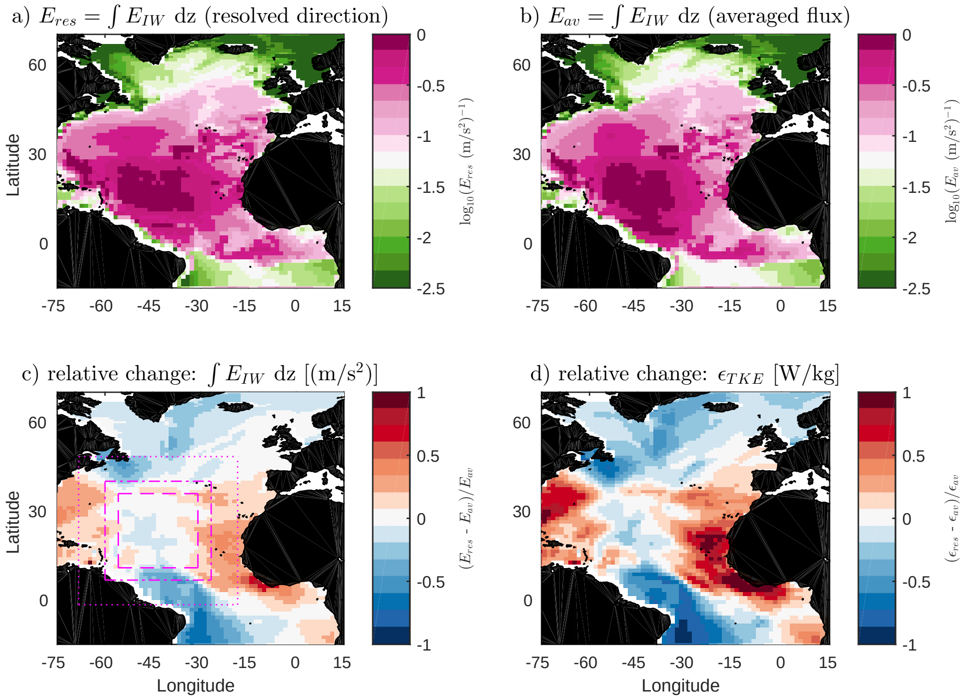

Figure 3.8: The vertically integrated energy of the internal wave continuum modeled by IDEMIX when (a) resolving the direction of the tidal forcing and (b) using in each patch the corresponding averaged energy flux in all directions. Their relative difference (c) and that of the corresponding vertically averaged TKE dissipation rates ϵ_{TKE} (d) demonstrate the implications for the far-field energy content and wave-induced mixing. The tidal forcing is taken from the realistic topography simulation for the mode-2 M_2 tide shown in Fig. 3.6, with magenta lines in subplot (c) delimiting the untapered (dashed), tapered (dashed-dotted), and filled with zeroes (dotted) topography field used as input for these calculations. Refer to the main text for details.

The interpretations presented above are supported by the behavior observed in the experiments with a purely meridional tidal velocity (see Fig. 5.2 in Appendix 5.1), where the internal wave energy is increased in the northern and southern parts of the domain and decreased in the east-west direction when resolving the direction of the tidal energy conversion. In this case, the difference between the scenarios with directionally variable and invariable tidal forcing is more pronounced, with vertically integrated internal wave energy levels increasing (decreasing) by up to a factor of 3 (14) at some locations and TKE dissipation rates increasing (decreasing) by up to a factor of 13 (20). As suggested by the results shown in Fig. 3.7, the orientation of the bottom topography near the MAR that forces internal tides of the wavenumbers considered here is such that the energy conversion is most efficient for meridional tidal flow. This possibly explains why the internal wave parameters modeled by IDEMIX are more sensitive to resolving the horizontal direction of the tidal forcing when the tidal flow is taken to be meridional rather than zonal. When considering different modes, the geographic variation of the total energy conversion changes because of the relation between topographic ridge width and the wavenumber of the internal tides generated at that ridge [$\kappa \propto \Lambda^{-1}$, LSY02]. As illustrated in Fig. 5.3 for the mode-4 internal tide with $\kappa_4 = 0.178\,\mathrm{km}^{-1}$, this also affects the difference between simulations with directionally variant and invariant tidal forcing (for example, there is no longer an increase in energy levels and TKE dissipation rates north of 35° N when the direction of the tidal forcing is resolved). The overall differences are however rather small, although it is interesting to note that the effect of varying the orientation of the tidal ellipse is more pronounced for the mode-2 than for the mode-4 M_2 tide (not shown).

Changes in TKE dissipation rates and energy levels are not only observed in the area where the tidal forcing is applied, but on the contrary manifest themselves in the entire model domain. This is due to the fact that internal tides can propagate over large distances before they break and underlines that resolving the direction of the barotropic energy conversion in internal gravity wave models and mixing parameterization based thereon is essential for the correct simulation of how the internal wave field's energy content as well as the wave-induced mixing vary geographically. The experiments with different settings for the tidal velocity show that the orientation of the tidal ellipse has important consequences for the energy conversion; it is hence only in combination with a realistic simulation of the barotropic tides that the new method resolving the horizontal direction of the tidal energy conversion can ensure a more realistic description of this mechanism than the current standard in IDEMIX. Moreover, the results presented in Fig. 5.3 suggest that because of the relation between topographic length scales and internal tide wavenumbers [LSY02], it is similarly important to consider not only one but several internal tide modes in the computation of the forcing.

3.8 Summary and conclusions

A new method to calculate both the magnitude and direction of the tidal forcing of internal gravity waves is presented. The main difference to previously applied schemes is that the energy conversion is derived from the energy flux instead of the integral over the sources. This offers the noteworthy advantage that the conversion rates are positive definite in contrast to the integrated energy sources, which can produce negative values [e.g. Zilberman et al., 2009; Falahat et al., 2014b]. Underlying assumptions of this semi-analytical method, based on the vertical mode treatment of LSY02, involve for example that the source regions should be bounded (radiation condition) and that the tidal velocity be constant, which do not hold for global calculations using realistic bathymetry. In consequence, the method is implemented by considering individual, overlapping circular patches, in which the topography is multiplied by a Gaussian centered at the circle's center in order to smoothly decrease the influence of the remote topography. The energy flux from each patch is then calculated by computing the Fourier spectrum of the topography within the patch.

This approach introduces some numerical parameters: the size of the patches, the size of the Gaussian, and the extent to which neighboring patches overlap. Convergence tests based on idealized and realistic topography permits the identification of suitable parameter settings, showing that the patch size should be at least 2.5 times the size of the Gaussian standard deviation r_g and that this Gaussian width should be approximately 30 times the wave number of the given mode (for modes higher than 2) and slightly larger than the patch center spacing dx_c.

The choice of the Gaussian width r_g relative to the wavenumber is the most difficult one. The effect of multiplying the topography with a Gaussian is that coherent interaction such as wave interference is neglected on length scales larger than r_g. In the ocean, factors such as nonlinear effects or inhomogeneities caused by eddies impede coherent interaction over large distances [e.g. Olbers, 1983], and ideally, the size of the Gaussian r_g should reflect this decorrelation length scale. Its properties, which possibly vary both in space and time, are however too little understood to be of practical use for the numerical parameter choices. Instead, we performed test simulations with increasing r_g until the total energy conversion saturated. Using realistic topography, this saturation takes the form of smaller and smaller oscillations around an asymptotic value, that is only reached for impractically large choices of $f_\kappa = \kappa r_g$, i.e. for patch diameters comparable to the total domain size. Clearly there is a tradeoff between numerical convergence and the applicability of the assumption that wavenumber and barotropic velocity can be considered constant within each patch. The sensitivity tests performed in this study serve as a rough guideline for the choice of this numerical parameter, but it seems that such tests would have to be repeated for different regions of the global ocean, depending on the details of the topography and the stratification.

The effects of natural decorrelation could also be accounted for by including a linear damping in Eq. 3.1 instead of considering circular patches of limited size. This might be physically more appealing, but implies that the total flux decreases exponentially away from the sources, so that the far-field expression cannot be used and the integration over the energy sources remains as the only possibility to calculate the conversion. In consequence, linear damping is no real alternative for the present purpose.

Another source of uncertainty stemming from the application of linear theory is the inherent assumption of subcritical topography. In the global ocean, however, some regions are characterized by supercritical slopes and the results obtained from linear theory are hence biased. The conversion rate in the subcritical domain is known to scale quadratically with the steepness parameter

$$\gamma = \frac{|\nabla h|}{\alpha} = |\nabla h| \left(\frac{N_B^2 - \omega^2}{\omega^2 - f^2} \right)^{\frac{1}{2}}, \tag{3.40}$$

where α is the slope of the tidal beam and $\gamma < 1$ characterizes the subcritical regime. The dependency in the supercritical regime is not known, but numerical and analytical studies suggest that the conversion rate saturates for large ridge height [Khatiwala, 2003; Nycander, 2006; Balmforth and Peacock, 2009], so that the application of linear theory to supercritical topography possibly overestimates the conversion rates. In consequence, Melet et al. [2013a] suggested to correct for supercriticality by dividing the conversion rates by γ^2 wherever γ was larger than unity. Following this approach, we calculate the steepness parameter on the fine topographic grid (1/120° resolution), approximating the gradients by forward differences. If in a 2.5°-circle around each patch center point (corresponding approximately to the Gaussian width for the scenario depicted in Fig. 3.6) at least 1 % (2 %) of the steepness parameter estimates exceed a value of unity, the correction proposed by Melet et al. [2013a] is applied. The correction factor is calculated as the squared average of all steepness parameter estimates in the 2.5°-circle in question that exceed unity. This correction is only implemented for untapered topography and affects 41 (12) out of the 225 patches depicted in Fig. 3.6. The total conversion rate in the entire domain is decreased by less than 4 % (1 %). Since the majority of topography taken into account for the computation of the energy conversion shown in Fig. 3.6 is subcritical—less than 1 % of all the steepness parameter values is larger than unity—, the uncertainty due to the application of linear theory to supercritical slopes is in this case, at least based on the simple approach by Melet et al. [2013a] and for the given resolution of the topographic data and that of the slopes ∇h, very small. In other areas of the global ocean or in a global integral, however, this uncertainty might be more prominent (Nycander [2005] and Falahat et al. [2014b] find that about half of the energy conversion into internal tides stems from supercritical slopes).

The proposed method with the standard settings identified in the scenarios tested here yields results in very good agreement with analytical solutions for idealized test cases. This motivates the application to realistic ocean bathymetry (recognizing however the caveats discussed above). The results for the North Atlantic (see Fig. 3.6) underline that the magnitude of the energy flux varies substantially with direction. Klymak et al. [2010] observe that modes with eigenspeeds higher than that of the barotropic velocity (modes 1 through 6 in the scenario in Fig. 3.6) radiate away from their generation site and contribute to the remote mixing in the ocean's interior, whose horizontal and vertical distribution significantly impacts the ocean's state and dynamics [Samelson, 1998; Zhang et al., 1999; Melet et al., 2013a]. It is therefore crucial for the consistency and reliability of ocean general circulation models to take the direction of the tidally generated internal gravity waves into account in internal wave-based mixing parameterizations. Simplified simulations of the internal gravity wave model IDEMIX [Olbers and Eden, 2013; Eden and Olbers, 2014] support this conclusion by demonstrating a robust sensitivity of internal wave energy levels and TKE dissipation rates to resolving the directional variations of the tidal forcing. Naturally, the next step will be the application of the method presented here to global ocean bathymetry with realistic and horizontally variable barotropic tidal velocities and stratification to produce a data base that can serve as a realistic input for global-scale simulations with IDEMIX or other internal wave models.

3.9 Appendix

3.9.1 Forced wave equation in complex notation

This section illustrates the relation between the physical, time-dependent form of the forced wave equation and its formulation in complex notation, providing an interpretation of Eq. 3.13. This wave equation for a field variable $\theta(\mathbf{r}, t)$ including a source $\psi(\mathbf{r}, t)$ is given by

$$\frac{1}{c^2}\frac{\partial^2\theta}{\partial t^2} = \nabla^2\theta - \psi. \tag{3.41}$$

An energy conservation equation can be derived via multiplication by $\partial\theta/\partial t$:

$$\frac{\partial}{\partial t}\left[\frac{1}{2c^2}\left(\frac{\partial\theta}{\partial t}\right)^2 + \frac{1}{2}(\nabla\theta)^2\right] = \nabla\cdot\left(\frac{\partial\theta}{\partial t}\nabla\theta\right) - \psi\frac{\partial\theta}{\partial t}. \tag{3.42}$$

From Eq. 3.42, the energy flux $\mathbf{F}$ and the total energy conversion C can be identified:

$$\mathbf{F} = -\frac{\partial\theta}{\partial t}\nabla\theta, \tag{3.43}$$

$$C = -\int \psi\frac{\partial\theta}{\partial t}d\mathbf{r}. \tag{3.44}$$

In complex notation, assuming a fixed frequency, the field variables are written as

$$\theta(\mathbf{r}, t) = \Re\{\Theta(\mathbf{r})e^{-i\omega t}\} \tag{3.45}$$

$$\psi(\mathbf{r}, t) = \Re\{\Psi(\mathbf{r})e^{-i\omega t}\}, \tag{3.46}$$

where Θ and Ψ are complex amplitudes. Using these expressions in Eqs. 3.43 and 3.44, the energy flux and convergence become

$$\langle\mathbf{F}\rangle = \frac{\omega}{2}\Im\{\Theta^*\nabla\Theta\}, \tag{3.47}$$

$$\langle C\rangle = \frac{\omega}{2}\int\Im\{\Psi\Theta^*\}d\mathbf{r}, \tag{3.48}$$

exploiting the relation $\langle ab\rangle = 0.5\Re\{AB^*\}$ for $a = \Re\{Ae^{-i\omega t}\}$ and $b = \Re\{Be^{-i\omega t}\}$, where angle brackets denote the average over a period and the star the complex conjugate.

Inserting the complex expressions for the field variables (Eqs. 3.45 and 3.46) into the forced wave equation (Eq. 3.41) yields

$$\nabla^2\Theta + \kappa^2\Theta = \Psi \tag{3.49}$$

with $\kappa^2 = \omega^2/c^2$. After multiplication by the complex conjugate Θ^* and taking the imaginary part, Eq. 3.49 is transformed into

$$\nabla \cdot (\Im\{\Theta^* \nabla \Theta\}) = \Im\{\Psi \Theta^*\} \tag{3.50}$$

and the relation to Eq. 3.47 is evident:

$$\nabla \cdot \langle \mathbf{F} \rangle = \frac{\omega}{2} \nabla \cdot (\Im\{\Theta^* \nabla \Theta\}) = \frac{\omega}{2} \Im\{\Psi \Theta^*\}. \tag{3.51}$$

Integrating Eq. 3.51 over a bounded region that contains all sources and using Gauss' theorem, we find that the total conversion as given in Eq. 3.48 accounts for the total energy flux across the boundary of the region.

3.9.2 Modal pressure amplitude with asymptotic expression of Hankel transform

Using the asymptotic expression of the Hankel transform in Eq. 3.17 gives

$$P(\mathbf{r}) \approx \frac{1}{4} \sqrt{\frac{2}{\pi}} \int \frac{1}{\sqrt{\kappa |\mathbf{r} - \mathbf{r}'|}} e^{i(\kappa |\mathbf{r} - \mathbf{r}'| - \pi/4)} \sigma_0(\mathbf{r}') d\mathbf{r}'. \tag{3.52}$$

When the origin of the coordinate system is at the center of the source distribution, $|\mathbf{r}'| \ll |\mathbf{r}|$ and

$$|\mathbf{r} - \mathbf{r}'| \approx r - \frac{\mathbf{r}}{r} \cdot \mathbf{r}' + O\left(\frac{r'^2}{r}\right). \tag{3.53}$$

Following Eq. 3.53, the factor $(\kappa|\mathbf{r} - \mathbf{r}'|)^{-1/2}$ is approximated as $(\kappa r)^{-1/2}$, while in the phase of the exponential, the terms $O\left(\frac{r'^2}{r}\right)$ are neglected. For accuracy to order unity, this requires $\kappa r'^2/r \ll 1$, i.e. $r/r' \gg \kappa r'$, so that depending on the extent of the source region $\kappa r'$, the energy flux must be evaluated further and further away from it for the far-field expression to be valid.

Far away from the sources, Eq. 3.52 is hence approximated as

$$P(\mathbf{r}) \approx \frac{1}{4} \sqrt{\frac{2}{\pi \kappa r}} e^{i(\kappa r - \pi/4)} \int e^{-i\kappa \frac{\mathbf{r} \cdot \mathbf{r}'}{r}} \sigma_0(\mathbf{r}') d\mathbf{r}'. \tag{3.54}$$

The integral in Eq. 3.54 can be identified as the Fourier transform of the topography

$$\tilde{\sigma}_0(\mathbf{k}) = \int e^{-i\mathbf{k} \cdot \mathbf{r}'} \sigma_0(\mathbf{r}') d\mathbf{r}' \tag{3.55}$$

evaluated at wavenumber $\kappa \hat{\mathbf{r}}$. In consequence, using the far-field approximation of the Hankel transform allows us to express the pressure field in terms of the Fourier transform of the topography:

$$P(\mathbf{r}) \approx \frac{1}{4} \sqrt{\frac{2}{\pi \kappa r}} e^{i(\kappa r - \pi/4)} \tilde{\sigma}_0(\kappa \hat{\mathbf{r}}). \tag{3.56}$$

4 Summary and conclusions

4.1 Evaluating the internal wave model IDEMIX

1a) How do the finestructure estimates of TKE dissipation rates and internal gravity wave energy levels vary geographically? What is the uncertainty of these estimates?

The TKE dissipation rates estimated from finestructure information vary globally by three orders of magnitude with a typical range of $\epsilon = \left(3 \cdot 10^{-11} - 3 \cdot 10^{-8}\right)$ W kg^{-1}. Maximum values are found in the western boundary currents, in the wind-driven gyres of the subtropical oceans, and near rough topography, for example in the Indonesian seas. Elevated TKE dissipation rates can be observed in large parts of the ACC and over the MAR, very low rates are mainly confined to the eastern boundaries of the ocean basins and the Southern Ocean close to Antarctica. This mirrors the internal gravity wave forcing through winds, tides, and eddies. The dissipation rates typically decrease with depth, which is especially noteworthy in regions where the internal gravity wave field is predominantly forced by the wind. In areas of strong tidal forcing, the decrease of dissipation rates with depth is less pronounced and in some cases, they even increase toward the deeper end of the ocean's upper 2000 m that are profiled by Argo floats.

Internal gravity wave energy varies by two orders of magnitude in the global ocean between $E = 10^{-4}$ m^2 s^{-2} and $E = 10^{-2}$ m^2 s^{-2}. The estimates derived from strain and potential density spectra are very similar and exhibit maximum values around the equator and minimum values near the poles. Zonal variations are less distinct, but nevertheless the western boundaries of the ocean basins can be identified as regions of increased energy levels. Similarly, signals of enhanced forcing in the wind-driven gyres in the subtropical Pacific and in the ACC are also discernible. Energy levels typically also decrease with depth, but at some locations, the inverse is the case.

The uncertainty of these finestructure estimates embodies several factors: The statistical uncertainty was assessed by calculating 90 % bootstrap confidence intervals, which are largest in the upper depth range for both TKE dissipation rates and energy levels and range from 20 % to 80 % of the corresponding mean value. The difference between the energy level estimates obtained from strain and potential density spectra, which on average amounts to a factor of 1.5-2 depending on depth, further contributes to the energy levels' uncertainty. Another factor is the sensitivity of the finestructure estimates to the parameter settings inherent in the method. This was analyzed for the Atlantic Ocean for the year 2011 and showed that the only scenario for which a statistically significant difference from the reference case was observed in all depth ranges considered (250-500 m, 500-1000 m, and 1000-2000 m) was the one in which the maximum allowed strain variance was doubled, that is, $\langle \xi_z^2 \rangle \leqslant 0.2$. The TKE dissipation rates are more sensitive to parameter changes than energy levels, especially in the upper ocean, where modifications of segment length, vertical resolution, or the shear-to-strain ratio also induce statistically significant variations from the reference. An uncertainty estimate associated with the parameter sensitivity representative of all depth ranges is a factor of 2. The total uncertainty of the finestructure estimates was calculated as the sum of these different factors, replacing for TKE dissipation rates the parameter sensitivity by the difference between fine- and microstructures estimates observed by Whalen et al. [2015] plus the uncertainty of microstructure observations. For both energy and dissipation rates, this amounts to an average uncertainty of a factor of 5 compared to a factor of 8 for the worst-case scenario. For the evaluation of IDEMIX in its typical application, that is, coupled to a global ocean model, these geographically and vertically averaged uncertainty estimates are most representative and were hence considered.

Further caveats arise due to effects that cannot be quantified: For example, near the ocean boundaries, the internal wave spectrum typically departs from the smooth and slowly varying form it is assumed to have in the parameterizations of nonlinear wave-wave interactions that form the basis of the finestructure method. Similarly, the finestructure estimates close to the equator are to be treated with skepticism because of a singularity of the GM model at $f = 0$. Finally, the number of Argo profiles is significantly reduced below 1000 m, especially in the Atlantic and Southern Ocean, so that the averages computed higher up in the water column are more representative as they are based on a greater number of individual estimates.

1b) How well can IDEMIX reproduce these Argo-derived estimates in terms of their magnitude and their geographic variations? Which tuning parameter settings in IDEMIX lead to the best agreement?

The large-scale patterns as well as the magnitudes of the Argo-derived estimates described in the previous section are well reproduced by IDEMIX. Discrepancies arise for example at the continental margins, where IDEMIX consistently models higher values than those obtained from Argo profiles—since the finestructure method is not always reliable in these areas, this difference does not necessarily correspond to a shortcoming of IDEMIX. In the northwestern Pacific Ocean, IDEMIX was shown to reproduce the basic vertical structure, but in a rather smoothed form without the detailed variations observed in the Argo data. Moreover, areas characterized by high TKE dissipation rates such as the Kuroshio and its extension or the subtropical gyres of the Pacific Ocean are typically modeled to be smaller than suggested by the finestructure estimates.

The parameter settings taken as a reference in the analysis presented in Chapter 2 are the ones for which the best agreement with the Argo-derived energy estimates was found in all three depth ranges, that is, $j_* = 5$, $\mu_0 = 1/3$, and $\tau_\upsilon = 2$ days. In that case, more than 90 % of the modeled energy levels and more than 60 % (up to 75 %) of the modeled TKE dissipation rates agree with the corresponding Argo estimates within a factor of 3, both in the 1°- and the 2.8°-resolution simulations. The agreement with the Argo-derived estimates is better in regions of low dissipation rates ($\epsilon \leqslant 3 \cdot 10^{-9}$ W kg^{-1}), while energy levels are equally well reproduced in regions of high and low energy taking a threshold value of $E_{crit} = 0.003$ m^2 s^{-2}. Horizontal correlation coefficients range from 0.1 to 0.3 for TKE dissipation rates and from 0.4 to 0.7 for energy levels depending on the depth range considered; in both cases, these values vary regionally with higher correlation coefficients typically observed in the Southern Ocean and the northwestern Pacific and lower ones in the North Atlantic.

The qualitative and quantitative agreement between IDEMIX- and Argo-based estimates is only slightly affected by variations of the tuning parameters and even less for TKE dissipation rates than for energy levels. Compared to the standard parameter settings chosen in Olbers and Eden [2013], the correlation coefficients remain roughly the same, but there is a up to a fourfold increase in the percentage of modeled energy data agreeing with the corresponding Argo estimates within a factor of 3 and an even stronger increase when the agreement within a factor of 2 is analyzed.

1c) How is the model-data agreement affected by using different model versions (IDEMIX1 vs IDEMIX2) and different forcing settings, in particular with respect to the role of mesoscale eddies?

The model version IDEMIX2 explicitly describes near-inertial waves and internal tides as well as their interaction with the horizontally homogeneous continuum. The comparison with Argo finestructure estimates of TKE dissipation rates and energy levels showed, that the additional computational expenses required to resolve these low mode internal waves do not lead to a notably better agreement. In fact, the percentage of data agreeing within a factor of 3 as well as the horizontal correlation coefficients barely changed in a global comparison. Locally and also seasonally, the difference is more pronounced, but still far from significant within an uncertainty of the Argo estimates of a factor of 5.

In a global comparison, variations of the surface and bottom forcing only induced minor modifications of the model-data agreement. Locally, for example at the MAR, in the subtropical gyres of the Pacific Ocean, or around the Indonesian archipelago, the modeled TKE dissipation rates were notably reduced when the tidal and the wind forcing were removed. Simulations run without eddy forcing or with eddy forcing alone illustrate the importance of this mechanism for the adequate reproduction of the Argo-derived TKE dissipation rates. The strong signals in the western boundary currents and their extensions, for example, in the Kuroshio and the Gulf Stream, disappeared when forcing IDEMIX with winds and tides only. Moreover, the modeled dissipation rates were notably reduced in the ACC, particularly in Drake Passage. This decrease is significant even within the high uncertainty of the Argo estimates as localized comparisons for the Agulhas retroflection and Drake Passage showed.

4.2 The horizontal direction of the tidal energy conversion

2a) How can the direction of the energy flux from barotropic to internal tides be calculated? How can this method be applied to the global ocean?

Based on the vertical normal mode treatment of LSY02, the horizontal direction of the tidally generated internal waves can be resolved by calculating the conversion in terms of the energy flux instead of, as done in previous studies [e.g. Egbert et al., 2004; Nycander, 2005; Falahat et al., 2014b], the integrated energy sources. The energy flux is a function of the modal pressure amplitude, which can after some algebra be expressed in terms of the vertical eigenfunctions and the horizontal wavenumber, both calculated from the vertical stratification, the tidal velocity, the frequency of the tidal constituent, and the Fourier transformed topography in polar coordinates. A noteworthy advantage over previous approaches is that this new method always yields positive conversion rates. It is important to note that all of them are based on linear theory and hence only applicable to weak topography and small-amplitude flow Bell [1975a,b].

The new method can only be applied to delimited regions of the seafloor as it relies on the assumption of horizontally constant wavenumbers and tidal velocities. The approach proposed here is to subdivide the topography into overlapping circular patches, which are considered individually in the calculation of the total energy conversion rate. Since the internal tide generation is a local problem [LSY02], the influence of topography far away from the patch center is neglected by multiplying the topography by a Gaussian to smoothly reduce it to zero toward the circle's boundary. The option to first expand the topography in a Fourier series (FFT) and then interpolate it on a polar grid is computationally very expensive and hence not suitable for global calculations based on high-resolution topographic data. Instead, the topography is first interpolated and then Fourier transformed, exploiting the analogy to the angular Fourier series expansion and the radial Hankel transform shown by Baddour [2009]. This additionally saves computational expenses as the transform is only calculated for one specific wavenumber instead of all of them.

2b) How does this new method perform for idealized topographic settings? What are suitable numerical parameters for idealized and realistic topography?

Three numerical parameters have to be set to implement the new method calculating the direction of the barotropic to baroclinic energy flux: One, the size of the circular patch relative to that of the Gaussian used to taper the topography within the patch. With the patch radius r_p and the Gaussian width (standard deviation) r_g, this parameter is defined as $f_l = r_p/r_g$. Two, the size of the Gaussian itself, which is expressed relative to the wavenumber κ of the internal tide mode and controled by the parameter $f_\kappa = \kappa r_g$. Three, the degree to which neighboring patches overlap. This is determined by the parameter $f_p = r_g/dx_c$, with dx_c denoting the distance between adjacent patch centers. The resolution of the polar grid is set such that no information is lost and the resolution at the circle's boundary is the same as that of the Cartesian grid, that is, $n_r = r_p/dx$ and $n_\phi = 2\pi n_r$, where n_r is the number of points in radial direction, dx the grid spacing of the topographic grid, and n_ϕ the number of points in angular direction.

Suitable settings for these three parameters were determined considering the Agnesi Witch profile, a one-dimensional ridge for which the energy conversion can be calculated analytically. With the given resolution of the polar grid, the ratio of numerical and analytical solution approaches unity for $f_\kappa \geqslant 20$, $f_l \geqslant 2.5$, and $f_p \geqslant 0.8$, which corresponds to an overlap of 25 % of the effective patch area πr_g^2. This was confirmed for relevant conversion rates considering four different topographic scales Λ between 2.5 km and 20 km and the first five vertical modes assuming constant stratification with $\kappa = 0.1 - 0.5$ km^{-1}. Conversion rates above 0.002 W m^{-1} were reproduced within 10 % and conversion rates above 0.2 W m^{-1} within 1 % (within 0.1 % in case of lower modes for topographic scales of a few kilometers). Considering a variable stratification, the performance was similar. In both cases, the numerical solution deviated strongly from the analytical one for very low conversion rates, but since these do not significantly contribute to the internal tide energy budget, the quality of the method is not diminished.

For realistic topography, an analytical reference solution is not available and suitable parameter settings were determined by gradually increasing the numerical parameters and analyzing when the total conversion saturated. Here, an area of roughly seven million square kilometers over the MAR, taken from Becker et al. [2009], was analyzed. Convergence was observed for $f_p \geqslant 1.25$, corresponding to an overlap of 50 % of the effective patch area, and $f_l \geqslant 2.5$. Increasing the third parameter, f_κ, did not lead to to a smooth convergence toward some asymptotic value, but induced oscillations of ever smaller amplitude around that asymptote. This is possibly caused by the choice to taper the topography by a Gaussian, which smoothes the conversion to different degrees depending on the value of its standard deviation. In this regard, a compromise between angular and geographic resolution has to be found: while ever larger patch radii lead to a larger n_ϕ and hence a higher resolution of the energy flux, they also cause a smaller number of individual patches covering the seafloor and hence a flux density field that is horizontally less well resolved. In this study, the appropriate setting for f_κ was determined as the value for which oscillations in the total conversion reached 5 % or less of the asymptotic value in order to guarantee approximate numerical convergence while avoiding too large patch radii. For modes 3-5, a suitable choice was found to be $f_\kappa \approx 30$; lower modes characterized by smaller wavenumbers required smaller values of f_κ in order to prevent patch diameters comparable to the domain width.

The analysis of this region of realistic topography with vertically variable, but horizontally constant stratification and with different directions of the constant tidal velocity underlined, that the energy flux into internal tides significantly varies with direction. In areas where the topography is to first order one-dimensional, the energy flux was largest in the direction across the obstacle, in areas characterized by more complex topographic features, internal gravity waves radiated away in several directions. In no case was the energy flux observed to be the same in all directions, as assumed in previous studies and also in the bottom boundary forcing of IDEMIX.

2c) How do internal gravity wave energy and TKE dissipation rates modeled by IDEMIX change when the tidal forcing varies with direction?

In order to assess how a directionally variable tidal forcing influences internal wave parameters in IDEMIX, a simplified version of IDEMIX2 was used in which the internal wave continuum was only forced through the interaction with the mode-2 M_2 tide. The bottom boundary condition for this tidal constituent was the barotropic energy conversion calculated by applying the new method in a region over the MAR, using a horizontally constant stratification and a zonal tidal velocity, as described above. This simulation was compared to a reference scenario, covering the same geographic region but considering the energy flux in a given patch constant in all directions. Because of the limited forcing, the modeled internal wave energy levels are not realistic, but the influence of resolving the direction of internal tide generation can be evaluated directly. Since the internal tide generation is most efficient for flow over rather than along topographic barriers and the tidal velocity was set to be zonal, the main effect of resolving the direction of the barotropic to baroclinic tide energy flux is that the modeled energy levels increased in the direction across the MAR and decreased in the direction along it. The energy content of the internal wave continuum was changed by up to a factor of 2 and the TKE dissipation rates by up to a factor of 10 compared to reference simulations with a directionally invariant tidal forcing. These differences were shown to be much enhanced when considering a meridional instead of a zonal tidal flow, albeit more so for the mode-2 M_2 tide than for the mode-4 tide. Since internal gravity waves can propagate over large distances before breaking, these effects were observed everywhere in the model domain and not only where the forcing was applied.

4.3 Conclusions and outlook

This section serves as a synthesis of the results presented in Chapters 2 and 3 and summarized in the previous sections. Its focus is on the main research questions underlying this PhD project:

- Can IDEMIX provide a realistic description of oceanic turbulent mixing in global general circulation models?

- What further improvements or steps of evaluation might be necessary to (better) achieve that objective?

The motivation for the development of IDEMIX ("Internal Wave Dissipation, Energy and Mixing") was to parameterize oceanic turbulent mixing in ocean general circulation models in an energetically consistent manner, linking the associated potential energy gain to the breaking of internal gravity waves and that in turn to their energy content [Olbers and Eden, 2013]. The internal wave energy is specified in terms of the forcing at large scales and the nonlinear wave-wave interactions, which transfer energy through the internal wave spectrum toward the small dissipation scales, and can be described in great detail in frequency-wavenumber space [e.g. Hasselmann, 1962; Olbers, 1976; McComas and Bretherton, 1977; Müller et al., 1986]. In order to arrive at an expression of practical use for three-dimensional, global simulations, the complexity of the analytical description has to be reduced and some of that detail is inevitably lost. The question is hence whether the assumptions (based on analytical, numerical, and observational evidence) made to simplify the internal wave energy balance and to derive IDEMIX result in a model which can reproduce the observed variations of turbulent mixing and to what degree.

The state of past and present measurement techniques is such that available observations of any ocean property are marked by a clear contrast between the resolution of individual profiles and the size of the survey area [e.g. Boyer et al., 2009; Waterhouse et al., 2014]: Direct observations of turbulent mixing require a lot of time and effort and are hence limited to select regions and times of the year. Decreasing the distance between sample points increases the area covered by measurements, especially when these are collected by autonomous devices instead of ship-born instruments, but simultaneously reduces the level of detail that can be detected. Since IDEMIX is meant to be used in global numerical simulations, it is crucial to assess its performance on global scales. Such a large observational data base can only be provided by the Argo program, which collects upper ocean measurements of pressure, salinity and temperature finestructure from which TKE dissipation rates, vertical diffusivities, and, as derived in this PhD project, internal wave energy levels can be inferred. Their average uncertainty was here specified as a factor of 5 in agreement with conclusions drawn from local comparisons of fine- and microstructure observations [Sheen et al., 2013; Frants et al., 2013; Whalen et al., 2015] or considerations of the associated theoretical biases and of practical issues with commonly applied instrumentation [Polzin et al., 2014]. As the TKE dissipation rates, vertical diffusivities, and internal wave energy levels were shown to vary globally by two to three orders of magnitude, the Argo finestructure estimates can nevertheless be considered a realistic description of oceanic turbulence. As such, and because they cover the global ocean, they are the appropriate reference for the evaluation of IDEMIX in terms of the first underlying research question.

The model-data comparison performed in this PhD project showed that IDEMIX can indeed capture the large-scale variations of energy levels and dissipation rates, both in terms of their magnitudes and their geographic structures. This holds true for vertical diffusivities with the only exception of regions where the ocean model pyOM, to which IDEMIX is coupled, simulates a vertical stratification that strongly differs from the observed one, that is, in the polar North Atlantic and in the Southern Ocean. This deviation is hence not a deficiency of the mixing parameterization itself. Shortcomings of IDEMIX are mainly related to the spatial extent of mixing hotspots, seeing that IDEMIX systematically models too small regions of high energy levels or dissipation rates, as well as the detailed vertical structure. In general, however, it can be concluded that IDEMIX well reproduces the Argo-derived finestructure estimates. This positive assessment applies to both model versions IDEMIX1 and IDEMIX2, which indicates that to first order, the treatment of all types of internal waves as part of a horizontally homogeneous continuum is a reasonable approximation. If only a general reproduction of oceanic turbulent mixing is desired, the additional computational expenses associated with the explicit description of near-inertial waves and internal tides in IDEMIX2 are not necessary.

For both model versions, the answer to the first research question is therefore affirmative, but has to be understood in a general sense because the high uncertainty of the Argo-based estimates limits the evaluation to spatial scales on which the variations of TKE dissipation rates and energy levels exceed a factor of 5. An important next step in the assessment of IDEMIX, motivated by its good performance on global scales, is hence the regional comparison with high-resolution observations. These include for example microstructure measurements [e.g. Polzin et al., 1997; Waterman et al., 2013, in the Brazil Basin and the ACC, respectively], glider data [e.g. Johnston et al., 2013], and also observations from Argo floats equipped with Iridium communications, which store and transmit more information than the standard systems [Hennon et al., 2014]. They allow the calculation of TKE dissipation rates as well as internal wave energy fluxes and displacement spectra and hence a more detailed evaluation of IDEMIX since, first, variables other than TKE dissipation rates and energy levels can be compared, and, second, the associated uncertainties are (much) lower than those of the finestructure estimates considered in this study. In consequence, strengths and weaknesses of IDEMIX as well as the differences between various model version can be identified with higher accuracy. Moreover, these comparisons can serve as a means to determine whether measures taken to improve IDEMIX are successful, which is difficult to assess based on the Argo estimates alone due to their high uncertainty.

Such measures promising to improve IDEMIX were identified based on the results presented in Chapter 2, in particular the observation that IDEMIX models mixing hotspots significantly smaller than the Argo-derived equivalents. This suggests on the one hand that the forcing functions and physical processes taken into account in IDEMIX should be described in greater detail, and on the other hand that mechanisms not represented in the parameterization should be included. The implementation of these steps, however, reveals a fundamental challenge of internal gravity wave research: several processes shaping the oceanic internal wave field are too rarely observed and/or not fully understood, which impedes their quantification and representation in parameterizations. This applies for example to the spontaneous generation of internal gravity waves from balanced flows as described in Section 1.1.1 or the choice of the tuning parameter j_*, the modal bandwidth of the GM model, which would be more realistically implemented by defining it as regionally variable but is currently set constant for the lack of a theory combining the existing observations [Polzin and Lvov, 2011]. A possible approach to account for spatial and temporal variations of this tuning parameter could be to solve the spectral energy equation by applying the variational principle [e.g. Stevenson, 1981]: instead of obtaining prognostic equations for the spectrum's total energy content by integrating the radiative transfer equation in frequency and wavenumber space as presently done in IDEMIX [Olbers and Eden, 2013], the total energy and the spectrum's bandwidth as well as their variations could be determined from the fundamental derivatives that result from the minimization condition for the functional representing the spectral energy balance [Erich Becker, personal communication].

Another aspect affected by such knowledge gaps and contributing to the uncertainty of IDEMIX is the wind forcing, as the exact amount of energy transferred to the internal wave field from near-inertial motions in the mixed layer is not well constrained [e.g. Rimac et al., 2013; Alford et al., 2016, see also Section 1.1.1]. These issues call for the synergy of observational, numerical, and analytical studies to deepen our understanding of these processes and to ultimately help to improve internal gravity wave models such as IDEMIX. This holds true for problems related to the theoretical basis of IDEMIX, for example whether the assumption of a GM-like energy spectrum adequately represents oceanic conditions and how the spectral shape modeled in IDEMIX could be adjusted should that not be the case. Similarly, the premises that nonlinear wave-wave interactions symmetrize the wave field with respect to the vertical wavenumber or that the internal wave energy dissipation can be parameterized in terms of the total energy content following McComas and Müller [1981] and Henyey et al. [1986] are not always applicable in the real ocean and, because they are hardly constrained by observations, determining the associated errors as well as when and how to correct for them is not at all straightforward.

In other cases the current state of research is sufficiently advanced to permit adding physical detail to IDEMIX. In this PhD project, one such case, the directional dependence of the internal tide generation (see Chapter 3), was investigated. Linear theory shows that this mechanism depends on the tidal velocity as well as the topographic slopes [Bell, 1975a,b] and consequently changes with direction, just like the barotropic flows and the steepness of the rough seafloor vary in space. Previous studies [e.g. Nycander, 2005; Jayne, 2009; Falahat et al., 2014b] and also IDEMIX, however, consider an average tidal forcing, which is the same in all directions. Since internal tides can propagate over long distances from their generation sites before they break and dissipate their energy [e.g. Olbers, 1983; MacKinnon et al., 2017], an accurate description of this far-field mixing relies on the correct specification of where the internal tide energy is directed. The results from simplified simulations of the North Atlantic show a robust sensitivity of the internal wave energy modeled by IDEMIX to applying a directionally variable tidal forcing instead of a constant one (Section 3.7). Together with the positive assessment of the method in idealized test scenarios presented in Section 3.5, this motivates its application to the global ocean as well as its implementation as the bottom boundary forcing in IDEMIX. The sensitivity experiments discussed in Section 3.7 underline that this should be based on realistic stratification and tidal velocity information and be realized for several internal tide modes, because these aspects influence how efficiently internal tides can be generated at the different topographic obstacles of various scales and geometries that make up the ocean floor. The drawback of this semi-analytical approach is that it is only valid for subcritical topography, that is, for topography whose slopes are less steep than those of the tidal beam, and that coherent interactions between waves are neglected on scales larger than approximately five wavelengths. Similar caveats are associated with existing models of the barotropic energy conversion, so that in conclusion the increased physical detail of the new method presented in Chapter 3 warrants a more accurate description of this internal wave forcing than the current standard in IDEMIX.

Another example is the energy transfer between mesoscale eddies and internal gravity waves, which is only crudely represented in IDEMIX by injecting 20 % of the dissipated eddy energy into the internal wave field at the ocean bottom to account for lee wave generation at rough topography. In this simplified setup, the eddy forcing was shown to significantly alter the modeled TKE dissipation rates and internal wave energy levels in regions of strong mesoscale activity such as the Agulhas retroflection or the ACC (see Section 2.5). This demonstrates the importance of a more realistic parameterization of how mesoscale eddies and internal gravity waves interact. The representation of lee wave generation could be improved by following Nikurashin and Ferrari [2011], who described this energy transfer based on the linear theory developed by Bell [1975a]. The interaction of near-inertial waves and eddies in the upper ocean, however, is currently to little understood to be modeled in great detail in IDEMIX [e.g. Kunze, 1985; Young and Jelloul, 1997; Kawaguchi et al., 2016]. A crude representation analogous to the present one of lee wave generation in IDEMIX could nevertheless serve as a first step to take this mechanism into account and to assess its importance.

Processes that are not considered in the IDEMIX versions analyzed here include the internal wave field's interaction with surface waves [Olbers and Herterich, 1979; Haney and Young, 2017] and with the mean flow [Polzin, 2010]. Both were added in recent updates [Olbers and Eden, 2016, 2017; Eden and Olbers, 2017] and can be taken into consideration in future evaluations. Physical detail could also be added with respect to the mixing efficiency δ: several studies have underlined that this ratio of potential energy increase and kinetic energy dissipation can vary by as much as an order of magnitude depending on the characteristics of the flow, and functional dependencies on characteristic length scales, the Richardson number, or the Reynolds number have been proposed [e.g. Smyth et al., 2001; Peltier and Caulfield, 2003; Ilıcak, 2014, and references therein]. Although an all-embracing theory of how to model the mixing efficiency is still lacking, it would be interesting to replace the global constant $\delta = 0.2$ in IDEMIX by a representation of any of these more detailed functions and assess the influence on the modeled diffusivities.

Any of these suggested improvements should not only be evaluated against fine- or microstructure observations with respect to their influence on TKE dissipation rates and internal wave energy levels, but also with respect to their impact on the mean circulation, regarding climatologically relevant variables such as the oceanic northward heat transport. A similar assessment was performed by Eden et al. [2014] for the basic version of IDEMIX, who found that the volume transport in the bottom overturning cell of the Pacific/Indian Oceans as well as the northward heat transport in the Atlantic Ocean were somewhat improved in the setups modeling an approximately closed energy cycle including IDEMIX and a mesoscale eddy parameterization compared to inconsistent setups neglecting any of the two. This serves as an additional motivation for the improvement of IDEMIX and underlines the main advantage of this mixing module over other formulations implemented in contemporary general circulation models: NEMO [Nucleus for European Modelling of the Ocean, Madec, 2008], the MITgcm [Massachusetts Institute of Technology General Circulation Model, Adcroft et al., 2017], or the software package developed by the CVMix (Community Ocean Vertical Mixing) project [Griffies et al., 2015], for example, comprise a collection of parameterizations of wave-induced mixing processes such as the near-field tidal mixing, a constant internal wave background activity, and mixing related to wave breaking due to convective or shear instability. In some cases this involves regional adjustments—in NEMO, for example, there is a specific treatment of tidally driven mixing in the Indonesian Throughflow region as proposed by Koch-Larrouy et al. [2010]—but all of them treat the different processes in isolation. The internal wave energy budget can therefore not be considered in total and a consistent link between the energy input at large scales and the energy loss at small scales is precluded. By accounting for the global internal wave energy balance, IDEMIX on the other hand overcomes these limitations. This approach is not only justified by the observation that internal gravity waves are a ubiquitous feature of the ocean and forced by global-scale mechanisms, but is also prerequisite for the setup of energetically consistent ocean models. Contrary to most state-of-the-art ocean models, energetically consistent ones do not artificially create and remove energy from the different parameterized dynamical regimes, but connect them in such a way that the ocean's global energy budget is closed up to machine accuracy [Eden et al., 2014]. If climatic conditions very different from the ones we can characterize by means of observations are to be simulated reliably, energy consistency in general circulation models is crucial.

This PhD project demonstrates that IDEMIX well reproduces the internal wave and turbulence fields estimated from Argo observations and thus confirms that it forms a valuable alternative to the heuristic mixing parameterizations currently in use because it provides both a realistic and a more consistent description. As a pivotal element of energetically consistent ocean models, IDEMIX as well as the possible extensions outlined in this section are of interest to a large community of ocean and climate modelers. Naturally, the improvements of IDEMIX should go hand in hand with improvements of the numerical schemes and of the other parameterizations, that is, the representations of small-scale turbulence and mesoscale eddies. Together, these steps contribute to the construction of physically sound and energetically consistent climate models, which is crucial if numerical models are to promote understanding of past, present, and future climate conditions and to form the basis of political action.

5 Appendix

5.1 Topographically generated internal gravity waves

The flow of an ocean current over the rough sea floor generates pressure differences which exert a net horizontal force on the bottom,

$$F = \frac{1}{A} \iint_A p(x, y, z_B, t) \nabla h(x, y) dA, \tag{5.1}$$

where A is the area, p the perturbation pressure, z_B the vertical coordinate at the ocean bottom and h the topographic height [Bell, 1975b]. According to Newton's third law, a balanced state requires an equal and opposite force acting on the ocean, so that Eq. 5.1 essentially describes the momentum removed from the flow and converted into internal gravity waves or eddies [Warner and MacCready, 2014]. These internal gravity waves arise as a small, localized perturbation to the ocean current and can be described by the linearized Boussinesq equations [Olbers et al., 2012]:

$$\frac{\partial u}{\partial t} - fv = -\frac{1}{\rho_0}\frac{\partial p}{\partial x}, \tag{5.2}$$

$$\frac{\partial v}{\partial t} + fu = -\frac{1}{\rho_0}\frac{\partial p}{\partial y}, \tag{5.3}$$

$$\frac{\partial w}{\partial t} = -\frac{1}{\rho_0}\frac{\partial p}{\partial z} - \frac{g}{\rho_0}\rho, \tag{5.4}$$

$$\frac{\partial \rho}{\partial t} = \frac{\rho_0 N^2}{g} w, \tag{5.5}$$

$$\frac{\partial u}{\partial x} + \frac{\partial v}{\partial y} + \frac{\partial w}{\partial z} = 0, \tag{5.6}$$

where $\mathbf{u} = (u, v, w)$, p and ρ are the velocity, pressure and density perturbations associated with the internal gravity waves, ρ_0 is the constant reference density, f the Coriolis frequency, g the acceleration due to gravity and $N = (-g/\rho_0 d\rho_r/dz)^{\frac{1}{2}}$ the buoyancy frequency as a function of the background density $\rho_r(z)$, which characterizes the water column in the absence of wave perturbations. This system of equations can be rewritten in terms of the vertical velocity w as

$$\frac{\partial^2}{\partial t^2}\nabla^2 w + \left(\nabla_H^2 N^2 + f^2 \frac{\partial^2}{\partial z^2}\right) w = 0, \tag{5.7}$$

where ∇^2 is the Laplacian and ∇_H^2 denotes its horizontal component. Considering a solution of the form

$$w = \hat{w} \exp(-i(\mathbf{K} \cdot \mathbf{X} - \omega t), \tag{5.8}$$

where $\mathbf{K} = (k_1, k_2, m)$ is the wavenumber and $\mathbf{X} = (x, y, z)$ the coordinate vector, Eq. 5.7 can be solved for the frequency ω (see also Section 1.1.2).

Assuming a constant stratification in a non-rotating, semi-infinite ocean, Bell [1975a] derived the energy flux into topographically generated internal waves based on the linearized, two-dimensional system of equations similar to the one given above, describing the mean flow as $\mathbf{U} = (U, 0)$ with $U = U_0 \cos(\omega_0 t)$. The vertical boundary conditions are that the energy flux be upward away from the bottom and that there be no flow orthogonal to the bottom at depth z_B:

$$w(z = z_B) = (\mathbf{U} + \mathbf{u}) \cdot \nabla h. \tag{5.9}$$

Neglecting the term $\mathbf{u} \cdot \nabla h$ in the bottom boundary condition 5.9 is in the linearized framework analogous to requiring that the slope of the internal wave rays $\alpha = \sqrt{(N^2 - \omega^2)/(\omega^2 - f^2)} = k/m$ be significantly larger than the slope of the topographic obstacle ∇h that forces their motion [Bell, 1975a]. Balmforth et al. [2002] investigate the behavior of the energy conversion, calculated from the Fourier decomposition of the streamfunction, if these slopes become comparable and their ratio, $\gamma = \nabla h/\alpha$, is increased toward unity. For different idealized topographic shapes (e.g. sinusoids or Gaussian seamounts), they find that the generated internal waves are characterized by steeper gradients as γ is increased, so that even for very weak tidal flow overturns occur that destabilize the internal wave field. The total conversion rate, however, increases smoothly and only moderately compared to the results based on the formula of Bell [1975a], suggesting that the assumption of weak topography with $\gamma \ll 1$ is an able approximation for both gentle and steep slopes [see also Khatiwala, 2003; Nycander, 2006; Garrett and Kunze, 2007, as well as Chapter 3].

Other important non-dimensional parameters are the ratio ω_0/N and the tidal excursion $U_0/(\omega_0 L)$, which is the ratio of the mean flow amplitude U_0/ω_0 to the width of the topographic obstacle L. Depending on their magnitudes, two limiting cases can be identified: the quasi-steady limit for $\omega_0/N \to 0$ and the acoustic limit for $U_0/(\omega_0 L) \ll 1$ [Bell, 1975a]. Quasi-steady motions are similar to static flows in that they generate lee waves, which can propagate away from the ocean bottom if $N > U_0/L > f$; for the latter inequality to be valid, horizontal topographic scales must be rather small, on the order of $\mathcal{O}(1\,\text{km})$, which does not produce a significant energy flux and is moreover too small to be resolved by satellite-based bathymetry data sets [Garrett and Kunze, 2007, and references therein]. Bell [1975b] argues that due to the characteristics of the ocean bathymetry, these lee waves typically have intrinsic frequencies $\omega = U(z)/L$ close to the Coriolis frequency, so that already slight velocity perturbations can result in sub-inertial internal wave frequencies and critical layer absorption—as the wave frequency

ω approaches f, the vertical group velocity tends toward zero and the wave's path becomes horizontal, so that due to the small vertical scales dissipation is likely to occur (see Olbers et al. [2012] and also Section 1.1.2).

The sloshing of the barotropic tide over topographic obstacles at the ocean bottom on the other hand is characterized by a small tidal excursion parameter [the acoustic limit of Bell, 1975a]. Depending on the amplitude of the tidal excursion, internal gravity waves are generated at the fundamental tidal frequency and, as $U_0/(\omega_0 L)$ increases, also at higher harmonics [e.g. Garrett and Kunze, 2007, Fig. 4]. Due to their higher frequencies, these waves are typically not trapped close to the ocean bottom by deep critical layers, and because of the larger horizontal scales of the tidal flow, its interaction with the rough sea floor generally leads to a more efficient generation of internal gravity waves than that of the quasi-steady mean flow [Bell, 1975b; Garrett and Kunze, 2007]. Based on linear theory, Bell [1975a] estimated the conversion into internal tides for zonal topography $h = h(x)$ as

$$C = \rho_0 U_0^2 L N_B \sqrt{1 - \frac{f^2}{\omega_0^2}} \int_0^\infty k\tilde{h}(x)\tilde{h}^*(x)\frac{dk}{2\pi}, \tag{5.10}$$

where $N_B = N(z = z_B)$, the tilde denotes the Fourier transform and the asterisk the complex conjugate (LSY02, see also Section 1.1.1).

Section 3.2 includes a discussion of how this expression of the conversion rate was refined during the past decades to remove some of the assumptions made during its derivation [see e.g. Nycander, 2005, LSY02 for details] and introduces a new method to analytically calculate the horizontal direction of this energy flux. Fig. 5.1 shows this angular dependence for four different types of idealized topographies, based on Eq. 3.23, illustrating how both the topographic shape and the orientation of the tidal flow affect the internal wave generation.

Fig. 5.2 illustrates the influence of using a directionally variable tidal forcing, calculated following the new method presented in Chapter 3, in IDEMIX when the tidal velocity is set to be purely meridional in contrast to the scenario discussed in Section 3.7 (see also Fig. 3.8). Note that not only the total energy conversion but also the difference between resolving and not resolving the horizontal direction of the tidal forcing is strongly enhanced compared to the case of zonal tidal flow (refer to Section 3.7 for details). Fig. 5.3 shows the same comparison but for the mode-4 internal tide and for zonal tidal flow. Because of the relation between the horizontal length scales of the topographic obstacles and the wavenumbers of the generated internal tides [LSY02], the differences between simulations with resolved and unresolved tidal forcing are not the same as for the mode-2 M_2 tide shown in Fig. 3.8, but these variations are rather small in comparison to these differences themselves or to the changes observed when varying the orientation of the tidal ellipse.

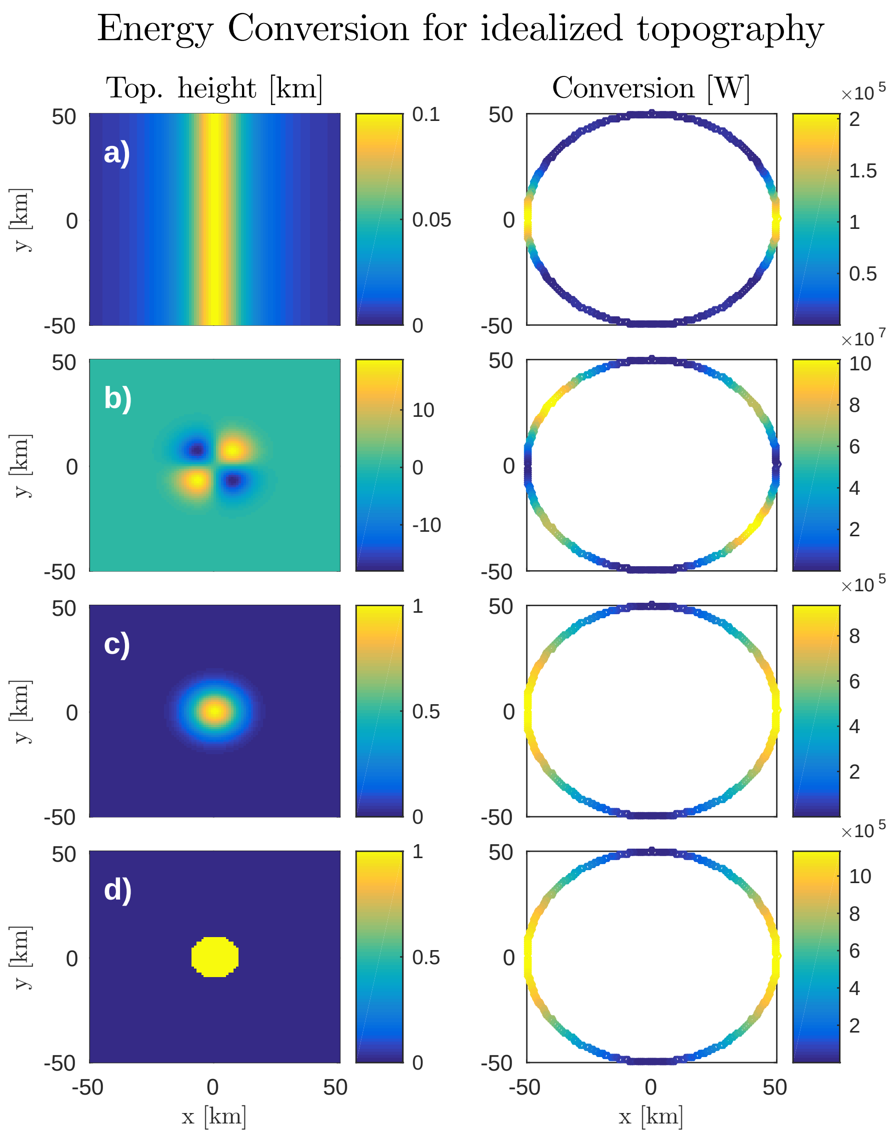

Figure 5.1: The energy flux from barotropic to baroclinic tides for four different types of idealized topography and a zonal background flow, with the left column showing the topographic height and the right column the corresponding energy flux. The energy conversion is calculated following the method detailed in Chapter 3, but considering a single circular patch only that covers the entire domain (the color plots in the right column illustrate the size of this circle). The topographic settings chosen are (a) the Agnesi Witch-profile $h(x) = h_0/(1 + x^2/\Lambda^2)$ with $\Lambda = 10$ km and $h_0 = 0.1$ km, (b) a modified Gaussian with $h(x) = (1 + xy)\exp(-r^2/r_s^2)$, (c) a Gaussian with $h(x) = \exp(-r^2/r_s^2)$ and (d) a top hat with $h(x) = 1$ for $r < r_s$ and $h(x) = 0$ otherwise, all taking $r_s = 10$ km and with $r^2 = x^2 + y^2$. The other parameters are set as in Chapter 3, i.e. $U_0 = 4$ cm s^{-1}, $f = 8 \cdot 10^{-4}$ s^{-1}, $\omega_0 = 1.4 \cdot 10^{-4}$ s^{-1}, $H = 4$ km, $\rho_0 = 1040$ kg m^{-3} and $N = 8 \cdot 10^{-4}$ s^{-1}. Note the different axis scalings.

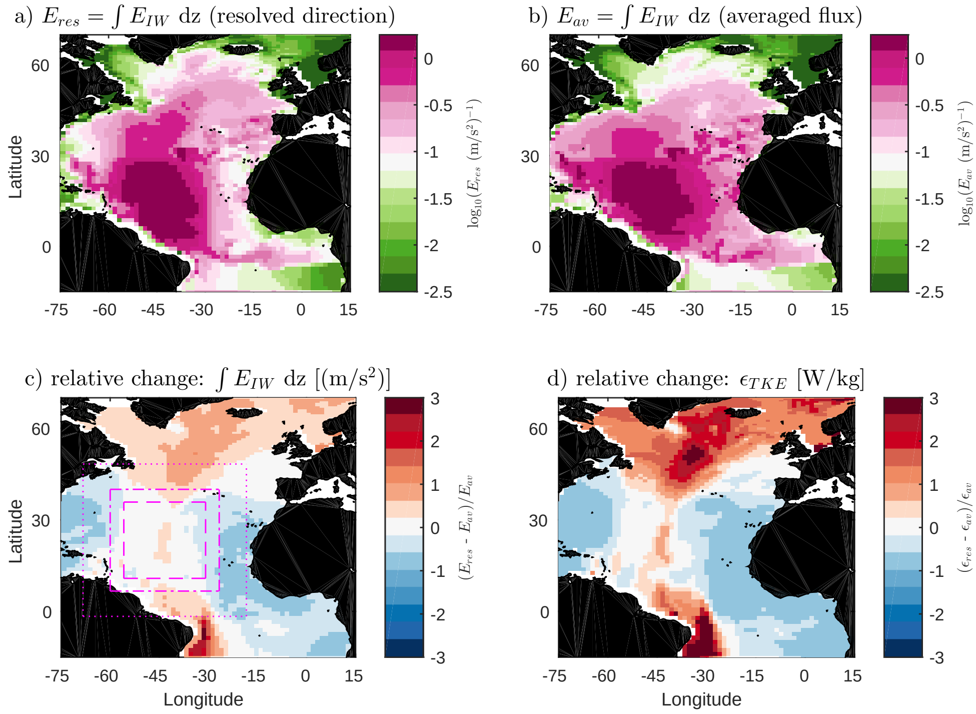

Figure 5.2: As Fig. 3.8 but using a meridional tidal velocity of $\mathbf{U} = (0, 4)$ cm s^{-1}.

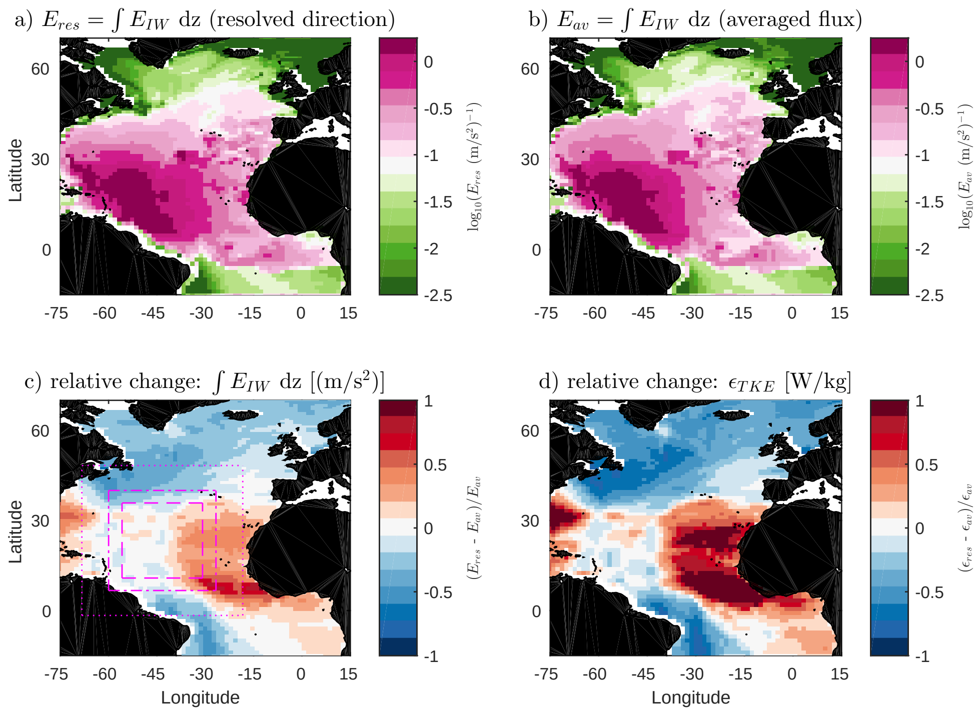

Figure 5.3: As Fig. 3.8 but for the mode-4 M_2 tide.

5.2 Estimating the internal gravity wave energy from strain information

The derivation of internal wave energy from strain ξ_z starts from the eigenvector (polarization vector) representation of an internal gravity wave field [see e.g. Olbers et al., 2012]:

$$\mathbf{\Phi} = \sum_{s=\pm} \sum_{\mathbf{K}} a^s_{\mathbf{K}} \hat{\mathbf{\Phi}}^s_{\mathbf{K}} e^{i(\mathbf{K}\cdot\mathbf{X} - \omega^s_{\mathbf{K}} t)}, \tag{5.11}$$

where $\mathbf{\Phi} = (\mathbf{u}_h, w, p, b, \xi)^T$ is the field vector comprising horizontal velocity $\mathbf{u}_h = (u, v)$, vertical velocity w, pressure p, buoyancy b, and vertical displacement $\xi = \partial w/\partial t = -b/N^2$ (N is the buoyancy frequency). $\mathbf{K} = (\mathbf{k}, m)$ and $\mathbf{X} = (\mathbf{x}, z)$ denote the three-dimensional wavenumber and position vector, respectively, and the notation $s = \pm$ accounts for the complex conjugate with $(a^s_{\mathbf{K}})^* = a^{-s}_{-\mathbf{K}}$, $(\hat{\mathbf{\Phi}}^s_{\mathbf{K}})^* = \hat{\mathbf{\Phi}}^{-s}_{-\mathbf{K}}$ and $\omega^s_{\mathbf{K}} = -\omega^{-s}_{-\mathbf{K}}$ such that $\mathbf{\Phi}$ is real. The quantity $a^s_{\mathbf{K}} = a^s_{\mathbf{K}}(\mathbf{X}, t)$ describes the amplitude of the wave of wavenumber $\mathbf{K}$ at a given position and time, and $\hat{\mathbf{\Phi}}^s_{\mathbf{K}}$ is the polarization vector, describing the relative amplitude of the different variables:

$$\hat{\mathbf{\Phi}}^s_{\mathbf{K}} = \begin{pmatrix} \hat{\mathbf{u}}_h \\ \hat{w} \\ \hat{p} \\ \hat{b} \\ \hat{\xi} \end{pmatrix} = \left(\frac{k^2}{m^2 K^2} \right)^{\frac{1}{2}} \begin{pmatrix} (i\mathbf{k} + f/\omega \underset{\neg}{\mathbf{k}}) m^2/k^2 \\ -im \\ i(N^2 - \omega^2)/\omega \\ -mN^2/\omega \\ m/\omega \end{pmatrix} \tag{5.12}$$

with $\underset{\neg}{\mathbf{k}} = (-k_2, k_1)$, $K = |\mathbf{K}|$, and the Coriolis frequency f. Subscripts and superscripts were omitted for the sake of clarity.

The underlying approach is to treat ocean waves as a statistical phenomenon, describing their motion as a superposition of linear waves of random amplitudes and phases [Hasselmann, 1967; Olbers, 1983]. The evaluation of Eq. 5.11 for a specific set of amplitudes $a^s_{\mathbf{K}}(\mathbf{x}, t)$ can then be interpreted as a particular realization of the statistical ensemble [Olbers et al., 2012]. Far away from reflecting boundaries and if the WKB-approximation holds, i.e. if the internal waves' frequencies and wavenumbers only slowly change, it is reasonable to assume statistic independence of different waves [Olbers, 1983]. The correlation of the wave amplitudes can then be expressed as

$$\langle a^s_{\mathbf{K}}, a^{s'}_{\mathbf{K}'} \rangle = \frac{1}{2} \mathcal{E}(\mathbf{K}) \delta_{s,-s'} \delta(\mathbf{K} + \mathbf{K}'), \tag{5.13}$$

where angle brackets denote an average over an ensemble of realizations, which is equivalent to spatial or temporal averages of measured data if the observed wave field is statistically stationary and homogeneous [Müller and Olbers, 1975]. The interpretation of the function $\mathcal{E}(\mathbf{K}) = \mathcal{E}(\mathbf{K}, \mathbf{X}, t)$ depends on the normalization of the polarization vector. Rewriting Eq. 5.11 using the dispersion relation for internal gravity waves,

$$\omega^2 = \frac{N^2 k^2 + f^2 m^2}{K^2}, \tag{5.14}$$

shows that the normalization used here is oriented at the total mechanical (potential and kinetic) energy:

$$\begin{aligned} &\frac{1}{2}\left(\hat{\mathbf{u}}\hat{\mathbf{u}}^* + \hat{w}\hat{w}^* + N^2\hat{\xi}\hat{\xi}^*\right) \\ =&\frac{1}{2}\left(\left(1+\frac{f^2}{\omega^2}\right)\frac{N^2-\omega^2}{N^2-f^2} + \frac{\omega^2-f^2}{N^2-f^2} + \frac{N^2}{\omega^2}\frac{\omega^2-f^2}{N^2-f^2}\right) \\ =&1. \end{aligned} \tag{5.15}$$

The function $\mathcal{E}$ is hence the local energy spectrum (denoted S_E in Chapter 2), which completely determines the statistical properties of the internal wave field if is approximately Gaussian [valid for homogeneous fields of free dispersive waves, see Hasselmann, 1967]. The energy spectrum is the density in wavenumber space of the local, physical-space energy density $E(\mathbf{X}, t)$:

$$E(\mathbf{X}, t) = \int \mathcal{E}(\mathbf{K}, \mathbf{X}, t) d\mathbf{K}. \tag{5.16}$$

Based on the polarization vector given in Eq. 5.12, relations between the total energy spectrum and the spectrum of different field variables can be expressed:

$$S_\xi(m, \omega) = \frac{1}{\omega^2}\frac{\omega^2-f^2}{N^2-f^2} S_E(m, \omega), \tag{5.17}$$

$$S_{\xi_z}(m, \omega) = m^2 \frac{1}{\omega^2}\frac{\omega^2-f^2}{N^2-f^2} S_E(m, \omega), \tag{5.18}$$

$$S_{\rho'}(m, \omega) = \frac{\rho_0^2}{g^2} N^4 S_{\xi_z}(m, \omega) = \frac{\rho_0^2}{g^2} N^4 \frac{1}{\omega^2}\frac{\omega^2-f^2}{N^2-f^2} S_E(m, \omega), \tag{5.19}$$

where we changed to the notation S_E for the energy spectrum. The quantity $\rho' = \rho - \rho_{\mathtt{fit}}$ is the potential density perturbation, $\rho_{\mathtt{fit}}$ a vertical fit to the data, and $\rho_0 = 1027\,\mathrm{kg\,m^{-3}}$ the constant reference density. The potential density is related to the internal wave strain according to $b = -g\rho'/\rho_0 = -N^2\xi$.

The goal is to calculate the internal wave energy from finescale strain information, which is here given in terms of vertical profiles that are transformed into vertical wavenumber space through Fourier expansion (FFT). By integration over a suitable wavenumber range, the strain variance $\langle \xi_z^2 \rangle$ is obtained (see Section 2.3 for details). Based on Eq. 5.17, the strain variance can be related to the energy spectrum as follows:

$$\langle \xi_z^2 \rangle = \int_{m_1}^{m_2}\int_f^N S_{\xi_z} d\omega dm = \int_{m_1}^{m_2}\int_f^N m^2 \frac{1}{\omega^2}\frac{\omega^2-f^2}{N^2-f^2} S_E(m, \omega) d\omega dm. \tag{5.20}$$

Without any information about how the observed internal wave energy spectrum varies in frequency and wavenumber space, some assumptions need to be made: First, it is assumed that it can be factorized in the same way as the GM model energy spectrum into the total energy density in physical space, which in this case is only a function of z as the Argo profiles are one-dimensional, a frequency-dependent function, and a wavenumber-dependent function. Second, it is assumed that the latter two can be described by the corresponding functions of the GM model:

$$S_E = E(z) A_{GM}(m) B_{GM}(\omega) \tag{5.21}$$

with

$$\begin{aligned} A_{GM}(m) &= \frac{n_A}{1 + \frac{m^2}{m_*^2}} \frac{1}{m_*} \\ B_{GM}(\omega) &= \frac{f}{\omega} \frac{n_B}{\sqrt{\omega^2 - f^2}} \\ n_A &= \left(\arctan\left(\frac{m_h}{m_*}\right) - \arctan\left(\frac{m_l}{m_*}\right) \right)^{-1} \\ n_B &= \frac{2}{\pi} \left(1 - \frac{2}{\pi} \arcsin\left(\frac{f}{N}\right) \right)^{-1} . \end{aligned} \tag{5.22}$$

Here $m_* = N/c_*$ is the vertical wavenumber bandwidth, with

$$c_* = \frac{1}{j_* \pi} \int_{-h}^{0} N(z) dz, \tag{5.23}$$

where h is the water depth and j_* the modal bandwidth. In all experiments described in this thesis, c_* is computed from the global climatology of Gouretski and Koltermann [2004] with $j_* = 10$. The high and low wavenumber cutoffs are denoted by m_h and m_l, respectively, and the expressions of the normalization factors n_A and n_B are chosen such that $\iint S_E \, dm d\omega = E(z)$ (see Chapter 2). In consequence, Eq. 5.20 can be expressed as:

$$\langle \xi_z^2 \rangle = E(z) \int_{m_1}^{m_2} \int_{f}^{N} m^2 \frac{1}{\omega^2} \frac{\omega^2 - f^2}{N^2 - f^2} A_{GM}(m) B_{GM}(\omega) d\omega dm. \tag{5.24}$$

We first deal with the integral over the wavenumber-dependent part, which we denote as C:

$$\begin{aligned} C &= \int_{m_1}^{m_2} \frac{m^2}{m_*} \frac{1}{1 + \frac{m^2}{m_*^2}} dm = \int_{m_1}^{m_2} \frac{m^2 m_*}{m_*^2 + m^2} dm \\ &= m_*(m_2 - m_1) - m_*^2 \left(\arctan\left(\frac{m_2}{m_*}\right) - \arctan\left(\frac{m_1}{m_*}\right) \right) . \end{aligned} \tag{5.25}$$

For the integration of the frequency-dependent part, denoted G, we make use of the following relation [e.g. Bronstein et al., 2012]:

$$\int \frac{\sqrt{X}}{x^3} dx = -\frac{\sqrt{X}}{2x^2} + \frac{1}{2a} \arccos\left(\frac{a}{x}\right) \qquad X = x^2 - a^2. \tag{5.26}$$

This leads to the following expression:

$$\begin{aligned} G &= \int_f^N \frac{f}{\omega^3} \frac{\sqrt{\omega^2 - f^2}}{N^2 - f^2} d\omega \\ &= \frac{f}{N^2 - f^2} \left[-\frac{\sqrt{N^2 - f^2}}{2N^2} + \frac{1}{2f} \arccos\left(\frac{f}{N}\right) \right]. \end{aligned} \tag{5.27}$$

In consequence, the internal wave energy $E(z)$ is related to the strain variance as

$$E(z) = \frac{\langle \xi_z^2 \rangle}{n_A n_B C G}. \tag{5.28}$$

With the GM model energy spectrum $S_E^{GM} = E_{GM} A_{GM}(m) B_{GM}(\omega)$, Eq. 5.28 can also be expressed as

$$E(z) = E_{GM} \frac{\langle \xi_z^2 \rangle}{\langle \xi_{z,GM}^2 \rangle}. \tag{5.29}$$

This procedure can be repeated for other variables. For example, the potential density variance $\langle \rho'^2 \rangle$ can also be calculated from Argo CTD profiles and is linked to the internal wave energy spectrum according to Eq. 5.19. The integral over the wavenumber-dependent part of this expression is given by

$$C_2 = \int_{m_1}^{m_2} \frac{1}{m_*} \frac{1}{1 + \frac{m^2}{m_*^2}} dm = \arctan\left(\frac{m_2}{m_*}\right) - \arctan\left(\frac{m_1}{m_*}\right) \tag{5.30}$$

and the total internal wave energy is estimated as

$$E(z) = \frac{\langle \rho'^2 \rangle}{n_A n_B C_2 G} \frac{g^2}{\rho_0^2 N^4}. \tag{5.31}$$

Older GM model versions involve different wavenumber-functions. The version used e.g. by Whalen et al. [2012] or Kunze et al. [2006b], called “GM75m” in Chapter 2, is a modified version of the GM75 model and characterized by a wavenumber dependence

$$A_{GM75m}(m) = \frac{\hat{n}_A}{\left(1 + \frac{m}{m_*}\right)^2} \frac{1}{m_*} = \frac{\hat{n}_A m_*}{(m + m_*)^2}, \tag{5.32}$$

where $\hat{n}_A$ is the appropriate scaling factor for GM75m. The integrals C and C_2 then become

$$\begin{aligned}
C_{GM75m} &= \int_{m_1}^{m_2} \frac{m^2 m_*}{(m+m_*)^2} dm = \int_{m_1}^{m_2} m_* \left[1 - \frac{2mm_*}{(m+m_*)^2} - \frac{m_*^2}{(m+m_*)^2}\right] dm \\
&= m_* \int_{m_1}^{m_2} 1 dm - m_* \int_{m_1}^{m_2} \frac{2m_*}{m+m_*} dm + m_* \int_{m_1}^{m_2} \frac{m_*^2}{(m+m_*)^2} dm \\
&= m_*(m_2 - m_1) - 2m_*^2 \left(\ln(m_2+m_*) - \ln(m_1+m_*)\right) \\
&\quad - m_*^3 \left(\frac{1}{m_2+m_*} - \frac{1}{m_1+m_*}\right),
\end{aligned} \tag{5.33}$$

$$C_{2,GM75m} = m_* \left(\frac{1}{m_1+m_*} - \frac{1}{m_2+m_*}\right). \tag{5.34}$$

5.3 Quality control of Argo finestructure data

The quality of Argo CTD measurements is controled in two steps: First, a series of automatic tests is run that for example check if the measured values as well as the associated time and location are realistic, if there are spikes or too large gradients in the measurements, or if there is a significant drift in the sensors [see Wong et al., 2015, for details]. In some cases, this already involves a correction of pressure and salinity offsets. If these tests are passed, the data is made available within 24-48 hours after collection (denoted "real-time data"). Second, all data are forwarded to the Global Argo Data Assembly Centers, where they are tested and corrected more thoroughly. These so-called "delayed mode data" are made available about 6-12 months after collection. The difference between these two steps manifests for example in their treatment of large surface pressure variations: In the real-time quality tests, surface pressure offsets of more than ± 20 db are not corrected and profiles fail if such high values are observed for 5 or more consecutive cycles. This is because these automatic tests cannot distinguish between large sensor drifts and measurement errors. At the Global Argo Data Assembly Centers, on the other hand, such profiles can be examined visually and, if the differences indeed represent large sensor drifts, adjusted and retained in the data base [Carval et al., 2014].

In practice, there is yet another step, namely the quality checks performed by the user. For the evaluation of IDEMIX performed in this PhD project, the procedure by Whalen et al. [2012] was followed whenever its details were known. The data base for the model data comparison presented in Chapter 2 comprises all CTD profiles from the years 2006 to 2015, taking the delayed mode or real-time adjusted data (data mode "D" or "A") and only those profiles with a quality flag "A" for all three sensors, i.e. at all vertical levels, temperature, salinity, and pressure measurements pass all real-time quality tests. Temperatures were required to remain between $-10 \leqslant T \leqslant 40°$ C and salinity between $0 \leqslant S \leqslant 45$ psu, but changing these ranges to $5 \leqslant T \leqslant 100°$ C and $5 \leqslant S \leqslant 50$ psu [as used by Whalen et al., 2012, personal communication] led to no differences in average dissipation rates or that of some exemplary single profiles. If the Argo quality and data transfer routines worked fine, these tests are redundant and all data points are in the range of $-2.5 \leqslant T \leqslant 40.0°$ C and $2 \leqslant S \leqslant 41$ psu. Profiles were despiked by first removing all data points that deviated by more than two standard deviations from the vertical mean. Then a new vertical average was computed and all data points were removed that deviated from it by more than ten standard deviations. If in the first step the threshold value was set to three instead of two standard deviations, there was no difference in the number of profiles kept or in the average dissipation rate in the upper Atlantic (i.e. 250-500 m depth), considering only profiles from the year 2006. The same holds true for using 5 or 15 standard deviations instead of 10 in the second step and 2 in the first. Only when taking 20 standard deviations as a threshold value in the second step and changing from 2 to 3 standard deviations in the first, was there any effect on the outcome, albeit a small one: the average dissipation rate in the 250-500 m depth range increased by 0.7 % and the number of estimates in that range by 0.5 % to 10592. The somewhat arbitrary choice of threshold values consequently barely affects the computed dissipation rates and is hence irrelevant for the general evaluation of IDEMIX performed in this study.

In the mixed layer and areas of low stratification, the method's key assumption that all finescale variance can be interpreted as internal waves is typically violated. These areas were removed by applying the variable temperature criterion [de Boyer Montégut et al., 2004] twice (once the mixed layer was removed, its bottom was interpreted as the surface). Starting at the bottom of each profile, these were then divided into half-overlapping segments of 200 m length, discarding profiles with a resolution coarser than 10 m, and calculating for each the buoyancy frequency N^2 based on the adiabatic leveling method as in IOC et al. [2010]. The choice of resolution is a compromise between data quality and quantity: For the 2006 data from the Atlantic Ocean, the number of estimates in the upper, middle and lower depth range (250-500 m, 500-1000 m and 1000-2000 m) is 8824, 8295, and 1124 for a vertical resolution of at most 10 m. These numbers are increased to 15362, 8474, and 1124 for a maximum resolution of 15 m and decreased to 5688, 7822, and 732 for a maximum resolution of 5 m. On the one hand, a higher number of estimates allows for a more reliable statistical analysis of the results (e.g. when computing bootstrapped confidence intervals for the average quantities in each depth range, see Appendix 5.4), but the individual estimates of TKE dissipation rates become on the other hand more uncertain when the number of data points per 200 m segment is decreased. Setting the required minimum resolution to 10 m seems to be a good compromise, also for the comparison of the resultant global maps to those presented in Whalen et al. [2012].

Because of the poor signal-to-noise ratio, profiles with $N^2 < 10^{-9}$ s^{-2} were ignored as well as those for which the variation in N^2 exceeded $6 \cdot 10^{-4}$ s^{-2} (the method's key assumption might again have been violated). Moreover, in each segment the temperature was required to vary by more than 0.2° C and the salinity by more than 0.02 psu in order to actually resolve the finestructure variance. These buoyancy frequency profiles were then used to calculate the TKE dissipation rates as detailed in Chapter 2.

5.4 Geographic and seasonal variation of Argo-derived turbulence variables

The mixing module IDEMIX was mainly evaluated against TKE dissipation rates and internal gravity wave energy levels, focusing on temporal averages over several years. The global Argo data base, however, provides information about other fields as well and is especially valuable because after 15 years of operation, it offers the possibility to investigate their seasonal and shorter-term variation. In this section, some of the global maps that were produced (and considered) for the evaluation of IDEMIX but not shown in the publication re-printed in Chapter 2 are presented.

Figs. 5.4 and 5.5 depict the geographic variation of internal wave energy (computed both from strain and potential density spectra), diffusivity, and buoyancy frequency in the three depth ranges 250-500 m, 500-1000 m, and 1000-2000 m. The number of estimates contributing to the TKE dissipation rate or diffusivity averages for the years 2006-2015 in each bin is shown in Fig. 5.6.

In order to estimate the uncertainty of the TKE dissipation rate, energy level, or diffusivity averages shown in Chapter 2 and in this section, the bootstrap method is applied. It approximates the confidence intervals of an estimator (here, the mean) by replacing the true but unknown distribution function by the empirical distribution function obtained from resampling the original data (with replacement); these converge toward the true confidence intervals for a large number of bootstrap samples [e.g. Efron and Tibshirani, 1986; von Storch and Zwiers, 2001]. Following Whalen et al. [2012], we calculate the 90 %-bootstrap confidence intervals based on 1000 bootstrap samples for each $1.5^\circ \times 1.5^\circ$-bin that contains at least 10 estimates. Figs. 5.7 to 5.9 show the upper and lower confidence intervals for the global averages presented in this and in previous sections.

As already demonstrated by Whalen et al. [2012], the Argo data base allows the investigation not only of the spatial, but also of the temporal variability of wave-induced mixing. Global maps of average TKE dissipation rates for different seasons are presented in Fig. 5.10. In the northwest Pacific, for example, the dissipation rates are consistently higher during the winter months (January through March) than during summer (July through September), in line with the findings of Whalen et al. [2012]. This coincides with a distinct seasonal cycle of near-inertial mixed-layer energy in that area estimated from drifter trajectories by Chaigneau et al. [2008]. For clarification, Fig. 5.11 shows a time series of TKE dissipation rates and upper ocean eddy kinetic energy density (EKE) derived from satellite information[9] for different latitude bands in the area between 150° E and

[9] The altimeter products were produced by Ssalto/Duacs and distributed by Aviso, with support from Cnes (http://www.aviso.altimetry.fr/duacs/)

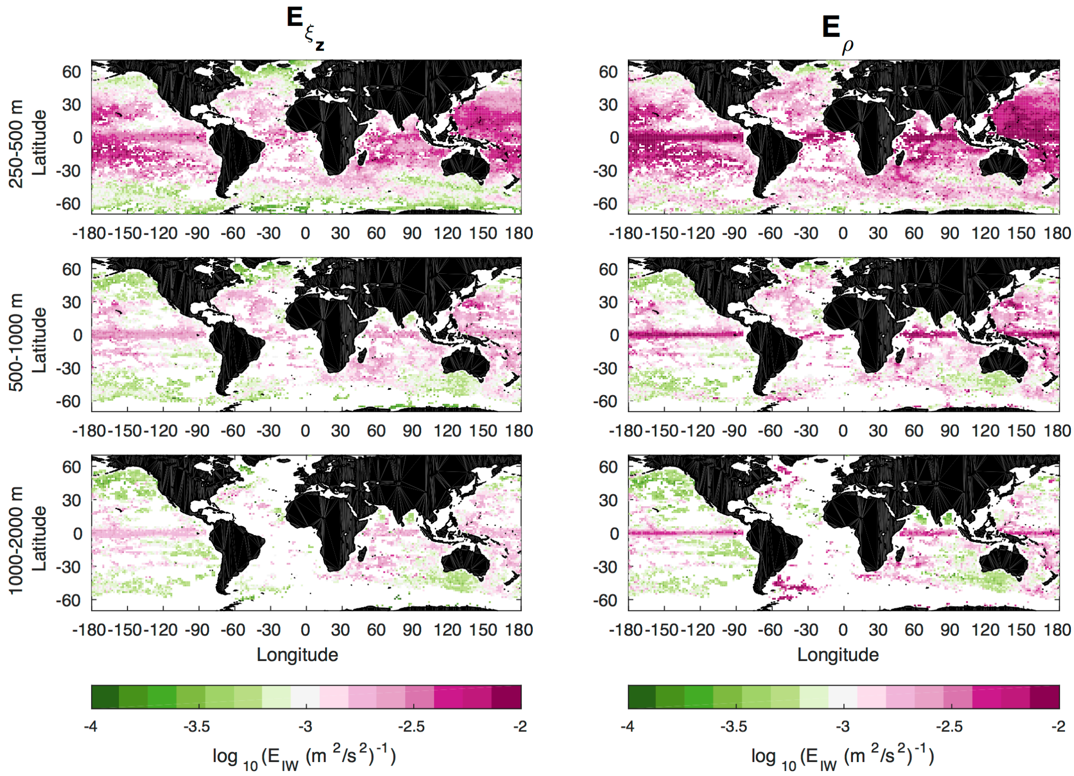

Figure 5.4: Internal gravity wave energy estimated from finestructure spectra of (left) strain and (right) potential density, calculated as detailed in Chapter 2 and Appendix 5.2 for the depth ranges 250-500 m, 500-1000 m, and 1000-2000 m. Results are shown if at least 4 estimates exist in each 1.5° × 1.5°-bin.

180° E. Both exhibit a distinct seasonal cycle in addition to the month-to-month variations, particularly in the latitude band of 39°-45° N. TKE dissipation rates typically peak in winter, with minimum values reached during the summer months. The seasonal variations of EKE are most obvious during later years of the time series, where maxima are observed during late summer and fall and minima during winter. As reviewed by Chang et al. [2002], Pacific storm track intensity, which predominantly forces the inertial currents in the North Pacific [Chaigneau et al., 2008], varies over decadal and interannual scales i.a. in response to the ENSO-cycle[10]. Seasonal variations are induced by the variations of the equator-to-pole temperature gradient and feature a midwinter minimum in the Pacific Ocean, where the upper tropospheric jets can be so strong during winter that the correlation with baroclinic wave activity becomes negative [e.g. Nakamura,

[10]The El Niño-Southern Oscillation is the largest interannual climate signal arising from ocean-atmosphere interactions in the tropical Pacific, characterized by the feedback between sea surface temperature anomalies, trade wind intensities, and ocean currents controling in turn these sea surface temperatures [see e.g. Neelin et al., 1998, and references therein].

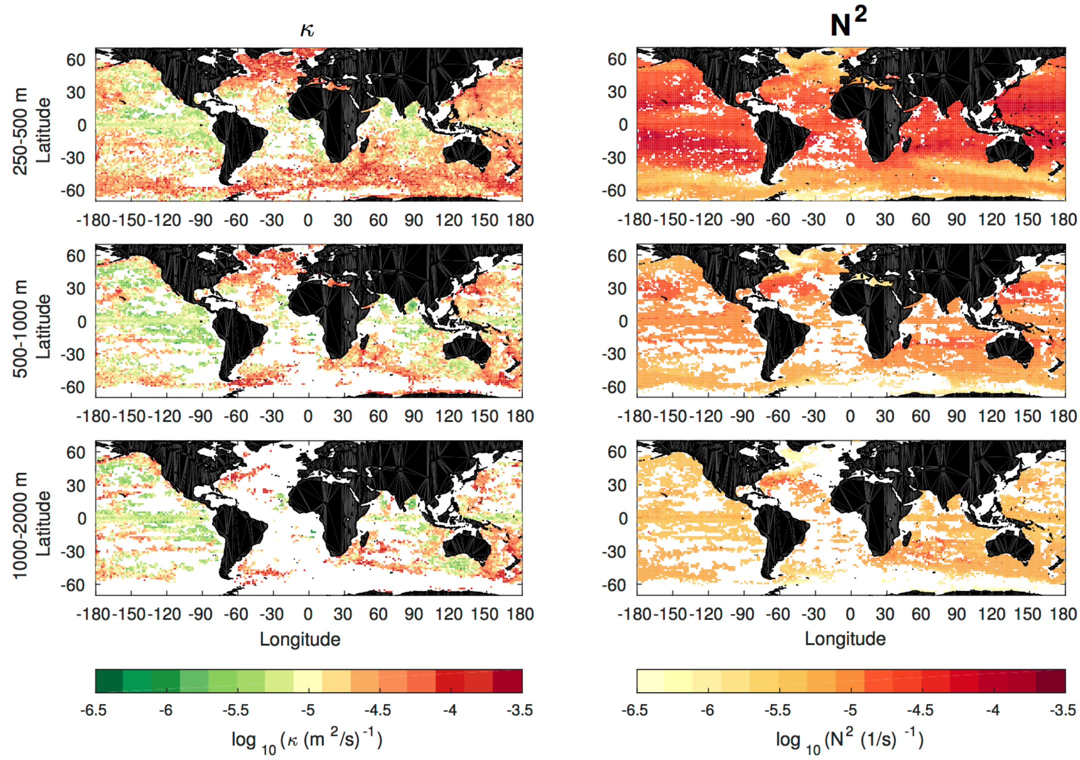

Figure 5.5: (Left) diffusivity κ and (right) buoyancy frequency N^2 estimated or calculated from Argo finestructure data for the depth ranges 250-500 m, 500-1000 m, and 1000-2000 m. Estimates of κ are shown only if at least 4 of these exist per $1.5^\circ \times 1.5^\circ$-bin.

1992; Chaigneau et al., 2008]. In the latitude band of 39°-45° N, there is a 3-4 month lag between the maxima of EKE and TKE dissipation rate. This is much longer than the approximately 20 days required by the storm-generated near-inertial currents observed by D'Asaro et al. [1995] to penetrate through the mixed laxer to a depth of 150 m (the TKE dissipation rate time series shown in Fig. 5.11 consists of averages from a depth of 300-400 m), but nevertheless suggests a relation between mesoscale eddy activity and internal gravity wave-induced mixing.

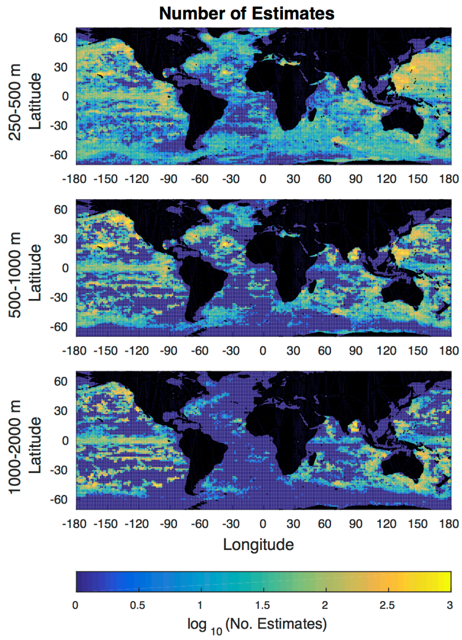

Figure 5.6: The number of TKE dissipation rate estimates in each $1.5° \times 1.5°$-bin derived from Argo data from the years 2006-2015, subject to the processing described in Chapter 2 and in Appendix 5.3.

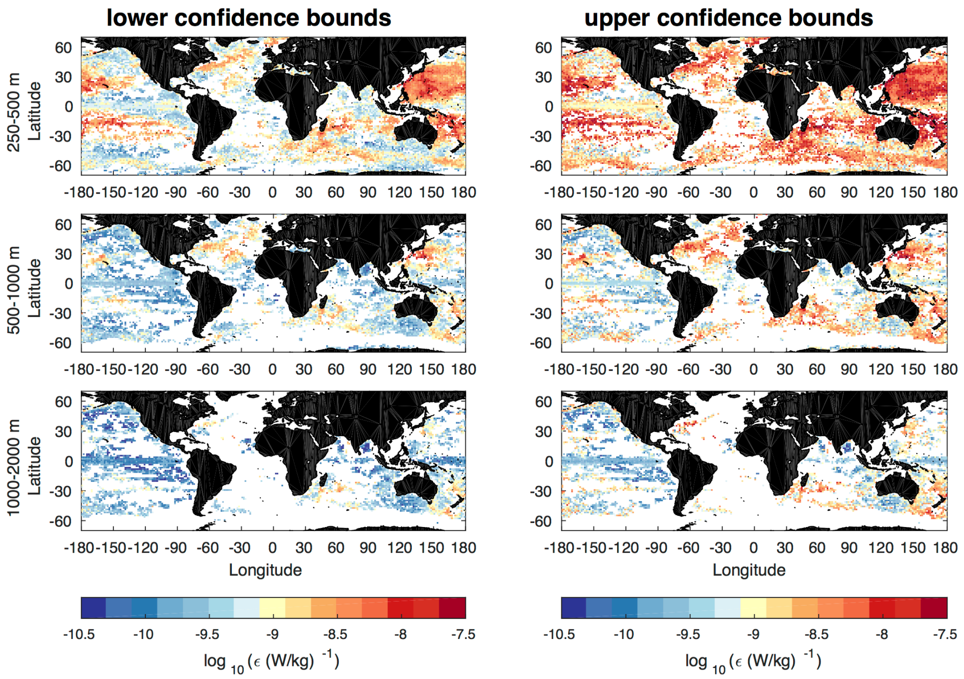

Figure 5.7: (Left) lower and (right) upper 90 %-bootstrap confidence intervals for TKE dissipation rates at 250-500 m, 500-1000 m, and 1000-2000 m depth.

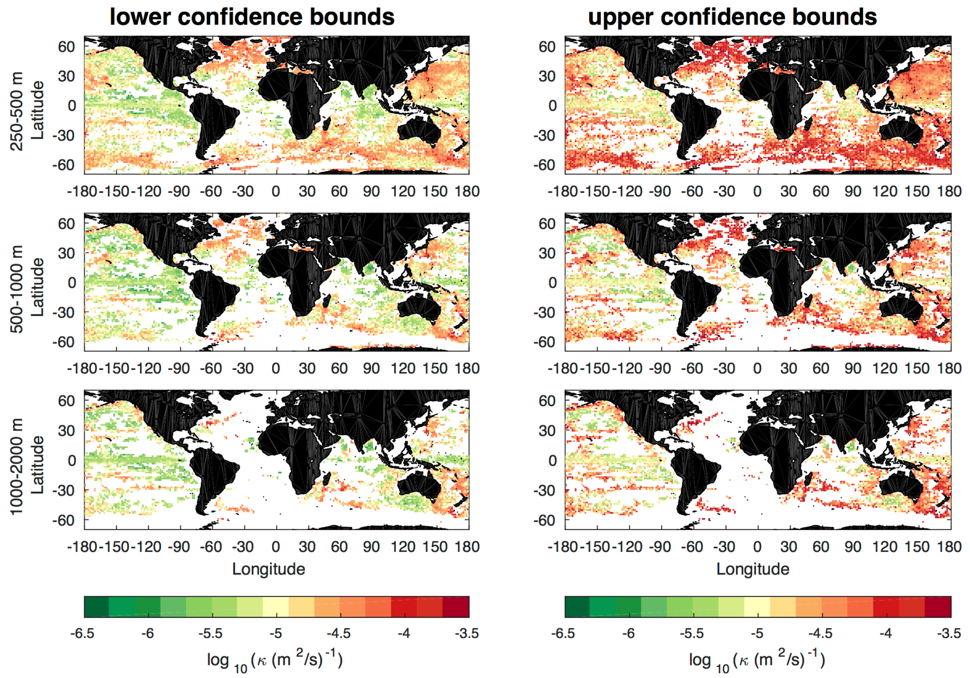

Figure 5.8: As in Fig. 5.7 but for diffusivity.

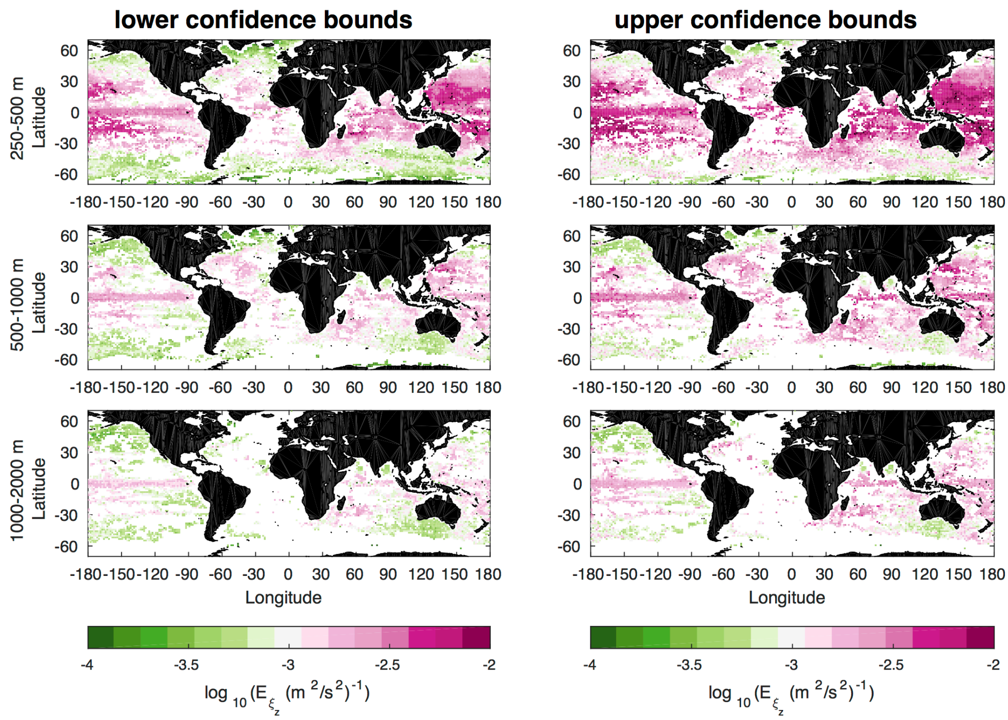

Figure 5.9: As in Fig. 5.7 but for internal gravity wave energy estimated from strain data.

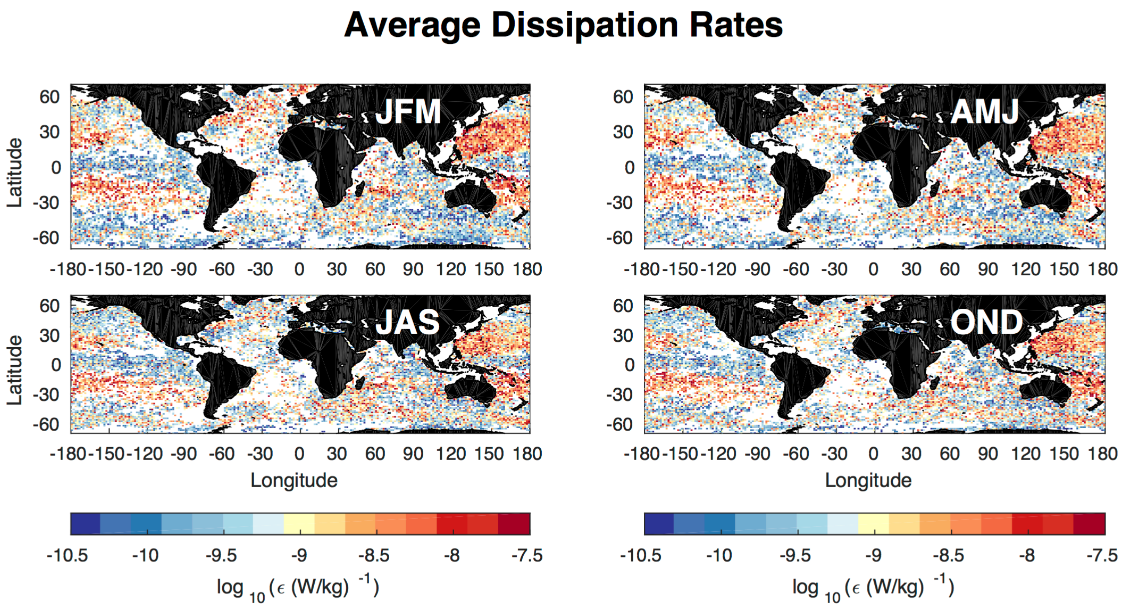

Figure 5.10: Seasonal variations of TKE dissipation rates at 250-500 m depth for January through March (JFM), April through June (AMJ), July through September (JAS), and October through December (OND).

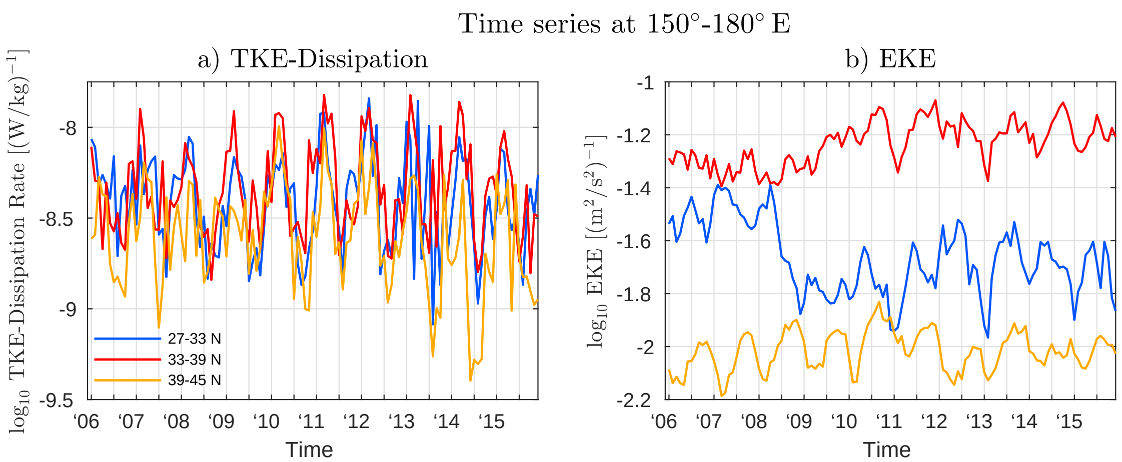

Figure 5.11: Timeseries of (a) TKE dissipation rate estimates at 300-400 m depth derived from Argo finestructure profiles and (b) eddy kinetic energy derived from sea-surface current anomalies (Aviso-altimetry products) in the northwest Pacific (150°-180° E) in three different latitude bands, revealing a distinct seasonal cycle. The x-axis labels characterize the month of January of the respective year.

Acknowledgements

First and foremost I would like to express my sincere gratitude toward my supervisors, Prof. Dr. Carsten Eden and Prof. Dr. Dirk Olbers, for giving me the possibility to realize this PhD project and for their support and guidance during these past three years. Thank you, Carsten, for letting me try out things on my own and for putting me on the right track whenever that did not lead to the desired outcome. And thank you, Dirk, for being available so often to patiently answer my questions. I am also very grateful to Prof. Dr. Jonas Nycander for offering to collaborate during the last year of my PhD time and for generously sharing his ideas and his experience.

Many thanks go to Prof. Dr. Johanna Baehr for serving as my panel chair and for interesting book recommendations and helpful advice, during and in between panel meetings. I am also much indebted to Dr. Fabien Roquet, not only for suggesting that I apply at the Institut für Meereskunde here in Hamburg, but also for his catching enthusiasm for oceanography and his continued interest after I had finished my master's thesis. Special thanks go to Dr. Caitlin Whalen and Prof. Dr. Eric Kunze for helpful comments and insightful discussions on the finestructure method, and to Dr. Jin-Song von Storch for offering advice on statistical issues.

I gratefully acknowledge financial support through the Cluster of Excellence cliSAP (EXC177), funded by the German Research Foundation (DFG), as well as the opportunities offered by the School of Integrated Climate System Sciences to participate in different courses and to meet PhD students from a variety of disciplines.

I would like to thank everyone on the fourth floor and in my working group for contributing to the friendly and collegial atmosphere, especially my fellow Phd students Philipp, Manita, and Rachael. Thank you, Nils, for answering so many questions and for freely giving advice; especially during the first and last stages of my PhD project, I benefitted a lot from your recommendations! And thank you, Jana, for sharing the ups and downs of Phd life—or for offering distractions from them—during countless lunch and coffee breaks. Special thanks also go to Philipp and my father for double-checking some of my calculations and to Tessa for proofreading.

I owe my deepest gratitude to my family and friends, in particular my parents, my sisters, and my partner, for their love and encouragement. I feel incredibly lucky to have received all your support!

List of Publications

Pollmann, F., Eden, C. and Olbers, D., 2017: Evaluating the Global Internal Wave Model IDEMIX Using Finestructure Methods, *J. Phys. Oceanogr.*, DOI: 10.1175/JPO-D-16-0204.1, in press.

Pollmann, F., Nycander, J., Eden, C. and Olbers, D., 2017: Resolving the horizontal direction of internal tide generation. In preparation for submission.

List of Figures

List of Tables

Bibliography

Abernathey, R., Ferreira, D., and Klocker, A. (2013). Diagnostics of isopycnal mixing in a circumpolar channel. *Ocean Model.*, 72:1–16.

Adcroft, A., Campin, J.-M., Dutkiewicz, S., Evangelinos, C., Ferreira, D., Forget, G., Fox-Kemper, B., Heimbach, P., Hill, C., Hill, E., Hill, H., Jahn, O., Losch, M., Marshall, J., Maze, G., Menemenlis, D., and Molod, A. (August 9, 2017). MITGCM User Manual. Technical report, MIT Department of EAPS, Cambridge, MA.

Alford, M. H. (2001). Internal swell generation: The spatial distribution of energy flux from the wind to mixed layer near-inertial motions. *J. Phys. Oceanogr.*, 31(8):2359–2368.

Alford, M. H. (2003). Redistribution of energy available for ocean mixing by long-range propagation of internal waves. *Nature*, 423(6936):159–162.

Alford, M. H., Cronin, M. F., and Klymak, J. M. (2012). Annual cycle and depth penetration of wind-generated near-inertial internal waves at Ocean Station Papa in the northeast Pacific. *J. Phys. Oceanogr.*, 42(6):889–909.

Alford, M. H., MacKinnon, J. A., Simmons, H. L., and Nash, J. D. (2016). Near-inertial internal gravity waves in the ocean. *Annu. Rev. Marine Science*, 8:95–123.

Alford, M. H., Shcherbina, A. Y., and Gregg, M. C. (2013). Observations of near-inertial internal gravity waves radiating from a frontal jet. *J. Phys. Oceanogr.*, 43(6):1225–1239.

Alford, M. H. and Whitmont, M. (2007). Seasonal and spatial variability of near-inertial kinetic energy from historical moored velocity records. *J. Phys. Oceanogr.*, 37(8):2022–2037.

Althaus, A. M., Kunze, E., and Sanford, T. B. (2003). Internal tide radiation from Mendocino Escarpment. *J. Phys. Oceanogr.*, 33(7):1510–1527.

Baddour, N. (2009). Operational and convolution properties of two-dimensional Fourier transforms in polar coordinates. *JOSA A*, 26(8):1767–1777.

Baines, P. G. (1973). The generation of internal tides by flat-bump topography. *Deep-Sea Res. Oceanogr. Abstr.*, 20(2):179–205.

Balmforth, N. J., Ierley, G. R., and Young, W. R. (2002). Tidal conversion by subcritical topography. *J. Phys. Oceanogr.*, 32(10):2900–2914.

Balmforth, N. J. and Peacock, T. (2009). Tidal conversion by supercritical topography. *J. Phys. Oceanogr.*, 39(8):1965–1974.

Becker, J. J., Sandwell, D. T., Smith, W. H. F., Braud, J., Binder, B., Depner, J. l., Fabre, D., Factor, J., Ingalls, S., Kim, S. H., et al. (2009). Global bathymetry and elevation data at 30 arc seconds resolution: SRTM30_PLUS. *Marine Geodesy*, 32(4):355–371.

Bell, T. H. (1975a). Lee waves in stratified flows with simple harmonic time dependence. *J. Fluid Mech.*, 67(04):705–722.

Bell, T. H. (1975b). Topographically generated internal waves in the open ocean. *J. Geophys. Res.*, 80(3):320–327.

Blanke, B. and Delecluse, P. (1993). Variability of the tropical Atlantic Ocean simulated by a general circulation model with two different mixed-layer physics. *J. Phys. Oceanogr.*, 23(7):1363–1388.

Boyer, T. P., Antonov, J. I., Baranova, O. K., Garcia, H. E., Johnson, D. R., Locarnini, R. A., Mishonov, A. V., O'Brien, T. D., Seidov, D., Smolyar, I. V., and Zweng, M. M. (2009). World Ocean Database 2009. In Levitus, S., editor, *NOAA Atlas NESDIS 66*, page 216 pp. U.S. Gov. Printing Office, Wash., D.C.

Briscoe, M. G. (1977). Gaussianity of internal waves. *J. Geophys. Res.*, 82(15):2117–2126.

Bronstein, I. N., Hromkovic, J., Luderer, B., Schwarz, H.-R., Blath, J., Schied, A., Dempe, S., Wanka, G., Gottwald, S., Zeidler, E., et al. (2012). *Taschenbuch der Mathematik*, volume 1. Springer-Verlag Berlin Heidelberg.

Brüggemann, N. and Eden, C. (2015). Routes to dissipation under different dynamical conditions. *J. Phys. Oceanogr.*, 45(8):2149–2168.

Bryan, K. and Lewis, L. J. (1979). A water mass model of the world ocean. *J. Geophys. Res.-Oceans*, 84(C5):2503–2517.

Burchard, H. (2002). Energy-conserving discretisation of turbulent shear and buoyancy production. *Ocean Model.*, 4(3):347–361.

Cairns, J. L. and Williams, G. O. (1976). Internal wave observations from a midwater float, 2. *J. Geophys. Res.*, 81(12):1943–1950.

Capet, X., McWilliams, J. C., Molemaker, M. J., and Shchepetkin, A. F. (2008). Mesoscale to submesoscale transition in the California Current System. Part II: Frontal processes. *J. Phys. Oceanogr.*, 38(1):44–64.

Carval, T., Keeley, R., Takatsuki, Y., Yoshida, T., Loch, S., Schmid, C., Goldsmith, R., Wong, A. P. S., McCreadie, R., Thresher, A., and Tran, A. (2014). *Argo User's Manual.* http://dx.doi.org/10.13155/29825.

Chaigneau, A., Pizarro, O., and Rojas, W. (2008). Global climatology of near-inertial current characteristics from Lagrangian observations. *Geophys. Res. Letters*, 35(13).

Chang, E. K. M., Lee, S., and Swanson, K. L. (2002). Storm track dynamics. *J. Climate*, 15(16):2163–2183.

Chassignet, E. P. and Marshall, D. P. (2008). Gulf Stream separation in numerical ocean models. *Ocean Modeling in an Eddying Regime*, pages 39–61.

Chelton, D. B., Deszoeke, R. A., Schlax, M. G., El Naggar, K., and Siwertz, N. (1998). Geographical variability of the first baroclinic Rossby radius of deformation. *J. Phys. Oceanogr.*, 28(3):433–460.

Chou, S. H., Luther, D. S., Guiles, M. D., Carter, G. S., and Decloedt, T. (2014). An empirical investigation of nonlinear energy transfer from the M2 internal tide to diurnal wave motions in the Kauai Channel, Hawaii. *Geophys. Res. Letters*, 41(2):505–512.

Chouksey, M., Eden, C., and Brüggemann, N. (2017). Fast gravity waves and how to find them. *J. Phys. Oceanogr., submitted.*

Comte-Bellot, G. (1976). Hot-wire anemometry. *Annu. Rev. Fluid Mech.*, 8(1):209–231.

Crawford, G. B. and Large, W. G. (1996). A numerical investigation of resonant inertial response of the ocean to wind forcing. *J. Phys. Oceanogr.*, 26(6):873–891.

Cummins, P. F., Holloway, G., and Gargett, E. (1990). Sensitivity of the GFDL ocean general circulation model to a parameterization of vertical diffusion. *J. Phys. Oceanogr.*, 20(6):817–830.

Cummins, P. F. and Oey, L.-Y. (1997). Simulation of barotropic and baroclinic tides off northern British Columbia. *J. Phys. Oceanogr.*, 27(5):762–781.

D'Asaro, E. A. (1985). The energy flux from the wind to near-inertial motions in the surface mixed layer. *J. Phys. Oceanogr.*, 15(8):1043–1059.

D'asaro, E. A. (1995a). Upper-ocean inertial currents forced by a strong storm. Part II: Modeling. *J. Phys. Oceanogr.*, 25(11):2937–2952.

D'asaro, E. A. (1995b). Upper-ocean inertial currents forced by a strong storm. Part III: Interaction of inertial currents and mesoscale eddies. *J. Phys. Oceanogr.*, 25(11):2953–2958.

D'Asaro, E. A., Eriksen, C. C., Levine, M. D., Paulson, C. A., Niiler, P., and Van Meurs, P. (1995). Upper-ocean inertial currents forced by a strong storm. Part I: Data and comparisons with linear theory. *J. Phys. Oceanogr.*, 25(11):2909–2936.

de Boyer Montégut, C., Madec, G., Fischer, A. S., Lazar, A., and Iudicone, D. (2004). Mixed layer depth over the global ocean: an examination of profile data and a profile-based climatology. *J. Geophys. Res.-Oceans*, 109(C12).

de Lavergne, C., Madec, G., Le Sommer, J., Nurser, A. J. G., and Naveira Garabato, A. C. (2016). On the consumption of Antarctic Bottom Water in the abyssal ocean. *J. Phys. Oceanogr.*, 46(2):635–661.

Denissenkov, P. A., Pinsonneault, M., and MacGregor, K. B. (2008). What prevents internal gravity waves from disturbing the solar uniform rotation? *Astrophys. J.*, 684(1):757.

Desaubies, Y. and Smith, W. K. (1982). Statistics of Richardson number and instability in oceanic internal waves. *J. Phys. Oceanogr.*, 12(11):1245–1259.

Dewey, R. and Stegen, G. (1999). The dispersion of CO2 in the ocean: consequences of basin-scale variations in turbulence levels. In Eliasson, B., Riemer, P., and Wokaun, A., editors, *Greenhouse Gas Control Technologies*. Elsevier Science Ltd, 1 edition.

Dhanak, M. R. and Xiros, N. I. (2016). *Springer Handbook of Ocean Engineering*. Springer International Publishing.

Echeverri, P. (2009). Internal tide generation by tall ocean ridges. dissertation, Woods Hole Oceanographic Institution.

Eden, C. (2015). Revisiting the energetics of the ocean in Boussinesq approximation. *J. Phys. Oceanogr.*, 45(3):630–637.

Eden, C. (2016). Closing the energy cycle in an ocean model. *Ocean Model.*, 101:30–42.

Eden, C., Czeschel, L., and Olbers, D. (2014). Toward energetically consistent ocean models. *J. Phys. Oceanogr.*, 44(12):3160–3184.

Eden, C. and Greatbatch, R. J. (2008). Towards a mesoscale eddy closure. *Ocean Model.*, 20(3):223–239.

Eden, C. and Olbers, D. (2014). An energy compartment model for propagation, nonlinear interaction and dissipation of internal gravity waves. *J. Phys. Oceanogr.*, 44(8):2093–2106.

Eden, C. and Olbers, D. (2017). A closure for internal wave-mean flow interaction. Part B: Wave drag. *J. Phys. Oceanogr.*, 47.

Efron, B. and Tibshirani, R. (1986). Bootstrap methods for standard errors, confidence intervals, and other measures of statistical accuracy. *Stat. Sci.*, pages 54–75.

Egbert, G. D. and Ray, R. D. (2000). Significant dissipation of tidal energy in the deep ocean inferred from satellite altimeter data. *Nature*, 405(6788):775–778.

Egbert, G. D. and Ray, R. D. (2001). Estimates of M2 tidal energy dissipation from TOPEX/Poseidon altimeter data. *J. Geophys. Res.-Oceans*, 106(C10):22475–22502.

Egbert, G. D., Ray, R. D., and Bills, B. G. (2004). Numerical modeling of the global semidiurnal tide in the present day and in the last glacial maximum. *J. Geophys. Res.-Oceans*, 109(C3).

Eriksen, C. C. (1982). Observations of internal wave reflection off sloping bottoms. *J. Geophys. Res.-Oceans*, 87(C1):525–538.

Estrada, M. and Berdalet, E. (1997). Phytoplankton in a turbulent world. *Sci. Mar.*, 61:125–140.

Falahat, S., Nycander, J., Roquet, F., Thurnherr, A. M., and Hibiya, T. (2014a). Comparison of calculated energy flux of internal tides with microstructure measurements. *Tellus*, 66.

Falahat, S., Nycander, J., Roquet, F., and Zarroug, M. (2014b). Global calculation of tidal energy conversion into vertical normal modes. *J. Phys. Oceanogr.*, 44(12):3225–3244.

Ferron, B., Mercier, H., Speer, K., Gargett, A. E., and Polzin, K. L. (1998). Mixing in the Romanche fracture zone. *J. Phys. Oceanogr.*, 28(10):1929–1945.

Fischer, H. B., List, J. E., Koh, C. R., Imberger, J., and Brooks, N. H. (1979). *Mixing in inland and coastal waters*. Academic Press.

Fleury, M. and Lueck, R. G. (1994). Direct heat flux estimates using a towed vehicle. *J. Phys. Oceanogr.*, 24(4):801–818.

Ford, R. (1994). Gravity wave radiation from vortex trains in rotating shallow water. *J. Fluid Mech.*, 281:81–118.

Frants, M., Damerell, G. M., Gille, S. T., Heywood, K. J., MacKinnon, J. A., and Sprintall, J. (2013). An assessment of density-based finescale methods for estimating diapycnal diffusivity in the Southern Ocean. *J. Atm. Ocean. Techn.*, 30(11):2647–2661.

Fuller, J., Lecoanet, D., Cantiello, M., and Brown, B. (2014). Angular momentum transport via internal gravity waves in evolving stars. *Astrophys. J.*, 796(1):17.

Furuichi, N., Hibiya, T., and Niwa, Y. (2005). Bispectral analysis of energy transfer within the two-dimensional oceanic internal wave field. *J. Phys. Oceanogr.*, 35(11):2104–2109.

Furuichi, N., Hibiya, T., and Niwa, Y. (2008). Model-predicted distribution of wind-induced internal wave energy in the world's oceans. *J. Geophys. Res.-Oceans*, 113(C9).

Gad-el Hak, M. (2006). *Flow control: passive, active, and reactive flow management*. Cambridge University Press.

Gargett, A. E. (1984). Vertical eddy diffusivity in the ocean interior. *J. Mar. Res.*, 42(2):359–393.

Gargett, A. E. (1986). Small-scale parameterization in large-scale ocean models. In *Advanced Physical Oceanographic Numerical Modelling*, pages 145–154. Springer International Publishing.

Gargett, A. E. (1989). Ocean turbulence. *Annu. Rev. Fluid Mech.*, 21(1):419–451.

Gargett, A. E. (1990). Do we really know how to scale the turbulent kinetic energy dissipation rate ε due to breaking of oceanic internal waves? *J. Geophys. Res.-Oceans*, 95(C9):15971–15974.

Gargett, A. E. and Garner, T. (2008). Determining Thorpe scales from ship-lowered CTD density profiles. *J. Atm. Ocean. Techn.*, 25(9):1657–1670.

Gargett, A. E. and Moum, J. N. (1995). Mixing efficiencies in turbulent tidal fronts: Results from direct and indirect measurements of density flux. *J. Phys. Oceanogr.*, 25(11):2583–2608.

Garrett, C. J. R. and Kunze, E. (2007). Internal tide generation in the deep ocean. *Annu. Rev. Fluid Mech.*, 39:57–87.

Garrett, C. J. R. and Munk, W. H. (1972a). Oceanic mixing by breaking internal waves. *Deep-Sea Res. Oceanogr. Abstr.*, 19(12):823–832.

Garrett, C. J. R. and Munk, W. H. (1972b). Space-time scales of internal waves. *Geophys. Astro. Fluid*, 3(1):225–264.

Garrett, C. J. R. and Munk, W. H. (1975). Space-time scales of internal waves: A progress report. *J. Geophys. Res.*, 80(3):291–297.

Garrett, C. J. R. and Munk, W. H. (1979). Internal waves in the ocean. *Annu. Rev. Fluid Mech.*, 11(1):339–369.

Garrett, C. J. R. and St. Laurent, L. C. (2002). Aspects of deep ocean mixing. *J. Phys. Oceanogr.*, 58(1):11–24.

Gaspar, P., Grégoris, Y., and Lefevre, J.-M. (1990). A simple eddy kinetic energy model for simulations of the oceanic vertical mixing: Tests at station Papa and Long-Term Upper Ocean Study site. *J. Geophys. Res.-Oceans*, 95(C9):16179–16193.

Gent, P. C. and McWilliams, J. C. (1990). Isopycnal mixing in ocean circulation models. *J. Phys. Oceanogr.*, 20(1):150–155.

Getzlaff, J., Nurser, G., and Oschlies, A. (2010). Diagnostics of diapycnal diffusivity in z-level ocean models part I: 1-Dimensional case studies. *Ocean Model.*, 35(3):173–186.

Gill, A. E. (1984). On the behavior of internal waves in the wakes of storms. *J. Phys. Oceanogr.*, 14(7):1129–1151.

Gould, J., Roemmich, D., Wijffels, S., Freeland, H., Ignaszewsky, M., Jianping, X., Pouliquen, S., Desaubies, Y., Send, U., Radhakrishnan, K., et al. (2004). Argo profiling floats bring new era of in situ ocean observations. *Eos Trans. AGU*, 85(19):185–191.

Gouretski, V. and Koltermann, K. P. (2004). WOCE global hydrographic climatology. *Berichte des BSH*, 35:1–52.

Grant, H. L., Moilliet, A., and Stewart, R. W. (1959). A spectrum of turbulence at very high Reynolds number. *Nature*, 184(4689):808–810.

Green, J. A. M. and Nycander, J. (2013). A comparison of tidal conversion parameterizations for tidal models. *J. Phys. Oceanogr.*, 43(1):104–119.

Greene, A. D., Hendricks, P. J., and Gregg, M. C. (2015). Using an ADCP to estimate turbulent kinetic energy dissipation rate in sheltered coastal waters. *J. Atm. Ocean. Techn.*, 32(2):318–333.

Gregg, M. C. (1989). Scaling Turbulent Dissipation in the Thermocline. *J. Geophys. Res.*, 94(C7):9686–9698.

Gregg, M. C. and Kunze, E. (1991). Shear and strain in Santa Monica basin. *J. Geophys. Res.-Oceans*, 96(C9):16709–16719.

Gregg, M. C., Nodland, W., Aagaard, E., and Hirt, D. (1982). Use of a fiber-optic cable with a free-fall microstructure profiler. In *OCEANS 82*, pages 260–265. IEEE.

Gregg, M. C., Sanford, T. B., and Winkel, D. P. (2003). Reduced mixing from the breaking of internal waves in equatorial waters. *Nature*, 422(6931):513–515.

Griffies, S. M., Levy, M., Adcroft, A. J., Danabasoglu, G., Hallberg, R. W., Jacobsen, D., Large, W., and Ringler, T. (Draft from March 9, 2015). Theory and Numerics of the Community Ocean Vertical Mixing (CVMix) Project. Technical report, Geophysical Fluid Dynamics Laboratory, Princeton University.

Griffies, S. M., Pacanowski, R. C., and Hallberg, R. W. (2000). Spurious diapycnal mixing associated with advection in a z-coordinate ocean model. *Mon. Wea. Rev.*, 128(3):538–564.

Hall, M. M. and Bryden, H. L. (1982). Direct estimates and mechanisms of ocean heat transport. *Deep-Sea Res. Pt. I*, 29(3):339–359.

Haney, S. and Young, W. R. (2017). Radiation of internal waves from groups of surface gravity waves. *J. Fluid Mech., submitted.*

Hasselmann, K. (1962). On the non-linear energy transfer in a gravity-wave spectrum Part 1. General theory. *J. Fluid Mech.*, 12(4):481–500.

Hasselmann, K. (1967). Weak-interaction theory of ocean waves. In *Basic Developments in Fluid Dynamics*, volume 2, pages 117–182. M. Holt Ed., Academic Press.

Hennon, T. D., Riser, S. C., and Alford, M. H. (2014). Observations of internal gravity waves by Argo floats. *J. Phys. Oceanogr.*, 44(9):2370–2386.

Henyey, F. S., Wright, J., and Flatté, S. M. (1986). Energy and action flow through the internal wave field: An eikonal approach. *J. Geophys. Res.-Oceans*, 91(C7):8487–8495.

Hibiya, T., Nagasawa, M., and Niwa, Y. (2002). Nonlinear energy transfer within the oceanic internal wave spectrum at mid and high latitudes. *J. Geophys. Res.-Oceans*, 107(C11).

Hill, C., Ferreira, D., Campin, J.-M., Marshall, J., Abernathey, R., and Barrier, N. (2012). Controlling spurious diapycnal mixing in eddy-resolving height-coordinate ocean models—Insights from virtual deliberate tracer release experiments. *Ocean Model.*, 45:14–26.

Hogg, N., Biscaye, P., Gardner, W., and Schmitz Jr, W. J. (1982). On the transport and modification of Antarctic Bottom Water in the Vema Channel. *J. Mar. Res.*, 40(23):l–263.

Holton, J. R. (1983). The influence of gravity wave breaking on the general circulation of the middle atmosphere. *J. Atmos. Sci.*, 40(10):2497–2507.

Hoskins, B. J. and Bretherton, F. P. (1972). Atmospheric frontogenesis models: Mathematical formulation and solution. *J. Atmos. Sci.*, 29(1):11–37.

Huussen, T. N., Naveira-Garabato, A. C., Bryden, H. L., and McDonagh, E. L. (2012). Is the deep Indian Ocean MOC sustained by breaking internal waves? *J. Geophys. Res.-Oceans*, 117(C8).

Ilıcak, M. (2014). Energetics and mixing efficiency of lock-exchange flow. *Ocean Model.*, 83:1–10.

IOC, SCOR, and IAPSO (2010). The international thermodynamic equation of seawater 2010: Calculation and use of thermodynamic properties. Intergovernmental Oceanographic Commission, Manuals and Guides No. 56, UNESCO (English), 196 pp.

Jackett, D. R. and McDougall, T. J. (1997). A neutral density variable for the world's oceans. *J. Phys. Oceanogr.*, 27(2):237–263.

Jayne, S. R. (2009). The impact of abyssal mixing parameterizations in an ocean general circulation model. *J. Phys. Oceanogr.*, 39(7):1756–1775.

Jayne, S. R. and St. Laurent, L. C. (2001). Parameterizing tidal dissipation over rough topography. *Geophys. Res. Letters*, 28(5):811–814.

Jensen, F. B., Kuperman, W. A., Porter, M. B., and Schmidt, H. (2000). *Computational ocean acoustics*. Springer Science & Business Media.

Jiang, J., Lu, Y., and Perrie, W. (2005). Estimating the energy flux from the wind to ocean inertial motions: The sensitivity to surface wind fields. *Geophys. Res. Letters*, 32(15).

Jochum, M. (2009). Impact of latitudinal variations in vertical diffusivity on climate simulations. *J. Geophys. Res.-Oceans*, 114(C1).

Jochum, M., Briegleb, B. P., Danabasoglu, G., Large, W. G., Norton, N. J., Jayne, S. R., Alford, M. H., and Bryan, F. O. (2013). The impact of oceanic near-inertial waves on climate. *J. Climate*, 26(9):2833–2844.

Johnson, G. C. and Bryden, H. L. (1989). On the size of the Antarctic Circumpolar Current. *Deep-Sea Res. Pt. I*, 36(1):39–53.

Johnston, T. M., Rudnick, D. L., Alford, M. H., Pickering, A., and Simmons, H. L. (2013). Internal tidal energy fluxes in the South China Sea from density and velocity measurements by gliders. *J. Geophys. Res.-Oceans*, 118(8):3939–3949.

Jurgenowski, P., Olbers, D., and Eden, C. (2017). Wind-driven radiation of internal gravity waves from the surface mixed layer. *J. Phys. Oceanogr., submitted*.

Katija, K. and Dabiri, J. O. (2009). A viscosity-enhanced mechanism for biogenic ocean mixing. *Nature*, 460(7255):624–626.

Kawaguchi, Y., Nishino, S., Inoue, J., Maeno, K., Takeda, H., and Oshima, K. (2016). Enhanced diapycnal mixing due to near-inertial internal waves propagating through an anticyclonic eddy in the ice-free Chukchi Plateau. *J. Phys. Oceanogr.*, 46(8).

Kelley, D. E., Fernando, H. J. S., Gargett, A. E., Tanny, J., and Özsoy, E. (2003). The diffusive regime of double-diffusive convection. *Prog. Oceanogr.*, 56(3):461–481.

Kelly, S. M., Jones, N. L., Nash, J. D., and Waterhouse, A. F. (2013). The geography of semidiurnal mode-1 internal-tide energy loss. *Geophys. Res. Letters*, 40(17):4689–4693.

Khatiwala, S. (2003). Generation of internal tides in an ocean of finite depth: analytical and numerical calculations. *Deep-Sea Res. Pt. I*, 50(1):3–21.

Klocker, A. and McDougall, T. J. (2010). Influence of the nonlinear equation of state on global estimates of dianeutral advection and diffusion. *J. Phys. Oceanogr.*, 40(8):1690–1709.

Klymak, J. M. and Gregg, M. C. (2004). Tidally generated turbulence over the Knight Inlet sill. *J. Phys. Oceanogr.*, 34(5):1135–1151.

Klymak, J. M., Legg, S. M., and Pinkel, R. (2010). A simple parameterization of turbulent tidal mixing near supercritical topography. *J. Phys. Oceanogr.*, 40(9):2059–2074.

Klymak, J. M., Moum, J. N., Nash, J. D., Kunze, E., Girton, J. B., Carter, G. S., Lee, C. M., Sanford, T. B., and Gregg, M. C. (2006). An estimate of tidal energy lost to turbulence at the Hawaiian Ridge. *J. Phys. Oceanogr.*, 36(6):1148–1164.

Klymak, J. M. and Nash, J. D. (2009). Estimates of Mixing. In Steele, J. H., Turekian, K. K., and Thorpe, S. A., editors, *Encyclopedia of Ocean Sciences*, pages 3696–3706. Academic Press.

Klymak, J. M., Pinkel, R., and Rainville, L. (2008). Direct breaking of the internal tide near topography: Kaena Ridge, Hawaii. *J. Phys. Oceanogr.*, 38(2):380–399.

Koch-Larrouy, A., Lengaigne, M., Terray, P., Madec, G., and Masson, S. (2010). Tidal mixing in the Indonesian Seas and its effect on the tropical climate system. *Climate Dyn.*, 34(6):891–904.

Kolmogorov, A. N. (1941a). On the degeneration of isotropic turbulence in an incompressible viscous fluid. In *Dokl. Akad. Nauk SSSR*, volume 31, pages 319–323.

Kolmogorov, A. N. (1941b). The local structure of turbulence in incompressible viscous fluid for very large Reynolds numbers. In *Dokl. Akad. Nauk SSSR*, volume 30, pages 299–303.

Koltermann, K. P., Gouretski, V., and Jancke, K. (2011). *Hydrographic Atlas of the World Ocean Circulation Experiment (WOCE): Volume 3: Atlantic Ocean*. National Oceanography Centre.

Kuhlbrodt, T., Griesel, A., Montoya, M., Levermann, A., Hofmann, M., and Rahmstorf, S. (2007). On the driving processes of the Atlantic meridional overturning circulation. *Rev. Geophys.*, 45(2).

Kunze, E. (1985). Near-inertial wave propagation in geostrophic shear. *J. Phys. Oceanogr.*, 15(5):544–565.

Kunze, E., Dower, J. F., Beveridge, I., Dewey, R., and Bartlett, K. P. (2006a). Observations of biologically generated turbulence in a coastal inlet. *Science*, 313(5794):1768–1770.

Kunze, E., Firing, E., Hummon, J. M., Chereskin, T. K., and Thurnherr, A. M. (2006b). Global abyssal mixing inferred from lowered ADCP shear and CTD strain profiles. *J. Phys. Oceanogr.*, 36(8):1553–1576.

Kunze, E. and Llewellyn Smith, S. (2004). The role of small-scale topography in turbulent mixing of the global ocean. *Oceanography*, 17(1):55–64.

Large, W. G., McWilliams, J. C., and Doney, S. C. (1994). Oceanic vertical mixing: A review and a model with a nonlocal boundary layer parameterization. *Rev. Geophys.*, 32(4):363–403.

Ledwell, J. R., Montgomery, E. T., Polzin, K. L., St. Laurent, L. C., Schmitt, R. W., and Toole, J. M. (2000). Evidence for enhanced mixing over rough topography in the abyssal ocean. *Nature*, 403(6766):179–182.

Ledwell, J. R. and Watson, A. J. (1991). The Santa Monica Basin tracer experiment: A study of diapycnal and isopycnal mixing. *J. Geophys. Res.-Oceans*, 96(C5):8695–8718.

Ledwell, J. R., Watson, A. J., and Law, C. S. (1993). Evidence for slow mixing across the pycnocline from an open-ocean tracer-release experiment. *Nature*, 364(6439):701–703.

Ledwell, J. R., Watson, A. J., and Law, C. S. (1998). Mixing of a tracer in the pycnocline. *J. Geophys. Res.-Oceans*, 103(C10):21499–21529.

Legg, S. M., Hallberg, R. W., and Girton, J. B. (2006). Comparison of entrainment in overflows simulated by z-coordinate, isopycnal and non-hydrostatic models. *Ocean Model.*, 11(1):69–97.

Lhermitte, R. and Serafin, R. (1984). Pulse-to-pulse coherent Doppler sonar signal processing techniques. *J. Atm. Ocean. Techn.*, 1(4):293–308.

Li, M., Zahariev, K., and Garrett, C. J. R. (1995). Role of Langmuir circulation in the deepening of the ocean surface mixed layer. *Science*, 270(5244):1955.

Lighthill, M. J. (1952). On sound generated aerodynamically. I. General theory. *Proc. R. Soc. A*, 211(1107):564–587.

Lindzen, R. S. (1981). Turbulence and stress owing to gravity wave and tidal breakdown. *J. Geophys. Res.-Oceans*, 86(C10):9707–9714.

Llewellyn Smith, S. G. and Young, W. R. (2002). Conversion of the barotropic tide. *J. Phys. Oceanogr.*, 32(5):1554–1566.

MacKinnon, J. A. (2013). Oceanography: Mountain waves in the deep ocean. *Nature*, 501(7467):321–322.

MacKinnon, J. A., Alford, M. H., Ansong, J. K., Arbic, B. K., Barna, A., Briegleb, B. P., Bryan, F. O., Buijsman, M. C., Chassignet, E. P., Danabasoglu, G., et al. (2017). Climate Process Team on Internal-Wave Driven Ocean Mixing. *Bull. Amer. Meteor. Soc.*

MacKinnon, J. A. and Gregg, M. C. (2003). Mixing on the late-summer New England Shelf-solibores, shear, and stratification. *J. Phys. Oceanogr.*, 33(7):1476–1492.

MacKinnon, J. A. and Winters, K. B. (2005). Subtropical catastrophe: Significant loss of low-mode tidal energy at 28.9. *Geophys. Res. Letters*, 32(15).

Madec, G. (2008). *NEMO ocean engine*. Note du Pôle de modélisation, Institut Pierre-Simon Laplace (IPSL), France, No 27, ISSN No 1288-1619.

Mashayek, A., Caulfield, C. P., and Peltier, W. R. (2013). Time-dependent, non-monotonic mixing in stratified turbulent shear flows: Implications for oceanographic estimates of buoyancy flux. *J. Fluid Mech.*, 736:570–593.

McComas, C. H. and Bretherton, F. P. (1977). Resonant interaction of oceanic internal waves. *J. Geophys. Res.*, 82(9):1397–1412.

McComas, C. H. and Müller, P. (1981). The dynamic balance of internal waves. *J. Phys. Oceanogr.*, 11(7):970–986.

McDougall, T. J. (1987). Neutral surfaces. *J. Phys. Oceanogr.*, 17(11):1950–1964.

McDougall, T. J. (2003). Potential enthalpy: A conservative oceanic variable for evaluating heat content and heat fluxes. *J. Phys. Oceanogr.*, 33(5):945–963.

Melet, A., Hallberg, R. W., Legg, S. M., and Nikurashin, M. (2014). Sensitivity of the ocean state to lee wave–driven mixing. *J. Phys. Oceanogr.*, 44(3):900–921.

Melet, A., Legg, S. M., and Hallberg, R. W. (2016). Climatic impacts of parameterized local and remote tidal mixing. *J. Climate*, 29(10):3473–3500.

Melet, A., Nikurashin, M., Muller, C., Falahat, S., Nycander, J., Timko, P. G., Arbic, B. K., and Goff, J. A. (2013a). Internal tide generation by abyssal hills using analytical theory. *J. Geophys. Res.-Oceans*, 118(11):6303–6318.

Melet, A.and Hallberg, R. W., Legg, S. M., and Polzin, K. L. (2013b). Sensitivity of the ocean state to the vertical distribution of internal-tide-driven mixing. *J. Phys. Oceanogr.*, 43(3):602–615.

Mellor, G. L. and Yamada, T. (1982). Development of a turbulence closure model for geophysical fluid problems. *Rev. Geophys.*, 20(4):851–875.

Molemaker, M. J., McWilliams, J. C., and Capet, X. (2010). Balanced and unbalanced routes to dissipation in an equilibrated Eady flow. *J. Fluid Mech.*, 654:35–63.

Molemaker, M. J., McWilliams, J. C., and Yavneh, I. (2005). Baroclinic instability and loss of balance. *J. Phys. Oceanogr.*, 35(9):1505–1517.

Molenkamp, C. R. (1968). Accuracy of finite-difference methods applied to the advection equation. *J. Appl. Meteor.*, 7(2):160–167.

Moum, J. N., Farmer, D. M., Smyth, W. D., Armi, L., and Vagle, S. (2003). Structure and generation of turbulence at interfaces strained by internal solitary waves propagating shoreward over the continental shelf. *J. Phys. Oceanogr.*, 33(10):2093–2112.

Moum, J. N., Gregg, M. C., Lien, R. C., and Carr, M. E. (1995). Comparison of turbulence kinetic energy dissipation rate estimates from two ocean microstructure profilers. *J. Atm. Ocean. Techn.*, 12:346–366.

Müller, P. and Briscoe, M. G. (1999). Diapycnal mixing and internal waves. In *Dynamics of oceanic internal gravity waves, II. Proceedings Aha Huliko'a Hawaiian Winter Workshop*, pages 289–294. DTIC Document.

Müller, P., Holloway, G., Henyey, F., and Pomphrey, N. (1986). Nonlinear interactions among internal gravity waves. *Rev. Geophys.*, 24(3):493–536.

Müller, P. and Natarov, A. (2003). The internal wave action model (IWAM). In *Proceedings, Aha Huliko'a Hawaiian Winter Workshop, School of Ocean and Earth Science and Technology, Special Publication*, pages 95–105.

Müller, P. and Olbers, D. (1975). On the dynamics of internal waves in the deep ocean. *J. Geophys. Res.*, 80(27):3848–3860.

Müller, P., Olbers, D., and Willebrand, J. (1978). The IWEX spectrum. *J. Geophys. Res.-Oceans*, 83(C1):479–500.

Müller, P. and Xu, N. (1992). Scattering of oceanic internal gravity waves off random bottom topography. *J. Phys. Oceanogr.*, 22(5):474–488.

Munk, W. H. (1966). Abyssal recipes. *Deep-Sea Res. Oceanogr. Abstr.*, 13(4):707–730.

Munk, W. H. (1981). Internal waves and small-scale processes. In Warren, B. A. and Wunsch, C., editors, *Evolution of physical oceanography*, pages 264–291. The MIT Press Cambridge, MA.

Munk, W. H. and Anderson, E. R. (1948). Notes on the theory of the thermocline. *J. Mar. Res.*, 3:276–295.

Munk, W. H. and Wunsch, C. (1998). Abyssal recipes II: energetics of tidal and wind mixing. *Deep-Sea Res. Pt. I*, 45(12):1977–2010.

Nagasawa, M., Hibiya, T., Niwa, Y., Watanabe, M., Isoda, Y., Takagi, S., and Kamei, Y. (2002). Distribution of fine-scale shear in the deep waters of the North Pacific obtained using expendable current profilers. *J. Geophys. Res.-Oceans*, 107(C12).

Nakamura, H. (1992). Midwinter suppression of baroclinic wave activity in the Pacific. *J. Atmos. Sci.*, 49(17):1629–1642.

Neelin, J. D., Battisti, D. S., Hirst, A. C., Jin, F.-F., Wakata, Y., Yamagata, T., and Zebiak, S. E. (1998). ENSO theory. *J. Geophys. Res.-Oceans*, 103(C7):14261–14290.

Nikurashin, M. and Ferrari, R. (2010). Radiation and dissipation of internal waves generated by geostrophic motions impinging on small-scale topography: Theory. *J. Phys. Oceanogr.*, 40(5):1055–1074.

Nikurashin, M. and Ferrari, R. (2011). Global energy conversion rate from geostrophic flows into internal lee waves in the deep ocean. *Geophys. Res. Letters*, 38(8).

Niwa, Y. and Hibiya, T. (2004). Three-dimensional numerical simulation of M2 internal tides in the East China Sea. *J. Geophys. Res.-Oceans*, 109(C4).

Nycander, J. (2005). Generation of internal waves in the deep ocean by tides. *J. Geophys. Res.-Oceans*, 110(C10).

Nycander, J. (2006). Tidal generation of internal waves from a periodic array of steep ridges. *J. Fluid Mech.*, 567:415–432.

Nycander, J. (2011). Energy conversion, mixing energy, and neutral surfaces with a nonlinear equation of state. *J. Phys. Oceanogr.*, 41(1):28–41.

Oka, A. and Niwa, Y. (2013). Pacific deep circulation and ventilation controlled by tidal mixing away from the sea bottom. *Nat. Commun.*, 4:2419.

Olbers, D. (1974). *On the energy balance of small-scale internal waves in the deep sea*. Number 24 in Hamb. Geophys. Einzelschr. G. M. L. Wittenborn.

Olbers, D. (1976). Nonlinear energy transfer and the energy balance of the internal wave field in the deep ocean. *J. Fluid Mech.*, 74(02):375–399.

Olbers, D. (1981). The propagation of internal waves in a geostrophic current. *J. Phys. Oceanogr.*, 11(9):1224–1233.

Olbers, D. (1983). Models of the oceanic internal wave field. *Rev. Geophys.*, 21(7):1567–1606.

Olbers, D. and Eden, C. (2013). A global model for the diapycnal diffusivity induced by internal gravity waves. *J. Phys. Oceanogr.*, 43(8):1759–1779.

Olbers, D. and Eden, C. (2016). Revisiting the generation of internal waves by resonant interaction with surface waves. *J. Phys. Oceanogr.*, 46(8):2335–2350.

Olbers, D. and Eden, C. (2017). A closure for internal wave-mean flow interaction. Part A: Energy conversion. *J. Phys. Oceanogr.*, 47.

Olbers, D. and Herterich, K. (1979). The spectral energy transfer from surface waves to internal waves. *J. Fluid Mech.*, 92(02):349–379.

Olbers, D. and Visbeck, M. (2005). A model of the zonally averaged stratification and overturning in the Southern Ocean. *J. Phys. Oceanogr.*, 35(7):1190–1205.

Olbers, D., Wenzel, M., and Willebrand, J. (1985). The inference of North Atlantic circulation patterns from climatological hydrographic data. *Rev. Geophys.*, 23(4):313–356.

Olbers, D., Willebrand, J., and Eden, C. (2012). *Ocean dynamics*. Springer-Verlag Berlin Heidelberg.

Osborn, T.-R. (1974). Vertical profiling of velocity microstructure. *J. Phys. Oceanogr.*, 4(1):109–115.

Osborn, T. R. (1980). Estimates of the local rate of vertical diffusion from dissipation measurements. *J. Phys. Oceanogr.*, 10(1):83–89.

Osborn, T. R. and Cox, C. S. (1972). Oceanic fine structure. *Geophys. Astro. Fluid*, 3(1):321–345.

Pacanowski, R. C. and Philander, S. G. H. (1981). Parameterization of vertical mixing in numerical models of tropical oceans. *J. Phys. Oceanogr.*, 11(11):1443–1451.

Peeters, F., Kerimoglu, O., and Straile, D. (2013). Implications of seasonal mixing for phytoplankton production and bloom development. *Theor. Ecol.*, 6(2):115–129.

Peltier, W. R. and Caulfield, C. P. (2003). Mixing efficiency in stratified shear flows. *Annu. Rev. Fluid Mech.*, 35(1):135–167.

Pétrélis, F., Llewellyn Smith, S., and Young, W. R. (2006). Tidal conversion at a submarine ridge. *J. Phys. Oceanogr.*, 36(6):1053–1071.

Pinkel, R. (1979). Observations of strongly nonlinear internal motion in the open sea using a range-gated Doppler sonar. *J. Phys. Oceanogr.*, 9(4):675–686.

Polzin, K. L. (2004). A heuristic description of internal wave dynamics. *J. Phys. Oceanogr.*, 34(1):214–230.

Polzin, K. L. (2009). An abyssal recipe. *Ocean Model.*, 30(4):298–309.

Polzin, K. L. (2010). Mesoscale eddy-internal wave coupling. Part II: Energetics and results from POLYMODE. *J. Phys. Oceanogr.*, 40(4):789–801.

Polzin, K. L. and Lvov, Y. V. (2011). Toward regional characterizations of the oceanic internal wavefield. *Rev. Geophys.*, 49(4).

Polzin, K. L. and Montgomery, E. T. (1996). Microstructure profiling with the high resolution profiler. In *Proc. Microstructure Sensor Workshop*, pages 109–115.

Polzin, K. L., Naveira Garabato, A. C., Huussen, T. N., Sloyan, B. M., and Waterman, S. (2014). Finescale parameterizations of turbulent dissipation. *J. Geophys. Res.-Oceans*, 119(2):1383–1419.

Polzin, K. L., Toole, J. M., Ledwell, J. R., and Schmitt, R. W. (1997). Spatial variability of turbulent mixing in the abyssal ocean. *Science*, 276(5309):93–96.

Polzin, K. L., Toole, J. M., and Schmitt, R. W. (1995). Finescale parameterizations of turbulent dissipation. *J. Phys. Oceanogr.*, 25(3):306–328.

Pomphrey, N., Meiss, J. D., and Watson, K. M. (1980). Description of nonlinear internal wave interactions using Langevin methods. *J. Geophys. Res.-Oceans*, 85(C2):1085–1094.

Pugh, D. T. (1996). *Tides, surges and mean sea-level.* John Wiley & Sons Ltd.

Reffray, G., Bourdalle-Badie, R., and Calone, C. (2015). Modelling turbulent vertical mixing sensitivity using a 1-D version of NEMO. *Geosci. Model Dev.*, 8(1):69–86.

Rennau, H. (2011). *Natural, Numerical and Structure-induced Mixing in Dense Gravity Currents: Idealised and Realistic Model Studies*. Dissertation, Universität Rostock.

Richardson, L. F. (1920). The supply of energy from and to atmospheric eddies. *Proc. R. Soc. A*, 97(686):354–373.

Rimac, A., Storch, J.-S., Eden, C., and Haak, H. (2013). The influence of high-resolution wind stress field on the power input to near-inertial motions in the ocean. *Geophys. Res. Letters*, 40(18):4882–4886.

Rimac, A., von Storch, J.-S., and Eden, C. (2016). The total energy flux leaving the ocean's mixed layer. *J. Phys. Oceanogr.*, 46(6):1885–1900.

Riser, S. C., Freeland, H. J., Roemmich, D., Wijffels, S., Troisi, A., Belbéoch, M., Gilbert, D., Xu, J., Pouliquen, S., Thresher, A., et al. (2016). Fifteen years of ocean observations with the global Argo array. *Nat. Clim. Change*, 6(2):145–153.

Robinson, R. M. (1969). The effects of a vertical barrier on internal waves. *Deep-Sea Res. Oceanogr. Abstr.*, 16(5):421–429.

Rodi, W. (1987). Examples of calculation methods for flow and mixing in stratified fluids. *J. Geophys. Res.-Oceans*, 92(C5):5305–5328.

Roemmich, D., Boebel, O., Desaubies, Y., Freeland, H., Kim, K., King, B., Le Traon, P.-Y., Molinari, R., Owens, B. W., Riser, S., et al. (2001). Argo: The global array of profiling floats. Technical report, Scripps Institution of Oceanography, University of California, San Diego.

Roquet, F., Williams, G., Hindell, M. A., Harcourt, R., McMahon, C., Guinet, C., Charrassin, J.-B., Reverdin, G., Boehme, L., Lovell, P., et al. (2014). A Southern Indian Ocean database of hydrographic profiles obtained with instrumented elephant seals. *Sci. Data*, 1.

Rye, C. D., Messias, M.-J., Ledwell, J. R., Watson, A. J., Brousseau, A., and King, B. A. (2012). Diapycnal diffusivities from a tracer release experiment in the deep sea, integrated over 13 years. *Geophys. Res. Letters*, 39(4).

Samelson, R. M. (1998). Large-scale circulation with locally enhanced vertical mixing. *J. Phys. Oceanogr.*, 28(4):712–726.

Sarkar, S. and Scotti, A. (2017). From topographic internal gravity waves to turbulence. *Annu. Rev. Fluid Mech.*, 49:195–220.

Schmitt, R. W. (1998). Double-diffusive convection. In Chassignet, E. P. and Verron, J., editors, *Ocean modeling and parameterization*, pages 215–234. Springer International Publishing.

Schmitt, R. W., Ledwell, J. R., Montgomery, E. T., Polzin, K. L., and Toole, J. M. (2005). Enhanced diapycnal mixing by salt fingers in the thermocline of the tropical Atlantic. *Science*, 308(5722):685–688.

Schott, F. and Zantopp, R. (1980). On the effect of vertical mixing on the determination of absolute currents by the beta spiral method. *Deep-Sea Res. Pt. I*, 27(2):173–180.

Scott, R. B., Goff, J. A., Naveira Garabato, A. C., and Nurser, A. J. G. (2011). Global rate and spectral characteristics of internal gravity wave generation by geostrophic flow over topography. *J. Geophys. Res.-Oceans*, 116(C9).

Sheen, K. L., Brearley, J. A., Naveira Garabato, A. C., Smeed, D. A., Waterman, S., Ledwell, J. R., Meredith, M. P., St. Laurent, L. C., Thurnherr, A. M., Toole, J. M., et al. (2013). Rates and mechanisms of turbulent dissipation and mixing in the Southern Ocean: Results from the Diapycnal and Isopycnal Mixing Experiment in the Southern Ocean (DIMES). *J. Geophys. Res.-Oceans*, 118(6):2774–2792.

Simmons, H. L. and Alford, M. H. (2012). Simulating the long-range swell of internal waves generated by ocean storms. *Oceanography*, 25(2):30–41.

Simmons, H. L., Jayne, S. R., St. Laurent, L. C., and Weaver, A. J. (2004). Tidally driven mixing in a numerical model of the ocean general circulation. *Ocean Model.*, 6(3):245–263.

Smyth, W. D., Moum, J. N., and Caldwell, D. R. (2001). The efficiency of mixing in turbulent patches: Inferences from direct simulations and microstructure observations. *J. Phys. Oceanogr.*, 31(8):1969–1992.

St. Laurent, L. C., Alford, M. H., and Paluszkiewicz, T. (2012). An introduction to the special issue on internal waves. *Oceanography*, 2(25):15–19.

St. Laurent, L. C. and Garrett, C. J. R. (2002). The role of internal tides in mixing the deep ocean. *J. Phys. Oceanogr.*, 32(10):2882–2899.

St. Laurent, L. C., Simmons, H. L., and Jayne, S. R. (2002). Estimating tidally driven mixing in the deep ocean. *Geophys. Res. Letters*, 29(23).

Stevenson, P. M. (1981). Optimized perturbation theory. *Phys. Rev. D*, 23(12):2916.

Stommel, H. and Schott, F. (1977). The beta spiral and the determination of the absolute velocity field from hydrographic station data. *Deep-Sea Res.*, 24(3):325–329.

Subramanian, G. (2010). Viscosity-enhanced bio-mixing of the oceans. *Curr. Sci*, 98(8):1103–1108.

Sun, H. and Kunze, E. (1999). Internal wave-wave interactions. Part II: Spectral energy transfer and turbulence production. *J. Phys. Oceanogr.*, 29(11):2905–2919.

Swallow, J. C. (1955). A neutral-buoyancy float for measuring deep currents. *Deep-Sea Res.*, 3(1):74–81.

Tailleux, R. (2012). Thermodynamics/dynamics coupling in weakly compressible turbulent stratified fluids. *ISRN Thermodynamics*, 2012.

Talley, L. D. (2013). Closure of the global overturning circulation through the Indian, Pacific, and Southern Oceans: Schematics and transports. *Oceanography*, 26(1):80–97.

Taylor, G. I. (1935). Statistical theory of turbulence. *Proc. R. Soc. A*, 151(873):421–444.

Thomas, W. H. and Gibson, C. H. (1990). Quantified small-scale turbulence inhibits a red tide dinoflagellate, *Gonyaulax polyedra* Stein. *Deep-Sea Res. Pt. I*, 37(10):1583–1593.

Thomson, R. E. and Emery, W. J. (2014). *Data analysis methods in physical oceanography*. Newnes.

Thorpe, S. A. (1973). Experiments on instability and turbulence in a stratified shear flow. *J. Fluid Mech.*, 61(4):731–751.

Thorpe, S. A. (1977). Turbulence and mixing in a Scottish loch. *Phil. Trans. R. Soc. A*, 286(1334):125–181.

Thorpe, S. A. (2007). *An introduction to ocean turbulence*. Cambridge University Press.

Thurnherr, A. M. and St. Laurent, L. C. (2012). Turbulence observations in a buoyant hydrothermal plume on the East Pacific Rise. *Oceanography*.

Toggweiler, J. R. and Key, R. M. (2003). Thermohaline circulation. In Thorpe, S. A. and Turekian, K. K., editors, *Encyclopedia of Ocean Sciences*. Academic Press.

Toggweiler, J. R. and Samuels, B. (1995). Effect of Drake Passage on the global thermohaline circulation. *Deep-Sea Res. Pt. I*, 42(4):477–500.

Toole, J. M., Ledwell, J. R., Polzin, K. L., Schmitt, R. W., Montgomery, E. T., St. Laurent, L. C., and Owens, W. B. (1997). The Brazil Basin tracer release experiment. *WOCE Newsletter*, 28:25–28.

Toole, J. M., Schmitt, R. W., and Polzin, K. L. (1994). Estimates of diapycnal mixing in the abyssal ocean. *Science*, 264(5162):1120–1123.

Trefethen, L. N. (1996). *Finite difference and spectral methods for ordinary and partial differential equations*. Cornell University-Department of Computer Science and Center for Applied Mathematics.

Umlauf, L. and Burchard, H. (2003). A generic length-scale equation for geophysical turbulence models. *J. Mar. Res.*, 61(2):235–265.

Vanneste, J. (2013). Balance and spontaneous wave generation in geophysical flows. *Annu. Rev. Fluid Mech.*, 45:147–172.

Visser, A. W. (2007). Biomixing of the oceans? *Science*, 316(5826):838.

von Storch, H. and Zwiers, F. W. (2001). *Statistical analysis in climate research*. Cambridge University Press.

Warner, S. J. and MacCready, P. (2014). The dynamics of pressure and form drag on a sloping headland: Internal waves versus eddies. *J. Geophys. Res.-Oceans*, 119(3):1554–1571.

Watanabe, M. and Hibiya, T. (2002). Global estimates of the wind-induced energy flux to inertial motions in the surface mixed layer. *Geophys. Res. Letters*, 29(8).

Waterhouse, A. F., MacKinnon, J. A., Nash, J. D., Alford, M. H., Kunze, E., Simmons, H. L., Polzin, K. L., St. Laurent, L. C., Sun, O. M., Pinkel, R., et al. (2014). Global patterns of diapycnal mixing from measurements of the turbulent dissipation rate. *J. Phys. Oceanogr.*, 44(7):1854–1872.

Waterman, S., Naveira Garabato, A. C., and Polzin, K. L. (2013). Internal waves and turbulence in the Antarctic Circumpolar Current. *J. Phys. Oceanogr.*, 43(2):259–282.

Watson, A. J., Messias, M. J., Fogelqvist, E., Van Scoy, K. A., et al. (1999). Mixing and convection in the Greenland Sea from a tracer-release experiment. *Nature*, 401(6756):902.

Whalen, C. B., MacKinnon, J. A., Talley, L. D., and Waterhouse, A. F. (2015). Estimating the mean diapycnal mixing using a finescale strain parameterization. *J. Phys. Oceanogr.*, 45(4):1174–1188.

Whalen, C. B., Talley, L. D., and MacKinnon, J. A. (2012). Spatial and temporal variability of global ocean mixing inferred from Argo profiles. *Geophys. Res. Letters*, 39(18).

Whitehead, J. A. and Worthington, L. V. (1982). The flux and mixing rates of Antarctic Bottom Water within the North Atlantic. *J. Geophys. Res.-Oceans*, 87(C10):7903–7924.

Wijesekera, H., Padman, L., Dillon, T., Levine, M., Paulson, C., and Pinkel, R. (1993). The application of internal-wave dissipation models to a region of strong mixing. *J. Phys. Oceanogr.*, 23.

Wilcox, D. C. (1988). Reassessment of the scale-determining equation for advanced turbulence models. *AIAA J.*, 26(11):1299–1310.

Willebrand, J., Müller, P., and Olbers, D. (1977). Inverse analysis of the Trimoored Internal Wave Experiment (IWEX) – Part 1. *Ber. Inst. f. Meereskunde Kiel, 20a*, pages 1–117.

Wilson, J. F. (2003). *Dynamics of offshore structures.* John Wiley & Sons.

Wong, A. P. S., Johnson, G. C., and Owens, W. B. (2003). Delayed-mode calibration of autonomous CTD profiling float salinity data by θ–S climatology. *J. Atm. Ocean. Techn.*, 20(2):308–318.

Wong, A. P. S., Keeley, R., Carval, T., and the Argo Data Management Team (2015). *Argo Quality Control Manual For CTD and Trajectory Data*. http://dx.doi.org/10.13155/33951.

Wright, C. J., Scott, R. B., Ailliot, P., and Furnival, D. (2014). Lee wave generation rates in the deep ocean. *Geophys. Res. Letters*, 41(7):2434–2440.

Wu, L., Jing, Z., Riser, S., and Visbeck, M. (2011). Seasonal and spatial variations of Southern Ocean diapycnal mixing from Argo profiling floats. *Nat. Geosci.*, 4(6):363.

Wunsch, C. and Ferrari, R. (2004). Vertical mixing, energy, and the general circulation of the oceans. *Annu. Rev. Fluid Mech.*, 36:281–314.

Young, W. R. (2010). Dynamic enthalpy, conservative temperature, and the seawater Boussinesq approximation. *J. Phys. Oceanogr.*, 40(2):394–400.

Young, W. R. and Jelloul, M. B. (1997). Propagation of near-inertial oscillations through a geostrophic flow. *J. Mar. Res.*, 55(4):735–766.

Zappa, C. J., McGillis, W. R., Raymond, P. A., Edson, J. B., Hintsa, E. J., Zemmelink, H. J., Dacey, J. W. H., and Ho, D. T. (2007). Environmental turbulent mixing controls on air-water gas exchange in marine and aquatic systems. *Geophys. Res. Letters*, 34(10).

Zeilon, N. (1912). *On tidal boundary-waves and related hydrodynamical problems*. Kungl. Svenska vetenskapsakademiens handlingar.

Zhang, J., Schmitt, R. W., and Huang, R. X. (1999). The relative influence of diapycnal mixing and hydrologic forcing on the stability of the thermohaline circulation. *J. Phys. Oceanogr.*, 29(6):1096–1108.

Zhao, Z. and Alford, M. H. (2009). New altimetric estimates of mode-1 M2 internal tides in the central North Pacific Ocean. *J. Phys. Oceanogr.*, 39(7):1669–1684.

Zilberman, N. V., Becker, J. M., Merrifield, M. A., and Carter, G. S. (2009). Model estimates of M2 internal tide generation over Mid-Atlantic Ridge topography. *J. Phys. Oceanogr.*, 39(10):2635–2651.